

AMERICAN UNIVERSITY OF BEIRUT

NUMERICAL SIMULATION OF WALL-BOUNDED FLOWS
THROUGH SCREEN-TYPE STATIC MIXERS

by
WALID MOHAMAD JAMAL ABOU HWEIJ

A dissertation
submitted in partial fulfillment of the requirements
for the degree of Doctor of Philosophy
to the Department of Mechanical Engineering
of the Maroun Semaan Faculty of Engineering and Architecture
at the American University of Beirut

Beirut, Lebanon
April 2022

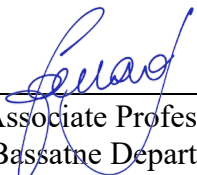
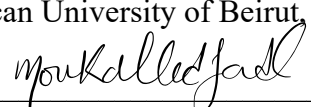
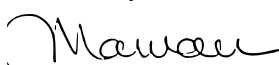
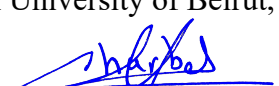

AMERICAN UNIVERSITY OF BEIRUT

NUMERICAL SIMULATION OF WALL-BOUNDED FLOWS
THROUGH SCREEN-TYPE STATIC MIXERS

by

WALID MOHAMAD JAMAL ABOU HWEIJ

Approved by:

 Dr. Fouad Azizi, Associate Professor Bahaa and Walid Bassatne Department of Chemical Engineering and Advanced Energy American University of Beirut, Lebanon	Advisor
 Dr. Fadl Moukalled, Professor Department of Mechanical Engineering American University of Beirut, Lebanon	Chair of Committee
 Dr. Marwan Darwish, Professor Department of Mechanical Engineering American University of Beirut, Lebanon	Member of Committee
 Dr. Charbel Habchi, Associate Professor Department of Mechanical Engineering Notre Dame University – Louaize, Lebanon	Member of Committee
 Dr. Talib Dbouk, Associate Professor Energy and Environment Research Center Institut Mines-Télécom Nord Europe, France	Member of Committee

Date of dissertation defense: April 26, 2022

ACKNOWLEDGEMENTS

Thank You, my Lord, Allah, for giving me the strength, patience, persistence, ambition, and the capability to achieve what I have achieved throughout my life. Please help me to always remember your Quotes in Quran “And my guidance cannot come except from Allah [Hud 88]”, “but over all those endowed with knowledge is the All-Knowing [Yousuf 76]”, “ and say: My Lord! Increase me in Knowledge [Taha 114]”, “It is only those who have knowledge among His servants that fear Allah [Fatir 28]”, and “Allah will exalt in degrees those of you who believe, and those who have been granted knowledge. And Allah is Well-Aquainted with what you do [Al-Mujadila 58]”.

I will always be grateful from deep inside to my research supervisor Dr. Fouad Azizi for his positive criticism, guidance, encouragement, and support throughout the course of this work. I am also grateful to the members of my Thesis guiding committee Dr. Fadl Moukalled, Dr. Marwan Darwish, Dr. Charbel Habchi, and Dr. Talib Dbouk for their interest and helpful comments.

I would also like to thank all the faculty and staff members at the Mechanical and Chemical Engineering Departments at the American University of Beirut for all their help throughout the past years.

The research computing team at AUB is highly appreciated. Special Thank you goes to Dr. Mher Kazandjian and Mr. Saadallah Itani.

I am indebted to my parents, Mohamad Jamal and Lina Abou Hweij, my brother Khaled, and my family for their constant support, encouragement, and dedication to my education.

Deepest gratitude is also expressed to my friends Ahmad Al Ghor, Hussein Daoud, Mohammad Ali Fakih, Mhamed Mahdi Allouch, Mohamad Hout, Mustafa kaddoura, Mohammad Ghadban, Abdelkader Baayoun, Mohamad Al Naser, Ali Al Abed, Ziad Ballouli, Mahmoud Abdallah, Manar Younis, and Mariam Itani for their support and understanding during the years of study.

ABSTRACT OF THE DISSERTATION OF

Walid Mohamad Jamal Abou Hweij

for

Doctor of Philosophy

Major: Mechanical Engineering

Title: Numerical Simulation of Wall-Bounded Flows through Screen-Type Static Mixers

Mixing is a critical operation in most chemical processes. It is found in a multitude of operations ranging from simple blending to complex multiphase flow contacting. While mechanically agitated tanks, bubble and packed columns were traditionally employed, many process industries are now shifting to in-line static mixing as an alternative mixing method because of their good performance at low operating costs and enhanced safety conditions. A multitude of designs is available on the market, one variant of them has proven efficient in processing multiphase operations. This relies on the use of woven meshes as screen-type static mixers (STSM).

This thesis numerically investigates the flow behavior and mixing performance of STSMs using single-phase flows under laminar and turbulent regimes. In addition, it proposes a new mixer design based on modifications to the flow through STSM in order to enhance their performances. For this purpose, a three-dimensional wall bounded flow model was developed and studied using computational fluid dynamics (CFD). The effect of varying the mixer geometry, number of mixer elements, inter-mixer spacing, and operating conditions on the hydrodynamics and mixing performance were detailed. The validation of the numerical results was performed by means of pressure drop measurements where a maximum relative error of 13.3% was recorded.

Under laminar flow conditions where the Reynolds number based on the empty pipe diameter (Re_{pipe}) ranged between 30 and 1850, screens were found capable of flattening the parabolic velocity profile until extended downstream distances. Moreover, the nature of the flow was found to be three-dimensional and cannot be simplified. Using a Lagrangian particle tracking technique, mixing was quantified, and screens were found inefficient at promoting radial mixing, however, this is counterbalanced by their high potential in delivering good dispersive mixing.

Under turbulent conditions where the Reynolds number varied between 9,000 and 56,000, the flow through screens revealed that the mean flow energy dissipation cannot be overlooked as it constitutes a major component of the total energy dissipation rate. In addition to the analysis of the velocity field, the study highlighted the high dispersive mixing potential of STSM and its low distributive mixing capability. Moreover, residence time distribution analysis showed that near plug flow conditions could be attained using these mixers.

Based on the outcome of these studies and to overcome the distributive mixing limitations of screen mixers a new design was proposed. It relies on the use of woven meshes in conjunction with specially designed downstream inserts. These inserts aimed at enhancing distributive mixing while maintaining the high dispersive action. The flow through this new mixer was then analyzed under turbulent conditions ($5,000 < (Re_{pipe}) < 30,000$) using a Eulerian approach. The results showed that the added cost of operation due to the presence of additional inserts is counterbalanced by further enhancing both dispersive and distributive mixing, where the new mixer provided about 95% homogenized flow, a feature which was almost absent in a STSM.

TABLE OF CONTENTS

ACKNOWLEDGEMENTS	1
ABSTRACT	2
ILLUSTRATIONS	9
TABLES	14
ABBREVIATIONS	15
1 INTRODUCTION	16
1.1 Background	16
1.2 Literature Review	21
1.2.1 Experimental investigations of flows through screens	23
1.2.2 Numerical investigations of flows through screens	25
1.3 Research statement	27
1.4 General methodology	28
1.5 Thesis Outline	31
2 CFD SIMULATION OF WALL-BOUNDED LAMINAR FLOW THROUGH SCREENS. PART I: HYDRODYNAMIC CHARACTERIZATION.....	33
Abstract	33
2.1 Introduction.....	34
2.2 Computational Methods.....	38
2.2.1 Computational domain.....	38

2.2.2	Boundary conditions and solution method	43
2.2.3	Grid independence	44
2.3	Results and discussion	45
2.3.1	Model validation	46
2.3.2	Hydrodynamic characterization	48
2.4	Conclusions.....	84
2.5	Nomenclature.....	85
2.6	Acknowledgements.....	87
2.7	References.....	88

3 CFD SIMULATION OF WALL-BOUNDED LAMINAR FLOW THROUGH SCREENS. PART II: MIXING CHARACTERIZATION.....92

Abstract.....	92
3.1 Introduction.....	93
3.2 Materials and Methods.....	94
3.2.1 Computational Domain.....	94
3.2.2 Model Validation	97
3.2.3 Mixing characterization	99
3.3 Results and discussions.....	107
3.3.1 Distributive mixing.....	107
3.3.2 Dispersive mixing.....	114
3.4 Conclusion	118
3.5 Nomenclature.....	118
3.6 Acknowledgments	122
3.7 References.....	122

4 HYDRODYNAMICS OF WALL-BOUNDED TURBULENT FLOWS THROUGH SCREENS: A NUMERICAL STUDY... 124

Abstract.....	124
4.1 Introduction.....	125
4.2 Computational methods	129
4.2.1 Computational Domain.....	129
4.2.2 Boundary conditions and solution methods.....	133
4.2.3 Grid Independence	136
4.3 Results and discussions.....	137
4.3.1 Model validation.....	137
4.3.2 Hydrodynamics Characterization	139
4.3.3 Macro-mixing characterization.....	157
4.4 Conclusion	161
4.5 Nomenclature.....	162
4.6 Acknowledgments	165
4.7 References.....	165

5 DESIGN OF A NOVEL STATIC MIXER..... 171

Abstract.....	171
5.1 Introduction.....	171
5.2 Methodology.....	173
5.2.1 Proposed mixer design.....	173
5.2.2 Computational domain.....	175
5.2.3 Boundary conditions and solution method	177
5.2.4 Mixing characterization	179
5.3 Results and discussion	182
5.3.1 Grid Independence.....	182
5.3.2 Model Validation	185
5.3.3 Hydrodynamic characterization.....	188
5.3.4 Mixing characterization	191

5.4	Comparison with other commercial static mixers	199
5.5	Conclusion	201
5.6	Nomenclature.....	201
5.7	Acknowledgments	204
5.8	References.....	204
6	CONCLUSIONS AND RECOMMENDATIONS	208
6.1	Hydrodynamics of laminar flows through STSM.....	208
6.2	Mixing performance of STSM under laminar flow conditions	208
6.3	Hydrodynamics of turbulent flows through STSM	209
6.4	Proposed enhanced mixer design.....	209
6.5	Recommendations.....	209
APPENDIX 1 COMPLEMENTARY INFORMATION		
REGARDING THE MACRO-MIXING CHARACTERIZATION		
WITHIN STSM USING RTD.....		
		211
1.1	RTD Theory.....	211
1.2	Method used for obtaining the RTD in ANSYS Fluent.....	213
APPENDIX 2 UDF AND MATLAB CODES		
		217
2.1	User defined function for the laminar parabolic profile	217
2.2	Grid convergence index (GCI)	217
2.3	Point to nearest neighbor	219
2.4	Mixing efficiency.....	222
2.5	Cumulative volume percentage for extensional efficiency.....	227
2.6	Residence time distribution (RTD).....	228

7	REFERENCES	232
---	------------------	-----

ILLUSTRATIONS

Figure

1.1. Commercially available in-line static mixers (Ghanem et al., 2013).	17
1.2. Schematic representation of a pipe equipped with plain square woven meshes.....	21
1.3. Schematic representation of a section of plain-square woven screen.....	22
2.1. Schematic representation of plain-square woven screen of (a) full screen geometry – rotated view and (b) section of screen – top view.	40
2.2. Schematic illustration of a woven mesh corresponding to $Mn = 80$ (a) quarter section of STSM and (b) sideview of the meshing regions.	42
2.3. Meshing configuration (a) boundary faces meshing, (b) interior body meshing, (c) screen meshing, and (d) magnified section of screen meshing.....	42
2.4. Euler number for an individual screen plotted against Re_b for the four screen geometries and compared to various empirical correlations. (a) Azizi (Azizi, 2019), (b) Bailey et al. (Bailey et al., 2003), and (c) Ehrhardt (Ehrhardt, 1983). Solid lines of varying colors refer to the correlation results for each specific screen geometry.	48
2.5. Normalized velocity components at the centerline as a function of non-dimensional axial position at different inter-screen spacing for $Mn = 20$ and $Mn = 80$ at (a) $Re_b = 1$ and (b) $Re_b = 20$ and (c) profiles zoomed around the 5 th screen for $4.4 < Z^* < 4.6$	54
2.6. Normalized velocity components at $1M$ from the wall as a function of non-dimensional axial position at different inter-screen spacing for $Mn = 20$ and $Mn = 80$ at (a) $Re_b = 1$ and (b) $Re_b = 20$ and (c) profiles zoomed around the 5 th screen for $4.4 < Z^* < 4.6$	58
2.7. Velocity contours through the 7 th screen at various axial locations at $Re_b = 20$ for $Mn = 20$ and $Mn = 80$	59
2.8. Vorticity contours through the 7 th screen at various axial locations at $Re_b = 20$ for $Mn = 20$ and $Mn = 80$	61
2.9. Velocity streamlines through the 1 st screen for different geometries at (a) $Re_b = 1$, (b) $Re_b = 10$, and (c) $Re_b = 20$	63
2.10. Velocity streamlines through the 1 st screen for different geometries, at $Re_{pipe} = 1,000$. ($Y = 0$ corresponds to the central axis and $Y = 6.35$ mm corresponds to the pipe wall).	64
2.11. Normalized axial velocity profile around the 1 st and the 2 nd screens for $L = 50$ mm at $Re_b = 1$ and $Re_b = 20$ for (a) $-4 \leq M^* \leq -0.5$ (b) $0 \leq M^* \leq 2$ and (c) Midway. ...	70
2.12. Normalized axial velocity profile around the 1 st and 2 nd screens for $L = 5$ mm at $Re_b = 1$ and $Re_b = 20$ for (a) $-2 \leq M^* \leq 0$ and (b) $0.5 \leq M^* \leq 2$ and Midway.....	73
2.13. Velocity streamlines for $Mn = 20$ at $Re_b = 20$ for (a) the first three screens for $L = 5$ mm and (b) first two screens for $L = 50$ mm. Red dotted lines refer to the halfway between two consecutive screens.	74

2.14. Position of upstream minimum and downstream maximum velocities for one screen in a pipe and $Re_b = 20$ along the central axis for (a) $Mn = 20$ and (b) $Mn = 80$, and along $1M$ from the wall for (c) $Mn = 20$ and (d) $Mn = 80$.	76
2.15. Parity plots showing the locations of the (a) minimum velocity and (b) maximum velocity for the flow through a screen.	77
2.16. Normalized pressure at $L = 50$ mm for $Mn = 20$ and $Mn = 80$ at $Re_b = 1$ and $Re_b = 20$.	79
2.17. Variation of the normalized pressure and normalized axial velocity around the screen for $Re_b = 20$ and $L = 50$ mm. (a) $Mn = 20$, centerline; (b) $Mn = 80$, centerline; (c) $Mn = 20$, at $1M$ from the wall; (d) $Mn = 80$, at $1M$ from the wall.	81
2.18. Normalized pressure at $L = 5$ mm for $Mn = 20$ and $Mn = 80$ at $Re_b = 1$ and $Re_b = 20$.	82
2.19. Variation of the normalized pressure and normalized axial velocity around the screen for $Re_b = 20$ and $L = 5$ mm. (a) $Mn = 20$, centerline; (b) $Mn = 80$, centerline; (c) $Mn = 20$, at $1M$ from the wall; (d) $Mn = 80$, at $1M$ from the wall.	82
2.20. Parity plot showing the location of the maximum velocity the flow through a screen	84
3.1. Schematic representation of STSM (a) quarter section and (b) section of screen – top view.	95
3.2. Geometric discretization	97
3.3. Model validation based on pressure drop for different screen geometries with one screen in a pipe.	99
3.4. Injection criteria (a) central injection of 1% inlet cross-section, (b) concentric injection with $r/r=0.5$	101
3.5. Illustration of the PNN method : (a) the hexagonal grid (Kukukova et al., 2011) , (b) search of the nearest neighbor of each grid point (Kukukova et al., 2011), (c) live grid points (red) and dead grid points (blue)	102
3.6. Distributive mixing representation for $Mn = 20$ at $L = 5$ mm and $Re_b = 20$ midway between consecutive screens, and outlet for the case of 1% central injection for (a) particles' dispersion and (b) PNN distribution	108
3.7. Distributive mixing representation at the pipe outlet for different screen geometries at $Re_b = 20$ and $L = 5$ mm for the case of 1% central injection	109
3.8. Filtered variance of the PNN method for different screen geometries and inter-screen spacing for the case of 1% central injection at (a) $Re_b = 1$ and (b) $Re_b = 20$	110
3.9. Normalized axial velocity profile at the midway between screens 2 and 3 for both screen geometries, inter-screen spacing, and operating conditions	112
3.10. Distributive mixing representation at the pipe outlet for different screen geometries and inter-screen spacing for the case of concentric injection at (a) $Re_b = 1$ and (b) $Re_b = 20$	114

3.11. Area weighted average of the extensional efficiency at different cross-sections along the axial direction of STSM for (a) $L = 5$ mm and (b) $L = 50$ mm of $Mn = 20$ at $Re_b = 1$	116
3.12. Extensional efficiency contours near the vicinity of the 7 th screen for both inter-screen spacing of $Mn = 20$ at $Re_b = 1$	117
4.1. Schematic illustration of a section of screen corresponding to $Mn = 20$ – Top view	130
4.2. Schematic representation of the computational domain corresponding to $Mn = 20$ (a) quarter pipe showing the first two screens in a row and (b) periodic plane with four screens in row.	131
4.3. Meshing configuration for $Mn = 20$ (a) sideview of the meshing regions, (b) mesh generation within the screen region, (c) zoom-in to the screen region showing inflation layers at the screen surfaces, and (d) zoom-in showing inflation layers at pipe wall and the screen surfaces at the periodic plane.....	133
4.4. Selected boundary conditions for the studied domain.	135
4.5. Comparison between correlation results and CFD prediction of the pressure drop across one screen: (a) $Mn = 20$ and (b) $Mn = 50$	139
4.6. Normalized velocity components at the central axis and near the wall as a function of the axial distance for different inter-screen spacing and screen geometries at $Re_b = 600$	141
4.7. Normalized velocity profiles at several locations around the 3 rd mixer element for $Re_b = 300$ and $Re_b = 1000$ while varying the inter-screen spacing	144
4.8. Velocity field at various cross-sections within the 3 rd mixer element of $Mn = 20$ at $Re_b = 600$. Top row presents the contours of the axial velocity, w , superimposed with the vector plots of the radial velocity components, u, v . Bottom row presents the surface streamlines colored by the axial vorticity, ω_z	145
4.9. Contour plots of the strain rate magnitude, vorticity magnitude, and extensional efficiency at various locations around the 3 rd mixer element of $Mn = 20$ at $Re_b = 300$ and $L = 15M$	148
4.10. Plots for β against normalized axial distance, Z^* , within the four mixer elements for both screen geometries and inter-screen spacing at $Re_b = 300$	149
4.11. Zoom in for β values around the 3 rd mixer element $1.8 \leq Z^* \leq 2.2$ for (a) $L=15M$ and (b) (a) $L=45M$	150
4.12. Cumulative volumetric distribution of β for both screen geometries at different inter-screen spacing and flow velocities. (a) $Re_b = 300$, (b) $Re_b = 600$, (c) $Re_b = 1,000$	151
4.13. Volume average of β for various screen geometries, inter-screen spacing, and operating conditions.....	152
4.14. Plots of the total dissipation rate and its various components around the 3 rd screen for $Mn = 50$ at $Re_b = 600$. (a) $L = 45M$ and (b) $L = 15M$	153

4.15. Ratio of dissipation rate components with respect to the total dissipation rate at $L = 15M$ at different operating conditions for (a) $Mn = 20$ and (b) $Mn = 50$.	154
4.16. Total dissipation rate plotted against normalized axial distance M^* after 3 rd screen starting from $M^* = 0.8$ up to $M^* = 40$ for $Mn = 20$ and $Mn = 50$ for $L = 45M$ at various operation conditions.	157
4.17. Effect of screen geometry and operating conditions on $E(\theta)$ and $F(\theta)$ for both screen geometries at and $Re_{pipe} = 5,000$ and $30,000$.	160
5.1. Schematic illustration of the new mixer design, (a) three-dimensional view of one mixer element, (b) side-view, (c) top view with various design parameters, and (d) section of a screen element with its geometrical characteristics.	174
5.2. Schematic representation of the computational domain of a contactor equipped by 4 mixer elements rotated by 90° with respect to each other (a) three-dimensional view and (b) side view	176
5.3. Grid discretization for the new mixer including zonal annotations. (1) Screen region, (2) Near screen region including inserts, and (3) Open pipe region.	177
5.4. Experimental pressure drop predictions for empty pipe, STSM, and new mixer.	186
5.5. Numerical and experimental pressure drop predictions (a) STSM, (b) new mixer, (c) parity plot for STSM, and (d) parity plot for new mixer.	188
5.6. Axial velocity contours plotted at the central vertical and horizontal planes for a screen element as well as the new mixer geometry at $Re_{pipe} = 16,500$ ($U_{avg} = 1.305 \text{ m}\cdot\text{s}^{-1}$). A zoom-in plot for the first two mixer elements of the new mixer is also presented.	189
5.7. Contour plots of the axial velocity overlaid by the surface streamlines at various locations downstream of the 3 rd and 4 th mixer element at $Re_{pipe} = 16,500$ ($U_{avg} = 1.305 \text{ m}\cdot\text{s}^{-1}$).	191
5.8. Contour plots of the tracer mass fraction at various cross-sections for different static mixers at (a) inlet (b) $Re_{pipe} = 5,000$ and (c) $Re_{pipe} = 30,000$.	193
5.9. Contour plots of the tracer mass fraction at $Re_{pipe} = 30,000$ for different static mixers at central vertical plane YZ.	194
5.10. CoV for various geometries along the pipe length for (a) $Re_{pipe} = 5,000$ and (b) $Re_{pipe} = 9,100$, (c) $Re_{pipe} = 16,500$, and (d) $Re_{pipe} = 30,000$. The homogenized level is shown by a horizontal green solid line. The center of screen element is presented by vertical dashed line.	195
5.11. Plot of CoV at pipe exit ($18D$) for various mixer elements and operating conditions.	196
5.12. Contour plots of the extensional efficiency for a STSM and new mixer at various axial locations for $Re_{pipe} = 9,100$.	198
5.13. Plots for averaged extensional efficiency versus axial length for various static mixers at $Re_{pipe} = 9,100$ (a) STSM and (b) New Mixer.	198

5.14. Cumulative volumetric percentage of extensional efficiency for various static mixers at (a) $Re_{pipe} = 5,000$, (b) $Re_{pipe} = 9,100$, $Re_{pipe} = 16,500$, and (d) $Re_{pipe} = 30,000$	199
5.15. Pressure loss coefficient resulting from experimental pressure drop for various static mixers.	200

TABLES

Table

1.1. Various definitions of Reynolds number.	23
2.1. Geometrical characteristics of plain-woven square meshes.	39
2.2. Pipe Reynolds number (Re_{pipe}) and corresponding wire Reynolds number (Re_b) for different screen geometries.	40
2.3. Wire Reynolds number (Re_b) and corresponding pipe Reynolds number (Re_{pipe}) for different screen geometries. The corresponding superficial velocity in (m/s) is shown in parentheses.	41
2.4. Grid Independence study for different screens.	45
3.1. Geometrical characteristics of plain-woven square meshes.	96
3.2. Mixing efficiency percentage at the pipe outlet for different screen geometries, inter-screen spacing and operating conditions for the case of concentric injection	114
3.3. Volume average extensional efficiency value within the STSM for different screen geometries, inter-screen spacing and operating conditions for the case of concentric injection	117
4.1. Geometrical characteristics of plain-woven square meshes.	130
4.2. Operating conditions for each screen geometry showing corresponding values of Re_b , Re_{pipe} , and average velocity.....	132
4.3. Grid independence test for different screen geometries.	137
4.4. Minimum peak ratio between the normalized axial component and the transverse components for different screen geometries and inter-screen spacing at $Re_b = 600$..	142
5.1. Various design parameters of the new mixer.....	175
5.2. Operating conditions based on the pipe Reynolds number (Re_{pipe}) and their corresponding average flow velocity, U_{avg} in ($m \cdot s^{-1}$)	176
5.3a. Grid independence test for STSM and New mixer.	184
1.1. Grid independence test for different screen geometries.	214
1.2. Comparison between Tetrahedral and Polyhedral grids.	215
1.3. Temporal grid convergence using the polyhedral grid.	216

ABBREVIATIONS

CFD	Computational Fluid Dynamics
GCI	Grid Convergence Index
MRE	Mean Relative Error
PDU	Particle Distribution Uniformity
PNN	Point to Nearest Neighbor
RTD	Residence Time Distribution
SST	Shear Stress Transport
STSM	Screen Type Static Mixer

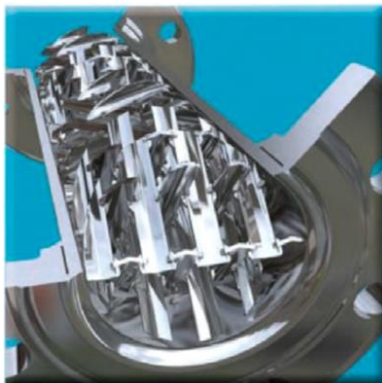
CHAPTER 1

INTRODUCTION

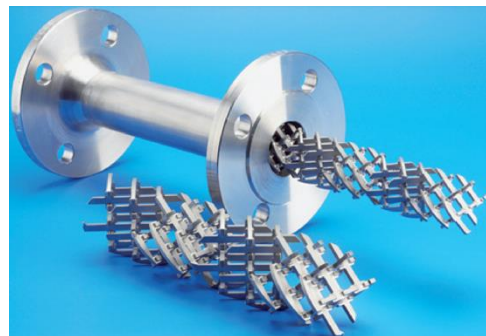
1.1 Background

Mixing is defined as the reduction of inhomogeneity in concentration, phase, or temperature. It plays a crucial role in many chemical processes ranging from simple blending to complex multiphase flow systems (Azizi and Al Taweel, 2015; Montante et al., 2016). Several equipment types are used for this purpose such as mechanically agitated tanks, bubble columns, packed columns, in-line static mixers, among others.

In-line Static mixers, or motionless mixers, are inserts in pipes, channels, or ducts the role of which is to redistribute the fluid elements in the radial and tangential directions such that the streamlines are divided in a sequential fashion (Ghanem et al., 2013). Figure 1.1 illustrates some of the commercially available static mixers (Ghanem et al., 2013).



KMX-V (Chemineer, Inc)



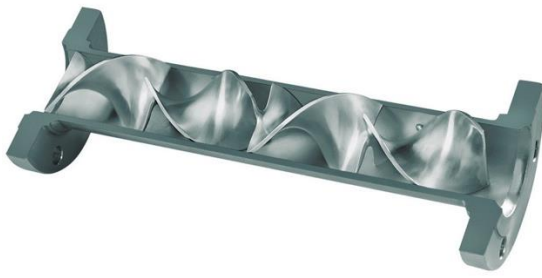
SMX (Sulzer, Inc)



Custody Transfer (Komax Systems, Inc)



Standard LPD (RossEngineering, Inc)



Kenics KM (Chemineer, Inc)



ZT-MX(ZelenTech, Ltd)

Figure 1.1. Commercially available in-line static mixers (Ghanem et al., 2013).

Nowadays, the use of static mixers is gaining strong momentum because of their ability to achieve good mixing performance at low operating costs, smaller reactor volumes, and the subsequent enhanced safety as compared to conventional dynamic mixers (Al Taweel et al., 2013; Ghanem et al., 2013; Madhuranthakam et al., 2009; Peschel et al., 2012; Thakur et al., 2003). This is further complemented by the accuracy with which numerical approaches are capable of quantifying their performance and characterizing their internal flow behavior (Haddadi et al., 2020; Meng et al., 2015, 2014).

Typically, mixing within a process is divided into three levels, macro-mixing, meso-mixing, and micro-mixing. Macro-mixing involves the scale of the whole vessel (Ghanem et al., 2013). This process is usually characterized by the residence time distribution (RTD) in which the distribution functions are a signature of fluid field uniformity (Habchi et al., 2009). Meso-mixing is an intermediate scale between macro-mixing and micro-mixing. It reflects the coarse scale turbulent exchange between the fresh feed and its surrounding governed by turbulent fluctuation (Baldyga and Pohorecki, 1995). It could be viewed as the inertial-convective disintegration of large eddies (Ghanem et al., 2013). The essential features of this scale is usually predicted by linking it to the root mean square of the velocity fluctuations or the kinetic energy

(Habchi et al., 2010). Micro-mixing takes place at the smallest scale which is a viscous-convection deformation of the fluid elements. At this level, the fluid elements continue breaking down to the diffusion scale (J. Baldyga and J.R.Bourne, 1989). This scale is characterized by micro-mixing time which is related to the turbulent kinetic energy dissipation rate (Jerzy Baldyga and Bourne, 1999).

The mixing performance of various static mixers have been addressed comprehensively in the open literature (González-Juárez et al., 2017; Haddadi et al., 2020; Hobbs and Muzzio, 1998, 1997a; Kukukova et al., 2011; Medina et al., 2019; Meng et al., 2017, 2015; Montante et al., 2016; Stec and Synowiec, 2017a, 2019). To accomplish this, two different numerical approaches are usually employed, namely, the Lagrangian and Eulerian methods. The former is based on particle tracking while the latter uses the species transport equation. The mixing behavior is then usually characterized qualitatively or quantitatively using different approaches. The qualitative method provides visualization of distributive mixing within the mixer; whereas, the quantitative one allows for the calculation of the degree of mixing.

The qualitative characterization is typically performed using Poincare plots (Hobbs and Muzzio, 1998), tracer injection which can be either central (Hobbs and Muzzio, 1998; Meng et al., 2017) or off-central (Hobbs and Muzzio, 1997a), tracer distribution of two mixing fluids either through concentric injection (Haddadi et al., 2020; Meng et al., 2015; Montante et al., 2016) or semicircle injection (Meng et al., 2015; Soman and Madhuranthakam, 2017; Stec and Synowiec, 2019), residence time distributions, RTDs (González-Juárez et al., 2017; Hobbs and Muzzio, 1997b), or by studying extensional efficiency contour plots (Meng et al., 2017).

Quantitative mixing characterization could be completed using particle distribution uniformity (PDU) (Meng et al., 2017; Rahmani et al., 2005), coefficient of variation (CoV) (Meng et al., 2015; Stec and Synowiec, 2019), point to nearest neighbor (PNN) (Al-Hassan et al., 2021; Kukukova et al., 2011), G-value (Meng et al., 2014; Rahmani et al., 2005), stretching histories/rates (Hobbs and Muzzio, 1997a; Meng et al., 2017, 2015, 2014), areal distribution (Alberini et al., 2013; Montante et al., 2016), M-parameter (Medina et al., 2019), and RTDs (González-Juárez et al., 2017).

A large number of studies that addresses the hydrodynamic and mixing performance of static mixers under laminar or turbulent regimes can be found in the open literature. For example, several studies addressed the performance of the widely used Kenics mixer (KSM) (Hobbs et al., 1998; Hobbs and Muzzio, 1998; Rahmani et al., 2008, 2005) and SMX (Hirschberg et al., 2009; Jegatheeswaran et al., 2018; Leclaire et al., 2020; Meijer et al., 2012; Pianko-Oprych and Jaworski, 2010; Soman and Madhuranthakam, 2017), while others proposed novel mixer designs and compared them to the performance of other established units (Haddadi et al., 2020; Meng et al., 2020, 2017, 2015, 2014; Stec and Synowiec, 2019, 2017a, 2017b). In these studies, numerical models based on finite volume methods (FVM) (Hobbs et al., 1998; Kumar et al., 2008; Meng et al., 2017, 2015, 2014; Regner et al., 2006; Soman and Madhuranthakam, 2017) or finite element methods (FEM) (Avalosse and Crochet, 1997; Kandhai et al., 1999; Rauline et al., 2000, 1998) were employed to characterize their hydrodynamic and mixing performance. These numerical models are typically validated using pressure drop data that are either directly measured (Kumar et al., 2008; Regner et al., 2006; Soman and Madhuranthakam, 2017) or in the form of empirical correlations (Meng et al., 2014; Regner et al., 2006). Based on such validations,

detailed analysis of the velocity field and the resulting shear rates are then typically conducted.

Recently, plain square woven meshes were used as one variant of static mixers (cf. Figure 1.2). (Abou Hweij and Azizi, 2015; Al Taweel et al., 2013; Azizi and Abou Hweij, 2017). Such screens when employed in tubular contactors superimpose adjustable, radially uniform velocity fields on the near plug flow conditions encountered in high velocity pipe flows (Al Taweel et al., 2005). Because of the capability of screens in producing very high energy dissipation rates in their immediate vicinity followed by a quasi-isotropic turbulence further downstream (Laws and Livesey, 1978), they were found effective in processing multiphase flows. The high energy dissipation rates and the elevated micro-mixing intensities generated in the vicinity of the screens (Bourne and Lips, 1991) provided not only fine dispersed phase entities (bubbles and/or drops) but also enhanced the interphase mass transfer rates (Al Taweel et al., 2013, 2007, 2005; Azizi and Al Taweel, 2015). For immiscible liquids, contacting was found to be 5-fold more energy efficient compared to conventional agitated tanks equipped by Ruston-type impellers (Al Taweel and Chen, 1996). In addition, volumetric mass transfer coefficients, k_{La} , reaching 13 s^{-1} were achieved in the case of liquid-liquid dispersions while reaching 99% of equilibrium conditions in less than 1s (Al Taweel et al., 2007). For gas-liquid systems, interfacial areas as high as $2200 \text{ m}^2/\text{m}^3$ were generated (Chen, 1996). High oxygen transfer efficiencies reaching 4.2 kg/KWh were measured by Al Taweel et al. (Al Taweel et al., 2005) while k_{La} values as high as 4.08 s^{-1} even in the presence of surfactants were reached by Azizi and Al Taweel (Azizi and Al Taweel, 2015). Moreover, the inter-screen spacing plays an important role in determining the mixing performance of screen mixers. For instance,

while short inter-screen spacing results in fine dispersions, which might be required for high mass transfer rates and fast reactions, long inter-screen spacing favors slow reactions and/or low energy consumption requirements (Al Taweel et al., 2013).

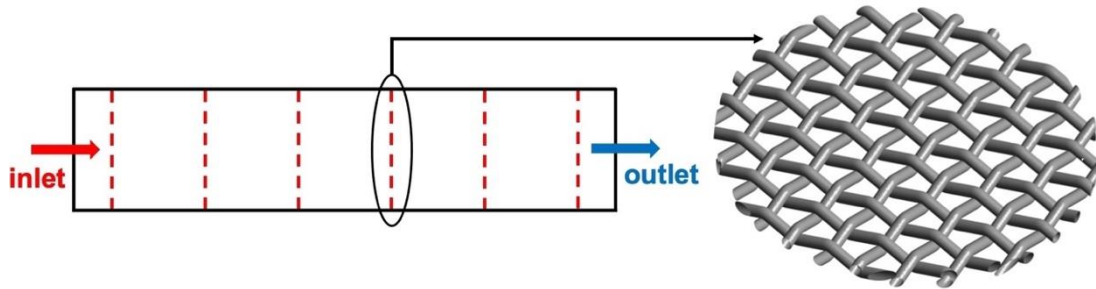


Figure 1.2. Schematic representation of a pipe equipped with plain square woven meshes.

Recently, Abou Hweij and Azizi (Abou Hweij and Azizi, 2015) and Azizi and Abou Hweij (Azizi and Abou Hweij, 2017) experimentally investigated the macromixing behavior of these mixers for single and two-phase turbulent flows, respectively. They studied the effect of changing the screen geometry, number of screens, inter-screen spacing, and operating conditions on the axial dispersion coefficients. Their findings reflected lower axial dispersion values when compared to empty pipes. Additionally, the results showed that the axial dispersion coefficient is directly related to the screen geometry and utilizing an appropriate characteristic length for the Reynolds number is very important for a proper analysis of the data.

1.2 Literature Review

A typical plain square woven screen is illustrated in Figure 1.3 where it consists of identical wires of diameter, b , placed at a center-to-center distance or mesh size, M . Such configuration results in a fractional open area, α , through which the fluid can pass. This fractional open area α is commonly computed as the projection of the screen's

wires to a plane normal to the flow. As such, it can be calculated according to Equation (1.1). Another common classification of woven gauzes follows their mesh number, Mn , which is the number of openings per unit length (Abou Hweij and Azizi, 2015). As such, Mn indicates the number of openings per inch (i.e. number of opening per 25.4 mm).

$$\alpha = \left(1 - \frac{b}{M}\right)^2 \quad (1.1)$$

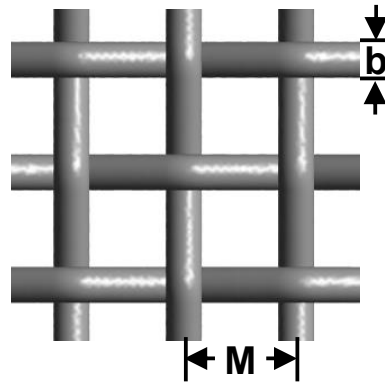


Figure 1.3. Schematic representation of a section of plain-square woven screen.

While Reynolds number was usually selected as a non-dimensional flow parameter, its formulation is based on the definition of its velocity and/or its characteristic length. As such, due to the prescribed behavior for flow through screens, different variants of Reynolds number could be established (Abou Hweij and Azizi, 2015; Azizi, 2019; Azizi and Abou Hweij, 2017) which are summarized in Table 1.1.

Table 1.1. Various definitions of Reynolds number.

Reynold number	Formulation
Pipe Reynolds number, Re_{pipe}	$\rho \cdot D \cdot U / \mu$
Macroscopic jet Reynolds number, Re_{jet}	$\rho \cdot D \cdot (U/\alpha) / \mu$
Wire Reynolds number, Re_b	$\rho \cdot b \cdot U / \mu$
Mesh Reynolds number, Re_M	$\rho \cdot M \cdot U / \mu$
Screen Reynolds number, Re_s	$\rho \cdot b \cdot (U/\alpha) / \mu$

1.2.1 Experimental investigations of flows through screens

Woven meshes are widely employed in a multitude of processes. They have been used for the production or reduction of large-scale velocity or pressure non-uniformities (Groth and Johansson, 1988; Kurian and Fransson, 2009; Pinker and Herbert, 1967; Roach, 1986), traditional screening, filtering, noise reduction at valves and/or aircraft landing gear, thickeners and coalescers, to greenhouse insect repellants (Armour and Cannon, 1968; Bailey et al., 2003; Ehrhardt, 1983; Okolo et al., 2019). In addition, they have been employed in more sophisticated operations such as Stirling engine regenerators (Costa et al., 2013; York and MacDonald, 2021), thermos-acoustic refrigerators (Wakeland and Keolian, 2003), catalyst support in oxidation chambers – catalytic wire gauzes – (Kołodziej et al., 2009), high-efficiency heat exchangers, energy-storage units, solar-receiving devices (Wu et al., 2005), and as static mixers in multiphase reactors/contactors (Al Taweel et al., 2013; Azizi and Al Taweel, 2015).

This is also reflected in the large number of studies on flows through them that can be found in the literature. Part of these studies deal with characterizing their resistance to flow by describing and analyzing the pressure drop across them (Abou

Hweij and Azizi, 2015; Armour and Cannon, 1968; Azizi, 2019; Bailey et al., 2003; Ehrhardt, 1983; G.B.Schubauer et al., 1948; J.R.Sodre and J.A.R.Parise, 1997; Kołodziej et al., 2009; Wakeland and Keolian, 2003; Wu et al., 2005). These experimental investigations have been recently summarized in the work of Azizi (2019) (Azizi, 2019). In addition, another large number of studies had investigated their turbulence characteristics which can be summarized in the next sections (Groth and Johansson, 1988; Irps and Kanjirakkad, 2016; Kurian and Fransson, 2009; Laws and Livesey, 1978; Roach, 1986; Santos et al., 2016).

Screens can be used as either turbulence suppressors or turbulence generators depending on their geometrical characteristics (Laws and Livesey, 1978). The former takes place when the downstream turbulent intensity in the vicinity of the screen is lower than its upstream value. On the other hand, a screen acts as a turbulence generator when the downstream turbulent intensity in the vicinity of the screen is larger than its upstream value.

Another common classification of screens is whether the flow through them is subcritical or supercritical. Groth and Johansson (Groth and Johansson, 1988) stated that subcritical flows were those with a wire Reynolds number less than 40 while supercritical screens are those having a wire Reynolds number greater than 40. Groth and Johansson (Groth and Johansson, 1988) attempted reducing turbulence using subcritical screens and found that they can attain large turbulence reduction levels; however, at the expense of a higher pressure drop when compared to a cascade combination of supercritical screens.

Further studies showed that the turbulence generated by supercritical screens exhibited an anisotropic behavior at its immediate vicinity before transforming to an

isotropic turbulence (Groth and Johansson, 1988; Roach, 1986). Roach (Roach, 1986) stated that a distance equivalent to 10 mesh widths was required for the turbulence to become isotropic, while Groth and Johansson (Groth and Johansson, 1988) showed that a distance equivalent to 25 mesh widths was required to reduce the intensities below their upstream values. Kurian and Fransson (Kurian and Fransson, 2009) also found that the level of anisotropy decreased with an increasing mesh Reynolds number (i.e. characteristic length based on the mesh width).

Irps and Kanjirakkad (Irps and Kanjirakkad, 2016) studied the modification of wall boundary layers in wind tunnels due to the presence of turbulence grids. By changing the grid geometry, they measured pressure drop, boundary layer velocity profiles, and turbulence modification. They found that length-scales scaled with the opening size of the mesh, and a thinning of the boundary layers with an overshoot in the local velocity. This overshoot was found to correlate with the mesh porosity as opposed to the pressure drop as was reported by earlier studies (Lau and Baines, 1968; Mehta, 1985; Owen and Zienkiewicz, 1957).

Santos et al. (Santos et al., 2016) also studied the effect of screens in wind tunnels and found that their presence reduced both the mean flow velocity and turbulence intensity non-uniformities. Although, the latter parameter (intensity of turbulence) was found to increase with the insertion of screens, it became more uniform.

1.2.2 Numerical investigations of flows through screens

Besides the large body of experimental investigations for flow through grids, fewer numerical studies were conducted to predict the hydrodynamic performance of

such screens under laminar or turbulent regimes (Azizi and Al Taweel, 2011a; Costa et al., 2013; Green et al., 2008; Middelstädt and Gerstmann, 2013; Okolo et al., 2019; York and MacDonald, 2021).

Green et al. (Green et al., 2008) investigated the pressure drop and velocity fields through a single layer of plain-woven meshes using Ansys Fluent[®], which is a FVM-based commercial software. Their computational fluid dynamics (CFD) simulations reproduced the experimental pressure drop data obtained using a wind tunnel within $\pm 10\%$. Their study also included the effect of variable screen filament spacing through laterally shifting some wires in order to understand the effect of non-uniform fabric-weave geometry.

Azizi and Al Taweel (Azizi and Al Taweel, 2011a) proposed a new correlation for predicting the spatial variation of the turbulent dissipation rate downstream of a screen. This correlation makes use of the homogeneous and isotropic assumption and extended it to the anisotropic region. The improvement of the correlation through varying the decay coefficient showed comparable results with experimental data over a wide range of operating conditions.

Middelstädt and Gerstmann (Middelstädt and Gerstmann, 2013) utilized Ansys Fluent[®] to calculate the resistance to flow through twilled dutch woven meshes at low and medium velocities. Their results agreed well with experimental measurements and their work also investigated the streamlines, local velocity, and pressure fields.

Costa et al. (Costa et al., 2013) simulated the flow through stacked and wound woven wire matrices and deduced correlations for the friction factor. Using an FVM method, they investigated stacked woven wire matrices and predicted the results of empirical correlations for pressure drop within $\pm 5\%$. This was considered as a

validation step before extending their work to wound woven wire regenerator matrices and propose a correlation for pressure losses of flows through them.

Okolo et al. (Okolo et al., 2019) simulated the pressure drop and the flow behavior through plain-woven square meshes under low turbulence conditions for applications of wire screens in the flow and noise control of aerodynamic components. The calculated pressure loss coefficients compared within $\pm 8\%$ to experimentally obtained measurements and correlations. They also qualitatively assessed the decay of turbulence intensity against correlations from the literature and found them to agree well.

Recently, York and MacDonald (York and MacDonald, 2021) also simulated the flow through stainless steel wire mesh regenerators where they studied the effects of wire misalignment and axial spacing on the pressure drop. The authors developed a new friction factor correlation which accounted for the wire misalignment. They also showed that the axial spacing was dependent on the wire misalignment such that the highest pressure drop reductions was recorded for highly misaligned cases.

1.3 Research statement

All aforementioned numerical studies were performed for the case of single-phase, three-dimensional, unbounded flow where in-depth investigations of the hydrodynamic effect of upstream velocity profiles (fully developed laminar/turbulent profiles) and pipe wall on the flow behavior of pipes equipped with screens were not investigated. In addition, no previous numerical study investigated the mixing performance of plain-woven wire meshes when utilized as static mixers. Studies on the

hydrodynamic and mixing characterization of three-dimensional wall-bounded single-phase flows through screens under laminar or turbulent regimes are therefore inexistent.

Consequently, the aim of this work is to numerically characterize the hydrodynamic behavior and the mixing performance of single-phase flows through screen-type static mixers under laminar and turbulent regimes for a wide range of operating conditions and design configurations. In particular, the effect of screen geometry, number of screens, and inter-screen spacing will be considered at various operating conditions. This work also proposes a new static mixer design that will be investigated for its potential to improve the distributive mixing performance of STSMs.

To achieve this, several research objectives will be addressed. These are listed below:

1. Perform a hydrodynamic characterization of single-phase bounded flow through screens under laminar flow conditions,
2. Analyze micro-mixing performance under laminar flow conditions for single phase bounded flow through screens using a Lagrangian approach,
3. Perform a hydrodynamic characterization and a macro-mixing assessment of single-phase bounded flow through screens under turbulent flow conditions,
4. Propose a new mixer geometry to improve the mixing performance of STSM by employing downstream inserts.

1.4 General methodology

To accomplish each one of these thesis objectives, the methodology is highlighted below.

1. To perform a hydrodynamic characterization of single-phase bounded flow through screens under laminar flow regimes, the following tasks will be performed:
 - a. Perform grid sensitivity test using the Grid Convergence index (GCI).
 - b. Validate the predicted pressure drop within selected screens with recent published correlations.
 - c. Use the validated model to report detailed characterizations of the hydrodynamic performance within STSM while investigating the velocity profiles/components, velocity contours, velocity streamlines, vorticity, and static pressure fields, etc.
2. To analyze micro-mixing performance under laminar flow conditions for single phase bounded flow through screens, the following tasks will be performed:
 - a. Use the validated laminar flow CFD model and assess the distributive mixing through the Lagrangian approach and the dispersive mixing through the extensional efficiency parameter.
 - b. Analyze the outcomes using a qualitative and quantitative approaches.
 - i. The qualitative distributive assessment will be presented through predicting particles' position at specified cross-section after being injected from a specified location at the inlet. While the qualitative dispersive mixing will be depicted in terms of extensional efficiency contours.
 - ii. The quantitative distributive assessment will be based on published methods namely, the point to nearest neighbor (PNN) and mixing efficiency proposed by Kukukova et al. (Kukukova et al., 2011) and

Medina et al. (Medina et al., 2019), respectively. Whereas the quantitative dispersive mixing will be interpreted in terms of local extensional efficiency at various cross-sections.

3. To perform a hydrodynamic characterization and a macro-mixing assessment of single-phase bounded flow through screens under turbulent flow conditions, the following tasks will be performed:
 - a. Perform grid sensitivity test using the Grid Convergence index (GCI).
 - b. Validate the predicted pressure drop within selected screens with recent published correlations.
 - c. Use the validated model to report detailed characterizations of the hydrodynamic performance within STSM while investigating the velocity profiles/components, velocity contours, velocity streamlines, vorticity, extensional efficiency, dissipation rates, etc.
 - d. Assess the macro-mixing performance within STSM using the Eulerian approach based on species transport equation where the residence time distribution function will be predicted and analyzed.
4. To investigate the performance of the proposed new mixer geometry, the following tasks will be performed:
 - a. Perform grid sensitivity test using GCI.
 - b. Validate the predicted pressure drop within the new mixer with experimental pressure drop data.
 - c. Investigate the hydrodynamic performance of the proposed mixer using contours for the velocity while presenting flow streamlines.

- d. Use the Eulerian approach to assess the distributive micro-mixing potential within the proposed static mixer and compare its distributive and dispersive mixing performance to the STSM. This will be done through a qualitative and quantitative assessments.
 - i. The distributive qualitative assessment will be presented as contour plots of the tracer mass fraction being injected from a specified location at the inlet while the quantitative assessment will be based on the well-known Coefficient of variation (CoV).
 - ii. The distributive dispersive mixing assessment will be investigated qualitatively using contour plots of the extensional efficiency and quantitatively using the cumulative extensional efficiency values within the mixing volume.
- e. The energy consumption within the proposed mixer will be compared with commercial static mixers using the pressure loss coefficient.

1.5 Thesis Outline

This thesis consists of six chapters and is a compilation of four manuscripts. The importance, relevance, and objectives of the current work are presented in Chapter 1. In Chapter 2, the CFD simulations were used to assess the hydrodynamic performance of pipes equipped with screens under laminar flow regimes. Through varying the screen geometry, number of screens, inter-screen spacing, and operating conditions, the study highlighted the hydrodynamics of flows through screens. This study provided the velocity flow field for Lagrangian assessment of the micro-mixing performance within STSM under laminar flow regime, which are presented in Chapter 3. This chapter provided a comprehensive analysis of the distributive and dispersive

micro-mixing performance of STSM, where both qualitative and quantitative assessments were presented. The study revealed that the STSM could be highly recommended if dispersive mixing is needed; however, these mixers are marred by a relatively low radial/distributive mixing performance. In Chapter 4, a comprehensive investigation of the hydrodynamic performance of wall-bounded turbulent flows through screens was addressed where again the effect of varying screen geometry, number of screens, inter-screen spacing, and operating conditions on the flow field were studied. This chapter also presents the potential of STSM in providing near plug flow conditions, which were interpreted numerically using the residence time distributions based on a Eulerian approach. Based on these studies, a new mixer geometry that enhances the distributive mixing of screens is proposed in Chapter 5. The new design relies on the use of specially designed inserts to ameliorate the distributive mixing performance of woven meshes. This resulted in a hybrid mixer, the mixing capabilities of which were investigated. Chapter 6 highlights the general conclusions of the various studies and proposes various recommendations for future work. All MATLAB codes and user defined functions (UDFs) that were used in the current work are attached in the appendix.

CHAPTER 2

CFD SIMULATION OF WALL-BOUNDED LAMINAR FLOW THROUGH SCREENS. PART I: HYDRODYNAMIC CHARACTERIZATION

W. Abou-Hweij and F. Azizi¹

B.&W. Bassatne Dept. of Chemical Engineering and Advanced Energy, M. Semaan Faculty of Engineering and Architecture, American University of Beirut, 1107 2020 Beirut, Lebanon

Published in European Journal of Mechanics / B Fluids, vol. (84), pp. 207-232 (2020)
<https://doi.org/10.1016/j.euromechflu.2020.06.008>

Abstract

This paper characterizes the hydrodynamics of laminar flows through circular ducts equipped with plain square woven meshes/screens in their role as static mixers. The CFD model was used to investigate the effect of screen geometry, number of screens, inter-screen spacing, and operating conditions on the velocity and pressure fields. This work therefore presents an analysis of the velocity contours, streamlines, and profiles at various locations within the pipe in addition to the pressure profiles to obtain a better understanding of the complex behavior of the flow.

The presence of screens normal to the flow was found to alter the fully developed parabolic profile and flatten it both upstream and downstream, hence simultaneously decelerating and accelerating regions in the cross-sectional area of the flow. Downstream of screens, the velocity profile was characterized by a sinusoidal shape that quickly decays, and vortices were observed under certain operating and design conditions.

The study of the pressure field helped delineate the contribution of static and dynamic pressures in addition to identifying a minimum inter-screen distance if

maximum pressure recovery is desired. Predictions of the pressure drop for various mesh geometries and under different operating conditions were validated using empirical correlations and the results reflected a very good accuracy with the maximum relative error falling within $\pm 7.3\%$.

Keywords: Wire gauze; Wire mesh; Hydrodynamics; Pressure Drop; Velocity Field; Pressure Field.

2.1 Introduction

Many process industries operate in the laminar flow regime. In these operations, the use of static mixers is gaining strong momentum because of their ability to achieve good mixing performance at low operating costs, smaller reactor volumes, and the subsequent enhanced safety (Al Taweel et al., 2013; Ghanem et al., 2013; Madhuranthakam et al., 2009; Peschel et al., 2012; Thakur et al., 2003). This is further complemented by the accuracy with which numerical approaches are capable of quantifying their performance and characterizing their internal flow behavior (Meng et al., 2015, 2014).

There exists numerous commercially-available static mixers, and the reader is referred to two major review articles that highlight their importance, applications, and characteristics (Ghanem et al., 2013; Thakur et al., 2003). The performance of standard static mixers (e.g. KSM and SMX) and other alternative novel designs under laminar regime has been the subject of numerous numerical studies in the open literature. In these studies, numerical models based on finite volume methods (FVM)(Hobbs et al., 1998; Kumar et al., 2008; Meng et al., 2015, 2014; Regner et al., 2006; Soman and Madhuranthakam, 2017) or finite element methods (FEM) (Kandhai et al., 1999;

Rauline et al., 1998) were employed to characterize their hydrodynamic performance. These numerical models are typically validated using pressure drop data that is either directly measured (Kumar et al., 2008; Soman and Madhuranthakam, 2017) or in the form of empirical correlations (Meng et al., 2014; Regner et al., 2006). Armed with such validation, detailed analysis of the different components of the velocity field and the resulting shear rates is then typically conducted.

Recently, plain square woven meshes were used as one variant of static mixers (Abou Hweij and Azizi, 2015; Al Taweel et al., 2013, 2005; Azizi and Abou Hweij, 2017; Azizi and Al Taweel, 2015, 2011a, 2011b, 2007) to superimpose an adjustable, radially-uniform, highly turbulent field on the near plug flow conditions encountered in high velocity pipe flows (Azizi and Al Taweel, 2011b). Their main characteristic is the production of very high energy dissipation rates in the immediate vicinity of the meshes followed by a quasi-isotropic turbulence further downstream. Such profile proved very efficient at promoting multiphase dispersion and mass transfer operations at low energy consumption rates (Al Taweel et al., 2013, 2007, 2005; Azizi and Al Taweel, 2015, 2007). They were also used for studying the effect of turbulent mixing on the evolution of chemical reactions as well as testing the applicability of micro mixing models (A.Bennani et al., 1985; Bourne and Lips, 1991). Recently, Abou Hweij and Azizi and Azizi and Abou Hweij (Azizi and Abou Hweij, 2017) proved that the plug flow behavior is prevalent using either single or two-phase turbulent flows.

Woven meshes, however, are widely employed in a multitude of processes, such as wind tunnels for the generation/dissipation of flow nonuniformities (Laws and Livesey, 1978), catalytic reactors as catalyst support material (Kołodziej et al., 2009), and Stirling engine regenerators (Costa et al., 2013). This is evident from the numerous

studies on their hydraulic resistance and turbulence characteristics that can be found in the literature, which describe and analyze the pressure drop of flows across them (Abou Hweij and Azizi, 2015; Armour and Cannon, 1968; Azizi, 2019; Bailey et al., 2003; Ehrhardt, 1983; G.B.Schubauer et al., 1948; J.R.Sodre and J.A.R.Parise, 1997; Wakeland and Keolian, 2003; Wu et al., 2005)(Kołodziej et al., 2009). However, fewer numerical studies were conducted to predict their hydrodynamic performance (Costa et al., 2013; Green et al., 2008; Middelstädt and Gerstmann, 2013; Okolo et al., 2019). These experimental investigations have been recently summarized in the work of Azizi (2019) (Azizi, 2019), therefore, only a brief review about the numerical studies will be presented here.

Green et al. (Green et al., 2008) investigated the pressure drop and velocity fields through a single layer of plain-woven meshes using Ansys Fluent[®], which is a FVM-based commercial software. Their CFD simulations reproduced the experimental pressure drop data obtained using a wind tunnel within $\pm 10\%$. Their study also included the effect of variable screen filament spacing through laterally shifting some wires in order to understand the effect of non-uniform fabric-weave geometry.

Middelstädt and Gerstmann (Middelstädt and Gerstmann, 2013) utilized Ansys Fluent[®] to calculate the resistance to flow through twilled dutch woven meshes at low and medium velocities. Their results agreed well with experimental measurements and their work also investigated the streamlines, local velocity, and pressure fields.

Costa et al. (Costa et al., 2013) simulated the flow through stacked and wound woven wire matrices and deduced correlations for the friction factor. Using an FVM method, they investigated stacked woven wire matrices and predicted the results of empirical correlations for pressure drop within $\pm 5\%$. This was considered as a

validation step before extending their work to wound woven wire regenerator matrices and propose a correlation for pressure losses of flows through them.

Recently, Okolo et al. (Okolo et al., 2019) simulated the pressure drop and the flow behavior through plain-woven square meshes under low turbulence conditions for applications of wire screens in the flow and noise control of aerodynamic components. The calculated pressure loss coefficients compared within $\pm 8\%$ to experimentally obtained measurements and correlations. They also qualitatively assessed the decay of turbulence intensity against correlations from the literature and found them to agree well.

All these aforementioned numerical studies were performed for the case of unbounded flows where the effect of upstream velocity profiles and pipe wall on downstream flow behavior was not investigated. Furthermore, none of the aforementioned studies considered the effect of screen geometry, number of screens, and inter-screen spacing on the overall hydrodynamics of the flow. In addition, the superior performance of these screens as static mixers in the turbulent regime served as a stimulus to investigate their performance in the laminar regime. Therefore, the aim of this work is to numerically characterize the hydrodynamic behavior of flows through them in the laminar flow regime under various operating conditions and design configurations. For this purpose, four different parameters, namely, screen geometry, number of screens, inter-screen spacing, and flow velocity will be investigated to assess their effect on both the flow and pressure fields.

2.2 Computational Methods

2.2.1 Computational domain

The computational domain consists of a circular pipe of inner diameter, $D = 12.7$ mm with a variable total length, in which a varying number of screens are equidistantly inserted normal to the flow at different inter-screen spacing. Taking advantage of the axisymmetric flow configuration in a pipe, the domain was modelled in three dimensions while accounting for one quadrant of the pipe cross-section.

Numerical simulations were conducted using four different screen geometries, the characteristics of which are listed in Table 2.1. A typical screen geometry is illustrated in Figure 2.1 where it is shown that the mesh consists of identical wires of diameter, b , placed at a center-to-center distance or mesh size, M . Such configuration results in a fractional open area, α , through which the fluid can flow. This fractional open area α is commonly computed as the projection of the screen's wires to a plane normal to the flow. As such, it can be calculated according to Equation (2.1).

$$\alpha = \left(1 - \frac{b}{M}\right)^2 \quad (2.1)$$

Different combinations of b , M , and α would therefore result in different mixer geometries, each of which would affect the flow differently. Another common classification of woven gauzes follows their mesh number, Mn , which is the number of openings per unit length (Abou Hweij and Azizi, 2015). In the current work, Mn indicates the number of openings per inch (i.e. number of opening per 25.4 mm).

Table 2.1. Geometrical characteristics of plain-woven square meshes.

Mn (–)	M (mm)	b (mm)	$(M-b)$ (mm)	α (%)
20	1.27	0.4064	0.8636	46.2
30	0.8382	0.3048	0.5334	40.5
50	0.508	0.2286	0.2794	30.3
80	0.3175	0.1397	0.1778	31.4

Simulations were performed using liquid-water with constant physical properties ($\rho = 998.2 \text{ kg/m}^3$ and $\mu = 0.001003 \text{ Pa}\cdot\text{s}$) as the working fluid. In addition, they were performed using two different variants of the Reynolds number. These were based on the choice of the characteristic length used to calculate the dimensionless group. Consequently, the Reynolds number based on pipe diameter (Re_{pipe}), and the Reynolds number based on wire diameter, Re_b , were employed. The former ensures similar flow conditions at the inlet to the mixer, while the latter permits the attainment of similar hydrodynamic effects within the mixer in order to highlight the effect of wire diameter and mesh opening on the downstream flow behavior. In this quest, Re_{pipe} was varied between 1 and 1,000, while Re_b ranged between 1 and 40.

The various operating conditions are listed in Table 2.2 and Table 2.3 where cross-correlations between Re_{pipe} and Re_b are shown. The conditions were selected such that Re_{pipe} always lies within the laminar regime for flow through a pipe, i.e. between 1 and 2,300. While choosing Re_b , and as shown in Table 2.3 if the choice of value resulted in $Re_{pipe} > 2,300$, the corresponding case was omitted from the simulations. However, this was observed for only one screen, $Mn = 80$ at $Re_b = 30$ and $Re_b = 40$.

Furthermore, simulations were always performed using equidistant and similar screens in the mixer. Following this, two different inter-screen spacings ($L = 5 \text{ mm}$ and $L = 50 \text{ mm}$) were employed while varying the number of screens between 1 and 8. Consequently, each individual screen domain was considered to span a distance equal to L divided equally between upstream and downstream sections, each corresponding to a length $L/2$. As a result, four different parameters were investigated in this work, namely, screen geometry, inter-screen spacing, number of screens, and flow velocity.

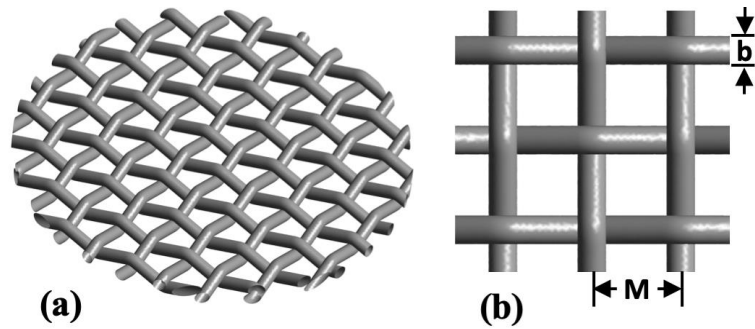


Figure 2.1. Schematic representation of plain-square woven screen of (a) full screen geometry – rotated view and (b) section of screen – top view.

Table 2.2. Pipe Reynolds number (Re_{pipe}) and corresponding wire Reynolds number (Re_b) for different screen geometries.

Re_{pipe}	$U \text{ (m/s)}$	Wire Reynolds number, Re_b			
		$Mn = 20$	$Mn = 30$	$Mn = 50$	$Mn = 80$
1	7.912×10^{-5}	0.032	0.024	0.018	0.011
10	7.912×10^{-4}	0.32	0.24	0.18	0.11
100	7.912×10^{-3}	3.2	2.4	1.8	1.1
1,000	7.912×10^{-2}	32	24	18	11

Table 2.3. Wire Reynolds number (Re_b) and corresponding pipe Reynolds number (Re_{pipe}) for different screen geometries. The corresponding superficial velocity in (m/s) is shown in parentheses.

Re_b	Wire Reynolds number, Re_b (U in m/s)			
	$Mn = 20$	$Mn = 30$	$Mn = 50$	$Mn = 80$
1	31.3 (0.00247)	41.7 (0.0033)	55.6 (0.0044)	90.9 (0.00719)
10	312.5 (0.0247)	417 (0.033)	556 (0.044)	909 (0.0719)
20	625 (0.0494)	833.33 (0.0659)	1,111.11 (0.0879)	1,818.18 0.1439
30	937.5 (0.0742)	1,250 (0.0989)	1666.7 (0.1319)	2727.3 (0.2158)
40	1,250 (0.0989)	1,666.7 (0.1319)	2,222.2 (0.1758)	3636.4 (0.2877)

The 3D geometry of the mixing section was then constructed using AutoCAD[®]. Due to the axial symmetric configuration, the flow field was reduced to a quarter section as shown in Figure 2.2a. This geometry cannot be reduced further because symmetry would be lost due to the square shape of the openings.

To reduce the computational cost associated with a constant (very fine) mesh throughout the computational domain, the flow field was subdivided into 3 meshing regions, namely, the open-pipe, near-screen, and screen regions as illustrated in Figure 2.2b. The screen and the near-screen regions were discretized using an unstructured tetrahedral grid scheme, whereas the open-pipe region was discretized using a structured hexahedral grid pattern. The screen geometry was the most refined region followed by the near-screen region and then the open-pipe region was the coarsest as shown in Figure 2.3. The geometric discretization was then performed using the

automatic meshing tool available in the commercial software ANSYS®. The CFD simulations of the screen type static mixer (STSM) were then conducted using ANSYS Fluent® v.18.2.

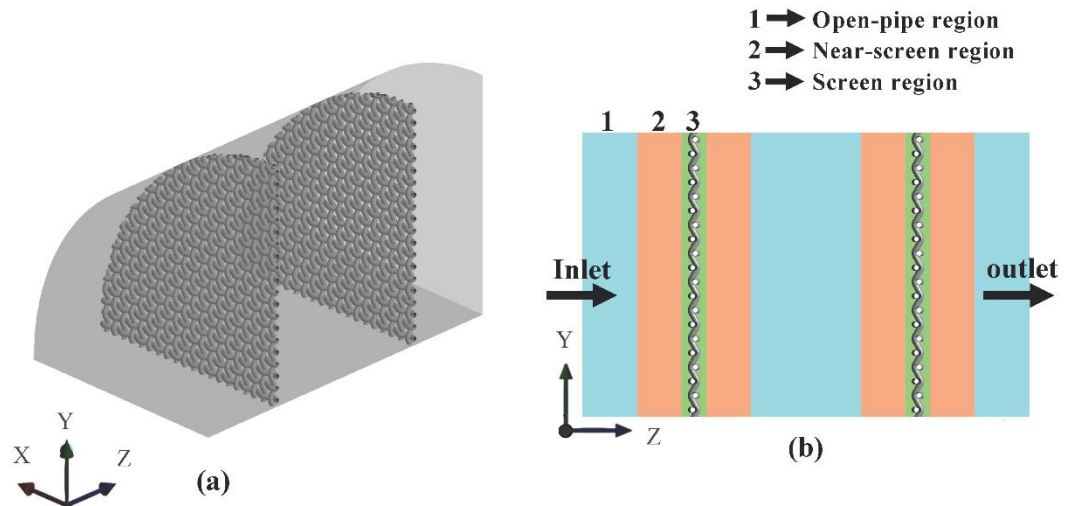


Figure 2.2. Schematic illustration of a woven mesh corresponding to $Mn = 80$ (a) quarter section of STSM and (b) sideview of the meshing regions.

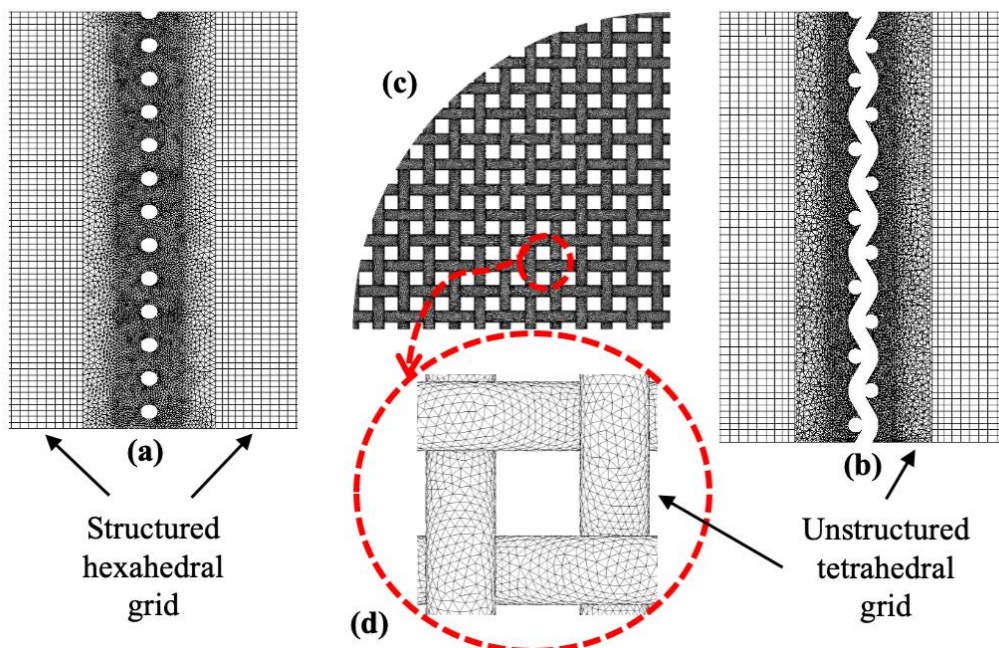


Figure 2.3. Meshing configuration (a) boundary faces meshing, (b) interior body meshing, (c) screen meshing, and (d) magnified section of screen meshing.

2.2.2 *Boundary conditions and solution method*

In the case of incompressible liquids, under steady state conditions, and in the absence of external body forces, the mass and momentum conservation equations reduce to:

$$\nabla \cdot \mathbf{V} = 0 \quad (2.2)$$

$$\rho \nabla \cdot \{\mathbf{V}\mathbf{V}\} = -\nabla P + \mu \nabla^2 \mathbf{V} \quad (2.3)$$

where \mathbf{V} is the 3D velocity vector, P is the static pressure, μ is the dynamic viscosity, and ρ is the density.

ANSYS Fluent[®] utilizes the finite volume method (FVM) to discretize and reduce the above set of equations into algebraic ones that will then be solved iteratively. This, however, requires a proper set of boundary conditions to be imposed.

At the inlet, a fully developed laminar flow, represented by the well-known parabolic profile, was always imposed through a user-defined function (UDF). This profile was generated as to reproduce the various operating conditions listed in Table 2.2 and Table 2.3. An outflow boundary condition was chosen and the walls of the pipe and faces of the screens were set to a no-slip boundary condition. Using one quadrant of the cross-section, the flow of a complete pipe could then be predicted using the rotational periodic boundary condition available in Ansys Fluent[®].

Because the work deals with incompressible fluids, the pressure-based solver was selected. The pressure and the velocity fields were predicted through the coupling of the mass and momentum equations using the SIMPLE algorithm. The gradient terms were computed using the Least Square Cell Based method. The convection term of the momentum equation was discretized using the Quadratic upwind interpolation for convective kinematics (QUICK) scheme. The second order scheme was selected for

pressure interpolation. Scaled residuals of the order of 10^{-6} were selected as a convergence criterion for the discretized equations. It should be noted that while the simulations were conducted under laminar flow regime, to accurately capture the circulation and vortices that might result from the flow around the screens, the turbulence model $k-\omega$ SST was always selected.

2.2.3 Grid independence

Grid independence tests were performed to ensure that a larger grid density will not affect the accuracy of the results. Table 2.4 shows the different grid densities and their main features for the selected screen geometries. The grid independence tests followed the grid convergence index (GCI) method proposed by Celik et al. (Celik et al., 2008), which aims at obtaining numerical results with acceptable accuracy at low computational costs. In this method, the grid refinement factor is recommended to be at least equal to 1.3. In the present study, grid independence tests were performed for one screen element while evaluating different parameters including the pressure drop along the STSM and the local velocities at different pipe cross sections. The grid independence tests were conducted at the highest velocities encountered by the screens. The results were then reported in terms of GCI and approximate relative error, ϵ . Table 2.4 presents the highest GCI value for the investigated parameters with their corresponding ϵ values if the fine grid is to be selected. For instance, the uncertainty in the numerical results of selecting the fine grid for $Mn = 50$ will reach a maximum GCI value of 1.2% with an approximate relative error, ϵ reaching 1.78%. Analyzing the various results, the fine grid was selected for all geometries as it is found to render acceptable results while minimizing the computational costs associated with finer grids.

As such the total number of grid cells for a full geometry would be equivalent to $8 \times n_{fine}$. For more details about the criterion followed in the evaluation of GCI and ϵ , readers can refer to Celik et al. (Celik et al., 2008).

Table 2.4. Grid Independence study for different screens.

Mesh number	Refinement Level	Number of elements, n	Refinement factor	Re_{pipe} (Re_b)	GCI_{fine} %	ϵ_{fine} %
$Mn = 20$	Finest	8,068,123	-			
	Fine	3,108,075	1.37	1250 (40)	0.70	1.33
	Coarse	1,295,606	1.34			
$Mn = 30$	Finest	10,566,024	-			
	Fine	4,316,873	1.35	1700 (40)	0.16	2.04
	Coarse	1,799,596	1.34			
$Mn = 50$	Finest	13,029,541	-			
	Fine	4,899,081	1.39	2225 (40)	1.2	1.78
	Coarse	1,985,388	1.35			
$Mn = 80$	Finest	16,340,387	-			
	Fine	6,987,661	1.33	1900 (20)	0.18	0.34
	Coarse	3,116,980	1.31			

2.3 Results and discussion

This section presents the outcome of the simulations starting with the model validation. This is followed by a detailed discussion of the velocity and pressure fields, including an analysis of the velocity components, contours, streamlines, and profiles.

2.3.1 Model validation

In order to validate the model predictions, numerical simulation results were compared to pressure drop data from the literature. The overall pressure drop in the mixer is the result of skin friction at the pipe wall in addition to losses resulting from the flow through the screen. Hence, the pressure drop across a screen element can be calculated using Equation (2.4) (Habchi and Azizi, 2018):

$$\Delta P_{\text{screen}} = \frac{(P_{in} - P_{out}) - \Delta P_o}{N_s} \quad (2.4)$$

where P_{in} and P_{out} are the area weighted average of the static pressure at the inlet and outlet of the STSM, and ΔP_o is the pressure drop in an empty pipe having the same length as the mixer, and N_s is the number of screen elements in the pipe.

Pressure drop across a screen (ΔP_{screen}) is typically reported in terms of a pressure loss coefficient, that is the equivalent of the Euler number (Eu). This number is the ratio of the pressure drop through the screen to the dynamic pressure (i.e. $\frac{1}{2}\rho U^2$). For flows through screens, Eu is typically a function of both the screen open area, α , and the wire Reynolds number ($Re_b = \rho Ub/\mu$) as shown in Equations (2.5) – (2.7).

$$Eu = \left[0.4537 + \left(\frac{10.76}{Re_b^{0.8213}} \right) \right] \cdot \left[\frac{1 - \alpha^2}{\alpha^2} \right] \quad (2.5)$$

$$Eu = \left[\left(\frac{18}{Re_b} \right) + \left(\frac{0.75}{\log_{10}(Re_b + 1.25)} \right) + (0.055 \log_{10}(Re_b + 1.25)) \right] \cdot \left[\frac{1 - \alpha^2}{\alpha^2} \right] \quad (2.6)$$

$$Eu = \left[0.72 + \frac{49}{(Re_b/\alpha)} \right] \cdot \left[\frac{1 - \alpha}{\alpha^2} \right] \quad (2.7)$$

Different correlations for the prediction of Eu have been proposed in the open literature, the most recent being that presented in Equation (2.5) and reported by Azizi (Azizi, 2019). It was developed after analyzing more than thousand experimental measurements and covered a wide range of flow conditions ($2 \leq Re_b \leq 14,000$). Equations (2.6) and (2.7) report the empirical correlations of Bailey et al. (Bailey et al., 2003) and Ehrhardt (Ehrhardt, 1983), respectively. These two correlations were selected in this work for validation purposes because of their different algebraic form or varying dependency on the open area. A more thorough analysis of these correlations can be found in the work of Azizi (Azizi, 2019).

To validate the simulation results, the Euler number predictions across one screen in a pipe were computed and compared against the values calculated using the aforementioned correlations at pre-defined Re_b values. Figure 2.4 shows how the empirical and simulated values compare against each other. It can be clearly observed that the results obtained from the CFD simulations for $Re_b \geq 10$ are in close agreement with the correlation predictions proposed by Azizi (Azizi, 2019) (cf. Figure 2.4a) with a maximum relative error of 7.3%. Larger relative errors were calculated at $Re_b = 1$, where they reached a maximum of 24.5%. This however is still acceptable for two reasons. First, the correlation of Azizi (Azizi, 2019) was developed for the range of $Re_b \geq 2$, and second, while Azizi correlated the data for a large number of experimental measurements, his correlation was reported to fall within $\pm 30\%$ of these points. Similarly, the maximum relative error reaches a maximum of 13.9% for $Re_b \geq 10$ when comparing the CFD results to the correlation of Bailey et al. (Bailey et al., 2003), but the error increases to 33.5% at $Re_b = 1$. The relative error, however, was almost

constant at around 20% when comparing the simulation results to the correlation of Ehrhardt (Ehrhardt, 1983).

It is worth mentioning that Eu values for $Mn = 50$ ($\alpha = 30.3\%$) and $Mn = 80$ ($\alpha = 31.4\%$) seem to be identical for the same Re_b . This was expected since they share almost identical open areas α , thereby rendering close values for the same Re_b . The pressure drop values, however, differ significantly because the empty pipe velocities would differ.

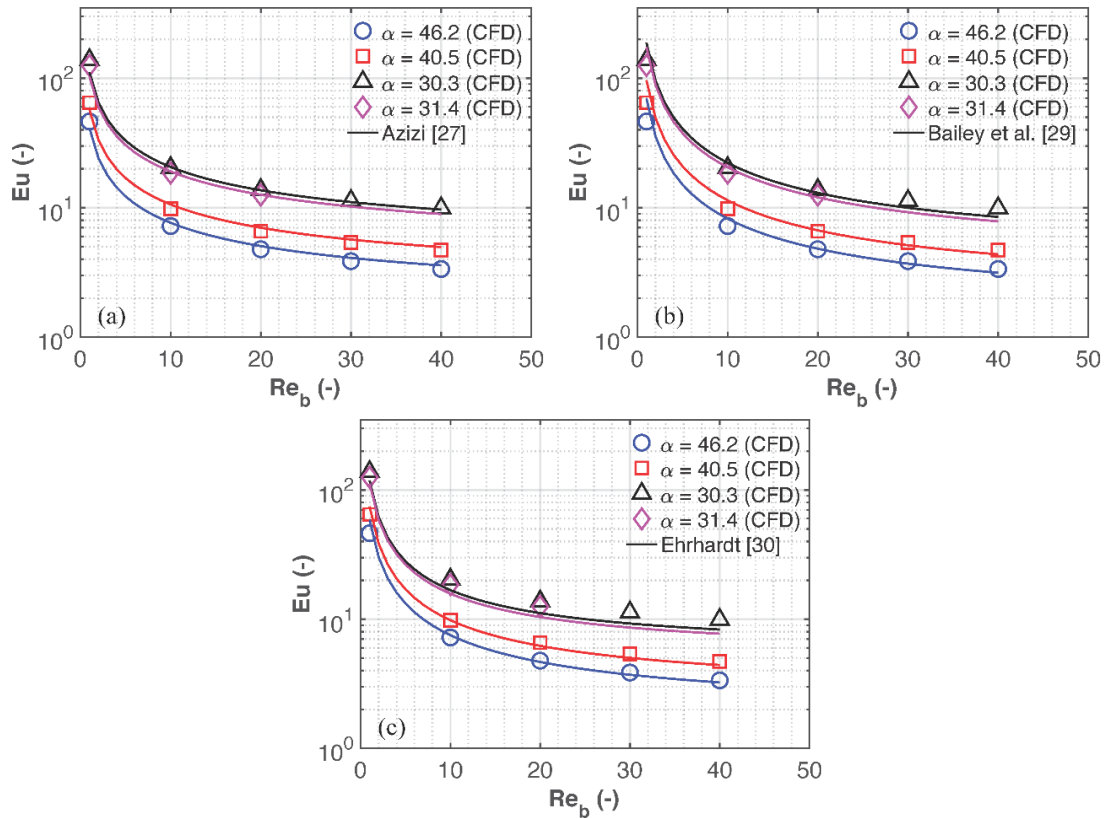


Figure 2.4. Euler number for an individual screen plotted against Re_b for the four screen geometries and compared to various empirical correlations. (a) Azizi (Azizi, 2019), (b) Bailey et al. (Bailey et al., 2003), and (c) Ehrhardt (Ehrhardt, 1983). Solid lines of varying colors refer to the correlation results for each specific screen geometry.

2.3.2 Hydrodynamic characterization

The hydrodynamic characterization of the mixer relies on the knowledge of the velocity and pressure fields. The former helps identifying the probable formation of

vortices and recirculation or flow irregularities as a result of the presence of screens, while the latter gives an indication of the resistance to flow introduced by the screen, which in turn affects the power required to operate the mixer.

Screen geometry, inter-screen spacing, number of screens, and flow velocity directly impact the flow within the mixer/contactor, whereby any alteration to their values would have subsequent effects on its velocity and pressure fields. This section will therefore highlight the impact of changing these parameters on the variations in velocity streamlines, centerline velocity, velocity profiles, as well as the pressure field.

2.3.2.1 Velocity field

2.3.2.1.1 Velocity components

The effect of screens on the velocity field is discussed in this section by analyzing the various components of the velocity vector (i.e. u , v , and w). To better highlight this effect the three velocity components are plotted along the centerline of the pipe for two different screen geometries, namely, $Mn = 20$ and $Mn = 80$, and two different Re_b values (i.e. $Re_b = 1$ in Figure 2.5a and $Re_b = 20$ in Figure 2.5b). These two geometries were selected as they represent the largest and smallest wire diameter, b , and mesh size, M , respectively. It should be noted that for $Mn = 20$, $w_{(x=0,y=0,z=0)} = 0.0049$ m/s at $Re_b = 1$, and $w_{(x=0,y=0,z=0)} = 0.0989$ m/s at $Re_b = 20$; while for $Mn = 80$, $w_{(x=0,y=0,z=0)} = 0.0144$ m/s at $Re_b = 1$, and $w_{(x=0,y=0,z=0)} = 0.2877$ m/s at $Re_b = 20$.

The axial variation of the normalized velocity components are plotted in Figure 2.5 which also shows the effect of varying the inter-screen spacing. In this figure, the three components of the centerline velocity were normalized with respect to the initial inlet centerline axial velocity $w_{(x=0,y=0,z=0)}$. It is therefore worth mentioning that the

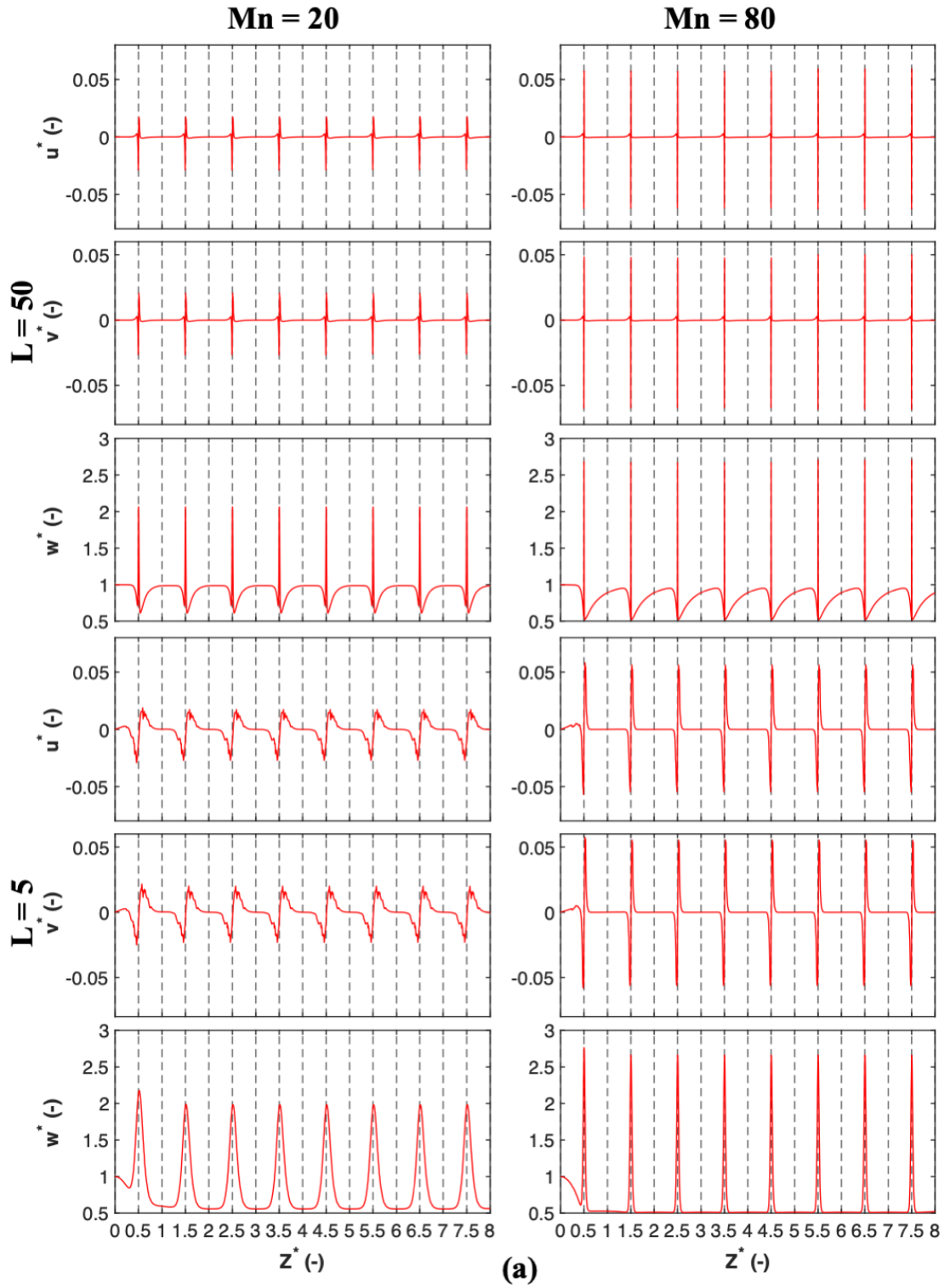
inlet velocity has only an axial (z-direction) component, w , with the other normal and tangential components being equal to zero at the inlet. The initial values of these components are shown in Equation (2.8).

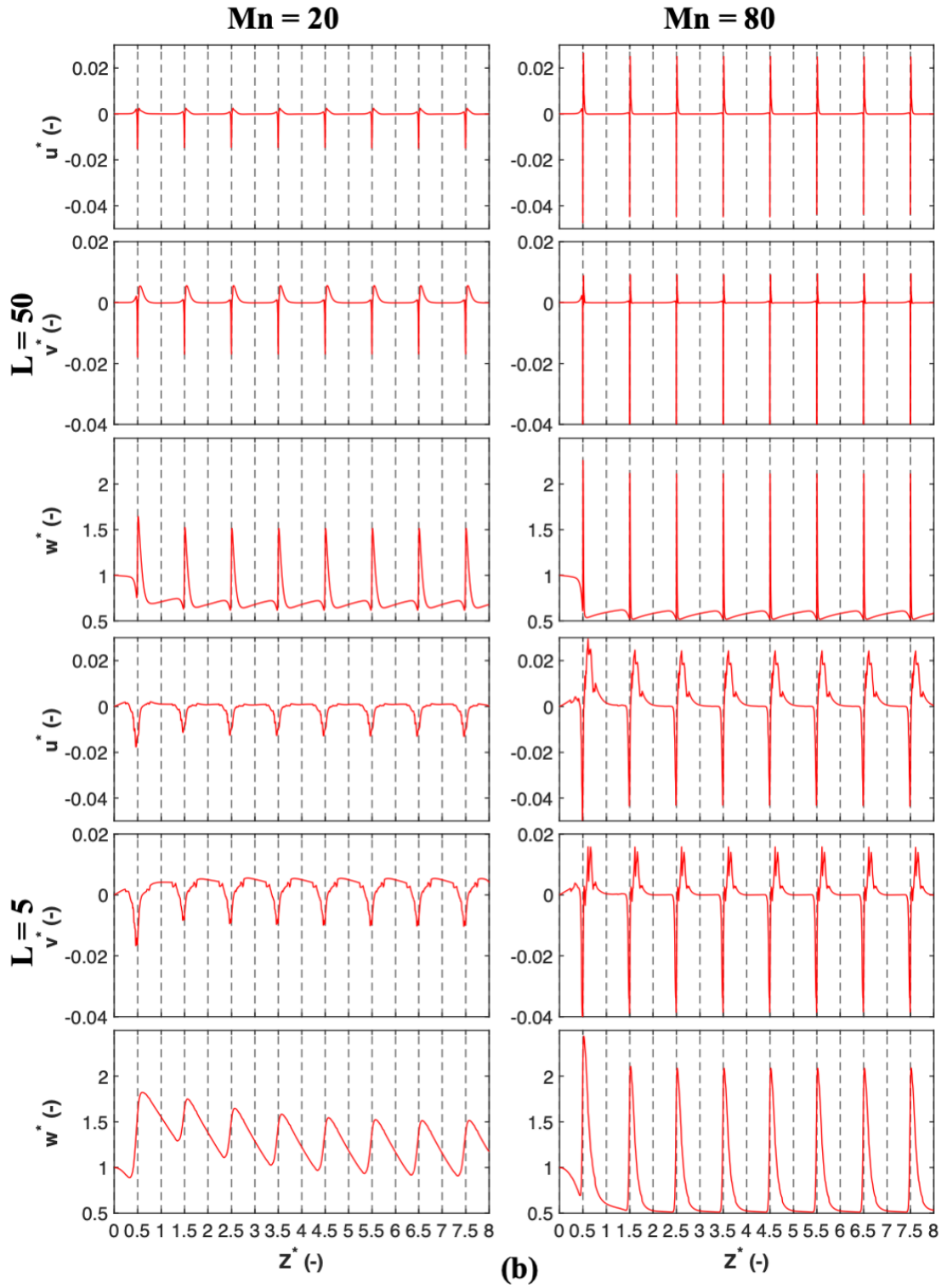
$$\begin{cases} u_{in}^* = v_{in}^* = 0 \\ w_{in}^* = 1 \end{cases} \quad (2.8)$$

These normalized centerline velocities are plotted against a normalized axial distance, Z^* , defined as the ratio of the local axial distance to the inter-screen spacing ($Z^* = Z/L$). Accordingly, due to the equidistant nature of the distribution of screens in the mixer, the location of any woven mesh, j , in a sequence would coincide with location $Z^* = (j - 1) + 0.5$.

It is clear from Figure 2.5 that the presence of screens does induce an alteration to the well-known stratified laminar flow by modifying the radial and tangential components of the velocity vector. These changes, however, quickly dissipate and disappear downstream of each screen with their decay profile being a function of Re_b , L , and the screen geometry. However, the magnitude of u^* and v^* is consistently much smaller than that of w^* , with minimum peak ratios of w^*/u^* and w^*/v^* reaching values of about 71.5 for $Mn = 20$ at $Re_b = 1$, and about 39.6 for $Mn = 80$ at $Re_b = 1$. This indicates that the flow is continuously an axial flow. Furthermore, it can be clearly discerned from Figure 2.5 that the flow is also repeatable/periodical after the first screen for most cases, whereby the magnitude and profile of the various velocity components become unchanged as the flow passes through consecutive screens. In addition, the difference in the magnitude of u^* , v^* , and w^* between different screen geometries under the same conditions of Re_b , and L , is due to the different velocity magnitudes required to maintain a constant Re_b when b is changing. It should be noted

that similar trends were obtained for $Mn = 30$ and $Mn = 50$. It should be mentioned that Figure 2.5c shows the various velocity components around the fifth screen in the pipe. It zooms to the region corresponding to $4.4 < Z^* < 4.6$ to capture additional details of these profiles.





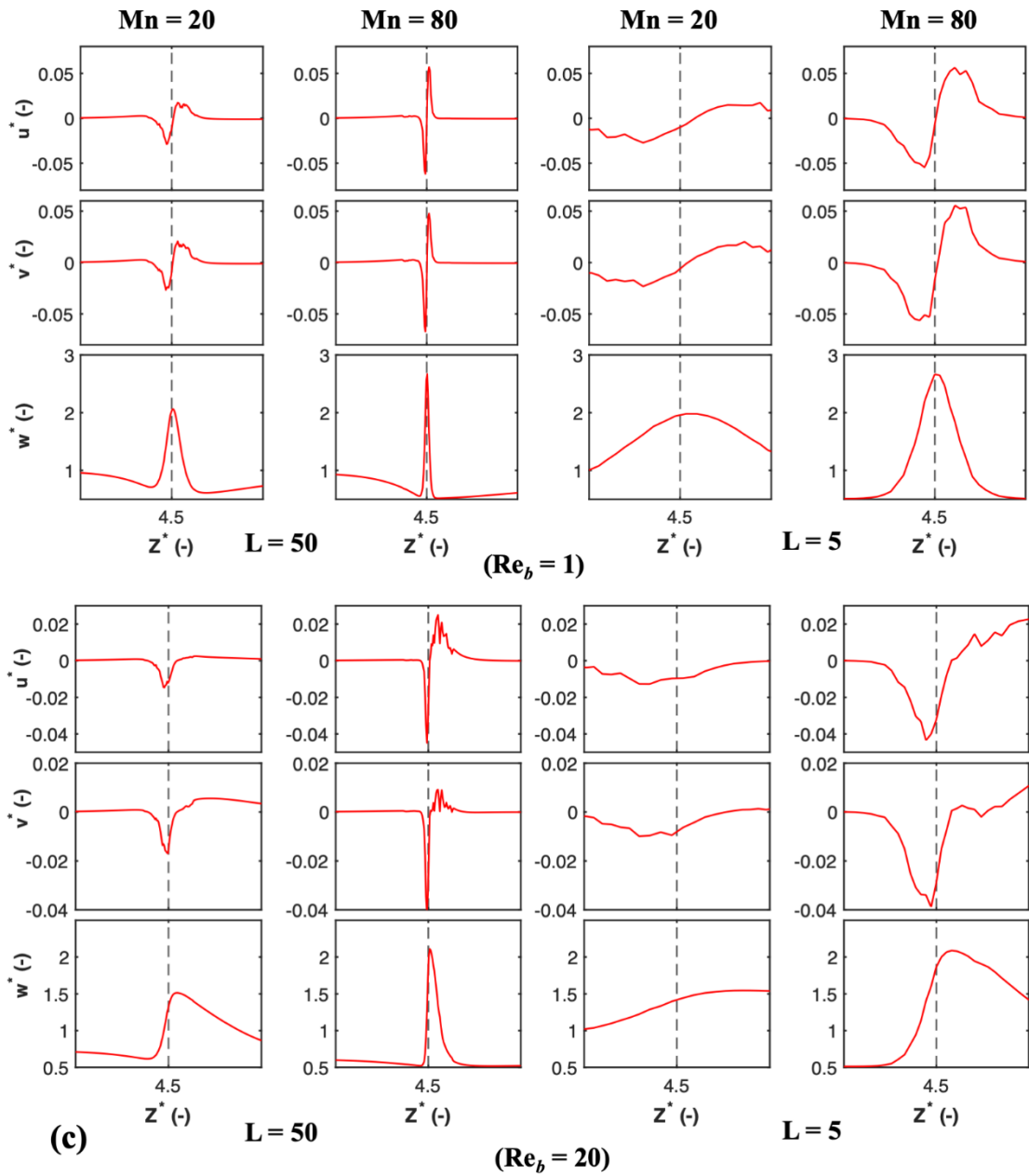
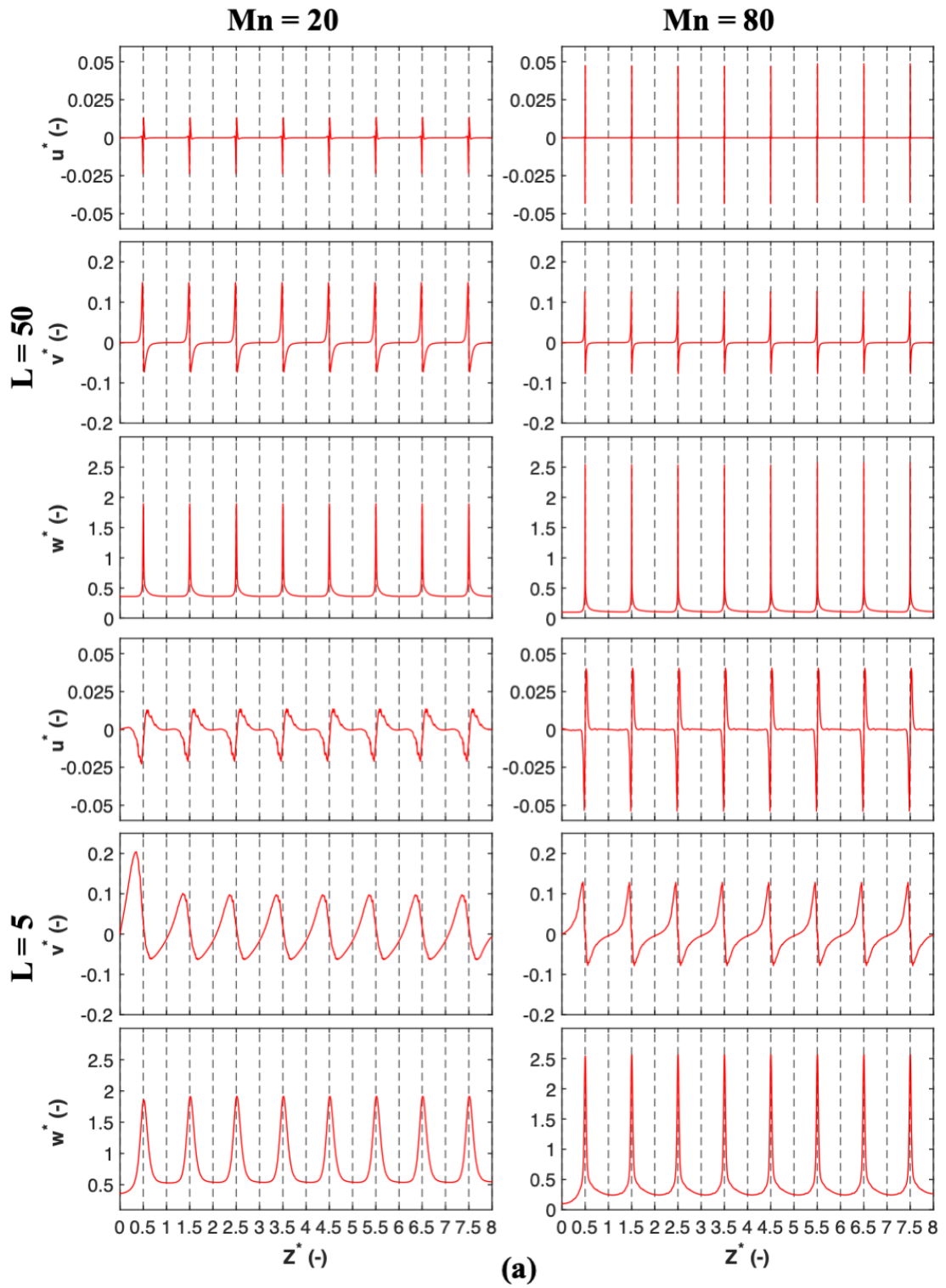


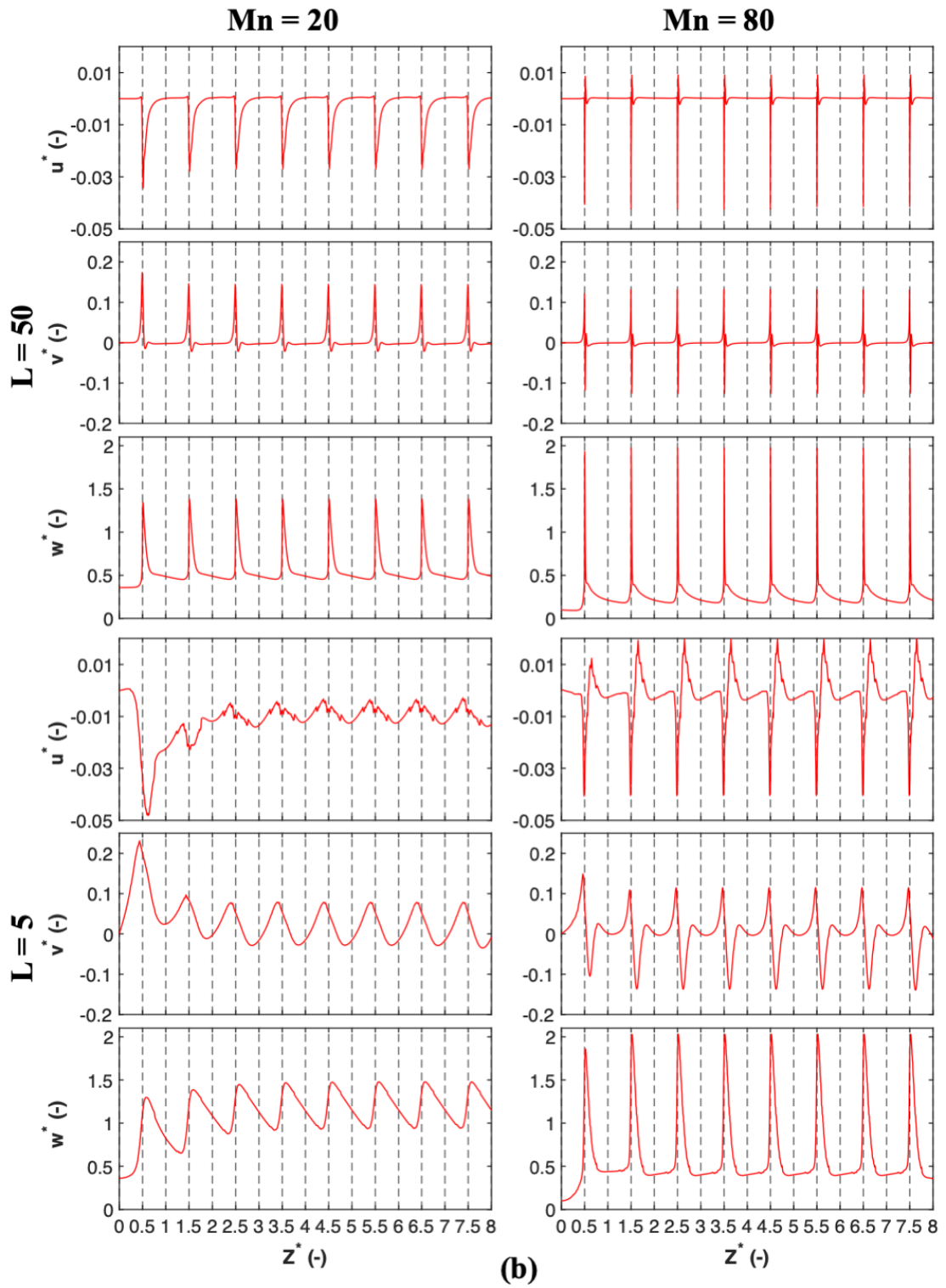
Figure 2.5. Normalized velocity components at the centerline as a function of non-dimensional axial position at different inter-screen spacing for $Mn = 20$ and $Mn = 80$ at (a) $Re_b = 1$ and (b) $Re_b = 20$ and (c) profiles zoomed around the 5th screen for $4.4 < Z^* < 4.6$.

To further generalize the analysis, the components of the velocity vector were also analyzed in a region away from the centerline but near the wall of the pipe.

Accordingly, u^* , v^* , and w^* were plotted along a line that is located at a distance of $1M$ from the wall for $Mn = 20$ and $Mn = 80$ at $Re_b = 1$ and 20 (i.e. $Re_b = 1$ in Figure 2.6a

and $Re_b = 20$ in Figure 2.6b). Figure 2.6 shows that the axial velocity near the wall no longer dominates the velocity field similarly to the central region. In other words, the minimum peak ratios of w^*/u^* and w^*/v^* reach dropped to about 6.4 for $Mn = 20$ at $Re_b = 1$ and about 13.6 for $Mn = 80$ at $Re_b = 20$ compared to ratios of 71.5 and 39.6 along the centerline. This indicates that the flow could be treated as nearly axial only within the central region of the pipe, whereas in regions near the wall, this assumption does not hold true. This stresses the need to model the full geometry (i.e. from centerline to the wall) instead of only considering the flow as symmetric around the centerline region as it is the case in various CFD studies of unbounded flows through screens. It should be mentioned that Figure 2.6c shows the various velocity components around the fifth screen in the pipe. It zooms to the region corresponding to $4.4 < Z^* < 4.6$ to capture additional details of these profiles.





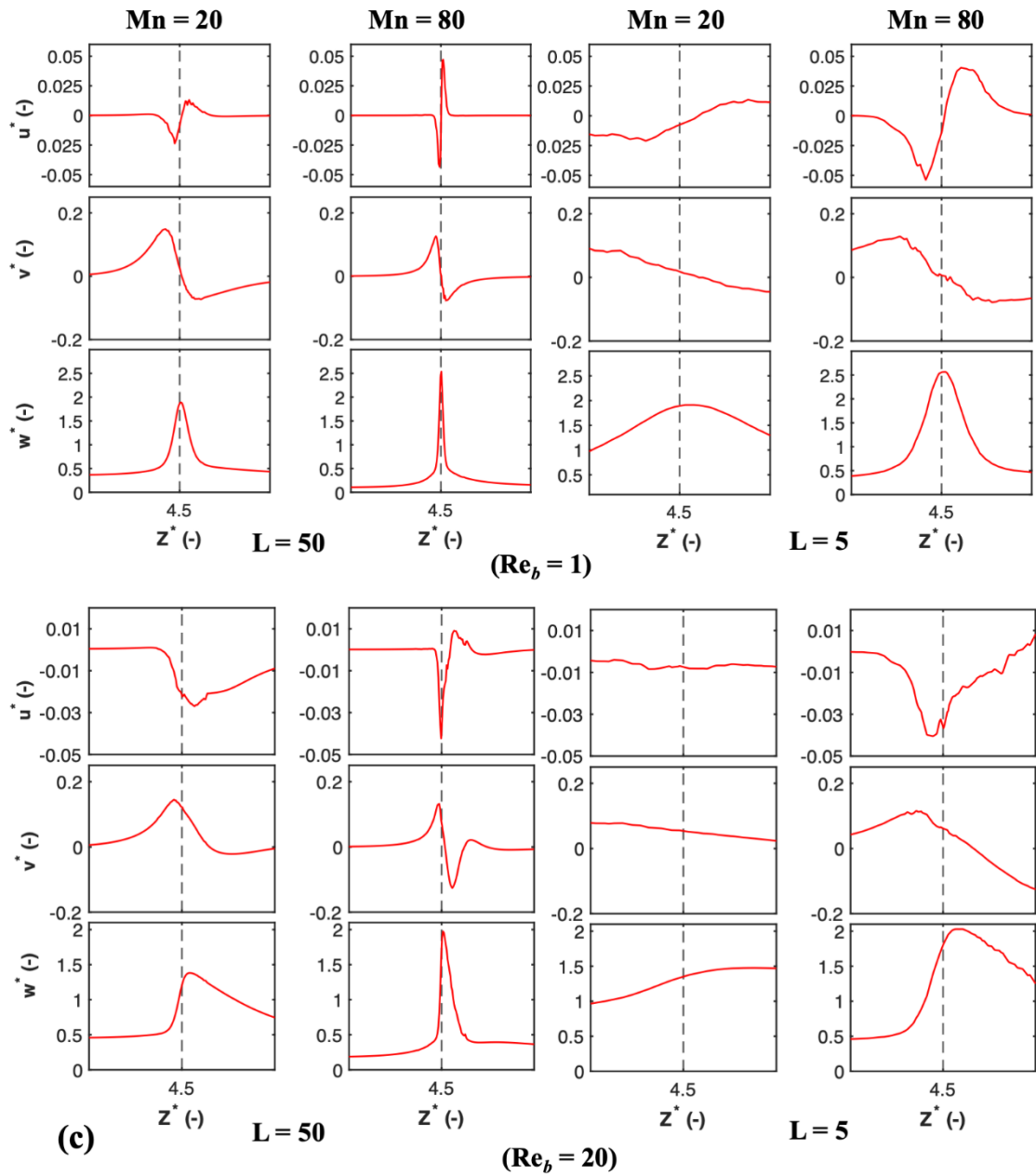


Figure 2.6. Normalized velocity components at $1M$ from the wall as a function of non-dimensional axial position at different inter-screen spacing for $Mn = 20$ and $Mn = 80$ at (a) $Re_b = 1$ and (b) $Re_b = 20$ and (c) profiles zoomed around the 5th screen for $4.4 < Z^* < 4.6$.

2.3.2.1.2 Velocity contours

The velocity contours around the 7th screen for $Mn = 20$ and 80 at $Re_b = 20$ and $L = 50$ mm at various upstream and downstream axial locations are shown in Figure 2.7. These locations were normalized with respect to the mesh size, M , to allow for

better generalization when different screen geometries are compared. The method of calculation of this normalized distance is presented in Equation (2.9), where, for example, $M^* = 0$ corresponds to the plane that cuts through the middle of the screen. Accordingly, three different axial locations, namely $M^* = -0.5, 0$, and 0.5 are shown in Figure 2.7. One cannot but notice the rotational behavior of the flow as it moves downstream of the screen. This is due to the nature of the woven mesh whereby the screen wall is shifting location relative to the fluid as it is flowing through it.

$$M^* = \frac{(Z - [jL - 0.5L])}{M} \quad (2.9)$$

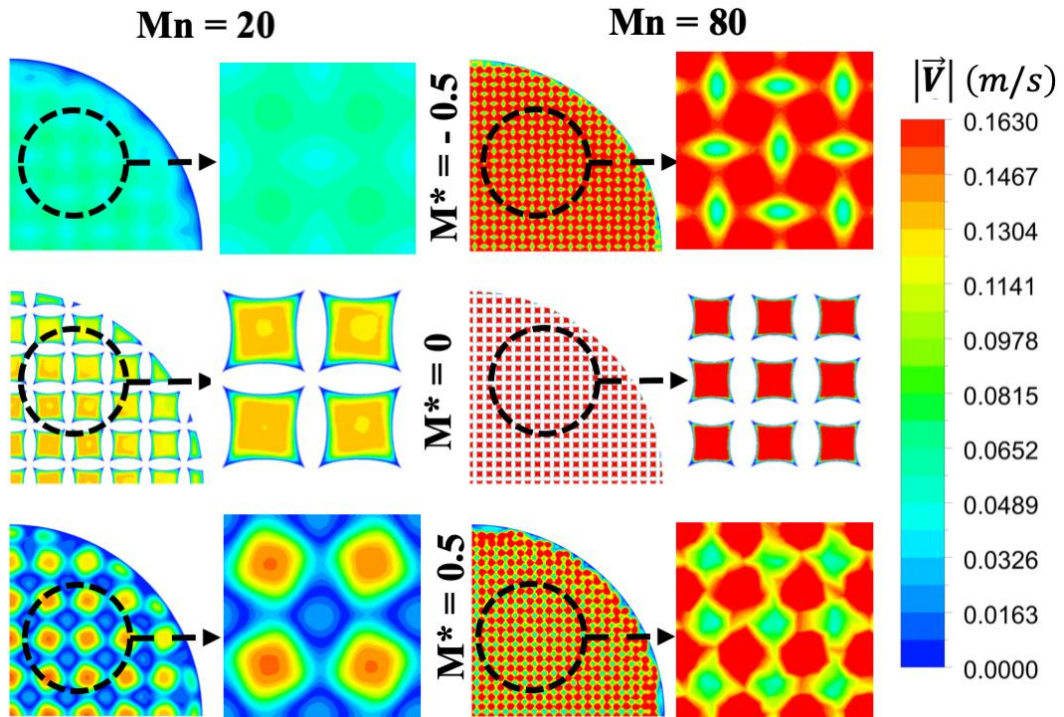


Figure 2.7. Velocity contours through the 7th screen at various axial locations at $Re_b = 20$ for $Mn = 20$ and $Mn = 80$.

Moreover, in order to clearly visualize the rotational behavior of the flow as it passes through the screen, the magnitude of the vorticity tensor, $|\psi|$, given in Equation (2.10a) was also calculated. The vorticity tensor is presented in Equation (2.10a). As

such, the contour plot of the vorticity magnitude through the 7th screen, for the same conditions as presented in Figure 2.7, are illustrated in Figure 2.8.

$$|\psi| = \sqrt{2\psi:\psi} \quad (2.10a)$$

$$\psi = \frac{1}{2}(\nabla\mathbf{V} - \nabla\mathbf{V}^T) \quad (2.10b)$$

This figure highlights three important features. First, the vorticity magnitude shows higher values near the walls of both the pipe and the screen. Such a behavior was expected because of the difference in velocities between the centerline and near-wall region would result in a substantial shear which translates into higher vorticities. Another important observation is that the large vorticities generated at the plane of the screen are maintained downstream in the close vicinity of the screen. This rotational behavior of the flow was also expected due to the high shear generated by the screen wires which would consequently produce high vorticities. These vorticities would then require a certain distance downstream of the screen to completely dissipate. Finally, the amplitude of the vorticity magnitude was found to be directly related to the screen geometry. This is clearly discerned by comparing the contour plots of $Mn = 20$ and 80 whereby a higher screen solidity (lower values of α , and M) results in higher shear values and consequently higher vorticities.

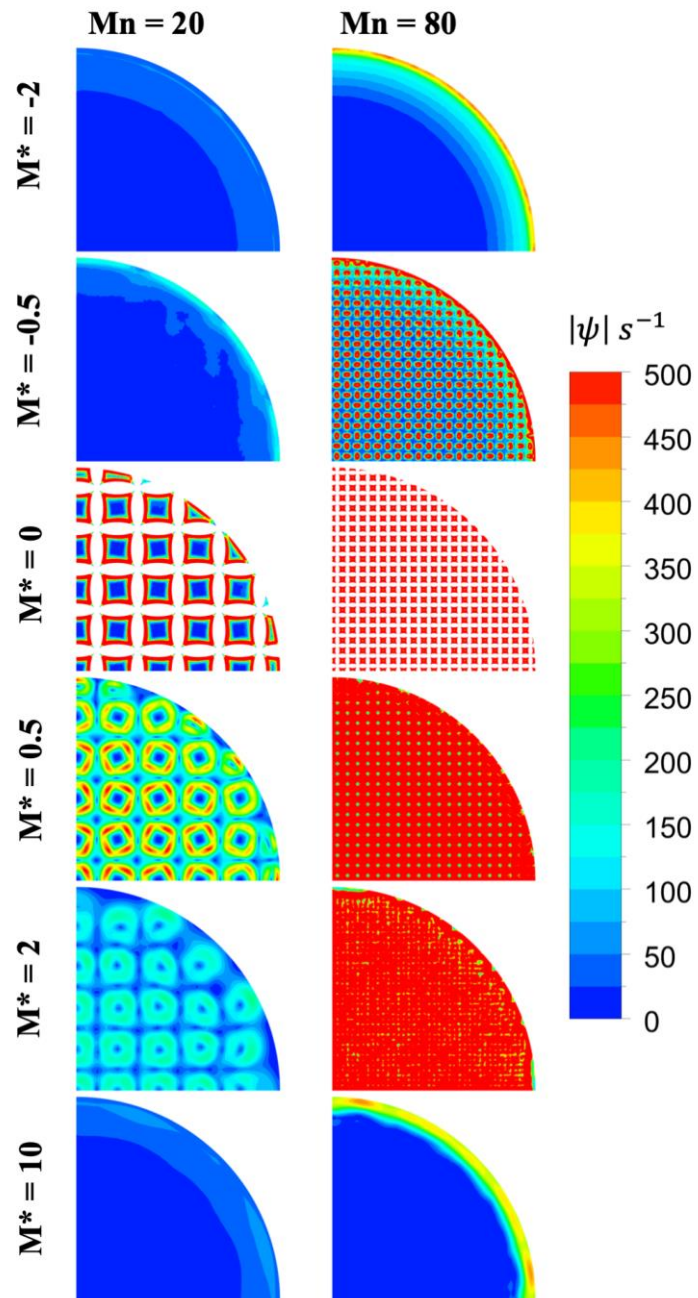


Figure 2.8. Vorticity contours through the 7th screen at various axial locations at $Re_b = 20$ for $Mn = 20$ and $Mn = 80$.

2.3.2.1.3 Velocity streamlines

Figure 2.9 shows the streamlines of the flow as it passes through the first screen while also presenting the effect of varying the screen geometry as well as Re_b .

Starting with a perfect parabolic profile, the streamlines reaching the screens are always smooth and laminar regardless of Re_b . At $Re_b = 1$ (cf.

Figure 2.9a), the streamlines pass through the screen where they spread then recombine quickly downstream of the screen indicating a typical laminar flow behavior past a wire. As the wire Reynolds number increases, vortex formation and recirculation are observed downstream of the screen such that the formation of these vortices increases as the value of the wire Reynolds number increases. Moreover, for the same hydrodynamic conditions (e.g. $Re_b = 20$), circulations and vortices are more pronounced for screens with a larger wire diameter, which consequently affect the inlet velocity magnitude required to achieve a constant Re_b . As the wire diameter decreases, a larger average velocity is required to maintain a constant Re_b , therefore, a higher momentum should have resulted in higher recirculation patterns, the fact that was not observed. To further investigate these findings, simulations at constant Re_{pipe} , i.e. different Re_b , were performed and their results are shown in Figure 2.10. Here, the results clearly show that for the same inlet flow conditions, the larger wire diameter had a more pronounced effect on flow disturbance and formation of vortices/recirculation patterns. This clearly highlight the important role of the wire diameter in determining the formation of vortices and disturbances within the flow and consequently the velocity field because a larger wire diameter would require a longer distance for the streamlines to re-coalesce and consequently the potential formation of dead zones.

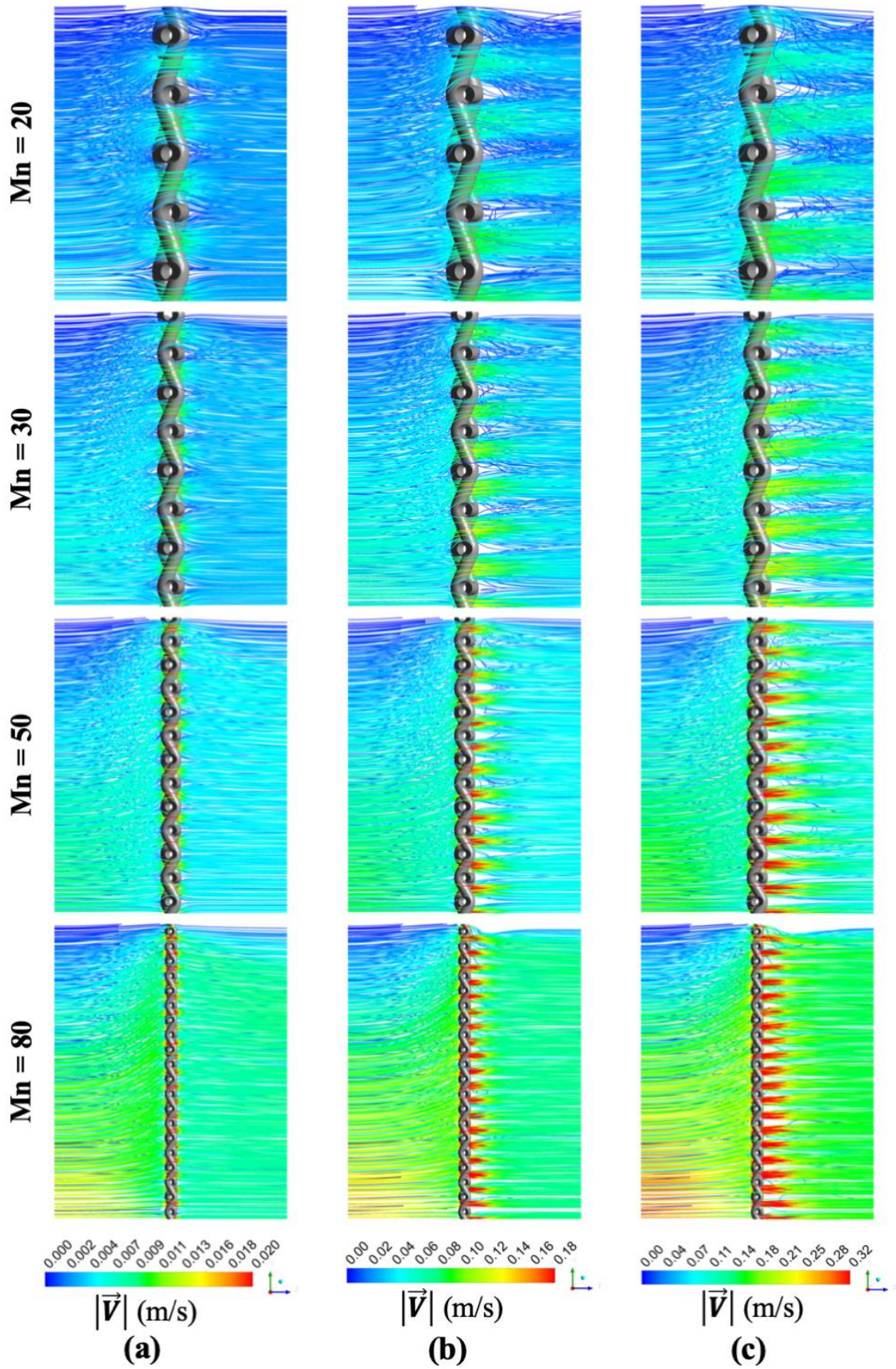


Figure 2.9. Velocity streamlines through the 1st screen for different geometries at (a) $Re_b = 1$, (b) $Re_b = 10$, and (c) $Re_b = 20$.

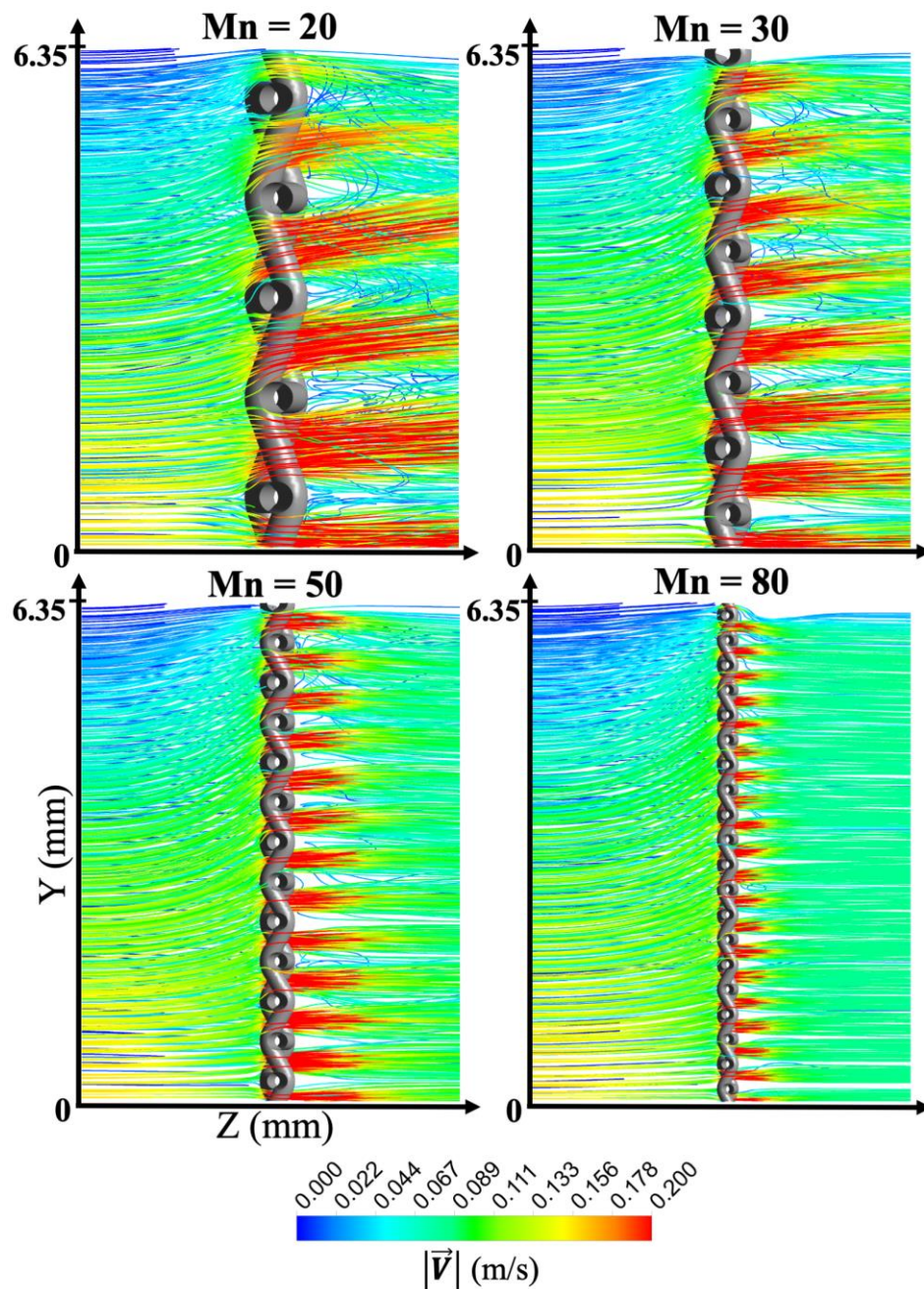


Figure 2.10. Velocity streamlines through the 1st screen for different geometries, at $Re_{pipe} = 1,000$. ($Y = 0$ corresponds to the central axis and $Y = 6.35$ mm corresponds to the pipe wall).

2.3.2.2 Velocity profiles

In order to provide a more comprehensive analysis for the flow field within the STSM, the axial velocity profiles were investigated. These profiles were examined for

various locations upstream and downstream of the screen along a fictitious line normal to the flow that goes through the YZ plane. These locations were normalized and represented in terms of M^* (cf. Equation (2.9)). It is to be noted that these velocity profiles are reported here for the first two screens in the series since repeatability of the flow took place starting from the second element in the majority of cases, as shown in Figure 2.5. Moreover, to better highlight the effect of inter-screen spacing on the profiles, the work was also analyzed halfway between screens. Velocity profiles are also presented in their normalized form with respect to the inlet centerline velocity similarly to §2.3.2.1, whereby a value of 1 reflects that $w = w_{(X=0,Y=0,Z=0)}$.

Figure 2.11 shows normalized axial velocity profiles for the flow passing through the first two screens for $L = 50$ mm and $Re_b = 1$ and 20. These profiles were reported at various locations ranging between $-4 \leq M^* \leq 2$ with respect to the first and second screens for two screen geometries, namely, $Mn = 20$ and $Mn = 80$.

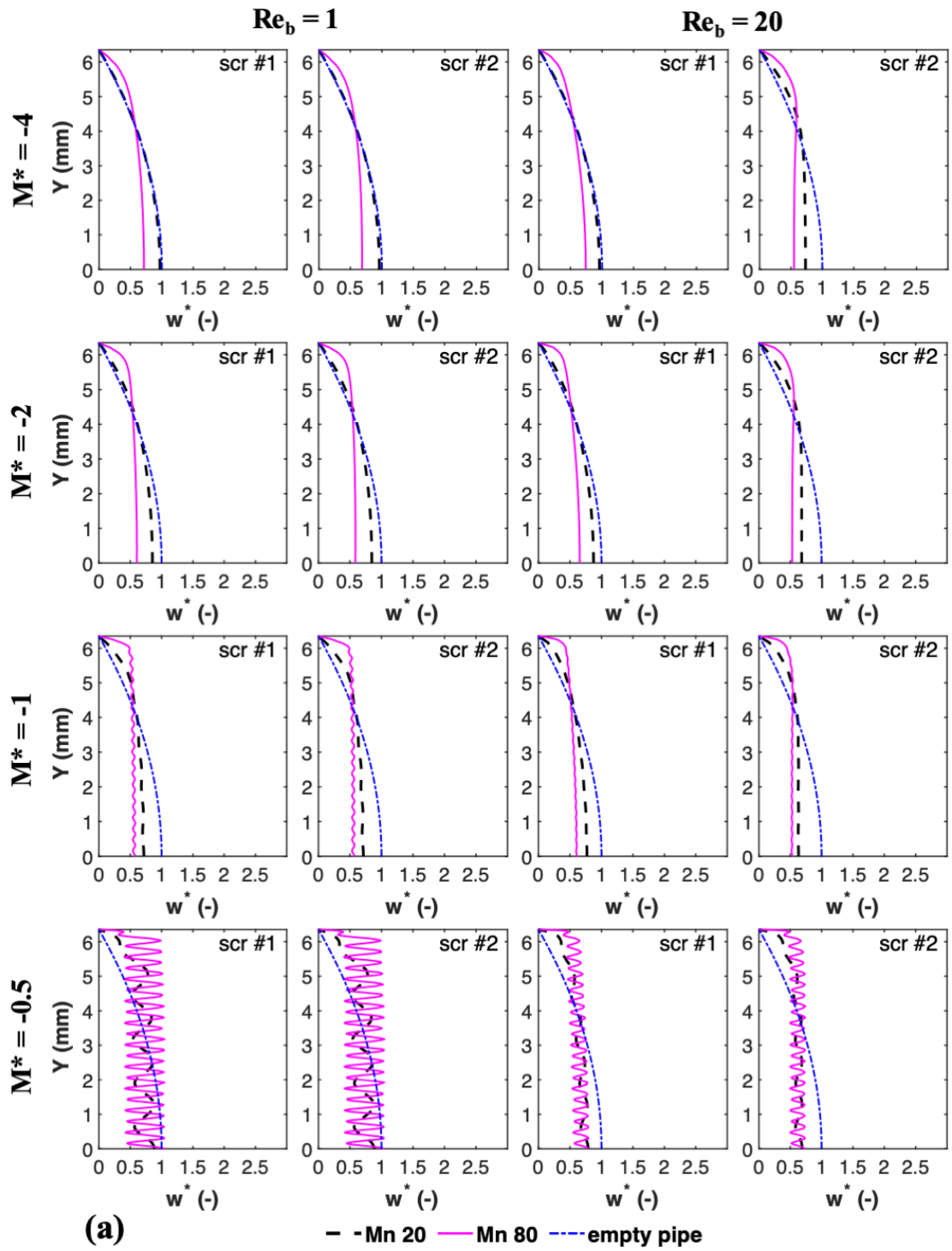
For the case of $Mn = 20$ at $Re_b = 1$, the normalized axial velocity profile shows no deviation from the inlet parabolic profile even at $M^* = -4$. However, as the flow approaches the screen, the hydrodynamics become more affected by its presence which causes more resistance to the flow. Hence, the velocity profile flattens with the maximum centerline velocity decreasing below that for the fully developed flow condition. This is, however, counterbalanced by an increase in the radial velocity away from the centerline to conserve the flow rate (i.e. mass conservation for an incompressible fluid). Closer to the screen, the velocity streamlines start converging in order to pass through the openings (cf. Figure 2.9). This behavior is reflected by a new form of the velocity profile which starts assuming a zigzag/sinusoidal shape (cf. Figure 2.11). As the flow passes through the screen ($M^* = 0$) all the fluid would pass through

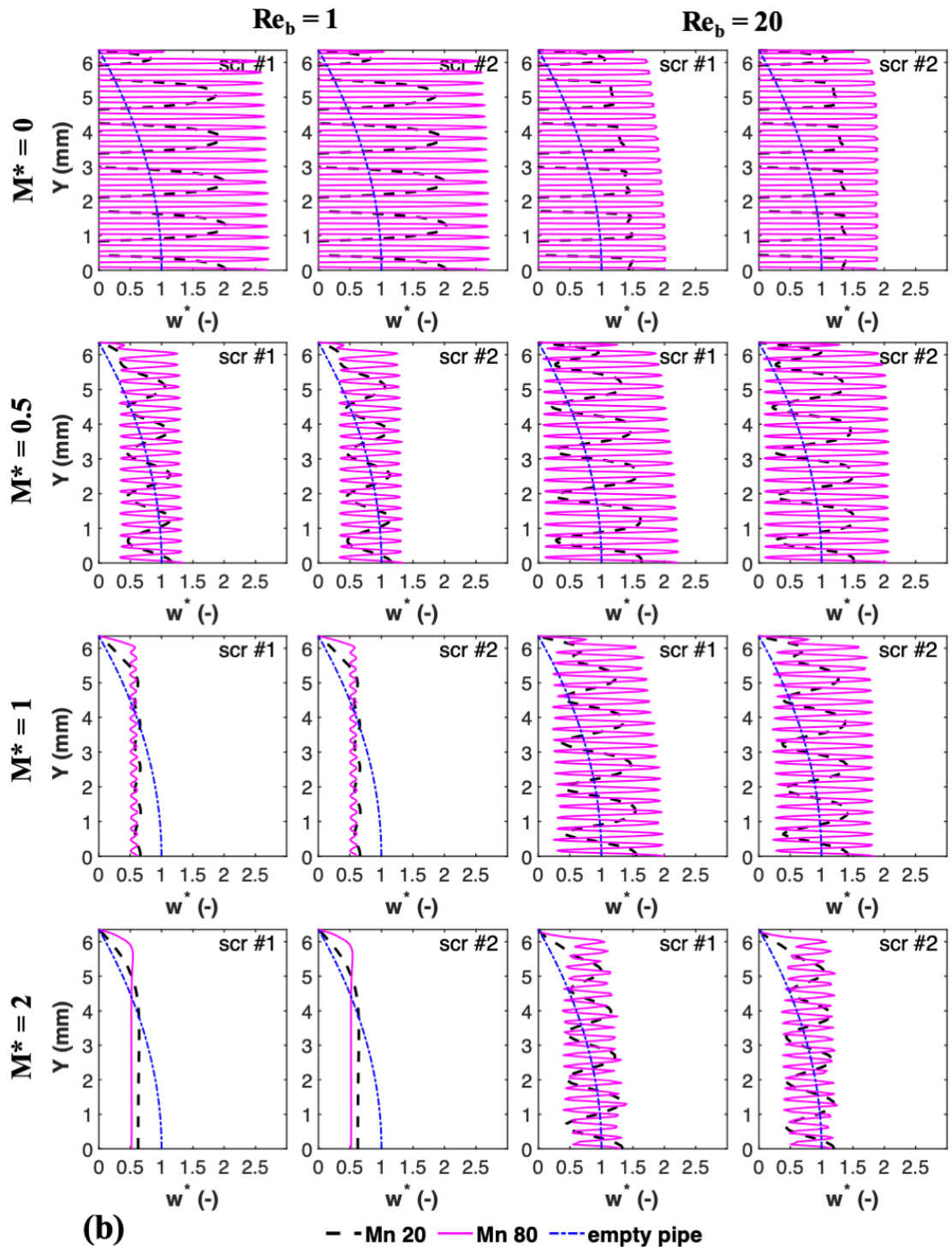
the openings of the screen, and hence high velocity jets can be observed with part of the profile reaching zero at locations where the wire elements exist. Downstream of the screen, the velocity profile starts assuming non-zero values as the effect of the screen body diminishes. Finally, the zigzag shape of the velocity profile starts to gradually dissipate as the flow reaches locations farther downstream. The farther the flow travels away from the screen, the velocity profile returns to its original parabolic shape. This clarifies the impactful presence of a screen on the velocity field and clearly highlights that its presence affects both the upstream and downstream flows up to a certain distance, beyond which the pipe flow returns to normal. It can also be seen from Figure 2.11 that no difference can be distinguished between the flow through the first or second screens.

2.3.2.2.1 Effect of screen geometry

The effect of screen geometry on the velocity profile is also highlighted in Figure 2.11 where the velocity profiles of screens with $Mn = 80$ are also presented. This screen has a smaller fraction open area, wire diameter, and mesh opening compared to those of $Mn = 20$. As expected, these geometrical parameters have a direct impact on the velocity profile. Upstream of the screen, it is clear from Figure 2.11 that the impact of this screen goes beyond 4 mesh sizes where the velocity profile can be seen to be already flat. However, as the flow further approaches the screen and passes through it and farther downstream, the velocity profile follows a similar trend to that of $Mn = 20$. As such, the profile shows a zigzag pattern that further accentuates near the screen and become a group of high velocity jets at the center of the screen. This profile further subsides and return to normal farther downstream from the screen. Since the screen of $Mn = 80$ contains more openings per cross-sectional area (20 vs. 80 per inch) the jets

leaving the screen are much more abundant with the distance between them being equal to the wire diameter. This explains why these jets are narrow and abundant for the case of $Mn = 80$ as opposed to few thicker ones in the case of $Mn = 20$. Additionally, the region in which the impact of the screen on the velocity field is persistent seems to be directly proportional to its geometry with finer screens having a longer impact zone. This is clearly obvious from the midway profiles for both screens. For the case of $Re_b = 1$, it can be clearly seen that the profile of the screen with $Mn = 20$ returns to the normal parabolic profile in an empty pipe, whereas that of the screen with $Mn = 80$ is not completely reached. This location corresponds to $M^* = 19.68$ for $Mn = 20$ whereas it corresponds to $M^* = 78.7$ for $Mn = 80$.





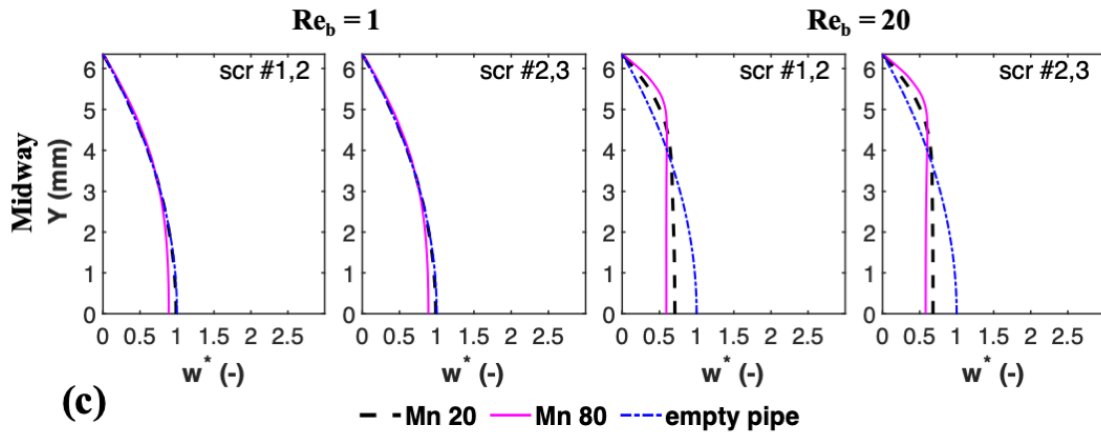


Figure 2.11. Normalized axial velocity profile around the 1st and the 2nd screens for $L = 50$ mm at $Re_b = 1$ and $Re_b = 20$ for (a) $-4 \leq M^* \leq -0.5$ (b) $0 \leq M^* \leq 2$ and (c) Midway.

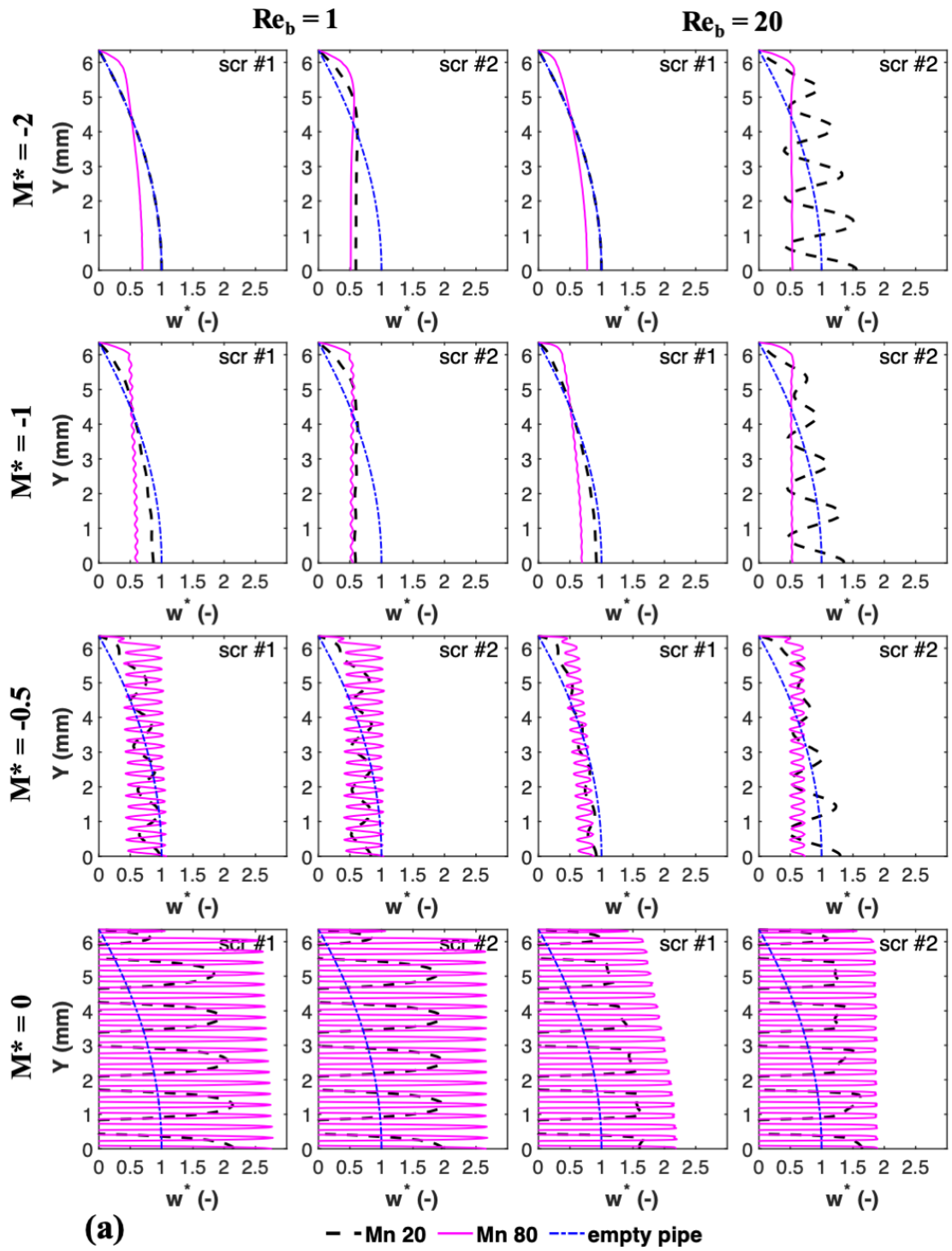
2.3.2.2.2 Effect of flow velocity

Figure 2.11 also shows the effect of changing Re_b on the velocity profile. While the major modification to the velocity profile are similar to the case of lower Re_b (e.g. flattening, zigzag, etc...) the reader cannot but distinguish a more pronounced effect for the presence of the screen on the velocity field for a much larger distance upstream or downstream. Furthermore, because the flow is affected as it passes through the first screen to a much longer distance, it consequently affects the profile as it passes through the second, and subsequent screens. This is reflected by the “flatter” profile compared to that going through the first screen. The other difference is the smaller amplitude in the velocity changes upstream of the screen ($M^* = -0.5$) as compared to the lower Re_b case, while this amplitude is much larger and is sustained to a much longer distance downstream of the screen. It can be clearly observed that midway between the screens the flow would have receded to a purely laminar one for low Re_b while the effect of the presence of a screen, manifested by the presence of a flat velocity profile, still dominates for the case of $Re_b = 20$.

2.3.2.2.3 Effect of inter-screen spacing

To highlight the effect of changing the inter-screen spacing, the velocity profiles were replotted in Figure 2.12 for the case of $L = 5$ mm. The profiles are presented for $-2 \leq M^* \leq 2$ since for $Mn = 20$, the interscreen distance of 5 mm has a midpoint value of $M^* \approx 1.96$. This value however corresponds to $M^* \approx 7.87$ for the case of $Mn = 80$.

As the flow passes through the first screen, and regardless of Re_b , similar profiles could be observed as the previous case of longer inter-screen spacing. This is to be expected. However, the situation changes when the flow goes through the second screen, whereby the flow did not have enough space to return to its normal parabolic profile before it goes through it. Hence, the flow passes through the second screen with a “deformed” profile, depending on the flow velocity. In these cases, the flow was found to approach the second screen with flatter velocity profiles for all screens, except for $Mn = 20$ at $Re_b \geq 10$. For this particular case (and subsequently at larger Re_b), and because of the short inter-screen distance, the velocity profile approaches the second screen while the effect of “jets” is still pronounced. This was also observed for screens with $Mn = 30$ (for the same conditions) and for screens with $Mn = 50$ and 80 for the case of $Re_b \geq 20$. Another observation is that the jets for the second and subsequent screens exit the mesh much more uniform and homogeneous when the screens are fine even in regions much closer to the wall. This is clearly observed when one compares the velocity profiles between the first and second screens of $Mn = 80$ at $M^* = 0$, and beyond, for the case of $Re_b = 20$. As such, one clearly distinguishes the uniformity of the flow after the second screen where the effects of a parabolic profile have clearly subsided.



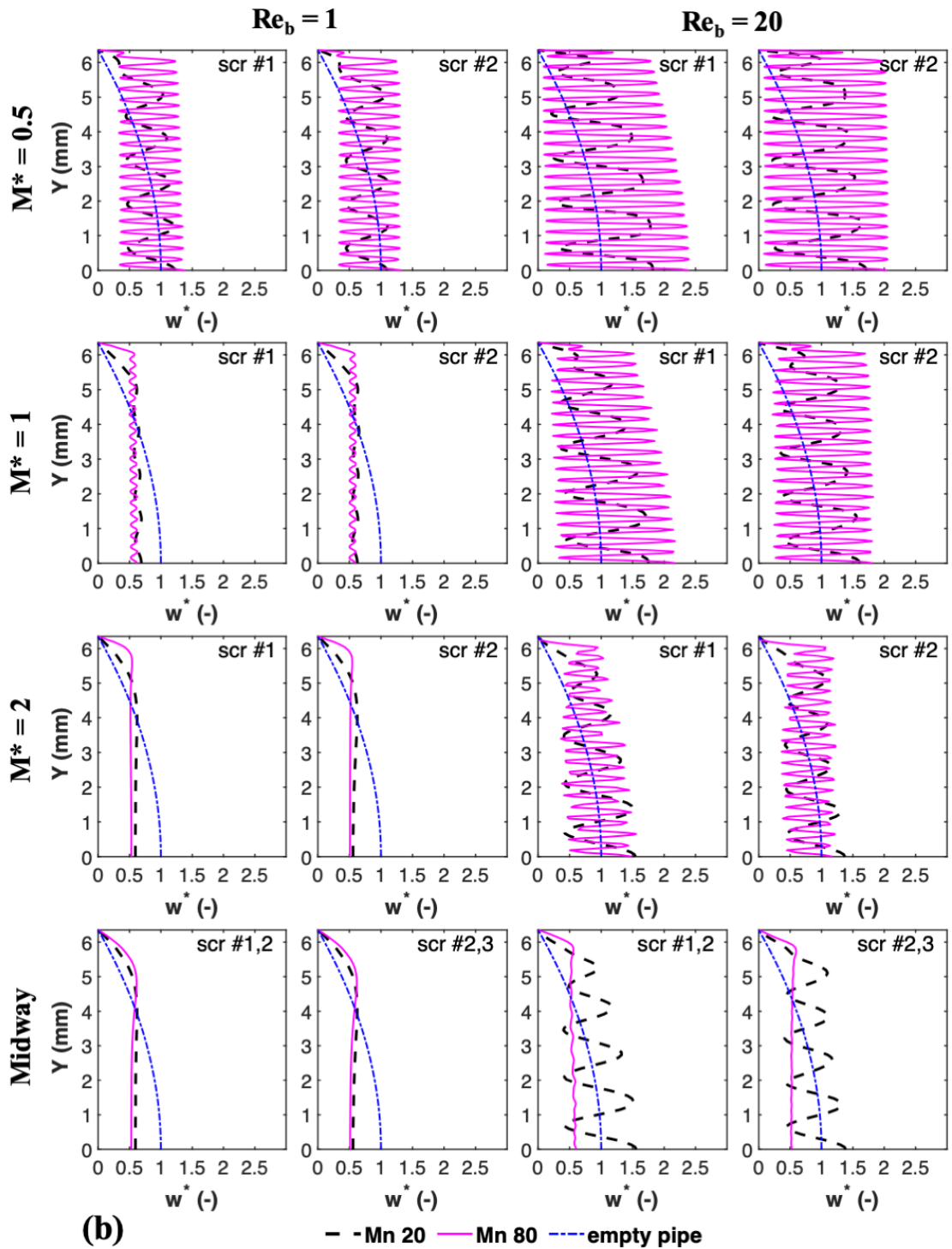


Figure 2.12. Normalized axial velocity profile around the 1st and 2nd screens for $L = 5$ mm at $Re_b = 1$ and $Re_b = 20$ for (a) $-2 \leq M^* \leq 0$ and (b) $0.5 \leq M^* \leq 2$ and Midway.

To better visualize the effect of a fluctuating velocity approaching the screen, similarly to the case of $Mn = 20$ at $Re_b = 20$ and $L = 5$ mm, the velocity streamlines

passing through the first three screens are shown in Figure 2.13a. In addition, the dampening effect of a longer inter-screen distance, as was the case for $Mn = 20$ at $Re_b = 20$ and $L = 50$ mm, is shown in Figure 2.13b. For the case of a short inter-screen spacing, flow perturbations produced by the first screen persist until they reach the following one. However, for a longer inter-screen spacing, these perturbations are dampened much earlier than they reach halfway between two consecutive screens.

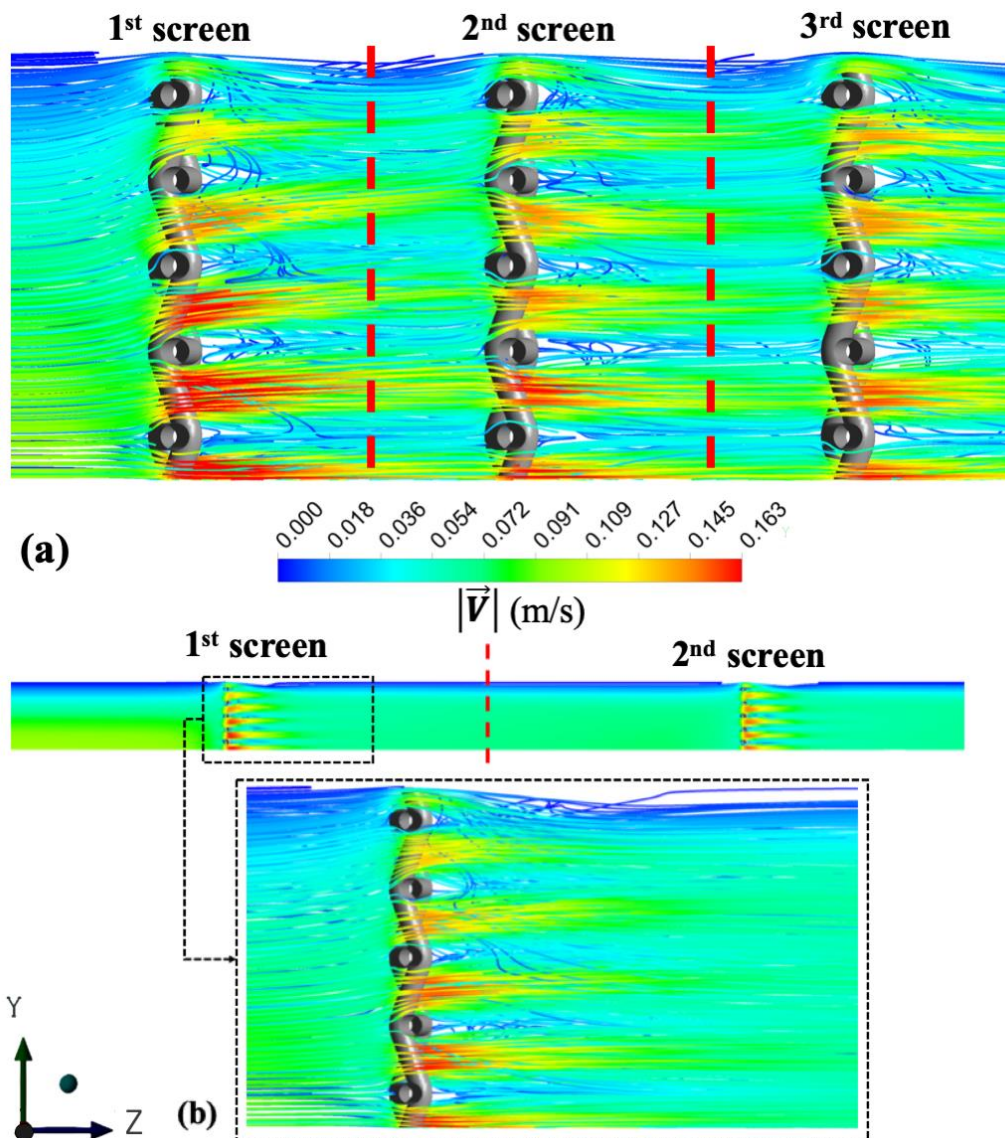


Figure 2.13. Velocity streamlines for $Mn = 20$ at $Re_b = 20$ for (a) the first three screens for $L = 5$ mm and (b) first two screens for $L = 50$ mm. Red dotted lines refer to the halfway between two consecutive screens.

2.3.2.3 Variation of the axial velocity

Two major theoretical approaches exist in the literature to describe the flow through woven meshes (Azizi, 2019; Kołodziej et al., 2009). One uses the analogy with flow around a cylinder while the other describes it like a flow through porous media. Consequently, the flow can be regarded as a flow through multiple orifices located on the same plane. Therefore, similarly to the well-known theory of a flow through an orifice, the velocity would reach its maximum value downstream of the opening where all jets change from a contraction to an expansion (McCabe et al., 2004). This point of maximum velocity is typically referred to as the “*vena contracta*” in the theory for a flow through an orifice. To better describe the change in the velocity as it goes through the screen, the centerline velocity along the central axis and along a line at $1M$ from the wall was observed as it passes through one screen element. Consequently, w^* is plotted against dimensionless axial location M^* in Figure 2.14 for the flow as it crosses the screen element at $Re_b = 20$ for screens $Mn = 20$ and 80. The dotted line thus represents the screen central line which is located at $M^* = 0$. It can be clearly discerned that the velocity magnitude goes through a minimum upstream of the screen then a maximum value downstream of it. These are shown by the blue and red circles on Figure 2.14, respectively. In contrast to the aforementioned point of maximum velocity, the minimum velocity point corresponds to the point where the kinetic energy is converted into static energy as the flow decelerates around the edges of the opening and builds the necessary pressure to accelerate the flow towards the *vena contracta* (Raymond Mulley, 2004) as shown in Figure 2.14(a-b). However, this minimum velocity was not observed for the case of $1M$ from the wall. The values of the maximum and minimum locations are displayed in Figure 2.14.

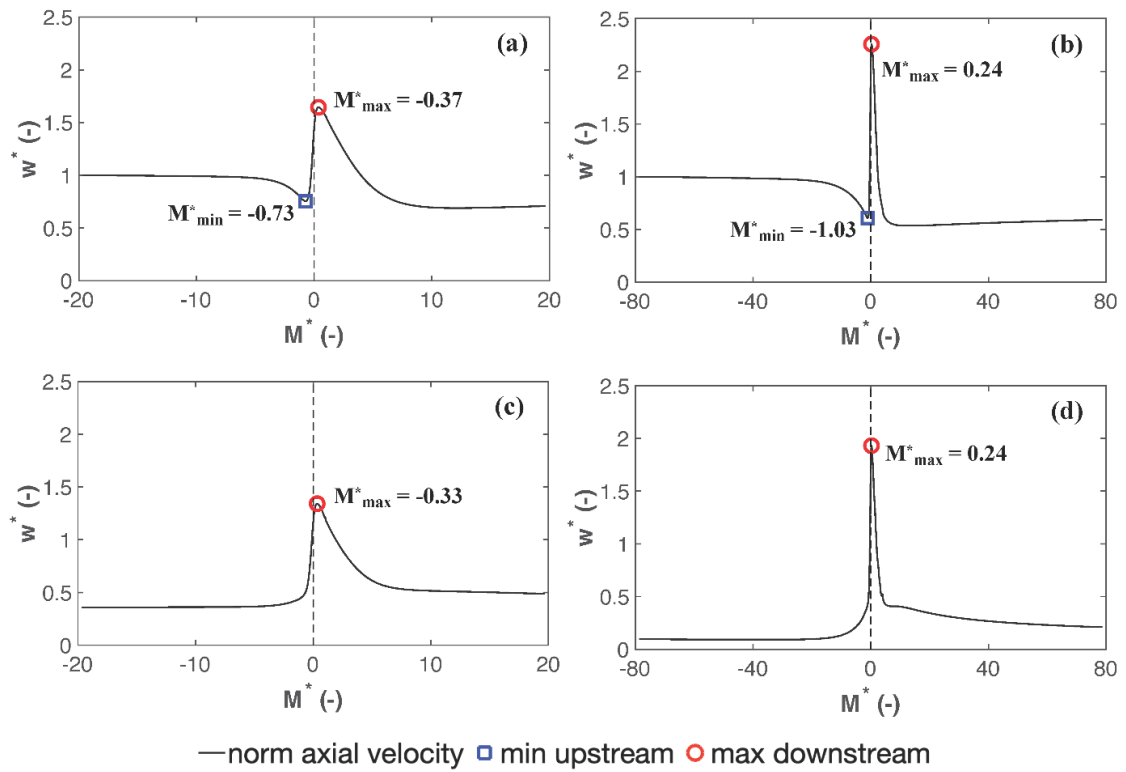


Figure 2.14. Position of upstream minimum and downstream maximum velocities for one screen in a pipe and $Re_b = 20$ along the central axis for (a) $Mn = 20$ and (b) $Mn = 80$, and along $1M$ from the wall for (c) $Mn = 20$ and (d) $Mn = 80$.

Figure 2.14 clearly shows that the location of the maximum and minimum values are highly dependent on the screen geometry, and radial position. It is also a direct function of the flow velocity. An attempt to correlate the position of the centerline minimum velocity upstream of the screen (L_{min}) and the centerline *vena contracta* (maximum velocity) downstream of the screen (L_{vc}) with the screen geometrical characteristics (e.g. M , b , and α) and the average flow velocity was undertaken using the simulation data for all 4 different geometries at $Re_b = 1, 10$, and 20 . The correlations are presented in Equations (2.11) and (2.12) respectively, where L_{min} denotes the distance from the center of the screen to the minimum velocity point, while L_{vc} denotes the distance from the center of the screen to the *vena contracta* point. It is to be noted that those correlations are held along the central axis where the highest

shifts both upstream and downstream were recorded (cf. Figure 2.14). All dimensions in the correlations are given in mm or mm/s and their results are shown on the parity plot in Figure 2.15 where the predictions of the correlations are plotted against the actual location as calculated using Ansys Fluent[®]. The correlations were found to predict reasonably well ($R^2 = 0.997$ for the minimum velocity and $R^2 = 0.931$ for the maximum velocity) the results. It should also be noted that the same $G(\alpha)$ function that is commonly used in correlating pressure drop was found to have the best impact when correlating the data as opposed to relying on the fractional open area alone.

$$L_{min} = -0.7954 \left(\frac{M}{mm} \right)^{0.8213} \left(\frac{U}{mm\ s^{-1}} \right)^{-0.0609} G(\alpha)^{0.1475} \quad (2.11)$$

$$L_{vc} = 0.0362 \left(\frac{M}{mm} \right)^{1.4189} \left(\frac{U}{mm\ s^{-1}} \right)^{0.6135} G(\alpha)^{-0.1521} \quad (2.12)$$

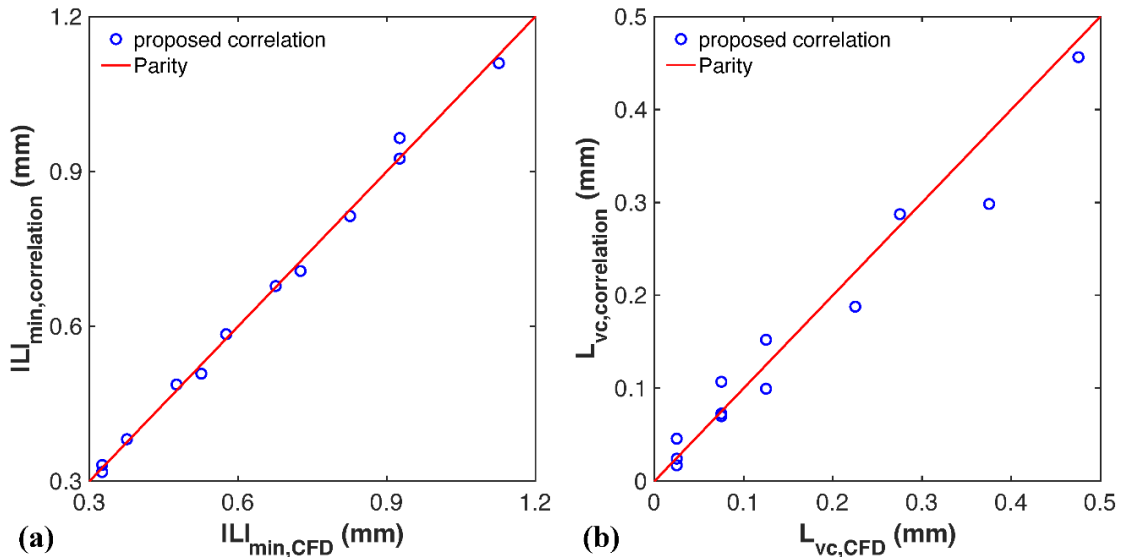


Figure 2.15. Parity plots showing the locations of the (a) minimum velocity and (b) maximum velocity for the flow through a screen.

2.3.2.4 Pressure field

2.3.2.4.1 Static pressure profile

Further to the velocity field analysis, the pressure along the flow was also examined. For this reason, the static pressure was reported along the central axis and another line positioned at $1M$ from the wall. This will help understand how the radial location affects the pressure field, especially that they are positioned in regions where the velocity recedes and increases, respectively.

Similar to the previous analysis, the static pressure was normalized for better generalization of the study. The normalized static pressure, P^* was calculated according to Equation (2.13) for every screen zone, where P^* would therefore vary between 0 and 1.

$$P^* = \frac{(P_j - P_j^{min})}{(P_j^{max} - P_j^{min})} \quad (2.13)$$

Where P_j is the axial static pressure for screen j in the pipe, P_j^{min} is the minimum static pressure within the zone of screen j , and P_j^{max} is the maximum pressure within the studied section. Each zone was defined as the distance stretching from the midpoint between screens $(j-1)$ and j to the midpoint with the subsequent downstream screen (i.e. screen $j+1$). Therefore, its length would be equivalent to the inter-screen spacing, L .

Figure 2.16 shows the axial variation of the static pressure along the aforementioned two lines, for an inter-screen distance of 50 mm. To better analyze these profiles, the reader is also referred to Figure 2.17, which shows the axial variation of both pressure and velocity on the same plot.

It is clear from Figure 2.16 that for the case of $Re_b = 1$, an increase in the normalized static pressure along the central axis can be observed starting at $M^* \approx -3$ (the

magnitude of which is proportional to Re_b , whereby the higher is the Re_b value the higher the relative increase in P^* would be); whereas, the normalized pressure along the axis at $1M$ from the wall shows a continuous decrease in the static pressure. As the fluid approaches the screen, the blockage of the flow path becomes significant, which was observed as a flattening of the velocity profile. As such, the centerline velocity decreases while an increase is observed in the area near the wall to conserve the flow rate (cf. Figure 2.11 and Figure 2.14). In terms of static pressure, the kinetic energy of the flow around the centerline is converted into static energy (similarly to a stagnation pressure), which explains the increase in the value of P^* upstream of the screen. However, the increase in the velocity near the wall, is translated into a continuous decrease of the static pressure.

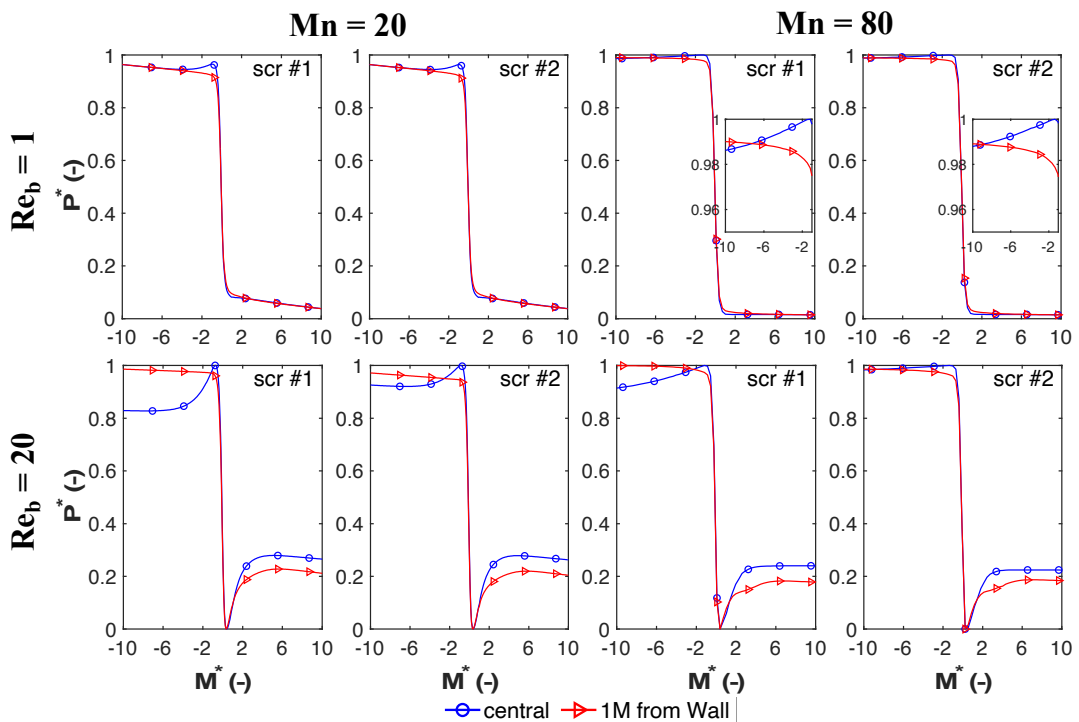


Figure 2.16. Normalized pressure at $L = 50$ mm for $Mn = 20$ and $Mn = 80$ at $Re_b = 1$ and $Re_b = 20$.

As the fluid passes through the screen, its static pressure undergoes a rapid and sharp decrease in its value until the downstream point of maximum velocity is reached, beyond which the static pressure decrease becomes slower. Such a rapid decrease in P^* is due to the increase in the velocity head at the expense of the static head. At higher velocities (e.g. $Re_b = 20$) a different behavior is observed whereby the minimum pressure is reached at the point of convergence of streamlines exiting the screen (cf. Figure 2.17). Beyond that point, part of the static head is recovered as reflected by an increase in the static pressure, followed by a gradual decline. Such a profile was described by Pinker and Herbert (Pinker and Herbert, 1967) who claimed that this “hump” downstream of the screen would take around 10 mesh sizes (i.e. $10M$) to disappear. This is in line with the current findings where this “hump” was also found to disappear within $10M$ from the screen. It should be noted, that the current profiles also match those of Morgan (P.G.Morgan, 1959) who reported similar axial variations to those obtained at low Re_b where this “hump” does not exist.

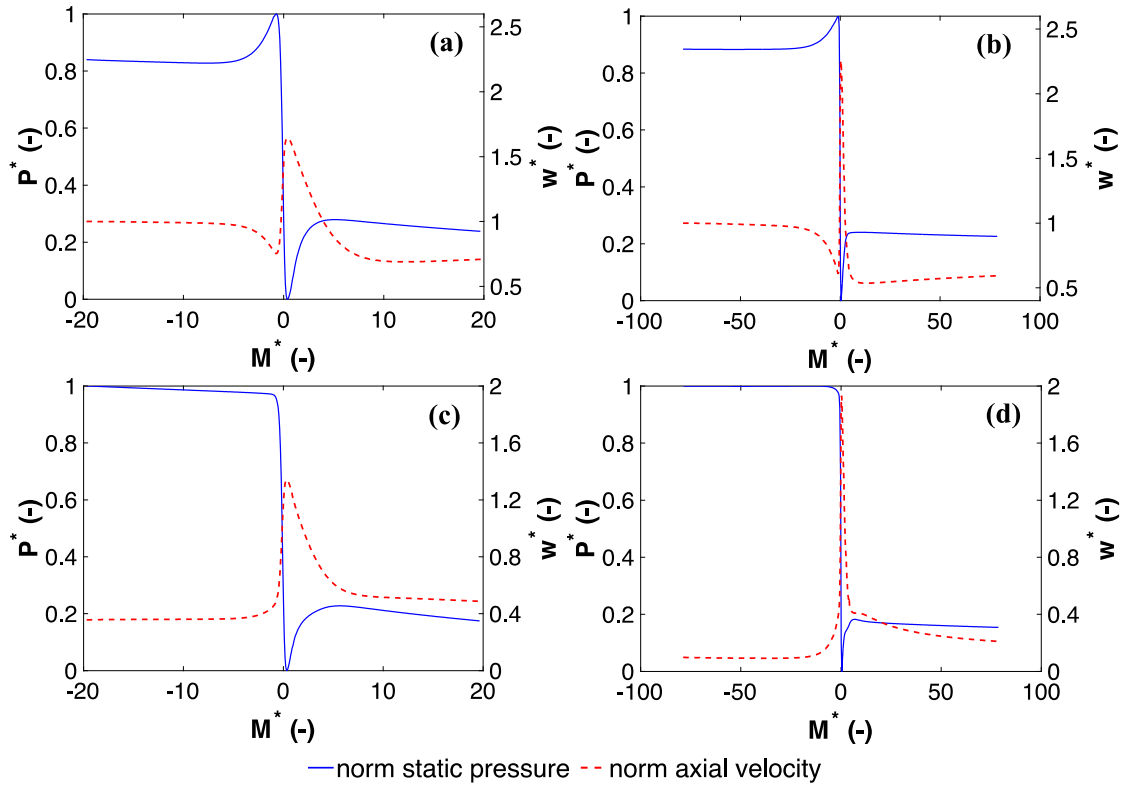


Figure 2.17. Variation of the normalized pressure and normalized axial velocity around the screen for $Re_b = 20$ and $L = 50$ mm. (a) $Mn = 20$, centerline; (b) $Mn = 80$, centerline; (c) $Mn = 20$, at $1M$ from the wall; (d) $Mn = 80$, at $1M$ from the wall.

The effect of inter-screen spacing was also investigated and is presented in Figure 2.18 and Figure 2.19 where static pressure profiles for a short inter-screen spacing, $L = 5$ mm, are presented. At low Re_b (cf. Figure 2.18) the profile follows a similar trend to that previously described for a longer inter-screen spacing. However, at higher velocities (i.e. $Re_b = 20$) it is interesting to note that the short inter-screen spacing for the case of $Mn = 20$ does not allow the pressure recovery to be completed, hence, a continuously ascending profile is observed exiting the first section and entering the second screen zone. This goes in hand with the description of the velocity profile where a fluctuating profile approaches the second screen downstream of the first.

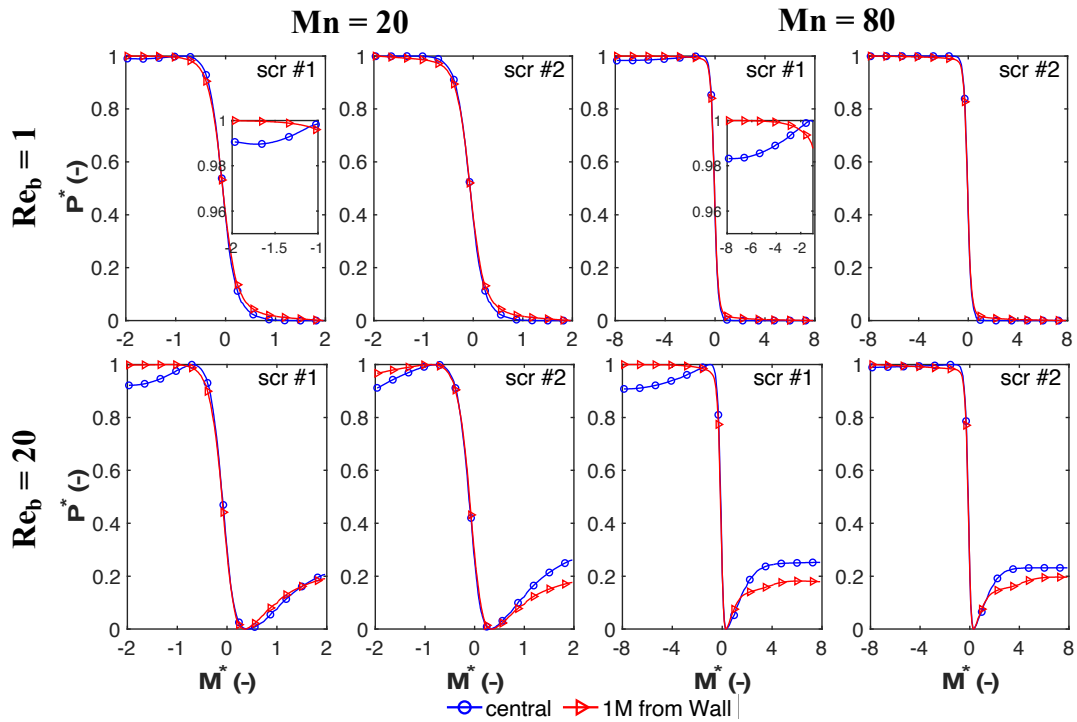


Figure 2.18. Normalized pressure at $L = 5$ mm for $Mn = 20$ and $Mn = 80$ at $Re_b = 1$ and $Re_b = 20$.

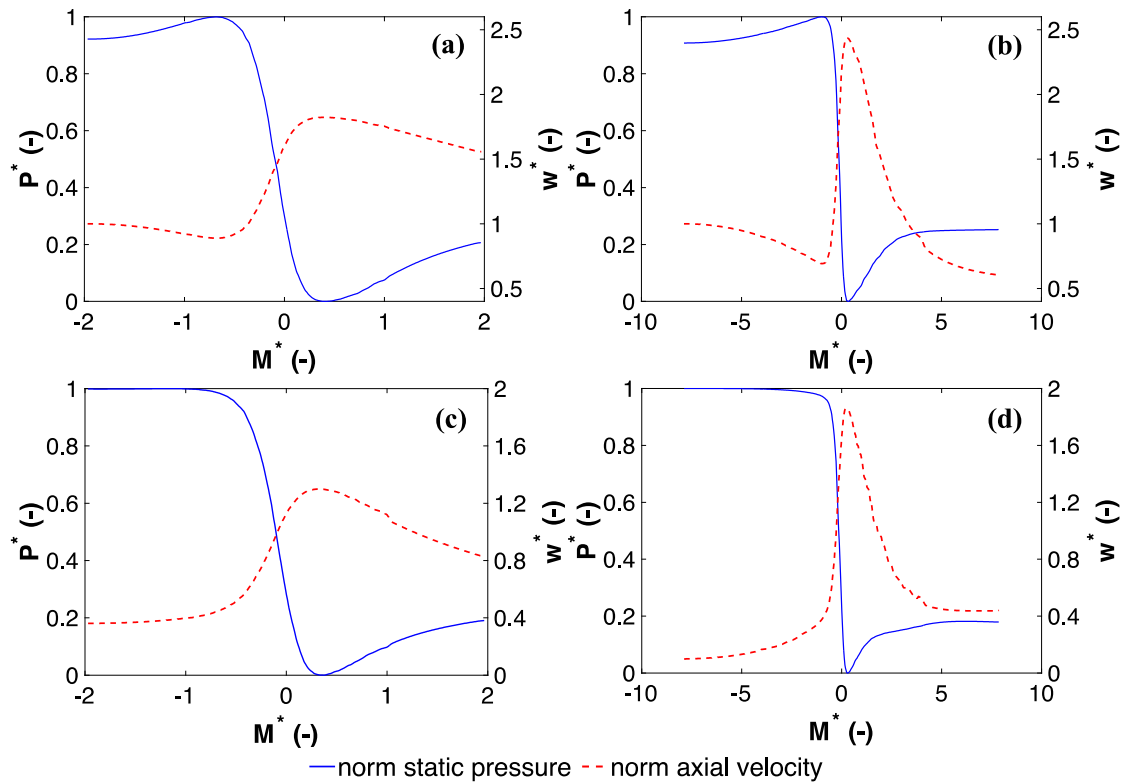


Figure 2.19. Variation of the normalized pressure and normalized axial velocity around the screen for $Re_b = 20$ and $L = 5$ mm. (a) $Mn = 20$, centerline; (b) $Mn = 80$, centerline; (c) $Mn = 20$, at $1M$ from the wall; (d) $Mn = 80$, at $1M$ from the wall.

2.3.2.4.2 Pressure recovery length

In order to quantify the location where the pressure would be completely recovered, the position of the maximum static pressure along the central axis downstream of one screen was recorded. It should be noted that the pressure recovery for the cases of $Re_b = 10$ and 20 were only studied since at $Re_b = 1$, no pressure zone was required.

Following the same procedure reported for *vena contracta*, a correlation using the simulation data for all 4 different geometries for $Re_b = 10$, and 20 was used to predict the position of the pressure recovery downstream of the screen. The correlation is presented in Equation (2.14), where L_{pr} denotes the distance from the center of the screen to the location of pressure recovery. All dimensions in this correlation are given in mm or mm/s and its results are shown on the parity plot in Figure 2.20 where the predictions of this correlation are plotted against the actual location as calculated using Ansys Fluent[®]. It can be clearly seen that the correlation predicted reasonably ($R^2 = 0.966$) well the simulation results.

$$L_{pr} = 1.1894 \left(\frac{M}{mm} \right)^{0.4582} \left(\frac{U}{mm \ s^{-1}} \right)^{0.5863} G(\alpha)^{-0.5970} \quad (2.14)$$

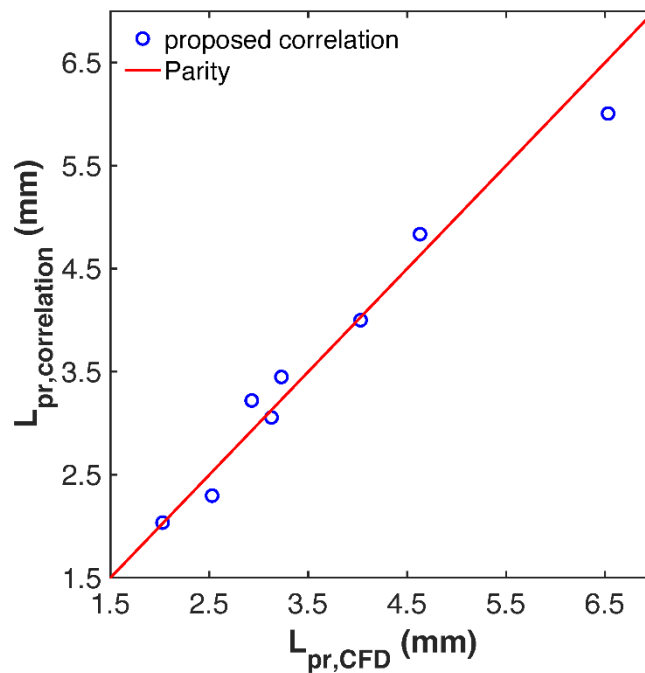


Figure 2.20. Parity plot showing the location of the maximum velocity the flow through a screen

2.4 Conclusions

The hydrodynamic performance of plain-woven wire meshes that are used as static mixers in chemical engineering applications was assessed numerically under laminar flow conditions using the commercial CFD solver ANSYS Fluent[®]. A full pipe 3D model was used to investigate the velocity and pressure fields of the flow. The effect of screen geometry, number of screens, inter-screen spacing, and operating conditions were investigated. Pressure drop data was further validated against data from literature.

The analysis of velocity components in upstream and downstream regions of the screen show that axial flow is dominant only in regions near the centerline, whereas in regions closer to the wall the flow become three dimensional. In these areas radial and tangential velocity components become significant. Moreover, it was found that the

flow is rotational in the vicinity of the screen. The formation of vortices and recirculation in regions near the screen was also observed, the extent of which being a function of the wire diameter, screen solidity, and flow velocity.

The velocity profiles along the centerline and in the near-wall region were also analyzed for a fully-developed laminar flow approaching the screen. These profiles revealed that the presence of screens has a major impact on their shape. The velocity profile was flattened in the upstream region and assumed a zigzag/sinusoidal shape up to a significant distance downstream of the screen. These profiles also showed various similarities with the flow through a bundle of orifices. Furthermore, pressure profiles showed the existence of a pressure recovery region downstream of the screen at relatively high Re_b while this was inexistent at low Re_b . This behavior was in line with various studies in the literature.

2.5 Nomenclature

b	Wire diameter	mm
D	Pipe diameter	mm
k	Turbulent kinetic Energy	$m^2 \cdot s^{-2}$
L	Inter-screen spacing	mm
L_{min}	Position of the centerline minimum velocity upstream of the screen	mm
L_{vc}	Position of the centerline <i>vena-contracta</i> downstream of the screen	mm
M	Mesh size	mm
M^*	Dimensionless mesh size	-
Mn	Mesh number	-

N_s	Number of screen elements in the pipe	screen
P	Static pressure	Pa
P^*	Normalized static pressure	-
P_j	Axial static pressure for screen j in the pipe	Pa
P_j^{max}	Maximum static pressure within the zone of screen j	Pa
P_j^{min}	Minimum static pressure within the zone of screen j	Pa
P_{in}	Average gauge static pressure at inlet	Pa
P_{out}	Average gauge static pressure at outlet	Pa
U	Superficial (approaching velocity)	$m \cdot s^{-1}$
u	Velocity component in x -direction	$m \cdot s^{-1}$
u^*	Normalized velocity component in x -direction	-
v	Velocity component in y -direction	$m \cdot s^{-1}$
v^*	Normalized velocity component in y -direction	-
V	Velocity vector	$m \cdot s^{-1}$
w	Axial velocity (velocity component in z -direction)	$m \cdot s^{-1}$
$w_{(X=0,Y=0,Z=0)}$	Inlet maximum (centerline) axial velocity	$m \cdot s^{-1}$
w^*	Normalized axial velocity	-
X	Distance away from the axis (Cartesian coordinates)	mm
Y	Distance away from the axis (Cartesian coordinates)	mm
Z	Axial distance (Cartesian coordinates)	mm
Z^*	Normalized axial distance	-
ΔP_o	Static pressure drop in an empty pipe	Pa
ΔP_{screen}	Static pressure drop across a screen	Pa

Greek symbols

α	Percent opening area	%
ϵ	Relative error	-
ℓ	Grid size	m
ρ	Density	$\text{kg} \cdot \text{m}^{-3}$
ω	Specific dissipation rate	s^{-1}
ψ	Vorticity tensor	s^{-1}

Dimensionless Group

Eu	Euler number	-
Re_b	Wire Reynolds number, $\rho Ub / \mu$	-
Re_{pipe}	Pipe Reynolds number, $\rho UD / \mu$	-
Re_s	Screen Reynolds number, $\rho Ub / (\mu \cdot \alpha)$	-

Abbreviations

CFD	Computational Fluid Dynamics
GCI	Grid Convergence Index
SST	Shear Stress Transport
STSM	Screen Type Static Mixer

2.6 Acknowledgements

The authors would like to acknowledge the financial support of the Lebanese National Council for Scientific Research (CNRS-L) and the University Research Board as well as the Arza HPC Unit at the American University of Beirut.

2.7 References

- A. Bennani, J.N. Gence, J. Mathieu, 1985. The Influence of a Grid-Generated Turbulence on the Development of Chemical Reactions. *AIChE J.* 31, 1157–1166.
- Abou Hweij, K., Azizi, F., 2015. Hydrodynamics and residence time distribution of liquid flow in tubular reactors equipped with screen-type static mixers. *Chem. Eng. J.* 279, 948–963. <https://doi.org/10.1016/j.cej.2015.05.100>
- Al Taweel, A.M., Azizi, F., Siriijeerachai, G., 2013. Static mixers: Effective means for intensifying mass transfer limited reactions. *Chem. Eng. Process. Process Intensif.* 72, 51–62. <https://doi.org/10.1016/j.cep.2013.08.009>
- Al Taweel, A.M., Li, C., Gomaa, H.G., Yuet, P., 2007. Intensifying mass transfer between immiscible liquids: Using screen-type static mixers. *Chem. Eng. Res. Des.* 85, 760–765. <https://doi.org/10.1205/cherd06180>
- Al Taweel, A.M., Yan, J., Azizi, F., Odedra, D., Gomaa, H.G., 2005. Using in-line static mixers to intensify gas-liquid mass transfer processes. *Chem. Eng. Sci.* 60, 6378–6390. <https://doi.org/10.1016/j.ces.2005.03.011>
- Armour, J.C., Cannon, J.N., 1968. Fluid Flow Through Woven Screens. *AIChE J.* 14, 415–420.
- Azizi, F., 2019. On the pressure drop of fluids through woven screen meshes. *Chem. Eng. Sci.* 207, 464–478. <https://doi.org/10.1016/j.ces.2019.06.046>
- Azizi, F., Abou Hweij, K., 2017. Liquid-Phase Axial Dispersion of Turbulent Gas–Liquid Co-Current Flow Through Screen-Type Static Mixers. *AIChE J.* 63, 1390–1403. <https://doi.org/10.1002/aic>
- Azizi, F., Al Taweel, A.M., 2015. Mass Transfer in an Energy-Efficient High-Intensity Gas-Liquid Contactor. *Ind. Eng. Chem. Res.* 54, 11635–11652. <https://doi.org/10.1021/acs.iecr.5b01078>
- Azizi, F., Al Taweel, A.M., 2011a. Hydrodynamics of Liquid Flow Through Screens and Screen-Type Static Mixers. *Chem. Eng. Commun.* 198, 726–742. <https://doi.org/10.1080/00986445.2011.532748>
- Azizi, F., Al Taweel, A.M., 2011b. Turbulently flowing liquid-liquid dispersions. Part I: Drop breakage and coalescence. *Chem. Eng. J.* 166, 715–725. <https://doi.org/10.1016/j.cej.2010.11.050>
- Azizi, F., Al Taweel, A.M., 2007. Population balance simulation of gas-liquid contacting. *Chem. Eng. Sci.* 62, 7436–7445. <https://doi.org/10.1016/j.ces.2007.08.083>
- Bailey, B.J., Montero, J.J., Perez Parra, J., Robertson, A.P., Baeza, E., Kamaruddin, R., 2003. Airflow Resistance of Greenhouse Ventilators with and without Insect Screens. *Biosyst. Eng.* 86, 217–229. [https://doi.org/10.1016/S1537-5110\(03\)00115-6](https://doi.org/10.1016/S1537-5110(03)00115-6)
- Bourne, J.R., Lips, M., 1991. Micromixing in grid-generated turbulence: theoretical analysis and experimental study. *Chem. Eng. J.* 47, 155–162.

- Celik, I.B., Ghia, U., Roache, P.J., Freitas, C.J., Coleman, H., Raad, P.E., 2008. Procedure for estimation and reporting of uncertainty due to discretization in CFD applications. *J. Fluids Eng. Trans. ASME* 130, 0780011–0780014. <https://doi.org/10.1115/1.2960953>
- Costa, S.C., Barrutia, H., Esnaola, J.A., Tutar, M., 2013. Numerical study of the pressure drop phenomena in wound woven wire matrix of a Stirling regenerator. *Energy Convers. Manag.* 67, 57–65. <https://doi.org/10.1016/j.enconman.2012.10.014>
- Ehrhardt, G., 1983. Flow Measurements for Wire Gauzes. *Int. Chem. Eng.*
- G.B.Schubauer, W.G.Spangenberg, P.S.Klebanoff, 1948. Aerodynamic Characteristics of Damping Screens. *Seventh Int. Congr. Appl. Mech. London*, Sept. 5-11.
- Ghanem, A., Lemenand, T., Della, D., Peerhossaini, H., 2013. Chemical Engineering Research and Design Static mixers : Mechanisms , applications , and characterization methods – A review. *Chem. Eng. Res. Des.* 92, 205–228. <https://doi.org/10.1016/j.cherd.2013.07.013>
- Green, S.I., Wang, Z., Waung, T., Vakil, A., 2008. Simulation of the flow through woven fabrics. *Comput. Fluids* 37, 1148–1156. <https://doi.org/10.1016/j.compfluid.2007.10.013>
- Habchi, C., Azizi, F., 2018. Heat transfer and turbulent mixing characterization in screen-type static mixers. *Int. J. Therm. Sci.* 134, 208–215. <https://doi.org/10.1016/j.ijthermalsci.2018.08.016>
- Hobbs, D.M., Swanson, P.D., Muzzio, F.J., 1998. Numerical characterization of low Reynolds number flow in the Kenics static mixer. *Chem. Eng. Sci.* 53, 1565–1584. [https://doi.org/10.1016/S0009-2509\(97\)00132-2](https://doi.org/10.1016/S0009-2509(97)00132-2)
- J.R.Sodre, J.A.R.Parise, 1997. Friction Factor Determination for Flow Through Finite Wire-Ivlesh Woven-Screen Matrices. *J. Fluids Eng.* 119, 847–851.
- Kandhai, D., Vidal, D.J.E., Hoekstra, A.G., Hoefsloot, H., Iedema, P., Slood, P.M.A., 1999. Lattice-Boltzmann and finite element simulations of fluid flow in a SMRX static mixer reactor. *Int. J. Numer. Methods Fluids* 31, 1019–1033. [https://doi.org/10.1002/\(SICI\)1097-0363\(19991130\)31:6<1019::AID-FLD915>3.0.CO;2-I](https://doi.org/10.1002/(SICI)1097-0363(19991130)31:6<1019::AID-FLD915>3.0.CO;2-I)
- Kołodziej, A., Jaroszyński, M., Janus, B., Kleszcz, T., Łojewska, J., Łojewski, T., 2009. An experimental study of the pressure drop in fluid flows through wire gauzes. *Chem. Eng. Commun.* 196, 932–949. <https://doi.org/10.1080/00986440902743851>
- Kumar, V., Shirke, V., Nigam, K.D.P., 2008. Performance of Kenics static mixer over a wide range of Reynolds number. *Chem. Eng. J.* 139, 284–295. <https://doi.org/10.1016/j.cej.2007.07.101>
- Laws, E.M., Livesey, J.L., 1978. Flow Through Screens. *Annu Rev Fluid Mech* 10, 247–266. <https://doi.org/10.1146/annurev.fl.10.010178.001335>
- Madhuranthakam, C.M.R., Pan, Q., Rempel, G.L., 2009. Residence time distribution and liquid holdup in Kenics® KMX static mixer with hydrogenated nitrile butadiene rubber solution and hydrogen gas system. *Chem. Eng. Sci.* 64, 3320–3328. <https://doi.org/10.1016/j.ces.2009.04.001>

- McCabe, W.L., Smith, J.C., Harriot, P., 2004. Unit Operations of Chemical Engineering 7th edition, McGraw-Hill, New York.
- Meng, H., Song, M., Yu, Y., Wang, F., Wu, J., 2015. Chaotic mixing characteristics in static mixers with different axial twisted-tape inserts. *Can. J. Chem. Eng.* 93, 1849–1859. <https://doi.org/10.1002/cjce.22268>
- Meng, H., Wang, F., Yu, Y., Song, M., Wu, J., 2014. A numerical study of mixing performance of high-viscosity fluid in novel static mixers with multitwisted leaves. *Ind. Eng. Chem. Res.* 53, 4084–4095. <https://doi.org/10.1021/ie402970v>
- Meng, H.B., Song, M.Y., Yu, Y.F., Jiang, X.H., Wang, Z.Y., Wu, J.H., 2017. Enhancement of Laminar Flow and Mixing Performance in a Lightning Static Mixer. *Int. J. Chem. React. Eng.* 15, 1–21. <https://doi.org/10.1515/ijcre-2016-0112>
- Middelstädt, F., Gerstmann, J., 2013. Numerical Investigations on Fluid Flow through Metal Screens. 5th Eur. Conf. Aeronaut. Sp. Sci.
- Okolo, P.N., Zhao, K., Kennedy, J., Bennett, G.J., 2019. Numerical assessment of flow control capabilities of three dimensional woven wire mesh screens. *Eur. J. Mech. B/Fluids* 76, 259–271. <https://doi.org/10.1016/j.euromechflu.2019.03.001>
- P.G.Morgan, 1959. High Speed Flow Through Wire Gauzes. *J. R. Aeronaut. Soc.* 63, 474–475. https://doi.org/10.1300/J184v06n04_07
- Peschel, A., Hentschel, B., Freund, H., Sundmacher, K., 2012. Design of optimal multiphase reactors exemplified on the hydroformylation of long chain alkenes. *Chem. Eng. J.* 188, 126–141. <https://doi.org/10.1016/j.cej.2012.01.123>
- Pinker, R.A., Herbert, M.V., 1967. Pressure loss associated with compressible flow through square-mesh wire gauzes. *J. Mech. Eng. Sci.* 9, 11–23.
- Rauline, D., TANGUY, P.A., Blevec, J.-M. Le, Bousquet, J., 1998. Numerical investigation of the performance of several static mixers. *Can. J. Chem. Eng.* <https://doi.org/10.1002/cjce.5450760325>
- Raymond Mulley, 2004. *Flow of Industrial Fluids-Theory and Equations*, CRC Press.
- Regner, M., Östergren, K., Trägårdh, C., 2006. Effects of geometry and flow rate on secondary flow and the mixing process in static mixers-a numerical study. *Chem. Eng. Sci.* 61, 6133–6141. <https://doi.org/10.1016/j.ces.2006.05.044>
- Soman, S.S., Madhuranthakam, C.M.R., 2017. Effects of internal geometry modifications on the dispersive and distributive mixing in static mixers. *Chem. Eng. Process. Process Intensif.* 122, 31–43. <https://doi.org/10.1016/j.cep.2017.10.001>
- Thakur, R.K., Vial, C., Nigam, K.D.P., Nauman, E.B., Djelveh, G., 2003. Static mixers in the process industries – a review. *Chem. Eng. Res. Des.* 81, 787–826. <https://doi.org/10.1205/026387603322302968>
- Wakeland, R.S., Keolian, R.M., 2003. Measurements of Resistance of Individual Square-Mesh Screens to Oscillating Flow at Low and Intermediate Reynolds Numbers. *J. Fluids Eng. Trans. ASME* 125, 851–862. <https://doi.org/10.1115/1.1601254>

Wu, W.T., Liu, J.F., Li, W.J., Hsieh, W.H., 2005. Measurement and correlation of hydraulic resistance of flow through woven metal screens. *Int. J. Heat Mass Transf.* 48, 3008–3017. <https://doi.org/10.1016/j.ijheatmasstransfer.2005.01.038>

CHAPTER 3

CFD SIMULATION OF WALL-BOUNDED LAMINAR FLOW THROUGH SCREENS. PART II: MIXING CHARACTERIZATION

W. Abou-Hweij and F. Azizi¹

B.&W. Bassatne Dept. of Chemical Engineering and Advanced Energy, M. Semaan Faculty of Engineering and Architecture, American University of Beirut, 1107 2020 Beirut, Lebanon

Published in Proceedings of the ASME 2020 Fluids Engineering Division Summer Meeting, FEDSM2020, July, 12-16, 2020, Orlando, Florida, USA

<https://doi.org/10.1115/FEDSM2020-20120>

Abstract

This paper characterizes the mixing behavior of laminar flows within a circular pipe equipped with plain woven meshes or screens, acting as static mixers. In this quest, their performance was numerically investigated using the Lagrangian particle method in a commercial CFD solver, whereby the effect of changing the screen geometry, number of screens, inter-screen spacing, and operating conditions were considered.

Mixing was addressed from a distributive and dispersive perspectives using both qualitative and quantitative descriptions. The distributive mixing indicated that a central injection of a single fluid should be coupled with a short inter-screen spacing to better spread the particles and enhance mixing as opposed to a larger inter-screen spacing. On the contrary, the mixing of two immiscible fluids of similar properties reveal that a large inter-screen spacing is recommended. From a dispersive mixing perspective, extensional efficiency contours revealed that the fluid would undergo all three modes of flow behavior, each of which dominating a certain region depending on the location with respect to the screen. Finally, it was interesting to find that a coarser

screen geometry consistently outperformed finer screens in spreading and mixing the particles.

Keywords: Laminar flow, screens, woven mesh, static mixers, mixing, PNN method, extensional efficiency.

3.1 Introduction

Inline static mixers are widely used in process operations that involve mixing of viscous fluids under laminar flow regime. Their low operating cost, small reactor volumes, and enhanced safety add to their superiority over conventional mixers (Al Taweel et al., 2013; Ghanem et al., 2013; Thakur et al., 2003). In addition, their simple geometry and recent advances in CFD facilitate the proper characterization of their mixing performance (Meng et al., 2017, 2015).

The mixing performance of commercially available static mixers (e.g. KSM and SMX) and other alternative novel designs under laminar regime has been the subject of numerous numerical studies in the open literature (Meng et al., 2017, 2015; Soman and Madhuranthakam, 2017). In such studies, the Lagrangian particle method based on particle tracking technique was used. The mixing behavior was then characterized either qualitatively or quantitatively through different approaches. The qualitative characterization is typically performed using Poincare plots (Hobbs and Muzzio, 1998), tracer injection which can be either central (Hobbs and Muzzio, 1998; Meng et al., 2017) or off-central (Hobbs and Muzzio, 1997a), tracer distribution of two mixing fluids either through concentric injection (Meng et al., 2015) or semicircle injection (Meng et al., 2015; Soman and Madhuranthakam, 2017), or by studying extensional efficiency contour plots (Meng et al., 2017). These methods provide visualization of distributive and dispersive mixing within the mixers. However, the quantitative

methods allow the calculation of the degree of mixing which could be predicted using particle distribution uniformity (PDU) (Meng et al., 2017; Rahmani et al., 2005) coefficient of variation (CoV) (Hobbs and Muzzio, 1998; Meng et al., 2015), point to nearest neighbor (PNN) (Kukukova et al., 2011), mixing efficiency (Medina et al., 2019), and RTD (Meng et al., 2015).

A novel mixer made of plain square woven meshes/screens was recently used to process flow under turbulent regime (Azizi and Al Taweel, 2011b). It proved very efficient at promoting multiphase dispersions and mass transfer operations at low energy consumption rates (Azizi and Al Taweel, 2015). Its superior performance served as a stimulus to investigate its mixing performance under laminar flow conditions.

The objective of this study is to numerically investigate the mixing efficiency of screen-type static mixer (STSM) using a particle tracking technique. This will be performed using the commercial CFD solver ANSYS Fluent[®]. For this purpose, four different parameters, namely, screen geometry, number of screens, inter-screen spacing, and flow velocity will be investigated to assess their effect on mixing using STSM. This work is considered first of its kind in characterizing micro-mixing numerically within STSM for a liquid flowing under laminar flow regime.

3.2 Materials and Methods

3.2.1 Computational Domain

The three-dimensional computational domain consists of a circular pipe of inner diameter, $D = 12.7$ mm, in which a number of screens, N_s , is placed normal to the flow. These elements are placed equidistant from each other at a varying inter-screen spacing, L . The full three-dimensional model of the STSM was simplified by taking advantage

of its axisymmetric configuration such that only one quadrant was modeled as shown in Figure 3.1a.

In this study, two different screen geometries were used, the characteristics of which are listed in Table 3.1. Moreover, these screens are commonly referred to by their mesh number, M_n , which reflects the number of openings per inch.

Simulations were then performed using liquid-water with constant physical properties $\rho = 998.2 \text{ kg/m}^3$ (0.036 lb/in³) and $\mu = 0.001003 \text{ Pa}\cdot\text{s}$ ($1.454 \times 10^{-7} \text{ lb}\cdot\text{s}/\text{in}^2$), as a working fluid. The operating conditions were based on Reynolds number whose characteristic length was the wire diameter (Re_b). This Reynolds number ensures the attainment of similar hydrodynamic effects in the various screens to highlight the effect of wire diameter and mesh opening on the downstream flow behavior. In this quest, two operating conditions, namely, $Re_b = 1$ and 20 were selected for this study. It is worth noticing that these two operating conditions were selected such that their corresponding pipe Reynolds number (characteristic length based on pipe diameter) $Re_{\text{pipe}} < 2300$ to ensure laminar flow conditions.

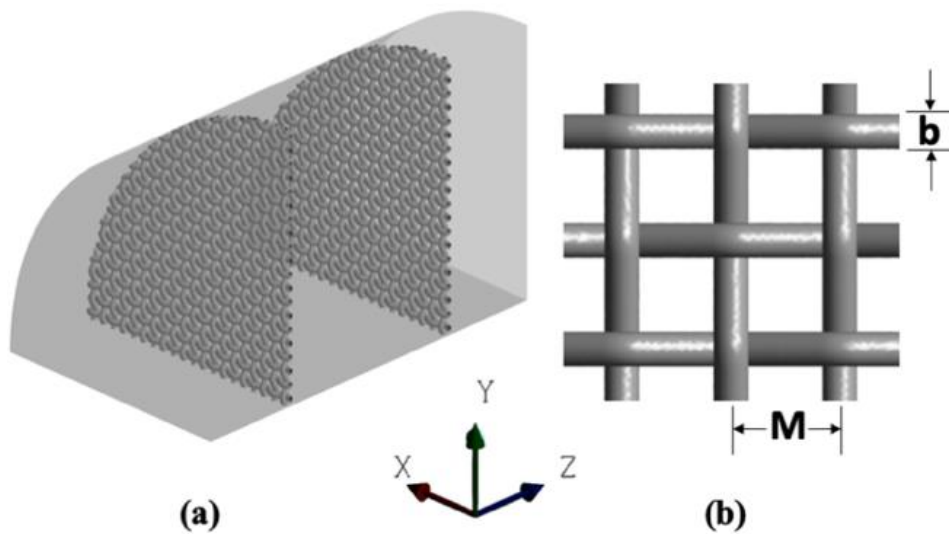


Figure 3.1. Schematic representation of STSM (a) quarter section and (b) section of screen – top view

Table 3.1. Geometrical characteristics of plain-woven square meshes.

Mn (–)	M (mm)	b (mm)	$(M-b)$ (mm)	α (%)
20	1.27	0.4064	0.8636	46.2
80	0.3175	0.1397	0.1778	31.4

Furthermore, simulations were always performed using equidistant and similar screens in the mixer. Following this, two different inter-screen spacing ($L = 5$ mm and $L = 50$ mm) were employed while varying the number of screens between 1 and 8.

The 3D geometry was constructed using AutoCAD[®]. The geometric discretization (cf. Figure 3.2) was then performed using the automatic meshing tool available in the commercial software ANSYS[®]. To overcome the high computational cost resulting from a constant fine mesh throughout the computational domain, the flow field was divided into 3 meshing regions, namely, screen region (unstructured grid), near screen region (unstructured grid), and the open pipe region (structured grid). Accordingly, the screen region was the finest followed by the near screen region and the open pipe region was the coarsest as shown in Figure 3.2.

The CFD simulations of the STSM were then conducted using ANSYS Fluent[®] v.18.2. Proper boundary conditions were selected, where a user defined function (UDF) imposes the well-known parabolic profile at the inlet. The walls of the pipe and the screens were set to no-slip boundary conditions, while the outlet was set to an outflow boundary condition. Dealing with one quadrant of the cross-section, the rotational periodic boundary condition was used to represent the flow within a complete pipe. Using the SIMPLE algorithm and high order discretizing schemes, the flow field variables including the velocity and pressure fields were obtained.

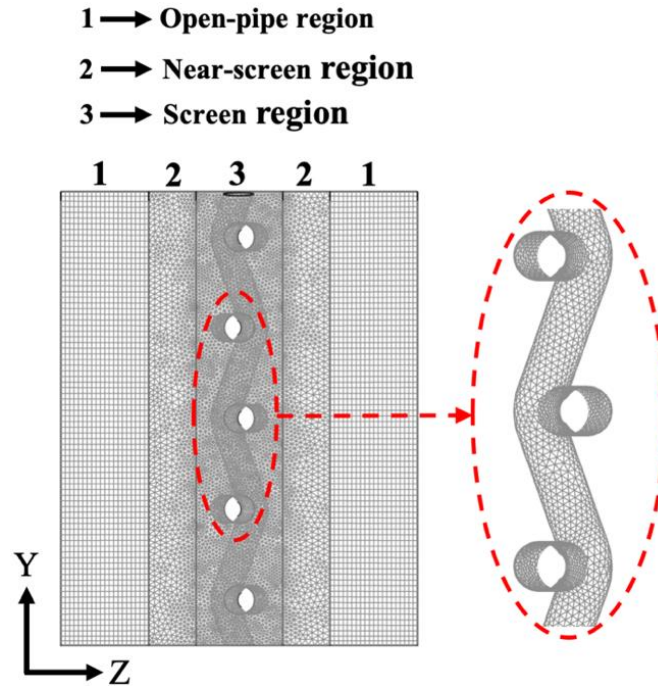


Figure 3.2. Geometric discretization

A grid independence test was then performed following the grid convergence index (GCI) method proposed by Celik et al. (Celik et al., 2008). Different parameters including the pressure drop and the local velocities at various cross-sections were used to assess grid sensitivity. Accordingly, three grid levels (coarse, fine, and finest) were used such that the grid refinement level was at least 1.3. Hence, a grid of 3,108,075 million elements was selected for $Mn = 20$ with a GCI value of 0.7% and a relative error of 1.3%, while a grid of 6,987,661 million elements was selected for $Mn = 80$ with a GCI value of 0.18% and a relative error of 0.34%.

3.2.2 Model Validation

The numerical predictions of the CFD model were validated by comparing pressure drop simulation results to experimental data. The overall pressure drop in the mixer is the result of skin friction at the pipe wall in addition to losses resulting from the flow through the screen. Hence, the pressure drop across a screen element can be

calculated using Equation (3.1). Accordingly, the predictions of ΔP_{screen} across a single element were compared against the empirical correlation (see Equation (3.2)) reported by Azizi (Azizi, 2019). This correlation covered a wide range of flow conditions ($2 \leq Re_b \leq 14,000$).

$$\Delta P_{screen} = \frac{(P_{in} - P_{out}) - \Delta P_o}{N_s} \quad (3.1)$$

$$\Delta P_{screen} = \frac{\rho U^2}{2} \times \frac{(1 - \alpha^2)}{\alpha^2} \times [0.4537 + (10.76 \times Re_b^{-0.8213})] \quad (3.2)$$

where P_{in} and P_{out} are the area weighted average of the static pressure at the inlet and outlet of the STSM, and ΔP_o is the pressure drop in an empty pipe having the same length as the mixer.

Figure 3.3 shows how the numerical and empirical values compare against each other. It is worth noting that the points corresponding to $Re_b = 30$ and 40 for $Mn = 80$ were excluded from the current validation as they fall outside the laminar regime ($Re_{pipe} > 2,300$). It can be clearly observed that the results obtained from the CFD simulations are in close agreement with the correlation predictions with a maximum relative error of 6.2% for $Re_b \geq 10$. Larger relative errors were calculated at $Re_b = 1$, where they reached a maximum of 22.1%. This however is still acceptable for two reasons. First, the correlation of Azizi (Azizi, 2019) was developed for the range of $Re_b \geq 2$, and second, while Azizi correlated the data of about one thousand experimental measurements, his correlation was reported to fall within $\pm 30\%$ of these points.

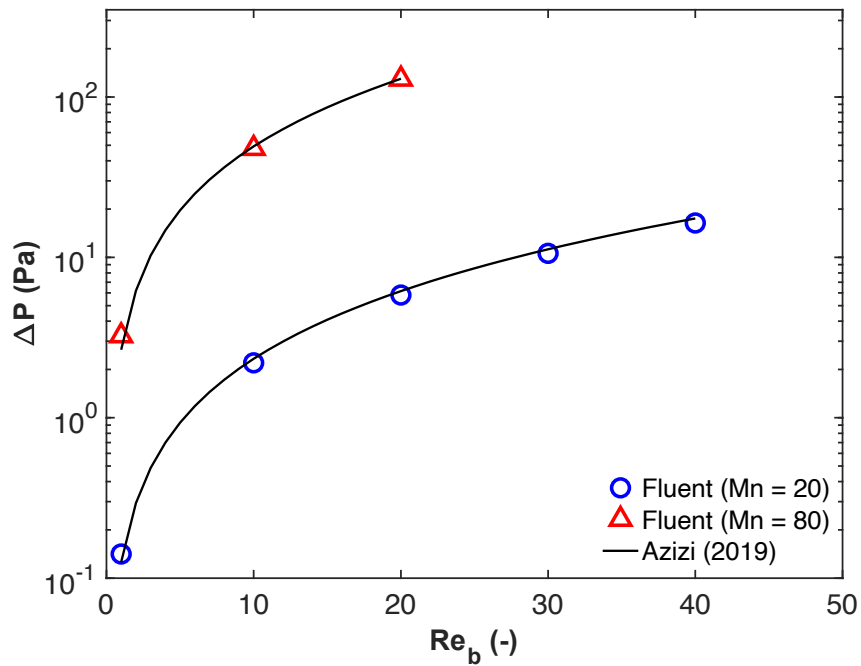


Figure 3.3. Model validation based on pressure drop for different screen geometries with one screen in a pipe.

3.2.3 *Mixing characterization*

Mixing is typically divided into distributive and dispersive types. The former illustrates the spatial distribution of fluid elements within a cross-section, and the latter reveals the breakup of fluid elements within the mixer.

3.2.3.1 Distributive mixing

Distributive mixing was predicted using the Lagrangian method where a set of massless particles were injected at the inlet of the computational domain. The trajectories of these particles were then predicted through integrating the vector equation of motion, Equation (3.3), using the converged velocity field. This approach was employed by several investigators who characterized mixing within a KSM mixer (Hobbs and Muzzio, 1998; Meng et al., 2017, 2015).

$$\frac{D\mathbf{X}_p}{dt} = \mathbf{V}_p \quad (3.3)$$

where \mathbf{V}_p is the particle's velocity vector and \mathbf{X}_p is the particle's position vector.

In this study, the discrete phase model (DPM) available in Fluent[®] was selected for the prediction of the particles' position within the mixer. These positions provide both a qualitative assessment of mixing through the visualization of the spread of particles within a specified cross-section, and a quantitative measure through the calculation of the degree of mixing within these cross-sections.

3.2.3.1.1 Qualitative assessment

Three different approaches were selected for the visualization of spatial distribution of the massless particles.

The first approach relies on the central injection of large number of massless particles [$O(10^4)$] at the inlet cross section. These particles have the same properties as the working fluid, where they are uniformly clustered within a circular area representing 1% of the inlet area as shown in Figure 3.4a.

In the second approach, concentric injection of a large number of uniformly-spaced massless particles [$O(10^4)$] of different colors were injected at the inlet as shown in Figure 3.4b such that $r/R = 0.5$, with each color having the same properties as the working fluid.

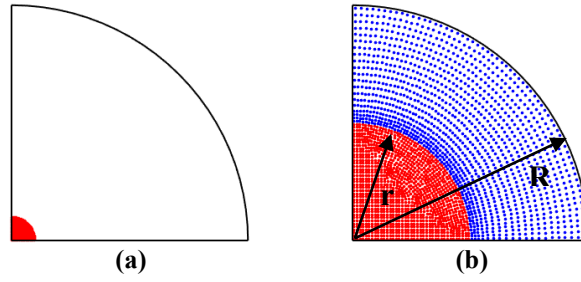


Figure 3.4. Injection criteria (a) central injection of 1% inlet cross-section, (b) concentric injection with $r/r=0.5$

The aforementioned injections would provide a qualitative visual assessment for the mixing behavior, whereby a cross section showing significant distribution of particles indicates good mixing and one that shows clustered regions is an indication of bad mixing.

The third qualitative approach follows that proposed by Kukukova et al. (Kukukova et al., 2008) which relies on finding the scale of segregation. Kukukova et al. (Kukukova et al., 2011) proposed a new method named the point to nearest neighbor (PNN) to qualitatively visualize the scale of segregation when the available samples considered in the study were particles.

As reported by Kukukova et al. (Kukukova et al., 2011) the PNN method divided the domain cross-section into regular hexagonal grid as shown in Figure 3.5a such that the mean grid spacing was $d_G \cong 1.08 dx$. Kukukova et al. (Kukukova et al., 2011) used a number of grid points that was approximately equal to the number of particles to maximize the usage of each particle in the analysis.

The code of Kukukova et al. (Kukukova et al., 2011) was used in this study to implement the PNN method which is represented schematically in Figure 3.5b. However, due to the geometrical difference between the current study (circular pipe) and that of Kukukova et al. (Kukukova et al., 2011) (rectangular duct), the code had to

be modified as shown in Figure 3.5c. As such, after generating the grid, the points that lied outside the domain cross-section were excluded from the study while maintaining only those inside the boundary (live grid points). Hence, the grid points were selected such that the live grid points, g , are approximately equal to the number of particles, N_{PNN} as recommended by Kukukova et al. (Kukukova et al., 2011).

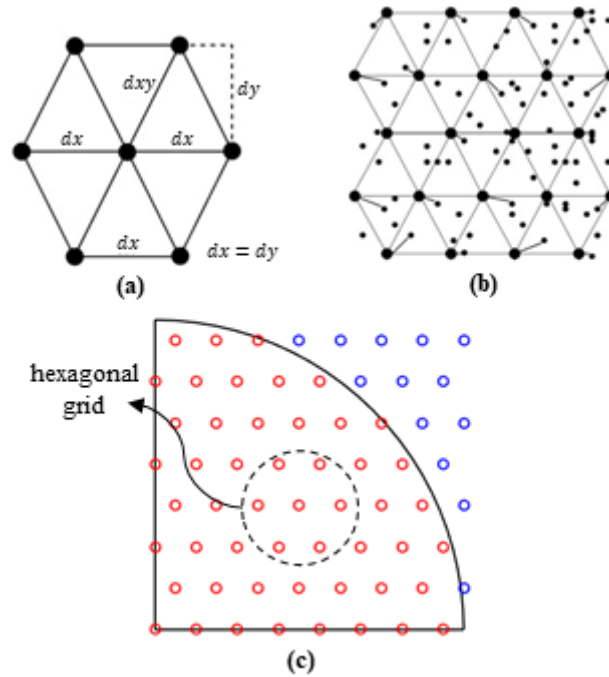


Figure 3.5. Illustration of the PNN method : (a) the hexagonal grid (Kukukova et al., 2011) , (b) search of the nearest neighbor of each grid point (Kukukova et al., 2011), (c) live grid points (red) and dead grid points (blue)

The distribution of particles was represented qualitatively using the PNN method through normalizing the nearest distance with respect to the pipe radius. These normalized distances were then classified in terms of frequency of appearance. These were then normalized with respect to the maximum frequency reported within the domain cross-section to generate a probability distribution. The normalized nearest distance was represented by δ^* displayed as percentage and the normalized frequency

was reported as f^* . Hence, a wide PNN distribution indicates high segregation, and a narrow PNN distribution is an indication of good dispersion.

3.2.3.1.2 Quantitative assessment

To quantify distributive mixing, the filtered variance of the PNN proposed by Kukukova et al. (Kukukova et al., 2011) was employed. This method indicates the uniformity of distribution of the particles. In addition, the mixing efficiency proposed by Medina et al. (Medina et al., 2019) was used to quantify mixing between two immiscible fluids.

3.2.3.1.2.1 *Filtered variance of the PNN method*

The filtered variance of the PNN method is depicted in Equation (3.4). In this method, the normalized distance d_i between a grid point and its nearest particle is reported and compared to a threshold value d_R . If $d_i < d_R$ then the particle lies within a virtual circle of radius d_R and centered at the grid point and d_i will be set equal to d_R . Hence, a variance of zero is an indication that all the particles have a spatial distribution resembling the homogeneous distribution of the grid point which reflects perfect mixing.

It should be noted that the threshold value d_R can assume a maximum value equals to half the mean grid spacing, thereby lower values of d_R would result in accurate values since the particles have to be closer to the grid points to designate a homogeneous distribution. In this study, a sensitivity test for d_R was held where it was set to $1/2 dx$, $1/8 dx$, and $1/32 dx$. The results revealed that $1/8 dx$ could provide acceptable results without excessive computational costs.

Moreover, for better generalization of the results, the variance at a specified cross-section was normalized with respect to the inlet variance such that a normalized value of 1 indicates poor distribution and a value of 0 indicates uniform distribution.

$$\sigma_R^2 = \frac{1}{g-1} \sum_{i=1}^g (d_i - d_R)^2 \quad (3.4)$$

if $d_i < d_R$ then $d_i = d_R$

3.2.3.1.2.2 Mixing efficiency

The mixing efficiency proposed by Medina et al. (Medina et al., 2019) is based on the entropy of mixing of two immiscible ideal gases. This method is briefly described below, for additional information, the reader is referred to Medina et al. (Medina et al., 2019).

The change in entropy at a certain cross section including two species of ideal gasses is given by:

$$\Delta S_{mix} = -n_m R_u \sum_{t=1}^N \frac{a_t}{A} [x_{1t} \ln x_{1t} + (1 - x_{1t}) \ln(1 - x_{1t})] \quad (3.5)$$

where ΔS_{mix} is the statistical entropy of a cross-section, n_m is the number of moles of species in a cross-section, R_u is the universal gas constant, A is the domain cross-sectional area, N is the total number of cells in the domain cross-section, a_t is the area of a cell within a cross-section, and x_{1t} is the fraction of a species 1 in cell t of a cross section.

The maximum entropy change for a certain cross section including two species of ideal gases is given by:

$$(\Delta S_{mix})_{max} = -n_m R_u [z_1 \ln z_1 + (1 - z_1) \ln(1 - z_1)] \quad (3.6)$$

$$z_1 = \sum_{t=1}^N \frac{a_t}{A} x_{1t} \quad (3.7)$$

where $(\Delta S_{mix})_{max}$ is the max statistical entropy of a cross-section and z_1 is the fraction of species 1 within a cross – section.

The mixing efficiency parameter (MEP) defined by ζ_M is therefore the ratio of entropy of mixing to maximum entropy of mixing, with ζ_M ranging between 0 and 1. A value of $\zeta_M = 0$ is an indicator of bad mixing (statistical order) and $\zeta_M = 1$ indicates good mixing (statistical disorder).

While this method dealt with the fraction of species, the current study dealt with particles. Hence, the fraction reported in the above equations were modified to quantify the mixing between particles represented by different colors occupying certain regions within the inlet cross-section as shown in Figure 3.4b.

In the current study, a square grid of $m \times m$ is used to cover the flow cross-section area, A . Therefore, the cell area a_t is evaluated as shown in Equation (3.8).

$$a_t = \frac{A}{m \times m} \quad (3.8)$$

Because this implies dealing with a circular pipe and a square grid, the cells that fully fall within the flow domain were considered “live cells”, and those that fall totally or partially outside the flow domain were considered “dead cells” and were neglected from the calculations. Hence, the total number of cells is replaced by the total number of live cells, h , each having an area, a_t . The total number of particles, N_{ζ_M} , is the sum of the blue particles, N_{blue} , and red particles, N_{red} , contained within the domain cross-section. It is important to note that the maximum number of live cells resulting in $z_r + z_b = 1$ is considered in order to make sure that every live cell contains particle of

either/both kinds. Hence, in each live cell t , there might be red particles represented by, N_{red}^t , and/or blue particles represented by, N_{blue}^t . Therefore, the total number of particles in a cell t is $N_{\zeta_M}^t$. Hence, the fraction of each fluid within each cell t is shown in Equations (3.9) and (3.10):

$$x_{rt} = \frac{N_{red}^t}{N_{\zeta_M}^t} \quad (3.9)$$

$$x_{bt} = \frac{N_{blue}^t}{N_{\zeta_M}^t} \quad (3.10)$$

The above equations could then be used to replace x_{1t} and $(1 - x_{1t})$ in Equation (3.6) by x_{rt} and x_{bt} , respectively.

3.2.3.2 Dispersive mixing

A key parameter for assessing the dispersive mixing within a static mixer is the extensional efficiency, β , which can be calculated using Equation (3.11). It reflects the amount of elongation, shearing, and/or rotation a fluid element is subjected to while flowing through a mixer.

$$\beta = \frac{|\gamma|}{|\gamma| + |\psi|} \quad (3.11)$$

where $|\gamma|$ and $|\psi|$ are the magnitudes of the strain rate tensor, γ , and the vorticity tensor, ψ , respectively. These are calculated according to Equations (3.12)-(3.15).

$$\gamma = \frac{1}{2} * (\nabla \mathbf{V} + \nabla \mathbf{V}^T) \quad (3.12)$$

$$|\gamma| = \sqrt{2\gamma:\gamma} \quad (3.13)$$

$$\psi = \frac{1}{2} * (\nabla\mathbf{V} - \nabla\mathbf{V}^T) \quad (3.14)$$

$$|\psi| = \sqrt{2\psi:\psi} \quad (3.15)$$

where $\nabla\mathbf{V}$ is the gradient of the velocity and the superscript T denotes its transpose. An extensional efficiency value of $\beta = 1$ indicates pure elongation, $\beta = 0.5$ represents simple shear, and $\beta = 0$ indicates pure rotational flow. Hence, a higher value of β indicates better dispersive mixing (Meng et al., 2015).

The dispersive mixing was reported qualitatively using contour plots at different locations to visualize whether the flow is rotational, elongational, or pure shear; and quantitatively, by calculating the area-average values of the extensional efficiency over several cross-sections within the STSM.

3.3 Results and discussions

The following shows the result of the various numerical experiments that were performed to assess the mixing behavior of screen-type static mixers under laminar flow conditions.

3.3.1 *Distributive mixing*

3.3.1.1 Single injection

3.3.1.1.1 Effect of number of screens

The distribution of particles resulting from a single injection (cf. Figure 4a) is shown in Figure 3.6. It is clearly shown that the number of screens affect the particles' distribution such that the particles' dispersion is directly proportional to the number of screens (cf. Figure 3.6a). This figure shows how a "point" injection spreads as it flows

through consecutive screens. Furthermore, the conversion of the PNN distribution from a wide to a narrower distribution is also shown in Figure 3.6b. It can be seen that the PNN distribution shrinks from a point reaching 90% to another reaching 50% for the case of $Mn = 20$, $L = 5$ mm, and $Re_b = 20$. This indicated that the particles were better distributed and are closer to the grid points. However, no good mixing can be concluded.

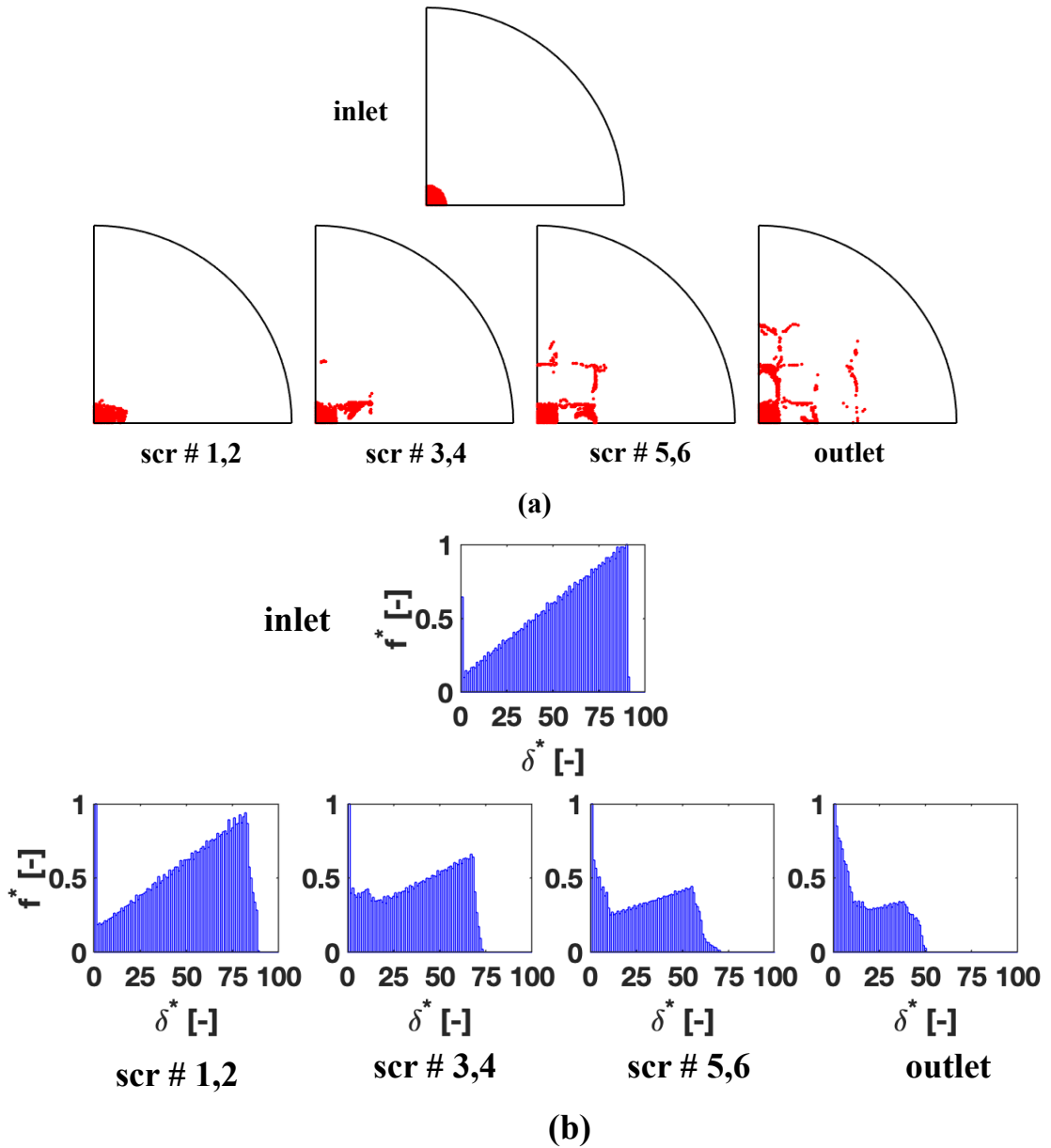


Figure 3.6. Distributive mixing representation for $Mn = 20$ at $L = 5$ mm and $Re_b = 20$ midway between consecutive screens, and outlet for the case of 1% central injection for (a) particles' dispersion and (b) PNN distribution

3.3.1.1.2 Effect of screen geometry

It can be clearly discerned from Figure 3.7 that the distribution of particles is affected by the variation of screen geometries, such that the screen with large openings, i.e. larger ($M-b$) value (see Table 3.1) shows more distributed particles. This large opening allows the particles not to be confined within small area as they are flowing through the screen but rather pass more freely.

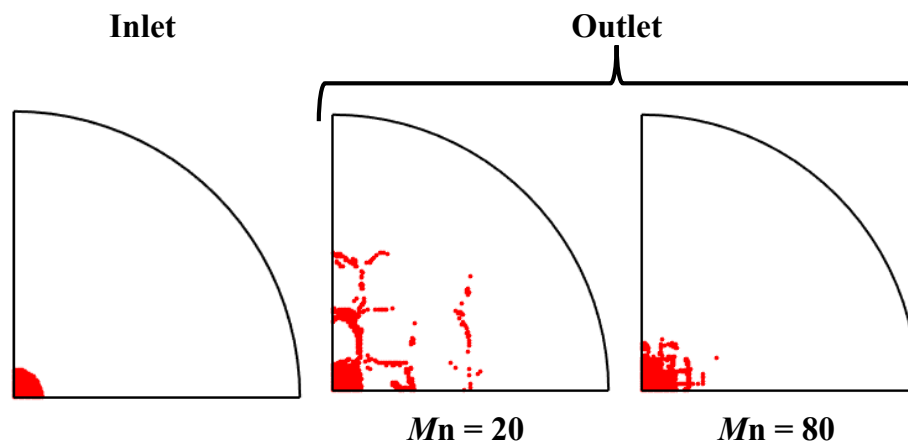


Figure 3.7. Distributive mixing representation at the pipe outlet for different screen geometries at $Re_b = 20$ and $L = 5$ mm for the case of 1% central injection

3.3.1.1.3 Effect of operating conditions

A quantitative assessment of the effect of flow velocity on mixing was performed using the single injection method. The results are shown in Figure 3.8 as values of the normalized filtered variance versus normalized distance in the pipe, Z^* , defined as $Z^* = Z/L$, where Z is the axial distance. As previously mentioned, a lower normalized filtered variance indicates better dispersion. This is mostly apparent for $Re_b = 20$ where the normalized filtered variance reached a value of 0.15, while it only reached a value of 0.62 at $Re_b = 1$, for $Mn = 20$, $L = 5$ mm. Moreover, the normalized filtered variance for $Mn = 80$ followed the same behavior as $Mn = 20$ but with higher

values. This further explains the qualitative assessment reported in §3.3.1.1.2. The better dispersion recorded at higher velocities is due to the induced vortices and recirculation within the flow field.

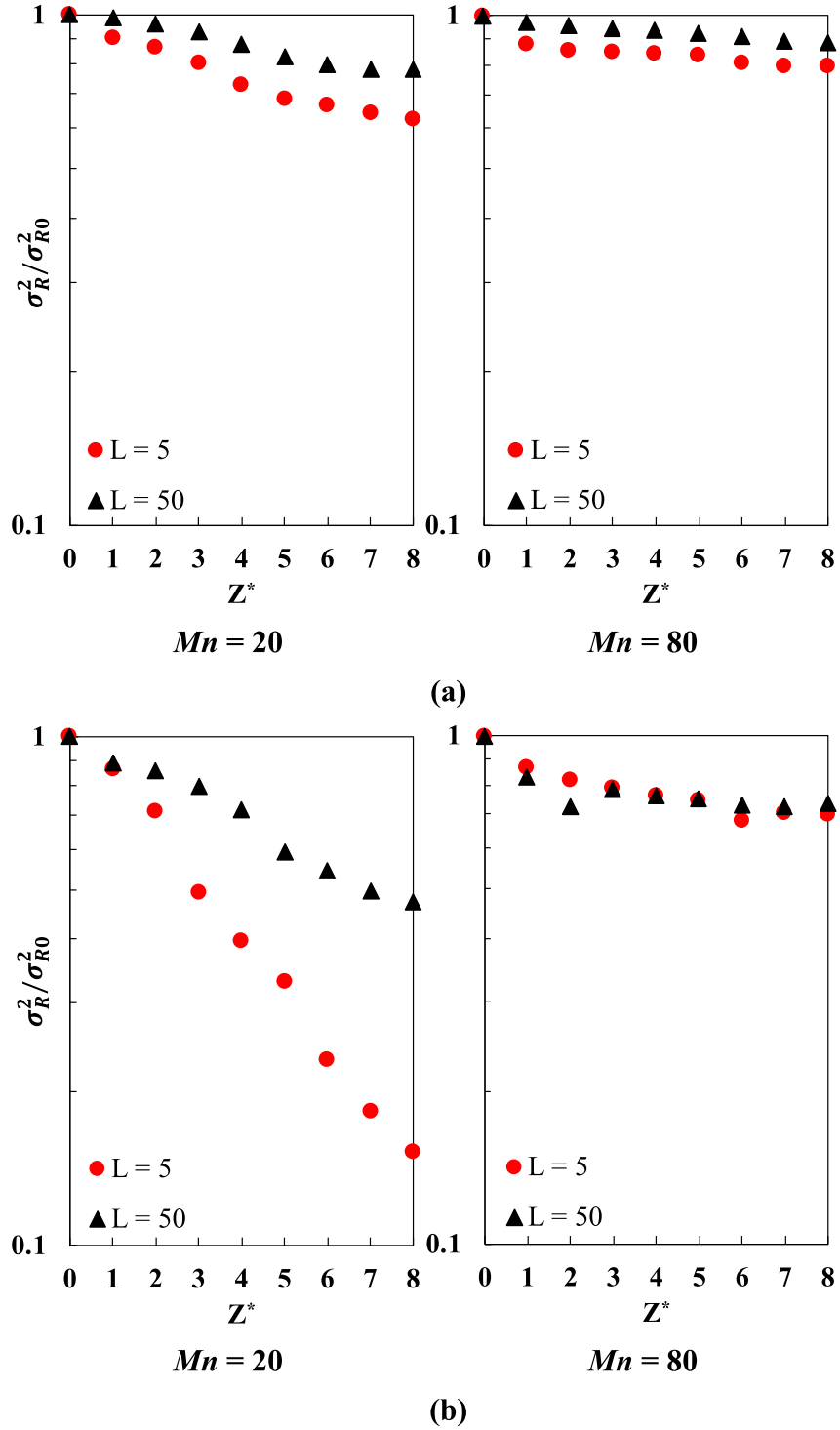


Figure 3.8. Filtered variance of the PNN method for different screen geometries and inter-screen spacing for the case of 1% central injection at (a) $Re_b = 1$ and (b) $Re_b = 20$

3.3.1.1.4 Effect of inter-screen spacing

The effect of inter-screen spacing was also assessed using the filtered variance of the PNN method and can also be seen in Figure 3.8. It can be easily discerned that the short inter-screen spacing ($L = 5$ mm) allowed better dispersion of particles compared to a larger inter-screen spacing ($L = 50$ mm), whereby lower normalized filtered variance values were recorded. This enhanced dispersion of particles at shorter inter-screen spacing can be attributed to the effect of screens on the local velocity profile. Referring to Figure 3.9 at $Re_b = 1$, the velocity profile is dominated by the common laminar parabolic profile for $L = 50$ mm, while it is flat at $L = 5$ mm. Such a modification to the velocity profile drives the particles to continuously accelerate and decelerate while potentially changing their radial location in the pipe. On the other hand, a maintained parabolic profile allows particles to retain their radial position over longer distances, and hence would have a very reduced mixing effect.

For $Re_b = 20$, it is interesting to observe that the normalized filtered variance for $Mn = 80$ showed almost similar values for large and short inter-screen spacing, while this was not the case for $Mn = 20$ (cf. Figure 3.8b). This could also be related to the velocity profile as previously explained.

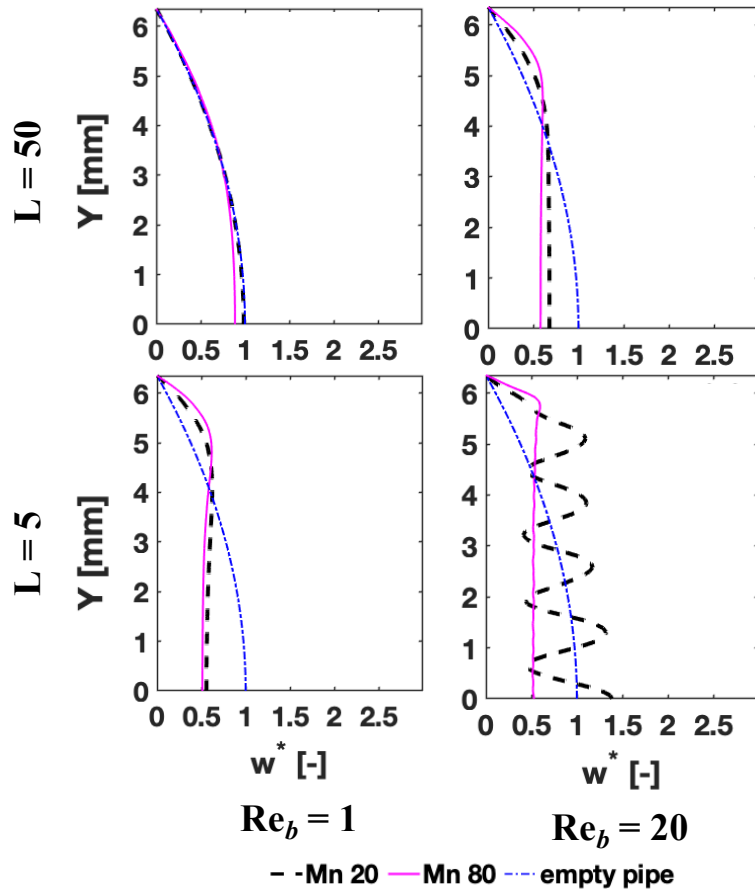


Figure 3.9. Normalized axial velocity profile at the midway between screens 2 and 3 for both screen geometries, inter-screen spacing, and operating conditions

3.3.1.2 Concentric injection

In order to better illustrate the mixing behavior, the results of injecting particles of different colors (method presented in Figure 3.4b) are shown in Figure 3.10

Figure 3.10a shows that at low Re and large L , both blue and red particles showed a tendency to migrate towards the central axis. However, for a short L (i.e. $L = 5$ mm), both red and blue particles tended to migrate towards the wall. But, for large Re (Figure 3.10b), better mixing was observed for the coarse screen only. This can be attributed to the aforementioned effect of velocity profile which is mostly disturbed at $Mn = 20$, and $Re_b = 20$.

Table 3.2 presents the calculated mixing efficiency parameter (Medina et al., 2019). This parameter was also compared to the case of an empty pipe where no mixing elements were introduced. At large inter-screen spacing and $Re_b = 20$ and $Mn = 20$, the highest mixing efficiency of 44.5% was calculated. This compares favorably to the worst mixing efficiency of 5.2 for an empty pipe. These results clearly show a poor mixing behavior for the screens under laminar flow conditions and the best situation is obtained for the highest Re_b values.

Furthermore, the results of the mixing efficiency calculated using concentric injection appear to contradict those from single central injection using the normalized filtered variance method, where the case of short inter-screen spacing at $Re_b = 20$ and $Mn = 20$ showed the highest dispersion. This is attributed to the fact that latter method takes into account the particles in the central area of the pipe as opposed to the former where the effect of changes to the velocity profile near the wall is also taken into account. In these regions, the effect of tangential and radial velocity components is more pronounced and hence better represented in the study of mixing.

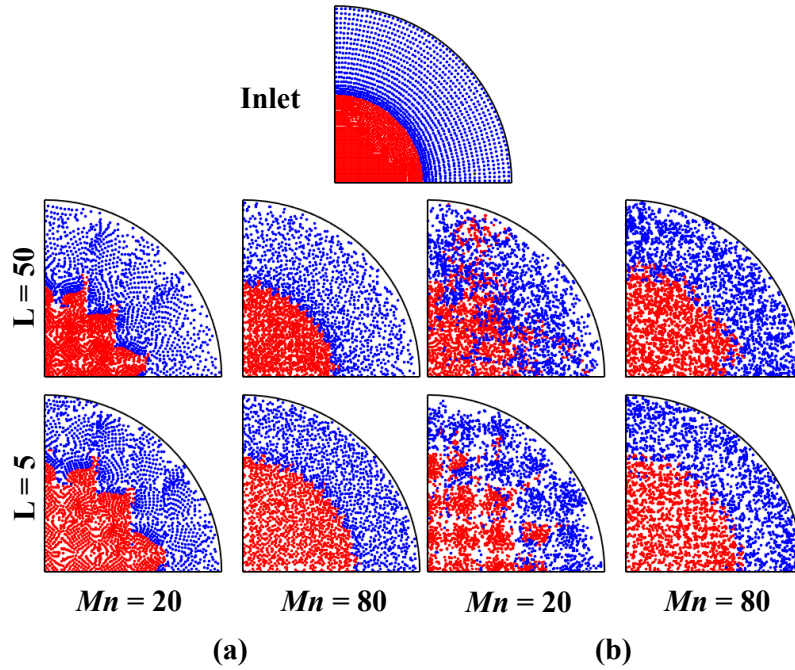


Figure 3.10. Distributive mixing representation at the pipe outlet for different screen geometries and inter-screen spacing for the case of concentric injection at (a) $Re_b = 1$ and (b) $Re_b = 20$

Table 3.2. Mixing efficiency percentage at the pipe outlet for different screen geometries, inter-screen spacing and operating conditions for the case of concentric injection

	L = 50		L = 5	
$\zeta_M\%$	$Re_b = 1$	$Re_b = 20$	$Re_b = 1$	$Re_b = 20$
$Mn = 20$	11.5	44.5	9.9	26.9
$Mn = 50$	7.14	12.8	7.4	9.4
Empty		5.2		

3.3.2 Dispersive mixing

Figure 3.11 displays the area-weighted average values of the extensional efficiency over a large number of cross-sectional planes in the axial direction. For the case presented here at $Re_b = 1$, three main points can be highlighted. Firstly, the value of the extensional efficiency at $Z^* = 0$ ($\beta = 0.5$ vs. 0.25) varies significantly with the

inter-screen spacing. This is because the extensional efficiency is related to the variation of the velocity with respect to the geometrical coordinates. In other words, at large inter-screen spacing the change of velocity is not as immediate as it is at short distances. Secondly, the extensional efficiency shows a repeatability pattern as the flow passes through consecutive screens. This is in line with the analysis of the velocity field that showed a similar behavior. Thirdly, the extensional efficiency undergoes noticeable fluctuations in the vicinity of the screen. The fluid elements that are being elongated due to the changes in the velocity profile, start to rotate as they go through the screen before undergoing elongation again. However, the average values around which the extensional efficiency fluctuates remain those of a shear flow. The true effect is however better observed through the contour plots of the extensional efficiency shown in Figure 3.12. This figure shows the contours as the flow passes the 7th screen at various normalized axial distances (M^*) as calculated using Equation (3.16) (where j corresponds to the screen number). This normalized axial distance provides a common representation while varying the screen geometry. One cannot but observe regions of purely elongational flow before it turns into rotational/shear as it goes through the screen followed by another elongational region. This is further followed by a region of pure shear flow as it is expected from laminar pipe flow.

$$M^* = \frac{(Z - [j \cdot L - 0.5 \cdot L])}{M} \quad (3.16)$$

In order to provide an overall extensional efficiency value for the flow within the STSM, the mean extensional efficiency is commonly used in the literature (Meng et al., 2017, 2015; Soman and Madhuranthakam, 2017). These values were calculated and reported in Table 3.3. The downside of using such a parameter is that the major

fluctuations that were observed disappear to give the impression of a completely shear flow dominating the system. For $Re_b = 1$, the results reveal that the flow within the STSM shows near shear flow ($\beta \cong 0.5$) at $L = 50$ mm; whereas, higher value ($\beta \cong 0.61$) at $L = 5$ mm is recorded which is an indicator of higher dispersive mixing at short inter – screen spacing.

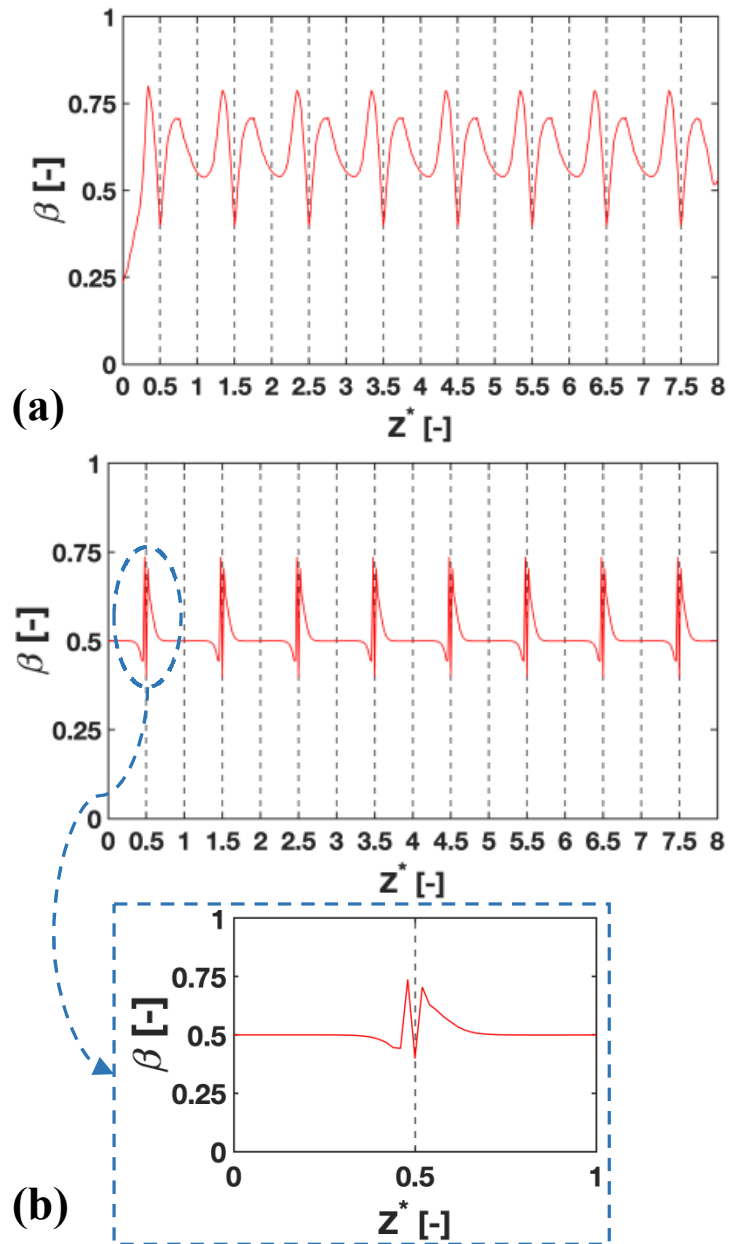


Figure 3.11. Area weighted average of the extensional efficiency at different cross-sections along the axial direction of STSM for (a) $L = 5$ mm and (b) $L = 50$ mm of $Mn = 20$ at $Re_b = 1$

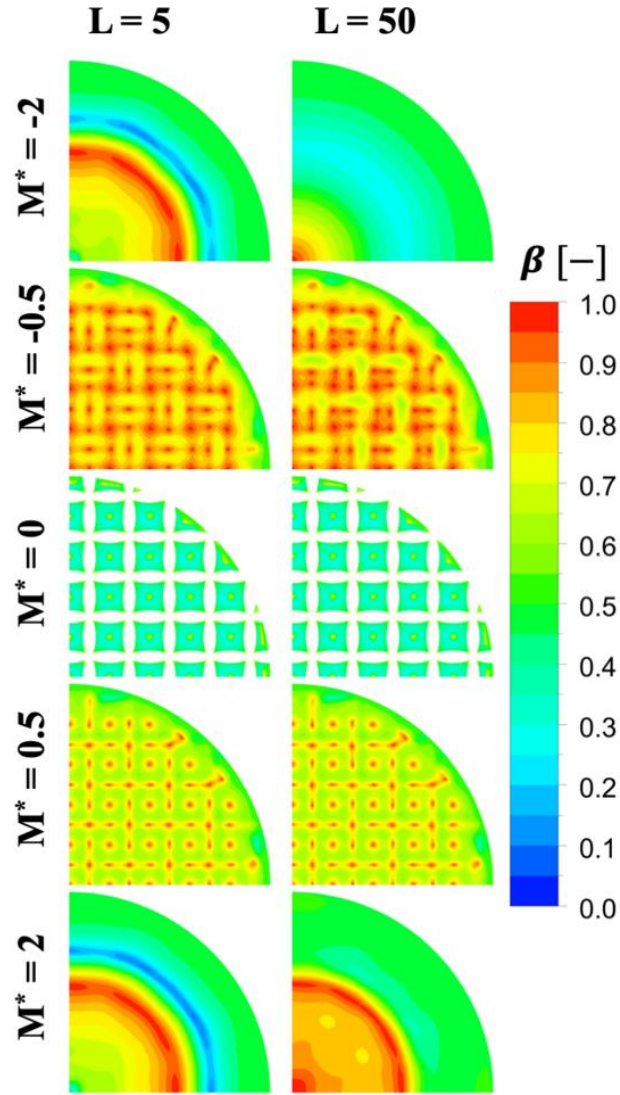


Figure 3.12. Extensional efficiency contours near the vicinity of the 7th screen for both inter-screen spacing of $Mn = 20$ at $Re_b = 1$

Table 3.3. Volume average extensional efficiency value within the STSM for different screen geometries, inter-screen spacing and operating conditions for the case of concentric injection

	L = 50		L = 5	
β	$Re_b = 1$	$Re_b = 20$	$Re_b = 1$	$Re_b = 20$
$Mn = 20$	0.5128	0.5163	0.6138	0.5272
$Mn = 50$	0.5193	0.5445	0.6120	0.5509
Empty	0.5			

Moreover, Table 3.3 presents the overall extensional efficiency within the STSM at $Re_b = 20$. It is clearly shown that the overall extensional efficiency values are close to the pure shear such that $Mn = 80$ recorded slightly higher values compared to $Mn = 20$. The high extensional efficiency values reported at low Re_b compared to a low extensional efficiency value recorded at high Re_b value could be related to high intense of breakup of fluid elements due to higher shear at high Re_b values.

3.4 Conclusion

The mixing performance of screen-type static mixers under laminar flow conditions was assessed using a Lagrangian method. The effect of changing the screen geometry, inter-screen spacing, number of screens and operating conditions on the mixing behavior was predicted using published methods for mixing assessment.

The results revealed that the overall mixing performance of these mixers is not ideal for laminar flow conditions where average and sometimes below average performance in dispersing fluid elements were recorded. However, it was observed that the presence of screens greatly alters the velocity profile with subsequent effects on the elongation, shearing, and rotation of fluid elements as they pass through them.

3.5 Nomenclature

A	Domain cross-sectional area
CFD	Computational Fluid Dynamics
CoV	Coefficient of variation
D	Pipe diameter
<i>GCI</i>	Grid convergence index

L	Inter-screen spacing
M	Center-to-center distance
M^*	Dimensionless center-to-center distance
Mn	Mesh number
m	Number of Grid cells for mixing efficiency evaluation
N_s	Number of screens
N_{blue}	Total number of blue particles of the mixing efficiency method
N_{blue}^t	Number of blue particles in the t^{th} cell of the mixing efficiency method
N_{PNN}	Total number of particles used in the PNN method
N_{red}	Total number of red particles of the mixing efficiency method
N_{red}^t	Number of red particles in the t^{th} cell of the mixing efficiency method
N_{ζ_M}	Total number of particles used in the mixing efficiency method
$N_{\zeta_M}^t$	Total number of particles in the t^{th} cell of the mixing efficiency method
PDU	Particle distribution uniformity
PNN	Point to nearest neighbor
P_{in}	Average gauge static pressure at inlet
P_{out}	Average gauge static pressure at outlet
R	Pipe radius
RTD	Residence time distribution
R_u	Universal gas constant
STSM	Screen Type Static Mixer

V	Velocity vector
V_p	Particle's velocity vector
U	Superficial (approaching velocity)
X_p	Particle position vector
Z	Axial distance
Z^*	Normalized axial distance
a_t	Area of a cell t within a cross-section
b	Wire diameter
dx	Normalized horizontal grid spacing with respect to pipe radius
dy	Normalized vertical grid spacing with respect to pipe radius
dxy	Normalized diagonal grid spacing with respect to pipe radius
d_G	Mean grid spacing
d_i	Normalized nearest distance between grid point and particles
d_R	Threshold for normalized nearest distance
f^*	Normalized frequency
g	Live grid points lying within the flow cross-section of the PNN method
h	Live cells lying within the flow cross-section of the mixing efficiency method
j	Screen number
n_m	Number of moles of species in a cross-section
r	Central injection radius
x_{1t}	fraction of a species 1 in the t^{th} cell of a cross-section
x_{2t}	fraction of a species 2 in the t^{th} cell of a cross-section

x_{rt}	fraction of red particles in the t^{th} cell of a cross-section
x_{bt}	fraction of blue particles in the t^{th} cell of a cross-section
z_1	Fraction of species 1 in a cross-section
z_r	Fraction of red particles in a cross-section
z_b	Fraction of blue particles in a cross-section

Greek Letters

ρ	Working fluid density
μ	Working fluid viscosity
α	Fraction opening area
β	Extensional efficiency
ω	Specific dissipation rate
δ^*	Normalized nearest distance in percentage
ζ_M	Mixing efficiency
γ	Strain rate tensor
ψ	Vorticity tensor
$\nabla \mathbf{V}$	Gradient of the velocity
ΔP_o	Static pressure drop in an empty pipe
ΔP_{screen}	Static pressure drop across a screen
ΔS_{mix}	Statistical entropy of a cross-section
$(\Delta S_{mix})_{max}$	Maximum statistical entropy of a cross-section

Dimensionless Group

Re_b	Wire Reynolds number, $\rho U b / \mu$
Re_{pipe}	Pipe Reynolds number, $\rho U D / \mu$

3.6 Acknowledgments

The authors would like to acknowledge the financial support of the Lebanese National Council for Scientific Research (CNRS-L) and the University Research Board as well as the Arza HPC Unit at the American University of Beirut.

3.7 References

- Al Taweel, A.M., Azizi, F., Siriijeerachai, G., 2013. Static mixers: Effective means for intensifying mass transfer limited reactions. *Chem. Eng. Process. Process Intensif.* 72, 51–62. <https://doi.org/10.1016/j.cep.2013.08.009>
- Azizi, F., 2019. On the pressure drop of fluids through woven screen meshes. *Chem. Eng. Sci.* 207, 464–478. <https://doi.org/10.1016/j.ces.2019.06.046>
- Azizi, F., Al Taweel, A.M., 2015. Mass Transfer in an Energy-Efficient High-Intensity Gas-Liquid Contactor. *Ind. Eng. Chem. Res.* 54, 11635–11652. <https://doi.org/10.1021/acs.iecr.5b01078>
- Azizi, F., Al Taweel, A.M., 2011. Turbulently flowing liquid-liquid dispersions. Part I: Drop breakage and coalescence. *Chem. Eng. J.* 166, 715–725. <https://doi.org/10.1016/j.cej.2010.11.050>
- Celik, I.B., Ghia, U., Roache, P.J., Freitas, C.J., Coleman, H., Raad, P.E., 2008. Procedure for estimation and reporting of uncertainty due to discretization in CFD applications. *J. Fluids Eng. Trans. ASME* 130, 0780011–0780014. <https://doi.org/10.1115/1.2960953>
- Ghanem, A., Lemenand, T., Della, D., Peerhossaini, H., 2013. Chemical Engineering Research and Design Static mixers : Mechanisms , applications , and characterization methods – A review. *Chem. Eng. Res. Des.* 92, 205–228. <https://doi.org/10.1016/j.cherd.2013.07.013>
- Hobbs, D.M., Muzzio, F.J., 1998. Reynolds number effects on laminar mixing in the Kenics static mixer. *Chem. Eng. J.* 70, 93–104. [https://doi.org/10.1016/S1385-8947\(98\)00065-5](https://doi.org/10.1016/S1385-8947(98)00065-5)
- Hobbs, D.M., Muzzio, F.J., 1997. Effects of injection location, flow ratio and geometry on kenics mixer performance. *AICHE J.* 43, 3121–3132. <https://doi.org/10.1002/aic.690431202>
- Kukukova, A., Aubin, J., Kresta, S.M., 2011. Measuring the scale of segregation in mixing data. *Can. J. Chem. Eng.* 89, 1122–1138. <https://doi.org/10.1002/cjce.20532>
- Kukukova, A., Noel, B., Kresta, Suzanne M., 2008. Impact of Sampling Method and Scale on the Measurement of Mixing and the Coefficient of Variance. *AICHE J.* 54, 3068–3083. <https://doi.org/DOI 10.1002/aic.11639>
- Medina, H., Thomas, M., Eldredge, T., Adebajo, A., 2019. The M Number: A Novel

- Parameter to Evaluate the Performance of Static Mixers. *J. Fluids Eng. Trans. ASME* 141. <https://doi.org/10.1115/1.4044070>
- Meng, H., Song, M., Yu, Y., Wang, F., Wu, J., 2015. Chaotic mixing characteristics in static mixers with different axial twisted-tape inserts. *Can. J. Chem. Eng.* 93, 1849–1859. <https://doi.org/10.1002/cjce.22268>
- Meng, H.B., Song, M.Y., Yu, Y.F., Jiang, X.H., Wang, Z.Y., Wu, J.H., 2017. Enhancement of Laminar Flow and Mixing Performance in a Lightnin Static Mixer. *Int. J. Chem. React. Eng.* 15, 1–21. <https://doi.org/10.1515/ijcre-2016-0112>
- Rahmani, R.K., Keith, T.G., Ayasoufi, A., 2005. Three-dimensional numerical Simulation and performance study of an industrial helical static mixer. *J. Fluids Eng. Trans. ASME* 127, 467–483. <https://doi.org/10.1115/1.1899166>
- Soman, S.S., Madhuranthakam, C.M.R., 2017. Effects of internal geometry modifications on the dispersive and distributive mixing in static mixers. *Chem. Eng. Process. Process Intensif.* 122, 31–43. <https://doi.org/10.1016/j.cep.2017.10.001>
- Thakur, R.K., Vial, C., Nigam, K.D.P., Nauman, E.B., Djelveh, G., 2003. Static mixers in the process industries – a review. *Chem. Eng. Res. Des.* 81, 787–826. <https://doi.org/10.1205/026387603322302968>

CHAPTER 4

HYDRODYNAMICS OF WALL-BOUNDED TURBULENT FLOWS THROUGH SCREENS: A NUMERICAL STUDY

W. Abou-Hweij and F. Azizi¹

B. & W. Bassatne Dept. of Chemical Engineering and Advanced Energy, M. Semaan Faculty of Engineering and Architecture, American University of Beirut, 1107 2020 Beirut, Lebanon

Submitted to Chemical Engineering Communications Journal on January – 3 – 2022
(under review 2nd round – GCEC–2021–0634)

Abstract

The hydrodynamic performance of turbulent flows in circular pipes equipped with screen-type static mixers is numerically assessed in this study. A three-dimensional computational fluid dynamics model is used to study the effect of changing the operating conditions and reactor configuration on the flow field. The accuracy of the numerical results is validated by comparing pressure drop predictions to empirical correlations where a maximum relative error of 13.3 % is recorded. The macro-mixing performance of screen type static mixers is also assessed using residence time distributions. The study shows that the flow through screens is three-dimensional by nature with secondary flows being prominent near the pipe walls. Moreover, the presence of the screen has a major impact on the turbulent velocity profile both up- and down-stream. The flow field and velocity gradients are interpreted using strain rate and vorticity. These parameters also show that the flow through screens is highly dispersive where 39.3% of the reactor volume has an extensional efficiency value greater than 0.6. This explains their good performance in processing multiphase flows and gives an insight on how to design systems that maximize this dispersive effect in their volume. The residence time distribution study shows that the presence of screens renders the

flow closer to plug flow with the effect being more pronounced using finer mesh screens operating at high flow velocities.

Keywords: Screens, Hydrodynamics, Extensional efficiency, Dispersive mixing, Macro-mixing, residence time distribution.

4.1 Introduction

Mixing plays a crucial role in many chemical processes ranging from simple blending to complex multiphase flow systems (Azizi and Al Taweel, 2015; Montante et al., 2016). Several equipment types are used for this purpose such as mechanically agitated tanks, bubble columns, packed columns, static mixers, among others.

Static mixers are now commonly used in the industry because of their inherent characteristics that allow achieving high mixing efficiencies at reduced operating costs. Compared to conventional dynamic mixers, they also offer the advantage of a much smaller volume for the reactor with its subsequent positive impact on the safety of the operation (Al Taweel et al., 2013; Ghanem et al., 2013; Madhuranthakam et al., 2009; Peschel et al., 2012; Thakur et al., 2003). Moreover, the recent advances in numerical approaches helped in properly characterizing their internal flow behavior making them popular in the field of mixing (Meng et al., 2015, 2014). A survey of the open literature reveals a large number of studies that addressed the hydrodynamics and mixing performance of static mixers under laminar or turbulent regimes for a wide array of mixer geometries. For example, several studies addressed the performance of the widely used Kenics mixer (KSM) (Belhout et al., 2020; Hobbs et al., 1998; Hobbs and Muzzio, 1998; Mahammedi et al., 2017; Rahmani et al., 2008, 2005) and SMX (Jegatheeswaran et al., 2018; Leclaire et al., 2020), while others presented the

performance of novel mixers in comparison with KSM and/or SMX (Haddadi et al., 2020, 2019; Meng et al., 2020, 2017, 2015, 2014; Stec and Synowiec, 2019, 2017b, 2017a).

Recently, screen-type static mixers (STSM), which are made of plain square woven meshes have been investigated for processing multiphase operations (Abou Hweij and Azizi, 2020; Al Taweel et al., 2013; Azizi and Abou Hweij, 2017; Azizi and Al Taweel, 2015). These elements can also be found in a large number of other processes including noise reduction (Okolo et al., 2019), Stirling engine regenerators (Costa et al., 2013), greenhouse insect repellents (Bailey et al., 2003), and more importantly, they have been used for the production or reduction of large-scale velocity or pressure non-uniformities (Groth and Johansson, 1988; Kurian and Fransson, 2009; Pinker and Herbert, 1967; Roach, 1986).

Such screens when employed in tubular contactors superimpose adjustable, radially uniform velocity fields in high velocity pipe flows (Al Taweel et al., 2005). Because of the capability of screens in producing very high energy dissipation rates in their immediate vicinity followed by a quasi-isotropic turbulence further downstream (Laws and Livesey, 1978), they were found effective in processing multiphase flows. The high energy dissipation rates and micro-mixing intensities generated downstream of the screens (Bourne and Lips, 1991) provided not only fine dispersed phase entities (bubbles and/or drops) but also enhanced the interphase mass transfer rates in the presence of contaminants (Al Taweel et al., 2013, 2007, 2005; Azizi and Al Taweel, 2015). In treating liquid-liquid dispersions, the use of screens increased the energy efficiency by 5-fold when compared to conventional stirred tanks equipped by Ruston-type impellers (Al Taweel and Chen, 1996). In addition, volumetric mass transfer

coefficients, k_{LA} , reaching 13 s^{-1} were achieved in the case of liquid-liquid dispersions while reaching 99% of equilibrium conditions in less than 1s (Al Taweel et al., 2007). For gas-liquid systems, interfacial areas as high as $2200 \text{ m}^2/\text{m}^3$ were generated (Chen, 1996). High oxygen transfer efficiencies reaching 4.2 kg/KWh were measured by Al Taweel et al. (Al Taweel et al., 2005) while k_{LA} values as high as 4.08 s^{-1} even in the presence of surfactants were found by Azizi and Al Taweel. (Azizi and Al Taweel, 2015).

From a hydrodynamic perspective, Irps and Kanjirakkad (Irps and Kanjirakkad, 2016) recently studied the modification of wall boundary layers in wind tunnels due to the presence of turbulence grids. By changing the grid geometry, they measured pressure drop, boundary layer velocity profiles, and turbulence modification. They found a thinning of the boundary layers with an overshoot in the local velocity. This overshoot was found to correlate with the mesh porosity as opposed to the pressure drop as was reported by earlier studies (Lau and Baines, 1968; Mehta, 1985; Owen and Zienkiewicz, 1957). Santos et al. (Santos et al., 2016) also studied the effect of screens in wind tunnels and found that their presence reduces turbulence intensity non-uniformities. Although, the authors noted an increase in turbulence intensity with the insertion of screens, its profile became more uniform.

In addition, several experimental studies investigated the turbulence field generated by the screens and found it to be anisotropic in their immediate vicinity before turning into isotropic further downstream (Groth and Johansson, 1988; Roach, 1986). Kurian and Fransson (Kurian and Fransson, 2009) found that the level of anisotropy decreased with an increase in the mesh Reynolds number (i.e. characteristic length based on the mesh width), while Roach (Roach, 1986) stated that a distance

equivalent to 10 mesh widths downstream of the screen was required for the turbulence to become homogeneous. Groth and Johansson (Groth and Johansson, 1988) showed that a distance equivalent to 25 mesh widths was required to reduce the turbulence intensities below their upstream values. More information can be found in the work of Azizi and Al Taweel (Azizi and Al Taweel, 2011a).

Besides the large body of experimental investigations for flow through grids, only a small number of numerical studies was undertaken to analyze their hydrodynamic performance under laminar or turbulent flow regimes (Costa et al., 2013; Green et al., 2008; Middelstädt and Gerstmann, 2013; Okolo et al., 2019). The common feature of such studies was the assumption of symmetrical configurations in an unbounded flow configuration. The reader is referred to the work of Abou-Hweij and Azizi (Abou-Hweij and Azizi, 2020) who presented a detailed survey of these numerical investigations for flow through screens. Abou-Hweij and Azizi (Abou-Hweij and Azizi, 2020) simulated wall-bounded laminar flows through plain-woven square meshes. They analyzed the effect of varying the geometry of the screen, reactor configuration and operating conditions on the velocity and pressure fields. Their simulation results showed the direct impact of screens on the hydrodynamics of the flow. Moreover, in another study, Abou-Hweij and Azizi (Abou Hweij and Azizi, 2020) investigated the mixing performance of screens in the laminar flow regime. Using the Lagrangian particle method, they studied the impact of changing the operating conditions and design configurations on the mixing performance using standard methods. Their results confirmed that this type of mixer is incapable of providing acceptable radial mixing in the laminar regime, but good dispersive mixing is achievable.

To the authors' best knowledge, no studies characterizing the hydrodynamic performance of 3D bounded turbulent flows through woven meshes exist in the literature. Consequently, this work aims to numerically characterize the hydrodynamic and macro-mixing behavior of wall-bounded turbulent flows through screens under various design configurations and operating conditions. For this purpose, the impact of varying four different parameters will be assessed. These are the geometry of the screen, number of mixing elements, the inter-screen distance, and flow velocity.

4.2 Computational methods

4.2.1 Computational Domain

Two different screen geometries (cf. Table 4.1) were used to conduct the numerical simulations. These two screens were selected in order to have large variation in their geometries. Commonly, screens are characterized by various geometric parameters. These include their fractional open area, α , mesh number, Mn , mesh opening, M , and wire size, b . It is to be noted that the mesh size, M , is the center-to-center distance between adjacent wires and the fractional open area, α , is commonly computed as the projection of the screen's wires to a plane normal to the flow (Abou-Hweij and Azizi, 2020) and is given by Equation (4.1). Mn represents the number of openings per unit length. In the context of this work, it is the number of openings in one inch (i.e., $Mn = 0.0254 \text{ m}/M$ in m). Figure 4.1 presents a schematic illustration of a screen showing all its geometric parameters.

Table 4.1. Geometrical characteristics of plain-woven square meshes.

Mn (-)	$M \times 10^3$ (m)	$b \times 10^3$ (m)	$(M - b) \times 10^3$ (m)	α (%)
20	1.27	0.4064	0.8636	46.2
50	0.508	0.2286	0.2794	30.3

$$\alpha = \left(1 - \frac{b}{M}\right)^2 \quad (4.1)$$

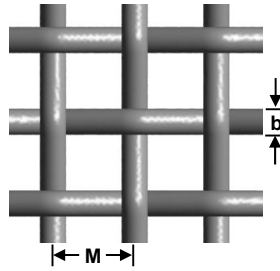


Figure 4.1. Schematic illustration of a section of screen corresponding to $Mn = 20$ – Top view

The computational domain used in the present investigation is a minor modification of the one used by Abou-Hweij and Azizi (Abou-Hweij and Azizi, 2020). In the current study four screens were employed and placed equidistantly at an inter-screen spacing of $L = 15M$ or $L = 45M$. The spacing was considered as a function of the geometric characteristics of each screen, namely, its mesh size (M). This choice was based on two main criteria. First, it was selected to homogenize the interpretation of the hydrodynamic results for different screen geometries. Second, it was chosen so the locations fall farther than the critical distance of $10M$ that is required to reach a homogeneous flow downstream of a screen (Roach, 1986). Figure 4.2 schematically represents the investigated computational domain.

A circular pipe of 12.7 mm inner diameter constituted the computational domain and liquid water was selected as the working fluid ($\rho = 998.2 \text{ kg} \cdot \text{m}^{-3}$ and $\mu = 0.001003 \text{ Pa} \cdot \text{s}$). To ensure similar hydrodynamic effects within the mixing section

when altering the screen geometry, the hydrodynamic simulations were performed while varying the wire Reynolds number, Re_b . Table 4.2 presents the selected operating conditions and their corresponding pipe Reynolds number, Re_{pipe} . It should be mentioned that an empty pipe length of $1D$ upstream of the first screen was used as the entry region while an empty pipe length of $3D$ was set downstream of the last mixing element (cf. Figure 4.2b). The wire Reynolds number, Re_b , and the pipe Reynolds number, Re_{pipe} , differ by the characteristic length used in calculating the inertial force. The wire diameter of the screen is employed to compute the former, while the empty pipe diameter is used in calculating the latter.

In contrast to the work of Okolo et al. (Okolo et al., 2019) who investigated unbounded flow field across screens under conditions where $Re_b \leq 170$, the current study considers flows in the range of $300 \leq Re_b \leq 1,000$.

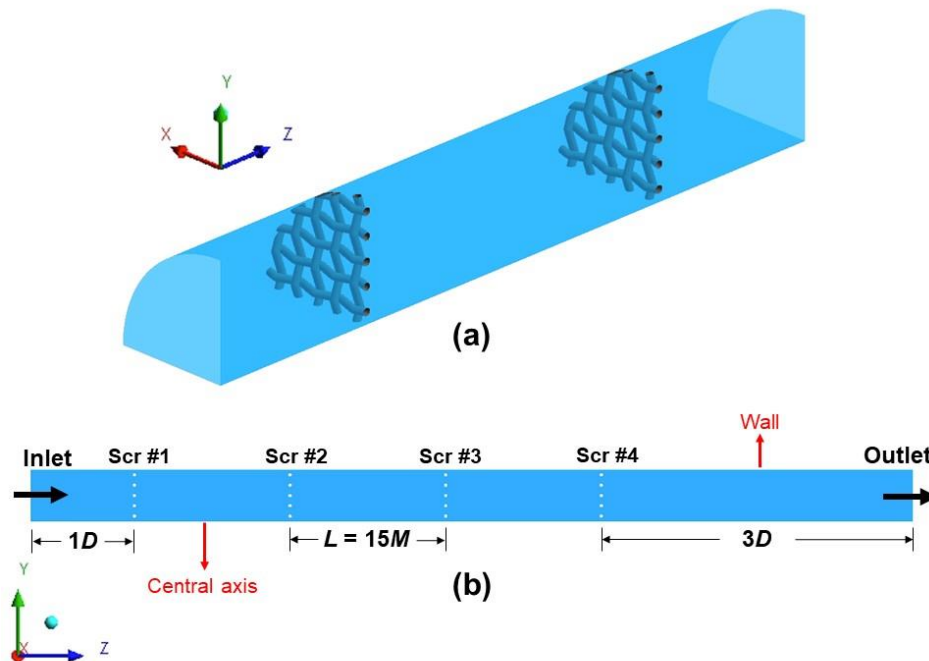


Figure 4.2. Schematic representation of the computational domain corresponding to $Mn = 20$ (a) quarter pipe showing the first two screens in a row and (b) periodic plane with four screens in row.

Table 4.2. Operating conditions for each screen geometry showing corresponding values of Re_b , Re_{pipe} , and average velocity.

	$Mn = 20$			$Mn = 50$		
Re_b	300	600	1,000	300	600	1,000
Re_{pipe}	9,375	18,750	31,250	16,666.7	33,333.3	55,555.5
U_{avg} (m·s ⁻¹)	0.7414	1.4835	2.4725	1.3186	2.6373	4.3955

An unstructured tetrahedral grid scheme was used to discretize the computational domain. To handle the small geometrical features associated with screens (i.e. mesh opening/wires) while dealing with large geometrical structures (i.e. empty pipe), the computational domain was split into three regions, namely, the screen, near-screen, and open-pipe regions as shown in Figure 4.3a. The screen region spans a length of $4b$ ($2b$ from either side of the screen), while the near-screen region extends to $12M$ from the center of the screen. The remaining volume was considered as the open pipe region. Figure 4.3(b-d) illustrate the grid discretization for the screen with a mesh number, $Mn = 20$. To accurately resolve the viscous sublayer, special attention was given to the near-wall refinement of all solid boundaries (pipe wall and screen surfaces) in order to account for the high gradients in these regions and ensure that y^+ values remain as close to 1 as possible (Habchi and Azizi, 2018). As such, several prism layers were generated at the pipe wall and screen surfaces as shown in Figure 4.3(c-d).

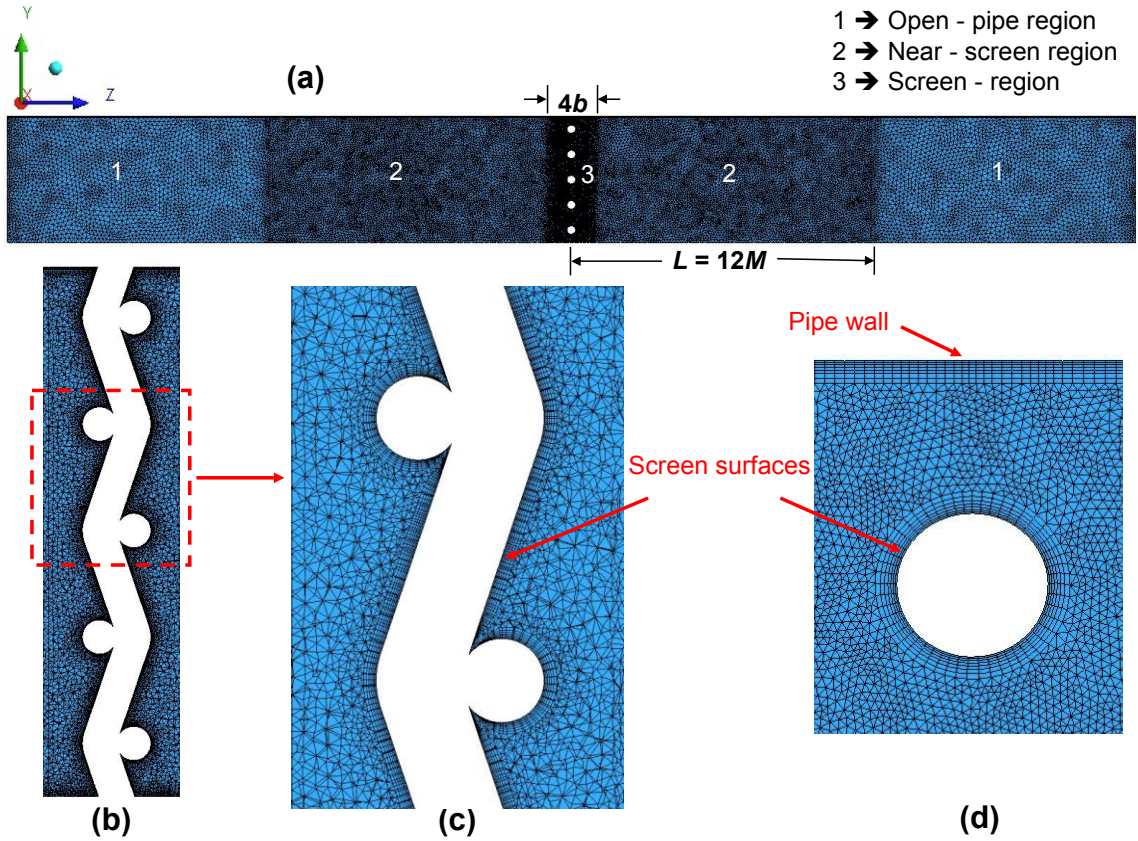


Figure 4.3. Meshing configuration for $Mn = 20$ (a) sideview of the meshing regions, (b) mesh generation within the screen region, (c) zoom-in to the screen region showing inflation layers at the screen surfaces, and (d) zoom-in showing inflation layers at pipe wall and the screen surfaces at the periodic plane.

4.2.2 Boundary conditions and solution methods

The CFD simulations were conducted using ANSYS Fluent[®] v.18.2 which employs the finite volume method (FVM). The turbulent flow field was modeled by applying Reynolds averaging for the mass and momentum equations. The continuity and momentum mean equations are shown in Equations (4.2) and (4.3) respectively, for a steady incompressible and Newtonian fluid.

$$\nabla \cdot \langle \vec{U} \rangle = 0 \quad (4.2)$$

$$\rho \nabla \cdot \{ \langle \vec{U} \rangle \langle \vec{U} \rangle \} = -\nabla p + \mu \nabla^2 \langle \vec{U} \rangle - \rho \nabla \cdot \langle \vec{u}' \vec{u}' \rangle \quad (4.3)$$

$$\vec{U} = \langle \vec{U} \rangle + \vec{u}' \quad (4.4)$$

where $\langle \vec{U} \rangle$ and \vec{u}' are the mean and fluctuating velocity components of the instantaneous velocity \vec{U} , p is the mean static pressure resulting from Reynolds' averaging.

The averaging procedure results in a Reynolds stress tensor $(-\langle \vec{u}' \vec{u}' \rangle)$ which could be predicted using Boussinesq eddy-viscosity hypothesis expressed by Equation (4.5) for an incompressible fluid (Hinze, 1975). This approach assumes that the turbulent viscosity, μ_t , is the constant proportionality between the Reynolds stresses and the mean velocity gradients. By omitting the density term due to the incompressibility condition, the turbulent kinematic viscosity, ν_t appears in the equation.

$$-\rho \langle \vec{u}' \vec{u}' \rangle = \mu_t \left(\nabla \langle \vec{U} \rangle + (\nabla \langle \vec{U} \rangle)^T \right) - \frac{2}{3} \rho k \mathbf{I} \quad (4.5)$$

where k is the turbulent kinetic energy and can be calculated using Equation (4.6) and \mathbf{I} is the identity matrix.

$$k = \frac{1}{2} \langle \vec{u}' \cdot \vec{u}' \rangle \quad (4.6)$$

The turbulent viscosity could be predicted using different eddy-viscosity models. Because the use of high-fidelity models such as DNS/LES is computationally very costly for the geometry at hand, the Realizable $k-\varepsilon$ turbulence model was used. This model is suitable for complex shear flows involving rapid strain and vortices that might arise as a result of boundary layers separation and vortex shedding behind bluff bodies (ANSYS, 2014). These features are omnipresent in flows through screen-type static mixers. In addition, a recent study by Okolo et al. (Okolo et al., 2019) tested the suitability of various turbulence models for flow through screens and concluded that the $k - \varepsilon$ family provided good prediction for the flow field. In the current study, the

enhanced wall treatment model was selected to predict the flow behavior in the near-wall region. The reader is referred to the ANSYS Theory Guide (ANSYS, 2017) for more details about the implemented turbulence model and the selected wall treatment model.

A fully developed flow was imposed as the inlet boundary condition (BC) while an outflow BC was set at the outlet. The no-slip BC was selected for all solid walls including the pipe wall and screen faces. The rotational periodic BC was also selected to simulate the complete pipe being represented by one-quadrant. Figure 4.4 presents the selected boundary conditions. The solution methods employed a pressure-based solver, while using the SIMPLE algorithm for the pressure-velocity coupling. The Least-Squares Cell Based method was used to evaluate the gradient terms, and the QUICK scheme was utilized for calculating the convection terms. In addition, 2nd order pressure interpolation was used and the residuals were always set to $< 10^{-6}$.

It is to be mentioned that the imposed fully developed profile was obtained by simulating a long empty pipe with a uniform inlet velocity profile. The profile was then extracted at a cross-section within the fully developed region. This approach resulted in more accurate results as opposed to employing a power law velocity profile.

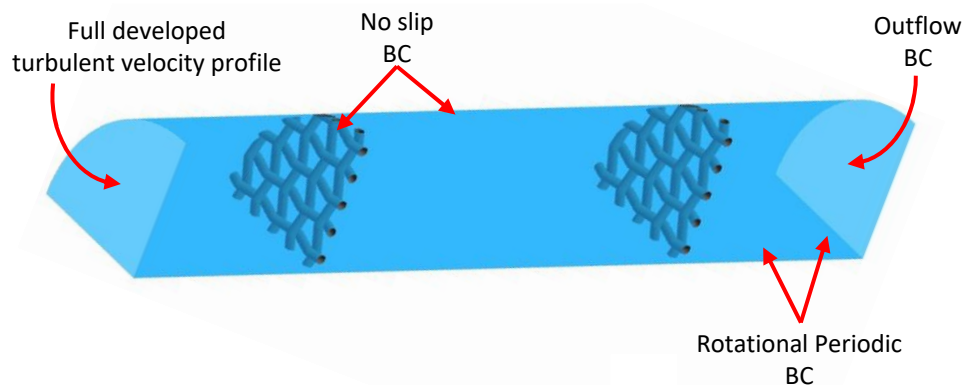


Figure 4.4. Selected boundary conditions for the studied domain.

4.2.3 Grid Independence

One screen element was used when performing grid independence tests following the grid convergence index (GCI) method of Celik et al. (Celik et al., 2008). The tests were conducted at $Re_b = 1,000$ and the pressure drop within the STSM, as well as the local and volume average turbulence quantities (dissipation rate and kinetic energy) within the screen and near-screen regions were monitored. Table 4.3 presents the GCI values for the medium and fine grids. The maximum GCI value within the tested parameters was 4.9 % if the medium grid was selected and 3.6% if the fine grid was selected (cf. Table 4.3). Hence, the medium grid was selected as it provided the best combination of computational cost and results reliability. This results also fell within the acceptable range of numerical uncertainty reported by Okolo et al. (Okolo et al., 2019). Moreover, the average and maximum values of y^+ for the medium grid are also presented in Table 4.3 with the maximum value not exceeding 3.5. This was used as an indicator that the viscous sublayer was well resolved (Habchi et al., 2010; Mohand Kaci et al., 2009). For the various geometries investigated here, the total number of grid cells is equivalent to the number of grid cells, N_e , shown in Table 3, multiplied by the number of mixer elements (i.e., 4). The numerical simulations were performed using the Octopus high performance computing (HPC) cluster available at the American University of Beirut using four parallel nodes each of 16 processors and 64GB RAM of Intel® Xeon® Processor E5-2665 @ 2.4 GHz. As such, dealing with geometries of different grid sizes, a computational domain composed of 4 screens in one row required a maximum of 20 hours of computational time and a minimum of 6 hours to reach a 10^{-6} order of convergence at a number of iterations not greater than 4000 iterations.

Table 4.3. Grid independence test for different screen geometries.

Mesh number	Refinement Level	Number of grid cells, N_e	GCI %	y^+_{avg}	y^+_{max}
$Mn = 20$	Fine	19,193,100	1.7		
	medium	7,108,637	4.9	1.02	2.51
	Coarse	2,632,137			
$Mn = 50$	Fine	27,094,857	3.6		
	medium	11,641,548	4.9	1.13	3.25
	Coarse	4,176,324			

4.3 Results and discussions

4.3.1 Model validation

The CFD model was validated using data for the pressure drop collected from the open literature. Typically, the pressure drop in STSM is the result of both the pipe wall skin friction and the pressure drop resulting from the flow through the screen. Accordingly, pressure losses across one screen element, Δp_{screen} , were calculated following Equation (4.7) (Abou-Hweij and Azizi, 2020):

$$\Delta p_{screen} = \frac{(p_{in} - p_{out}) - \Delta p_o}{N_s} \quad (4.7)$$

where p_{in} and p_{out} are the inlet and outlet average static pressure, Δp_o is the empty pipe pressure losses, and N_s is the number of mixing elements in the computational domain.

The flow resistance of a screen is typically measured using the pressure loss coefficient, K_s , which is the ratio of Δp_{screen} to the dynamic pressure of the flow (i.e., $\frac{1}{2}\rho U_{avg}^2$). This pressure loss coefficient is typically a function of both Re_b and the screen open area, α as shown in the set of correlations (4.8) and (4.9).

$$K_{s(A)} = \left[0.4537 + \left(\frac{10.76}{Re_b^{0.8213}} \right) \right] \cdot \left[\frac{1 - \alpha^2}{\alpha^2} \right] \quad (4.8)$$

$$K_{s(K\&F)} = \left[0.5 + \left(\frac{26}{Re_b} \right) \right] \cdot \left[\frac{1 - \alpha^2}{\alpha^2} \right] \quad (4.9)$$

Azizi (Azizi, 2019) recently proposed the correlation shown in Equation (4.8) for K_s following the analysis of a large number of experimental measurements, and covering a broad range of flow conditions ($2 \leq Re_b \leq 14,000$). This correlation was capable of predicting the experimental results within $\pm 30\%$. Equation (4.9) presents the empirical correlation of Kurian and Fransson (Kurian and Fransson, 2009) which is valid over the range $35 \leq Re_b \leq 800$. These two correlations were selected to validate the CFD simulations and the results for the pressure drop across one screen are shown in Figure 4.5. The good agreement between numerical predictions and these empirical correlations is very clear. A mean relative error (MRE) of 18.1% (maximum of 20.5%) was recorded using the correlation of Azizi (Azizi, 2019) and an MRE of 10.7% (maximum of 13.3%) using the correlation of Kurian and Fransson (Kurian and Fransson, 2009).

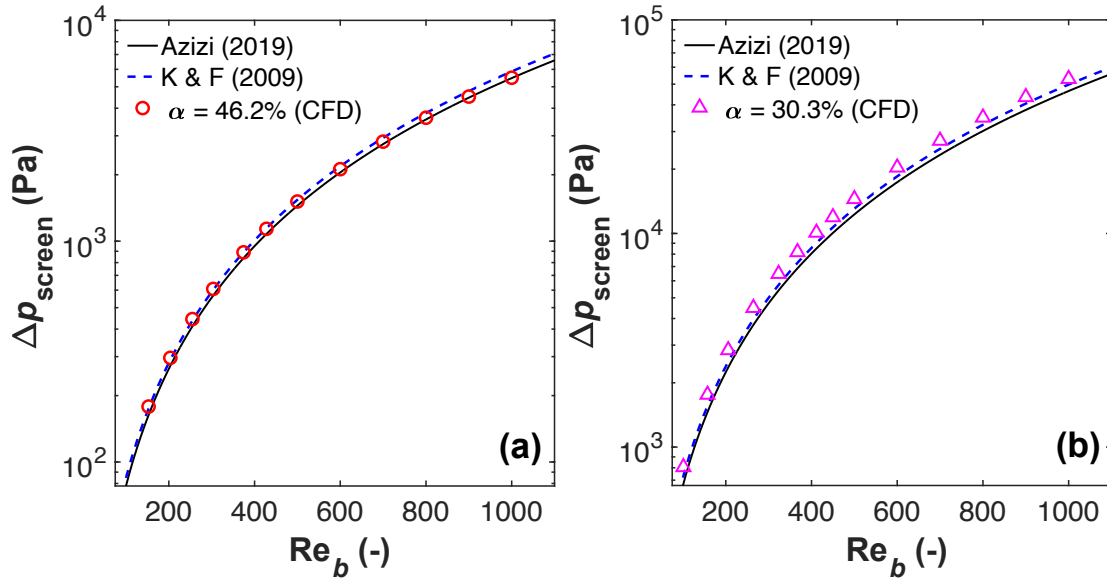


Figure 4.5. Comparison between correlation results and CFD prediction of the pressure drop across one screen: (a) $Mn = 20$ and (b) $Mn = 50$.

4.3.2 Hydrodynamics Characterization

The velocity field for the flow through screen mixers help in characterizing its hydrodynamics. It would provide comprehensive knowledge of the flow irregularities as they pass through these structures. This section will discuss the effect of varying the screen geometry, inter-screen spacing, number of screens and operating conditions on the velocity components, velocity profiles, extensional efficiency (strain rate and vorticity), and dissipation rate.

4.3.2.1 Velocity field

4.3.2.1.1 Velocity components

To better understand the three-dimensional behavior for flow screens, the various components of the mean velocity vector, $\langle \vec{U} \rangle$, (i. e. $\langle U \rangle_X = u, \langle U \rangle_Y = v, \langle U \rangle_Z = w$) are plotted along the centerline as well as near the wall along a fictitious axial line passing through the first aperture from the wall. The simulations were conducted at the

same wire Reynolds number, Re_b , which corresponds to different empty pipe velocities for screens with $Mn = 20$ and $Mn = 50$. For a better comparison between the different screens, the various velocity components were normalized with respect to the initial inlet centerline velocity which is only composed of an axial component $w_{(X=0,Y=0,Z=0)}$. Hence, u^* , v^* , and w^* depict the normalized velocities in the normal, tangential, and axial directions, respectively.

Figure 4.6 presents the normalized velocity components along the centerline and near the wall for both screen geometries while varying the inter-screen spacing ($L = 15M$ and $45M$) at $Re_b = 600$, in which $w_{(X=0,Y=0,Z=0)} = 1.7610 \text{ m} \cdot \text{s}^{-1}$ for $Mn = 20$ and $w_{(X=0,Y=0,Z=0)} = 3.1711 \text{ m} \cdot \text{s}^{-1}$ for $Mn = 50$. The vertical dotted lines on these figures present the location of the screens' central plane. It is clear from the plots that the screens alter the inlet fully developed turbulent profile by adding non-zero transverse components (in the x and y directions) whose magnitude is a function of screen geometry, radial distance, and inter-screen spacing. Moreover, the magnitude and profiles of the transverse components differ significantly near the wall. For the short inter-screen spacing, it can be noticed from Table 4.4 that the minimum peak ratio between the axial velocity component and the transverse components is reduced by almost 6.6 times for $Mn = 20$ and 3 times for $Mn = 50$ while moving from the centerline axis to the near wall axis. This is an indication that the flow through screens is three-dimensional by nature. It should be mentioned that for the larger inter-screen spacing, the reduction factors were calculated at 7.4 times for $Mn = 20$ and 3.9 times for $Mn = 50$. Hence, varying the inter-screen spacing did not have a noticeable impact on the nature of the flow (cf. Figure 4.6). In addition, it can be clearly discerned that the profile of the various velocity components and their magnitude remain unchanged from

the second screen onwards. This indicated that the flow becomes repeatable beyond the first screen.

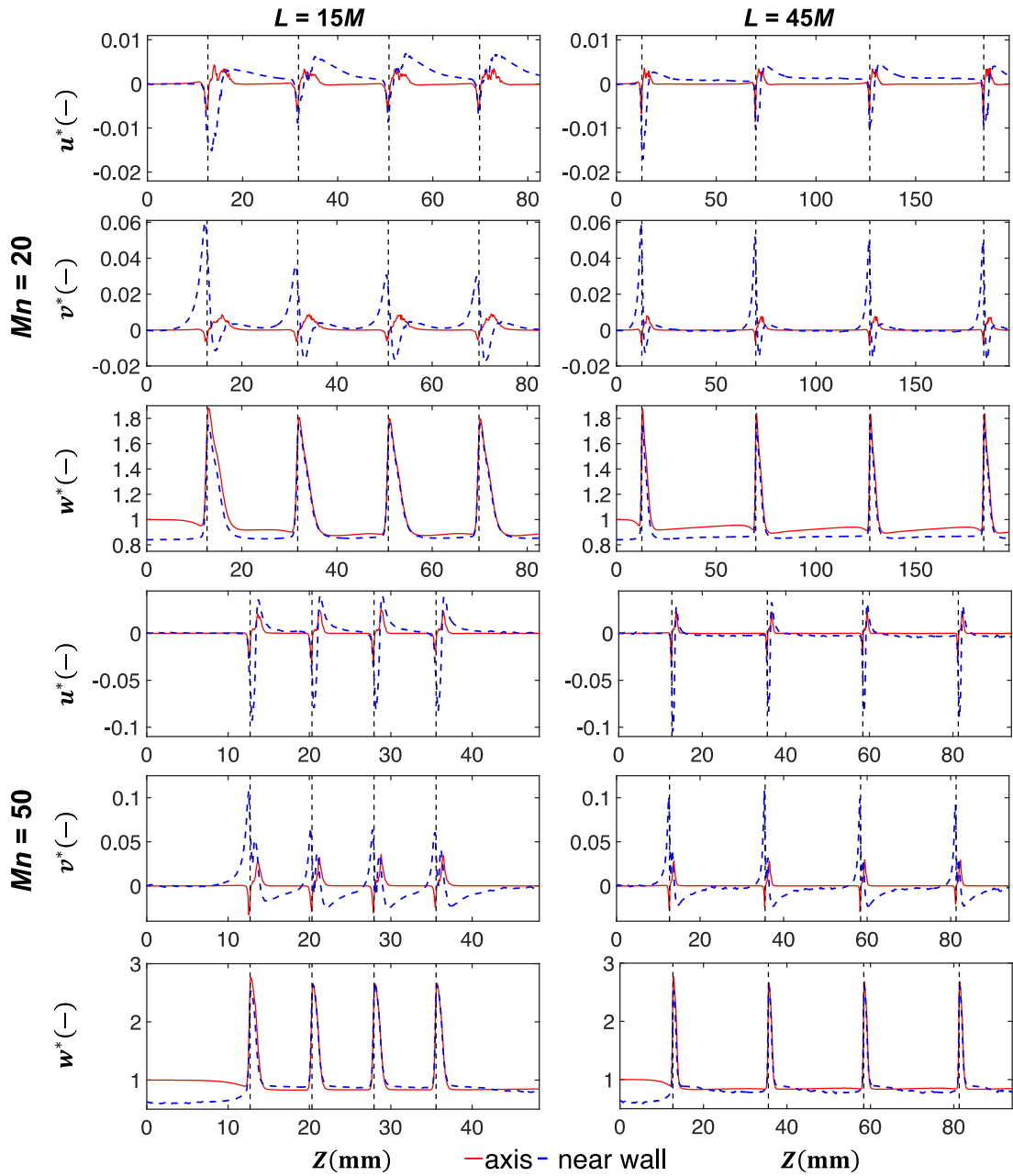


Figure 4.6. Normalized velocity components at the central axis and near the wall as a function of the axial distance for different inter-screen spacing and screen geometries at $Re_b = 600$.

Table 4.4. Minimum peak ratio between the normalized axial component and the transverse components for different screen geometries and inter-screen spacing at $Re_b = 600$.

Cases	$min\left(\frac{w^*}{u^*}, \frac{w^*}{v^*}\right)$		
	Centerline	Near the wall	Reduction factor
$Mn = 20, L = 15M$	208.4	31.4	6.6
$Mn = 20, L = 45M$	219.6	29.7	7.4
$Mn = 50, L = 15M$	77.3	25.7	3
$Mn = 50, L = 45M$	94.4	24.1	3.9

4.3.2.1.2 Velocity profiles

The axial velocity profiles provide detailed information on how the fully developed turbulent profile is altered as the flow crosses the screens. These profiles were plotted along a line normal to the YZ plane. The axial velocity profiles were plotted up-, and down-stream of the screen. These locations were normalized with respect to the mesh size, M , measured from the center of the screen. This normalization, reported as M^* , allows the generalization of the results when comparing different screen geometries. Hence, $M^* = 0$ corresponds to the screen's central plane, while $M^* = -1$ refers to the plane located at $1M$ upstream of the screen.

Due to the repeatable nature of the flow through screens, the normalized axial velocity profiles were plotted around the 3rd mixer element at different locations both upstream and downstream of the screen ranging from $M^* = -1$ to $M^* = 4$ as shown in Figure 4.7. These plots depict the flow behavior resulting from varying the screen geometries, inter-screen spacing, and operating conditions (at $Re_b = 300$ and $1,000$). From these plots and by comparison to a fully developed turbulent profile, one can

clearly observe the significant variation in the normalized axial velocity. The observed flattened profile can be attributed to the reduction of the velocity in the core region because of the increased resistance due to the presence of the screen body and the increase in velocity near the wall to counterbalance the decrease in the velocity in the core region (i.e., mass conservation). Moreover, at a distance $1M$ upstream of the fine screen ($Mn = 50$) an alternating (zigzag-like) flow behavior can be observed. This indicates that the presence of the screen is being sensed by the flow which is preparing to converge into the screen openings. This behavior, however, was not observed for the coarse mesh ($Mn = 20$).

Furthermore, as the flow passes through the screen, jets are formed similarly to the flow through orifices. The (velocity) magnitude of these jets is however a function of mesh parameters such that a smaller wire diameter, smaller opening area, and smaller mesh size result in higher magnitudes. Farther downstream of the screen, the high velocity gradients gradually dissipate for both screen geometries with the required distance being a function of the flow velocity. This sinusoidal behavior is more pronounced over longer normalized distances for the coarser screen. This could be attributed to the large wire diameter inducing large dead zones behind it compared to the smaller wire diameter of the finer mesh. In other words, a longer distance is required for the jets to re-coalesce after passing over large wire diameters. This observation was in line with the findings reported by Abou-Hweij and Azizi (Abou-Hweij and Azizi, 2020). A major distinction between the coarse and fine screen is noted near the wall in which the finer screen shows an overshoot in the local velocity, which is in line with the experimental observation of Irps and Kanjirakkad (Irps and Kanjirakkad, 2016).

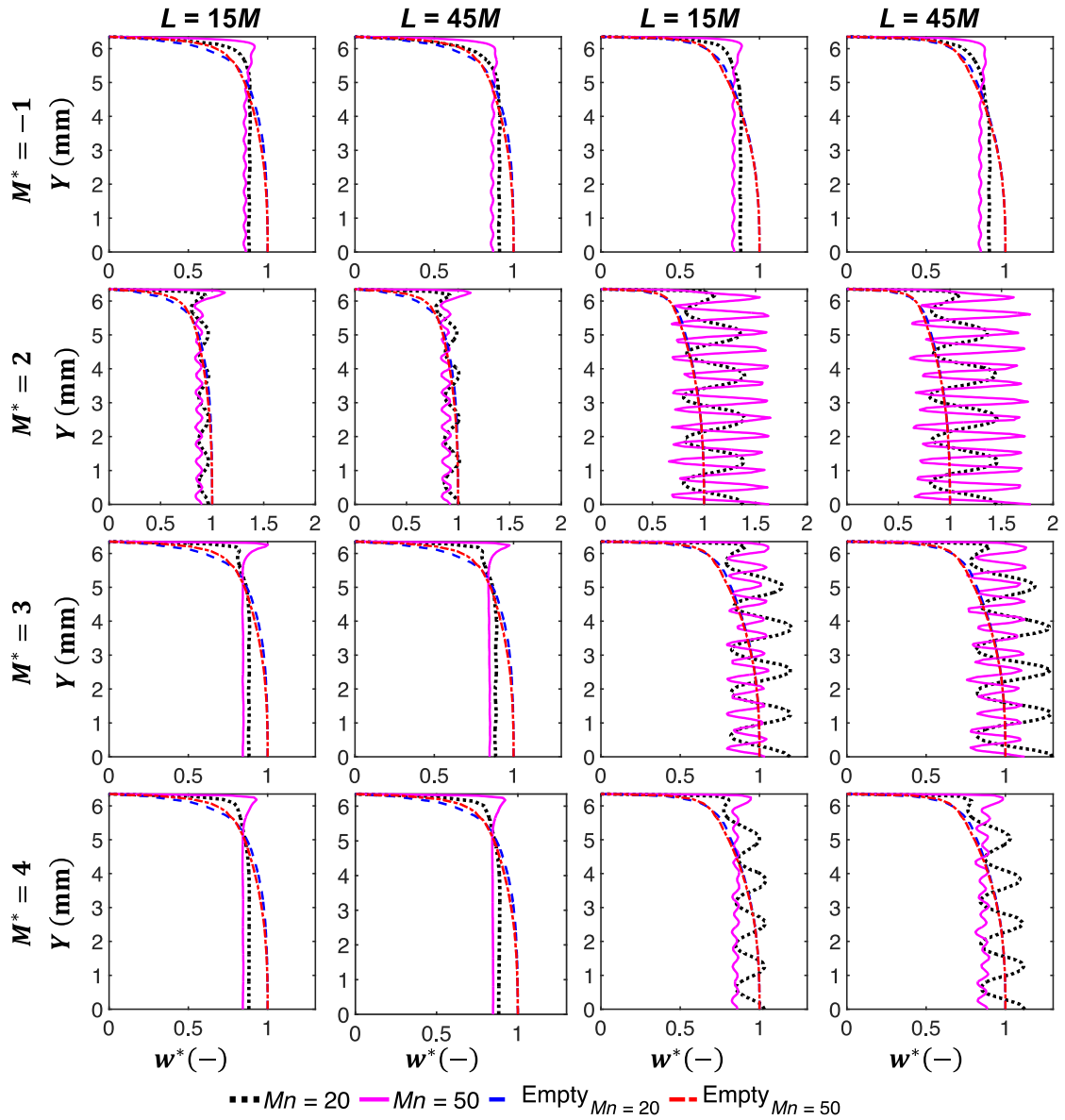


Figure 4.7. Normalized velocity profiles at several locations around the 3rd mixer element for $Re_b = 300$ and $Re_b = 1000$ while varying the inter-screen spacing.

4.3.2.1.3 Velocity contours and surface streamlines

For a detailed description of the velocity field inside the mixer, contours of the axial velocity, w , at different cross-sections around the 3rd mixer element of $Mn = 20$ are plotted in Figure 4.8. These contour plots are superimposed by the vector plots of the radial/transverse velocity components (u, v) to show the secondary flow within the cross-section. It can be clearly discerned from these plots that the secondary flow is

considerable near the walls, as previously mentioned, and cannot be neglected. Figure 4.8 also presents the surface streamlines as colored by the axial vorticity, which is defined by Equation (4.10). The streamlines showed that the axial vorticity recorded its highest values near the wall (pipe wall and screen wires) where the flow was found rotational as it passes over the wires ($M^* = 0$ and $M^* = 0.5$). This can be distinguished by observing the blue and red colors which present the clockwise and counterclockwise rotations, respectively. These observations helped conclude that the use of screens induces a rotational flow in their immediate vicinity which gradually subsides further downstream.

$$\langle \omega_z \rangle = \left(\frac{\partial v}{\partial x} - \frac{\partial u}{\partial y} \right) \quad (4.10)$$

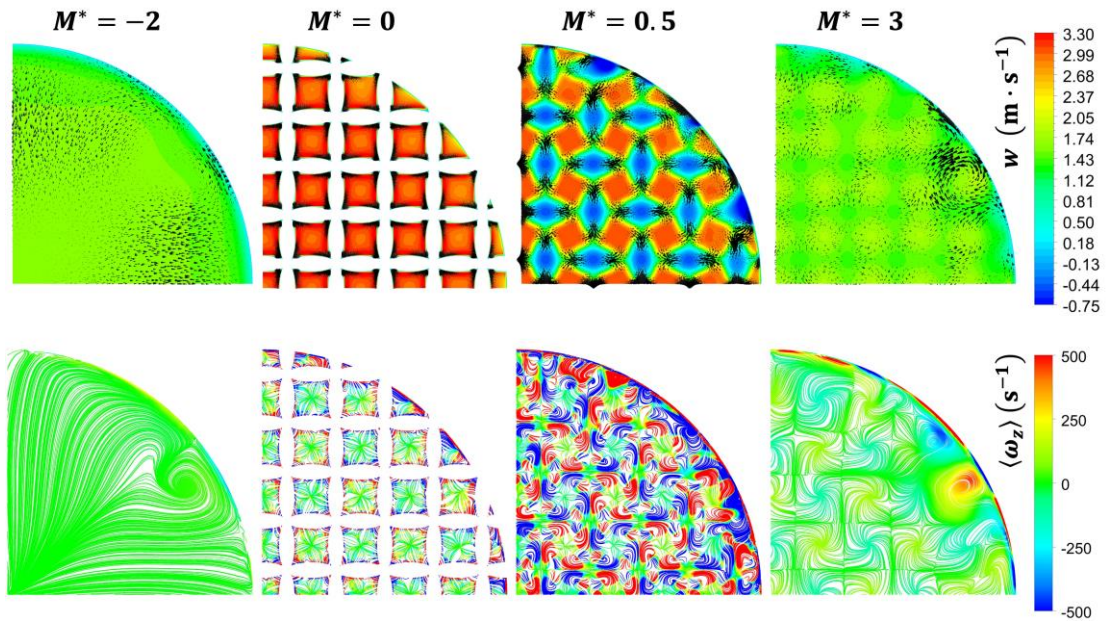


Figure 4.8. Velocity field at various cross-sections within the 3rd mixer element of $Mn = 20$ at $Re_b = 600$. Top row presents the contours of the axial velocity, w , superimposed with the vector plots of the radial velocity components, (u, v) . Bottom row presents the surface streamlines colored by the axial vorticity, $\langle \omega_z \rangle$.

4.3.2.1.4 Strain rate, vorticity, and extensional efficiency

A typical static mixer subjects the flow to elongation (high strain rates), rotation (high vorticity values), and shearing. To observe these phenomena, the strain rate and vorticity are usually examined. The mean strain rate tensor and its magnitude are mathematically presented by Equations (4.11) and (4.12) while the mean vorticity tensor and its magnitude are expressed by Equations (4.13) and (4.14), respectively.

$$\langle S \rangle = \frac{1}{2} \left(\nabla \langle \vec{U} \rangle + (\nabla \langle \vec{U} \rangle)^T \right) \quad (4.11)$$

$$|\langle S \rangle| = \sqrt{2 \langle S \rangle : \langle S \rangle} \quad (4.12)$$

$$\langle \Omega \rangle = \frac{1}{2} \left(\nabla \langle \vec{U} \rangle - (\nabla \langle \vec{U} \rangle)^T \right) \quad (4.13)$$

$$|\langle \Omega \rangle| = \sqrt{2 \langle \Omega \rangle : \langle \Omega \rangle} \quad (4.14)$$

where $|\langle S \rangle|$ and $|\langle \Omega \rangle|$ are the magnitudes of the mean strain rate tensor, $\langle S \rangle$, and the mean vorticity tensor, $\langle \Omega \rangle$, respectively. Figure 4.9 presents the contour plots of the strain rate magnitude as well as the vorticity magnitude through the 3rd mixer element for $Mn = 20$, $L = 15M$, and $Re_b = 300$, at various normalized locations in the streamwise direction. It can be clearly discerned that both the strain rate and vorticity magnitude showed high values near the pipe wall and the screen wires. This was expected due to the large variations in the velocity field at the centerline or the near wall region (cf. Figure 4.6). Moreover, the intensity of the strain rate and vorticity magnitudes increased as the flow passed through the screen at $M^* = 0$, which indicated that simultaneous stretching and rotation are taking place. These high values persisted until a certain distance downstream of the screen.

To better assess the magnitude of elongational flow compared to rotational flow, the extensional efficiency, β , was calculated. This parameter, also called dispersive mixing efficiency coefficient, was computed using Equation (4.15) for the various design and operating conditions investigated here. Pure elongation is reflected by a value of $\beta = 1$, while $\beta = 0$ suggests pure rotation, and $\beta = 0.5$ designates a simple shear flow (Manas-Zloczower, 1994). Therefore, good dispersive mixing is reflected by high values of β (Heniche et al., 2005; Meng et al., 2017, 2015).

$$\beta = \frac{|\langle S \rangle|}{|\langle S \rangle| + |\langle \Omega \rangle|} \quad (4.15)$$

The contour plots of the dispersive mixing efficiency coefficient are also shown in Figure 4.9 at various locations up-, and down-, stream of the screen. One can clearly notice how the extensional efficiency vary as the fluid approaches the screen, flows through its openings and is released into the open pipe region.

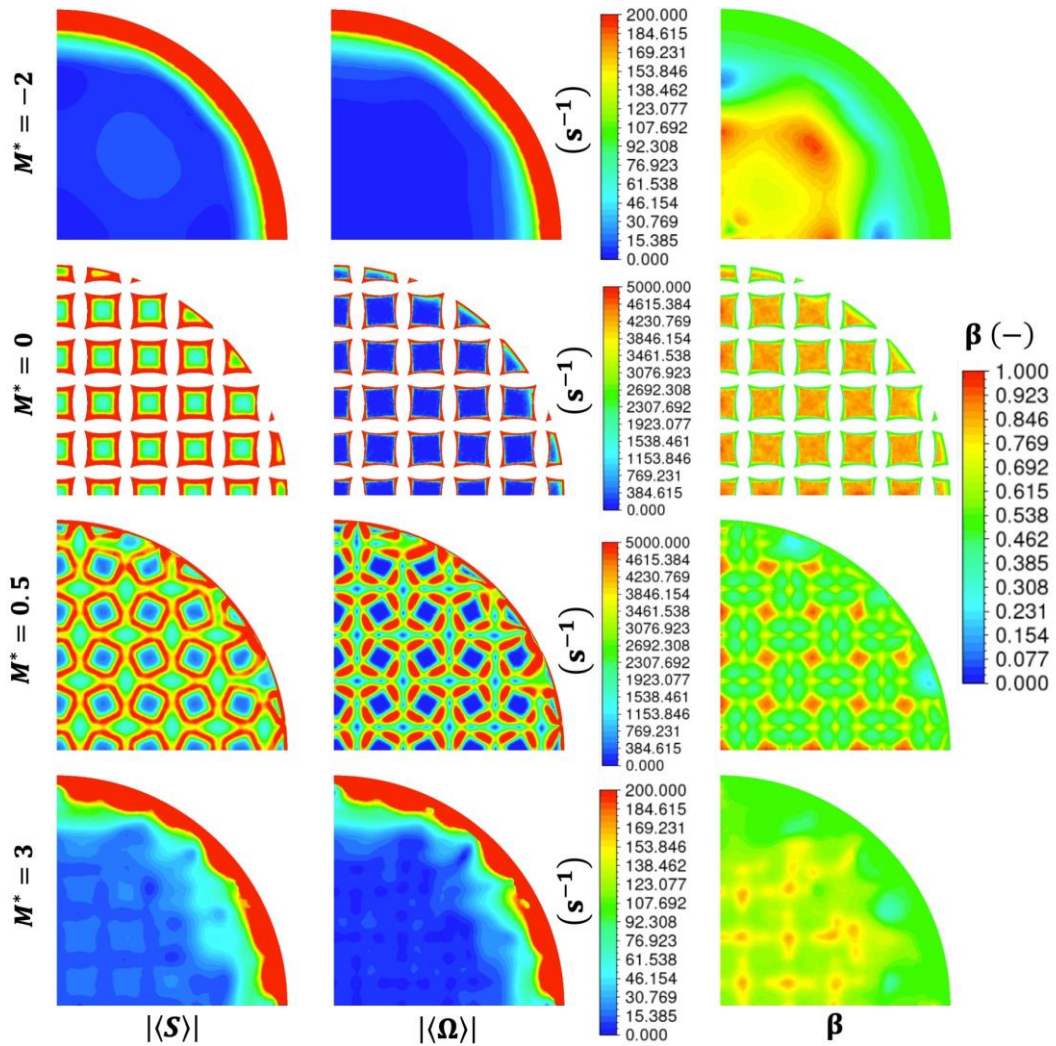


Figure 4.9. Contour plots of the strain rate magnitude, vorticity magnitude, and extensional efficiency at various locations around the 3rd mixer element of $Mn = 20$ at $Re_b = 300$ and $L = 15M$.

Figure 4.10 presents the average values of the extensional efficiency at several cross-sections in the XY plane. These values are plotted against the normalized axial distance, Z^* , given by Equation (4.16). To simplify the plotting of the data, Z^* renders the location of the central plane of the screen mixer at given integers (these can be seen as the dotted lines in the figure). Figure 4.10 displays the extensional efficiency values for the two screen geometries and inter-screen spacings at $Re_b = 300$.

$$Z^* = \frac{Z - 12.7}{L} \quad (4.16)$$

Figure 4.10 clearly shows the repeatability of the flow field as it passes through successive screens, whereby the profile of β after the 2nd screen ($Z^* \geq 1$) becomes repetitive. In addition, it can be observed that the mixer geometry can be designed in a fashion to render the flow mostly elongational or dispersive ($\beta \rightarrow 1$) by reducing the inter-screen distance.

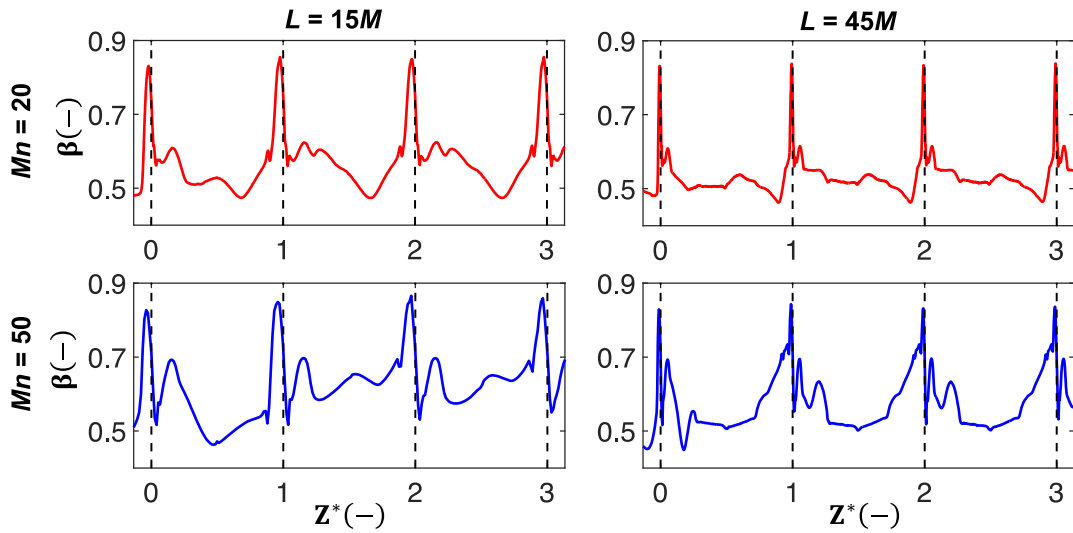


Figure 4.10. Plots for β against normalized axial distance, Z^* , within the four mixer elements for both screen geometries and inter-screen spacing at $Re_b = 300$.

Given the repetitive nature of the flow, the change in the value of β around the 3rd screen element is plotted in Figure 4.11. It can be observed that the value of β increases steadily as the flow approaches the screen with its maximum value being recorded in the upstream vicinity of the wire mesh. This is because the fluid elements must elongate before converging into the aperture of the screen. As the flow crosses the screen, shearing becomes dominant as it is indicated by the sudden drop in the value of the extensional efficiency.

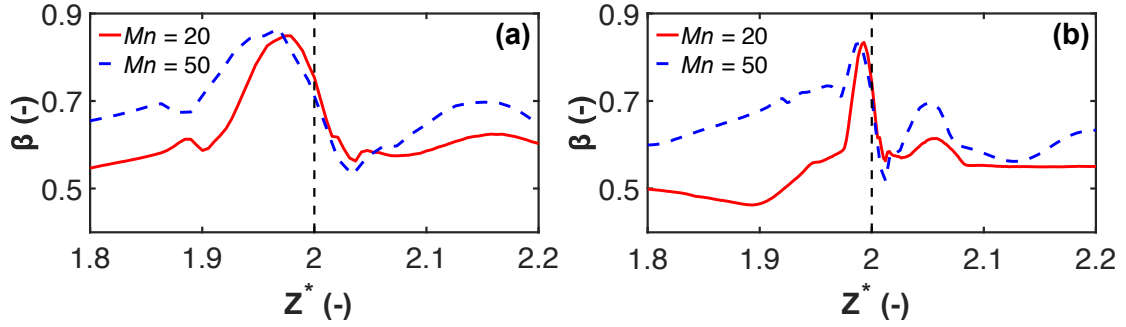


Figure 4.11. Zoom in for β values around the 3rd mixer element $1.8 \leq Z^* \leq 2.2$ for (a) $L=15M$ and (b) (a) $L=45M$.

To better highlight the effect of varying the screen geometry and inter-screen spacing, the cumulative volumetric distribution of β in the mixing zone is plotted in Figure 4.12 for the various flow velocities. In this context, the mixing zone was defined as the region bounded between $1D$ upstream of the first mixer element and $1D$ downstream of the last mixer element. This plot shows the volume fraction of the mixing zone where values larger than a given β dominate (Haddadi et al., 2020). For example, Figure 4.12a shows that 39.3% of the mixer volume has $\beta \geq 0.6$ when $Mn = 50$ and $L = 15M$, while this value drops to 26.6% if the inter-screen spacing is increased to $L = 45M$. From these charts, it can be reconfirmed that a shorter inter-screen spacing, or a finer mesh (at the same L) render higher values of β in a larger fraction of the mixing zone.

In addition, as the flow velocity increases, the extensional efficiency decreases for the same mixer design. This is clearly observed in Figure 4.13 which presents the volume average values of the extensional efficiency as a function of Re_b . These trends are in line with the findings of Soman et al. (Soman and Madhuranthakam, 2017) who reported a similar behavior using SMX mixers and attributed it to the increase in inertial flow which imposes a decrease in elongational flow. It can also be observed that the volume averaged extensional efficiency is indirectly proportional to the inter-screen

spacing with the screen with smaller openings rendering larger values. Hence, it can be concluded that a finer mesh with short inter-screen spacing is recommended for obtaining high dispersive mixing efficiency.

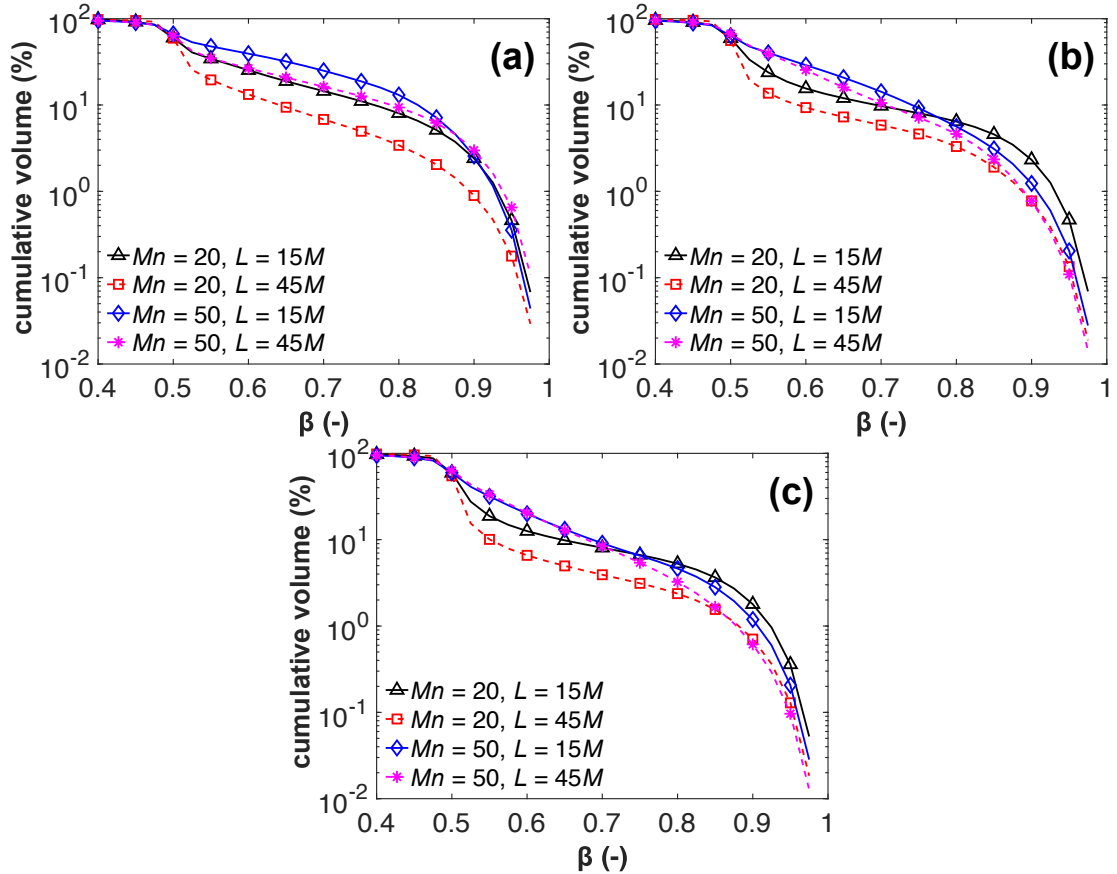


Figure 4.12. Cumulative volumetric distribution of β for both screen geometries at different inter-screen spacing and flow velocities. (a) $Re_b = 300$, (b) $Re_b = 600$, (c) $Re_b = 1,000$.

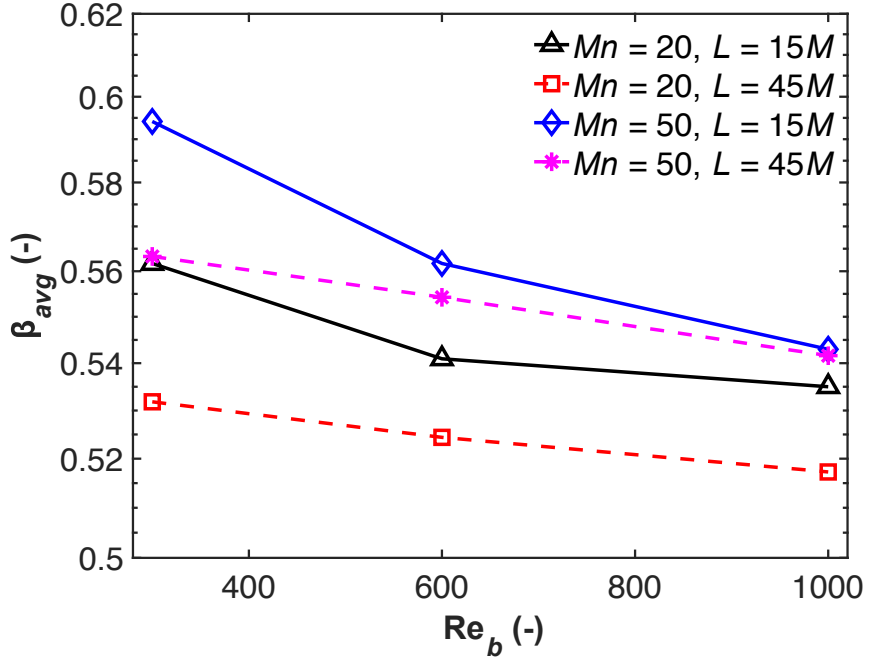


Figure 4.13. Volume average of β for various screen geometries, inter-screen spacing, and operating conditions.

4.3.2.2 Dissipation rate

The rate of energy dissipation can be divided into a mean flow component, ε_m , and a turbulent dissipation rate component, ε (Pope, 2001). These two components are given by Equations (4.17) and (4.18).

$$\varepsilon_m = 2\nu \langle S \rangle : \langle S \rangle = \nu |\langle S \rangle|^2 \quad (4.17)$$

$$\varepsilon = 2\nu \langle s' : s' \rangle \quad (4.18)$$

$$s' = \frac{1}{2} (\nabla \vec{u}' + (\nabla \vec{u}')^T) \quad (4.19)$$

where $\langle S \rangle$ and s' are the mean and fluctuating rates of strain.

Hence, the total energy dissipation rate, ε_T , is the summation of these two terms as shown in Equation (4.20) (Forde, 2012; Lane, 2015). It is worth mentioning that the contribution of the mean flow term to the total dissipation rate decreases as turbulence levels increase.

$$\varepsilon_T = \varepsilon_m + \varepsilon \quad (4.20)$$

Figure 4.14 shows the variation of the total dissipation rate around the 3rd screen element for $Mn = 50$ at $Re_b = 600$. This figure also shows the individual contribution of the mean flow and turbulent components. It is clear from the plots that the dissipation of the mean flow, ε_m , contributes the most to the total dissipation rate, ε_T near the screen region. This is expected because ε_m is a function of the strain rate (cf. Equation (4.17)) which is maximum in the vicinity of the screen due to the major changes in the mean velocity gradients (cf. Figure 4.9). Furthermore, the turbulent dissipation rate, ε , has its highest values immediately downstream of the screen, and gradually decays thereafter. This is in line with the findings reported by various authors (Groth and Johansson, 1988; Laws and Livesey, 1978; Roach, 1986). In addition, the plots clearly show that ε_m has a faster decay as compared to ε with the turbulent energy dissipation being much larger than the mean flow contribution. It was also found that the inter-screen spacings investigated in the current study had no impact on the dissipation rates as its magnitude diminishes by about two-orders of magnitude around $7.5M$ downstream of the screen.

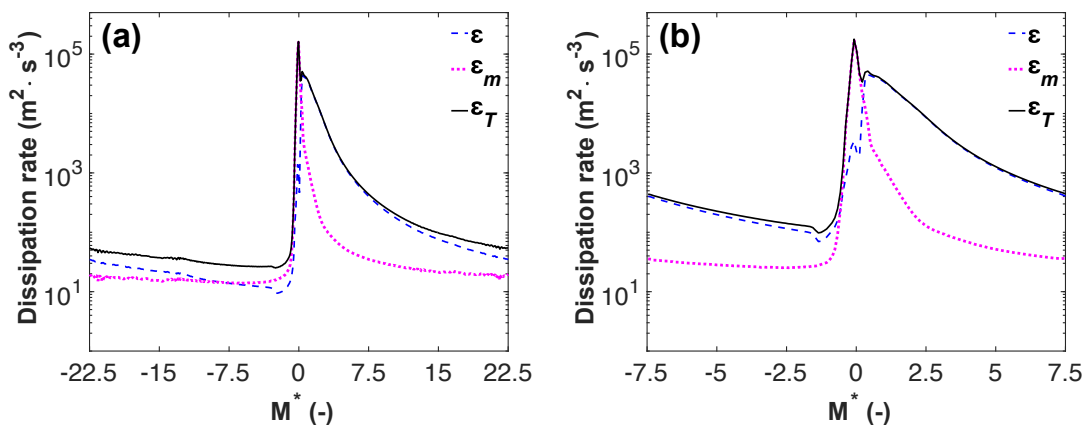


Figure 4.14. Plots of the total dissipation rate and its various components around the 3rd screen for $Mn = 50$ at $Re_b = 600$. (a) $L = 45M$ and (b) $L = 15M$.

Figure 4.15 presents the contribution of the various components of the dissipation rate to its total value. These components were evaluated around the 3rd mixer element for $L = 15M$ at various operating conditions and different screen geometries. This figure clearly shows that the contribution of the mean flow dissipation cannot be overlooked as it contributes significantly to the total dissipation rate. As previously mentioned, the contribution of the turbulence dissipation rate increases with an increasing Re_b . For the cases presented in Figure 4.15, the maximum contribution of the mean flow dissipation rate was for the coarsest mesh at the lowest Re_b value (i.e., 42% of ε_T).

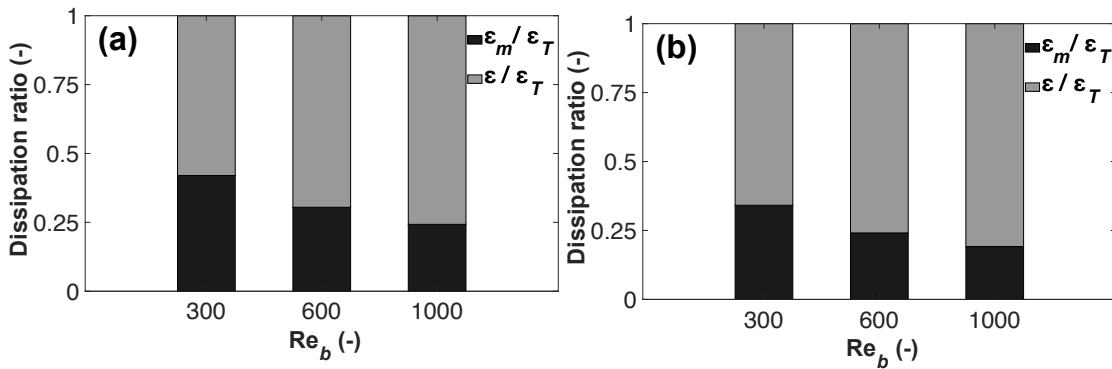


Figure 4.15. Ratio of dissipation rate components with respect to the total dissipation rate at $L = 15M$ at different operating conditions for (a) $Mn = 20$ and (b) $Mn = 50$.

Experimentally, the total dissipation rate can be computed from the ratio of the required pumping power per unit mass as shown in Equation (4.21).

$$\varepsilon_{T,exp} = \frac{\Delta p_{screen} \cdot U_{avg}}{\rho \cdot L} \quad (4.21)$$

Similarly to the pressure drop validation in this work, the experimental volume average values were obtained using pressure drop data obtained from the correlations of Azizi (Azizi, 2019) and Kurian and Fransson (Kurian and Fransson, 2009) given by

Equations (4.8) and (4.9), respectively. The CFD predictions, calculated using Equation (4.20), accurately predicted the experimental values with a maximum relative error of 10.2 % if $\varepsilon_{T,exp}$ was evaluated based on Equation (4.8) and 16.2% if $\varepsilon_{T,exp}$ was evaluated based on Equation (4.9).

4.3.2.2.1 Modeling the turbulent dissipation rate

Bourne and Lips (Bourne and Lips, 1991) and Stewart and Huq (Stewart and Huq, 2006) described the decay of the grid generated turbulence using power laws. Equation (4.22) presents the decay of turbulent kinetic energy in the streamwise direction (Pope, 2001).

$$\frac{k}{U_{avg}^2} = C_1 \left[\frac{Z}{M} - \left(\frac{Z}{M} \right)_0 \right]^{-n} \quad (4.22)$$

where C_1 is the amplitude, $(z/M)_0$ is the virtual origin of the turbulence decay, and n is the decay exponent. Using the definition $\varepsilon = -dk/dt$ along with Taylor hypothesis, the decay of ε can be easily derived from the decay of turbulent kinetic energy using $\varepsilon = -U_{avg} dk/dz$ (Torrano et al., 2015). Hence, the turbulence decay equation could be represented by Equation (4.23).

$$\varepsilon = \frac{n C_1 U_{avg}^3}{M} \left[\frac{Z}{M} - \left(\frac{Z}{M} \right)_0 \right]^{-(n+1)} \quad (4.23)$$

In their attempt to simulate multiphase flows through screen-type static mixers, Azizi and Al Taweel (Azizi and Al Taweel, 2011a) presented a one-dimensional approach to calculate the total energy dissipation rate downstream of a screen. They

hypothesized that the energy dissipation rate remains constant up to a distance of $0.8M$ at which the decay starts. The latter was described by extending the use of the homogeneous and isotropic turbulence decay equation to this anisotropic region adjacent to the screen. Accordingly, they predicted the total dissipation rate, ε_T , using Equation (4.24) and fixed the decay origin to point $z = 0.8M$, and the decay exponent, $n = 1.32$ where $C_1 = 3/(2C_2)$.

$$\varepsilon = \frac{3 n U_{avg}^3}{2 M C_2} \left[\frac{Z}{M} - \left(\frac{Z}{M} \right)_0 \right]^{-(n+1)} \quad (4.24)$$

$$C_2 = 1.304 \times M^{2.857} \times b^{-2.599} \quad (4.25)$$

where C_2 is the decay coefficient.

Figure 4.16 compares the CFD predictions to the profiles predicted by the approach of Azizi and Al Taweel (Azizi and Al Taweel, 2011a), at different Re_b values for $L = 45M$. In this figure, the total dissipation rate is plotted against the normalized distance, M^* , after the 3rd screen in the region of $0.8 \leq M^* \leq 40$. It is clear from the plots that the CFD predictions compares well with the prediction of Azizi and Al Taweel (Azizi and Al Taweel, 2011a) especially for the screen with $Mn = 50$. In addition, the two approaches were comparable up to $M^* = 10$ when the coarse screen was used (i.e., $Mn = 20$).

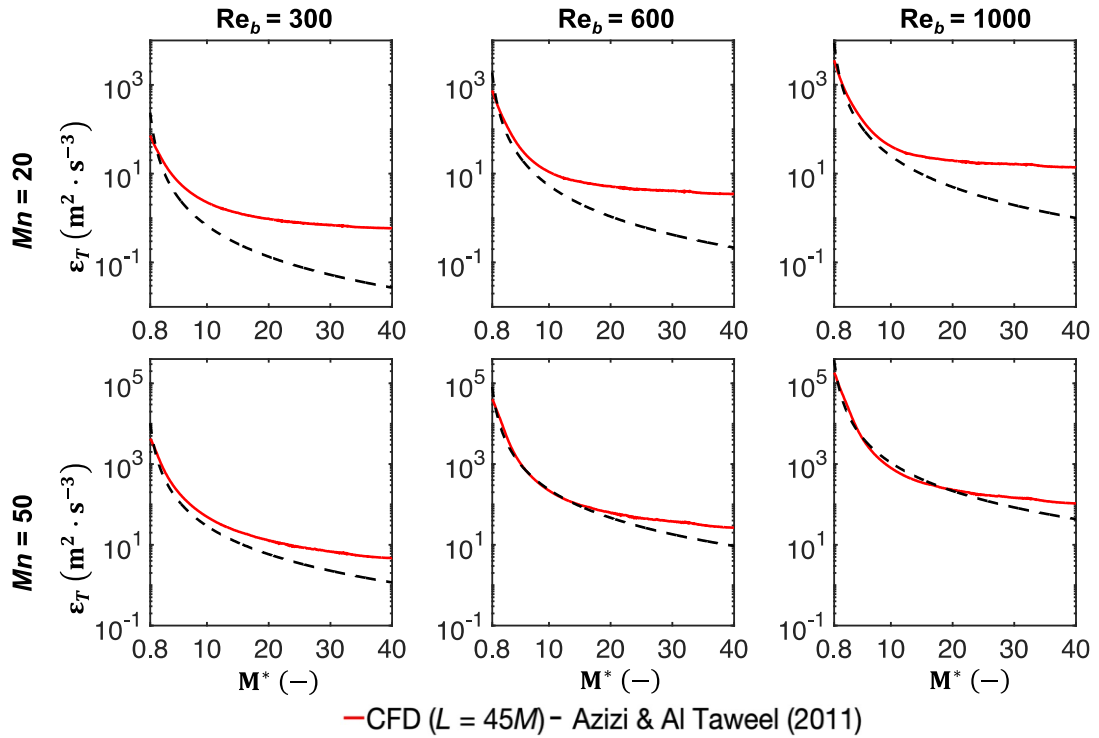


Figure 4.16. Total dissipation rate plotted against normalized axial distance M^* after 3rd screen starting from $M^* = 0.8$ up to $M^* = 40$ for $Mn = 20$ and $Mn = 50$ for $L = 45M$ at various operation conditions.

4.3.3 Macro-mixing characterization

To characterize macro-mixing in screen-type static mixers, residence time distributions (RTD) were assessed for a pipe section containing 4 screens. In this approach, the screens were placed at a fixed distance that is function of the pipe diameter, D , and not the mesh size as was used earlier. In addition, the flow conditions were varied based on the pipe Reynolds number, Re_{pipe} . These changes were implemented so residence times are independent of the screen geometry when the flow velocity is changed. The inter-screen spacing was set to $4D$ and the operating conditions were set to $Re_{pipe} = 5,000$ ($U_{avg} = 0.396 \text{ m} \cdot \text{s}^{-1}$) and $Re_{pipe} = 30,000$ ($U_{avg} = 2.374 \text{ m} \cdot \text{s}^{-1}$).

The species transport model available in ANSYS Fluent[®] v.18.2 was used to solve the species transport equation represented by Equation (4.26) (González-Juárez et al., 2017; Li et al., 2010). This model predicts the local mean mass fraction of each species, Y_l , resulting from Reynolds averaging, by solving the transport equation represented by the convection – diffusion for the l^{th} species (ANSYS, 2017).

$$\frac{\partial \rho Y_l}{\partial t} + \nabla \rho \langle \vec{U} \rangle Y_l = -\nabla \cdot \left[-\left(\rho D_{l,m} + \frac{\mu_t}{Sc_t} \right) \nabla Y_l \right] \quad (4.26)$$

where $D_{l,m}$ is the mass diffusion coefficient of species l in the mixture, m , μ_t is the turbulent viscosity, Sc_t is the Schmidt number given by $Sc_t = (\mu_t / \rho \cdot D_t)$, and D_t is the turbulent diffusivity. The Sc_t was kept at the default value of 0.7. This value is commonly used by several authors (Coroneo et al., 2012; Hartmann et al., 2006; Montante et al., 2016). It should be mentioned that $D_{l,m}$ was set to 2.229×10^{-9} , which represents the self-diffusion coefficient of water at a temperature of 25°C (González-Juárez et al., 2017).

For more information about the method used for obtaining the RTD, the reader is referred to the works of (Adeosun and Lawal, 2009; Li et al., 2010; Ramesh and Nilesh, 2015; Stec and Synowiec, 2017a). The transient simulation was carried out until the entire amount of the tracer washed out from the system (Stec and Synowiec, 2017a). The time step was evaluated such that it allows the species front, at maximum, to spread out approximately less than one grid cell size (Li et al., 2010). It should be mentioned that, for the species transport equation, the discretization of the transient term was done using the 2nd order implicit scheme (Adeosun and Lawal, 2009; González-Juárez et al., 2017) while the spatial discretization was done using the QUICK scheme (González-Juárez et al., 2017). Moreover, by proper selection of the

maximum number of iterations per step, the scaled species residuals dropped to an order $< 10^{-6}$ within each time step.

A grid independence test based on the aforementioned GCI method was performed at $Re_{pipe} = 30,000$ through monitoring the mean residence time, t_m , and the variance of the distribution, σ .

For reference, the time steps for $Mn = 20$ and $Mn = 50$ were set to 5.6×10^{-4} and 2.4×10^{-4} s, respectively, at $Re_{pipe} = 5,000$ and were set to 9.6×10^{-5} and 4.4×10^{-5} s at $Re_{pipe} = 30,000$.

4.3.3.1 Effect of varying screen geometry and operating conditions

The mean residence time computed using CFD was compared to the theoretical residence time that is computed as the ratio of the reactor volume, V , to the volumetric flow rate, Q ($\tau = V/Q$). The maximum percentage difference between the results was found to be 1% indicating that neither dead zones nor channeling/bypassing exist in these systems.

The effect of screen geometry was then assessed through normalized RTDs.. Figure 4.17 presents the normalized RTD function, $E(\theta)$, for $Re_{pipe} = 5,000$ and 30,000 for an empty pipe and another equipped with the screen mixers. These plots were recorded $2D$ downstream of the 3rd mixer element.

It is clear from these plots that screens, regardless of their geometry, alter the RTD as compared to an empty pipe with the extent of modification being a function of the screen geometry and the flow velocity. The plots clearly show that the effect of changing the screen geometry is not as pronounced at low flow velocities in contrast with the large differences at higher flow velocities. The narrower distribution of $E(\theta)$ for the finer mesh is an indication that the flow is approaching plug flow conditions.

This is in line with the findings of Juárez et al. (González-Juárez et al., 2017) who used multi-orifice baffled tubes as a static mixer and showed that the higher the number of orifices (similar to the finer woven mesh in the present study) the narrower is $E(\theta)$.

This effect is better illustrated when considering the normalized cumulative distribution function curves, $F(\theta)$, which are also shown in Figure 4.17. One cannot but notice how the presence of screens renders the flow closer to a plug flow with the effect more pronounced at higher velocities for the finer screens. These findings are also in line with the experimental observations of (Abou Hweij and Azizi, 2015) who reported lower axial dispersion coefficients when using screens (regardless of their geometry, number, and inter-screen spacing) as compared to empty pipe flows.

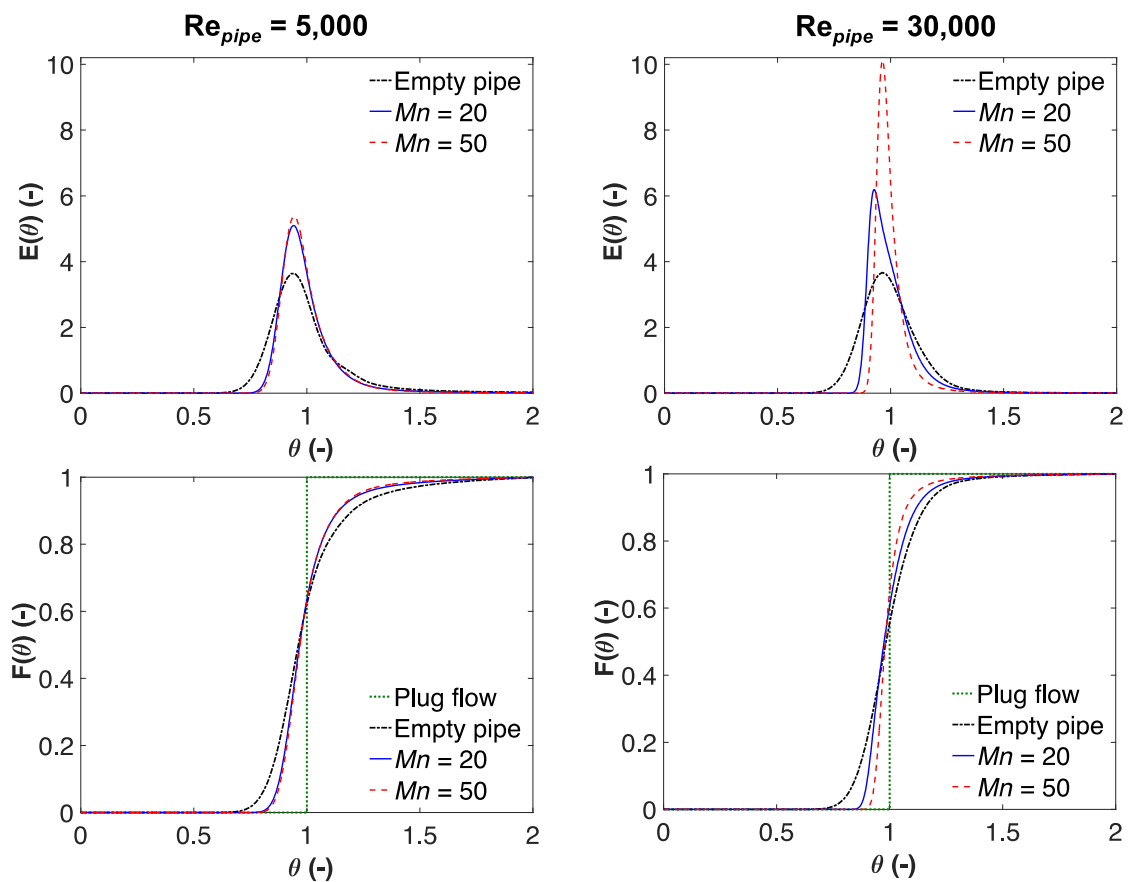


Figure 4.17. Effect of screen geometry and operating conditions on $E(\theta)$ and $F(\theta)$ for both screen geometries at and $Re_{pipe} = 5,000$ and $30,000$.

4.4 Conclusion

Screen-type static mixers have been successfully used to intensify gas-liquid and liquid-liquid dispersion and mass transfer operations, but their design relied to a certain degree on know-how and empiricism. Although the dynamics of flows through woven meshes are well investigated in the literature for the case of unbounded flows such as in wind tunnels, no previous study has considered the dynamics when the flow is bounded by walls where several elements are used in series. This work therefore presented a numerical assessment of the hydrodynamic performance of screen mixers under turbulent bounded flow conditions. It is an attempt to elucidate the impact of varying the screen design, number of screen elements, inter-screen spacing, and operating conditions on the flow field and its subsequent impact on various operational parameters. The accuracy of the numerical results was validated by comparing pressure drop predictions to empirical correlations.

The analysis of the velocity field showed that the flow is three-dimensional especially in the regions near the wall where the transverse components become significant and their impact on the flow cannot be neglected. The presence of screens also altered the well-known turbulent velocity profile by rendering it flatter both up- and down- stream of the mixer. It should be noted that the finer woven meshes showed higher local velocity near the wall than at the centerline downstream of the screen and this “overshoot” was sustained until a considerable distance downstream (that is a function of flow velocity and mesh number). This was in line with the experimental observations published in the open literature.

A qualitative and a quantitative assessment of the velocity spatial gradients were also undertaken by studying the strain rate, vorticity, and extensional efficiency. The

studies indicated that these parameters were significant near the screen wires and pipe walls. In addition, the analysis of the extensional efficiency highlighted the high dispersive mixing capability of the screens and gave an insight on how to design systems that maximize the dispersive effect within their volumes. In addition, the energy dissipation rate was analyzed, and it was shown that the mean flow dissipation rate cannot be neglected under the common flow conditions for these screens as static mixers. This is because it constituted a sizeable component of the total dissipation rate. Finally, RTD studies also showed that near plug flow conditions were attainable through the use of fine meshes especially at high velocities.

4.5 Nomenclature

b	Wire diameter	mm
C_1	Amplitude	-
C_2	Decay coefficient	-
D	Pipe diameter	mm
D_t	Turbulent diffusivity	$\text{m}^2 \cdot \text{s}^{-2}$
$D_{l,m}$	Mass diffusion coefficient of species l in mixture m	$\text{m}^2 \cdot \text{s}^{-2}$
E	Residence time distribution function	s^{-1}
F	Cumulative residence time distribution function	-
I	Identity matrix	-
k	Turbulent kinetic Energy	$\text{m}^2 \cdot \text{s}^{-2}$
K_s	Pressure loss coefficient	-
l	Species	
L	Inter-screen spacing	mm
m	Mixture	

M	Mesh size	mm
M^*	Normalized axial distance based on mesh size, M	-
Mn	Mesh number	-
N_s	Number of screen elements in the pipe	-
N_e	Number of grid cells	-
n	Decay exponent	-
p	Mean gauge static pressure resulting from Reynolds averaging	Pa
p_{in}	Area weighted average gauge static pressure at inlet	Pa
p_{out}	Area weighted average gauge static pressure at outlet	Pa
Q	Volume flow rate	$\text{m}^3 \cdot \text{s}^{-1}$
Sc_t	Schmidt number	-
$\langle S \rangle$	Mean strain rate tensor	s^{-1}
$ \langle S \rangle $	Magnitude of mean strain rate tensor	s^{-1}
s'	Fluctuating strain rate tensor	s^{-1}
t_m	Mean residence time	s
t	Tracer species	-
\vec{U}	Instantaneous velocity vector	$\text{m} \cdot \text{s}^{-1}$
$\langle \vec{U} \rangle$	Mean velocity vector resulting from Reynolds averaging	$\text{m} \cdot \text{s}^{-1}$
U_{avg}	Average velocity	$\text{m} \cdot \text{s}^{-1}$
u	Component of the mean velocity in the X direction	$\text{m} \cdot \text{s}^{-1}$
\vec{u}'	Fluctuating velocity vector	$\text{m} \cdot \text{s}^{-1}$
u^*	Normalized component of the mean velocity in the X direction	-
V	Domain Volume	m^3
v	Component of the mean velocity in the Y direction	$\text{m} \cdot \text{s}^{-1}$

v^*	Normalized component of the mean velocity in the Y direction	-
w	Component of the mean velocity in the Z direction	$m \cdot s^{-1}$
w^*	Normalized component of the mean velocity in the Z direction	-
X	Distance away from the axis (Cartesian coordinates)	mm
Y	Distance away from the axis (Cartesian coordinates)	mm
y^+	Dimensionless wall distance	-
Y_l	Mean species mass fraction resulting from Reynolds averaging	-
Z	Axial distance (Cartesian coordinates)	mm
Z^*	Normalized axial distance	-
Δp_o	Static pressure drop in an empty pipe	Pa
Δp_{screen}	Static pressure drop across a screen	Pa

Greek symbols

α	Percent opening area	%
β	Extensional efficiency	-
ε	Dissipation of turbulent kinetic energy	$m^2 \cdot s^{-3}$
ε_m	Dissipation of mean flow	$m^2 \cdot s^{-3}$
ε_T	CFD total dissipation	$m^2 \cdot s^{-3}$
$\varepsilon_{T,Exp}$	Experimental total dissipation	$m^2 \cdot s^{-3}$
ρ	Density	$kg \cdot m^{-3}$
$\langle \Omega \rangle$	Mean vorticity tensor	s^{-1}
$ \langle \Omega \rangle $	Magnitude of mean vorticity tensor	s^{-1}
μ	Dynamic viscosity	$Pa \cdot s$
μ_t	Turbulent viscosity	$Pa \cdot s$
σ	Standard deviation	s

θ	Normalized mean residence time	-
τ	Theoretical mean residence time	s
$\langle \vec{\omega} \rangle$	Vorticity vector	s ⁻¹

Dimensionless Group

Re_b	Wire Reynolds number, $\rho Ub/\mu$
Re_{pipe}	Pipe Reynolds number, $\rho UD/\mu$

Abbreviations

CFD	Computational Fluid Dynamics
FVM	Finite volume method
GCI	Grid Convergence Index
MRE	Mean relative error
RTD	Residence time distribution
STSM	Screen Type Static Mixer

4.6 Acknowledgments

The authors would like to acknowledge the financial support of both the Lebanese National Council for Scientific Research (CNRS-L) and the American University of Beirut through their University Research Board (URB) and their Research Computing Team.

4.7 References

- Abou-Hweij, W., Azizi, F., 2020. CFD simulation of wall-bounded laminar flow through screens. Part I: Hydrodynamic characterization. *Eur. J. Mech. B/Fluids* 84, 207–232. <https://doi.org/10.1016/j.euromechflu.2020.06.008>
- Abou Hweij, K., Azizi, F., 2015. Hydrodynamics and residence time distribution of liquid flow in tubular reactors equipped with screen-type static mixers. *Chem. Eng. J.* 279, 948–963. <https://doi.org/10.1016/j.cej.2015.05.100>
- Abou Hweij, W., Azizi, F., 2020. CFD Simulation of Wall-Bounded Laminar Flow

- Through Screens: Part II – Mixing Characterization. Proc. ASME 2020 Fluids Eng. Div. Summer Meet. FEDSM2020 V003T05A01, 1–10.
<https://doi.org/10.1115/FEDSM2020-20120>
- Adeosun, J.T., Lawal, A., 2009. Numerical and experimental studies of mixing characteristics in a T-junction microchannel using residence-time distribution. Chem. Eng. Sci. 64, 2422–2432. <https://doi.org/10.1016/j.ces.2009.02.013>
- Al Taweel, A.M., Azizi, F., Sirijeerachai, G., 2013. Static mixers: Effective means for intensifying mass transfer limited reactions. Chem. Eng. Process. Process Intensif. 72, 51–62. <https://doi.org/10.1016/j.cep.2013.08.009>
- Al Taweel, A.M., Chen, C., 1996. A novel static mixer for the effective dispersion of immiscible liquids. Chem. Eng. Res. Des.
- Al Taweel, A.M., Li, C., Gomaa, H.G., Yuet, P., 2007. Intensifying mass transfer between immiscible liquids: Using screen-type static mixers. Chem. Eng. Res. Des. 85, 760–765. <https://doi.org/10.1205/cherd06180>
- Al Taweel, A.M., Yan, J., Azizi, F., Odedra, D., Gomaa, H.G., 2005. Using in-line static mixers to intensify gas-liquid mass transfer processes. Chem. Eng. Sci. 60, 6378–6390. <https://doi.org/10.1016/j.ces.2005.03.011>
- ANSYS, 2017. Ansys Fluent Theory Guide, v.18.2. ANSYS Inc., USA.
- ANSYS, 2014. ANSYS – Turbulence Modelling and the Law of the Wall: Tutorial. ANSYS Inc., USA 1–48.
- Azizi, F., 2019. On the pressure drop of fluids through woven screen meshes. Chem. Eng. Sci. 207, 464–478. <https://doi.org/10.1016/j.ces.2019.06.046>
- Azizi, F., Abou Hweij, K., 2017. Liquid-Phase Axial Dispersion of Turbulent Gas–Liquid Co-Current Flow Through Screen-Type Static Mixers. AIChE J. 63, 1390–1403. <https://doi.org/10.1002/aic>
- Azizi, F., Al Taweel, A.M., 2015. Mass Transfer in an Energy-Efficient High-Intensity Gas-Liquid Contactor. Ind. Eng. Chem. Res. 54, 11635–11652. <https://doi.org/10.1021/acs.iecr.5b01078>
- Azizi, F., Al Taweel, A.M., 2011. Hydrodynamics of liquid flow through screens and screen-type static mixers. Chem. Eng. Commun. 198, 726–742. <https://doi.org/10.1080/00986445.2011.532748>
- Bailey, B.J., Montero, J.J., Perez Parra, J., Robertson, A.P., Baeza, E., Kamaruddin, R., 2003. Airflow Resistance of Greenhouse Ventilators with and without Insect Screens. Biosyst. Eng. 86, 217–229. [https://doi.org/10.1016/S1537-5110\(03\)00115-6](https://doi.org/10.1016/S1537-5110(03)00115-6)
- Belhout, C., Bouzit, M., Menacer, B., Kamla, Y., Ameer, H., 2020. Numerical Study of Viscous Fluid Flows in a Kenics Static Mixer. Mechanicka 26, 206–211.
- Bourne, J.R., Lips, M., 1991. Micromixing in grid-generated turbulence: theoretical analysis and experimental study. Chem. Eng. J. 47, 155–162.
- Celik, I.B., Ghia, U., Roache, P.J., Freitas, C.J., Coleman, H., Raad, P.E., 2008. Procedure for estimation and reporting of uncertainty due to discretization in CFD applications. J. Fluids Eng. Trans. ASME 130, 0780011–0780014.

<https://doi.org/10.1115/1.2960953>

- Chen, C., 1996. Dispersion and coalescence in static mixers.
- Coroneo, M., Montante, G., Paglianti, A., 2012. Computational fluid dynamics modeling of corrugated static mixers for turbulent applications. *Ind. Eng. Chem. Res.* 51, 15986–15996. <https://doi.org/10.1021/ie300398z>
- Costa, S.C., Barrutia, H., Esnaola, J.A., Tutar, M., 2013. Numerical study of the pressure drop phenomena in wound woven wire matrix of a Stirling regenerator. *Energy Convers. Manag.* 67, 57–65. <https://doi.org/10.1016/j.enconman.2012.10.014>
- Forde, O.O., 2012. Analysis of the Turbulent Energy Dissipation 56.
- Ghanem, A., Lemenand, T., Della, D., Peerhossaini, H., 2013. Chemical Engineering Research and Design Static mixers : Mechanisms , applications , and characterization methods – A review. *Chem. Eng. Res. Des.* 92, 205–228. <https://doi.org/10.1016/j.cherd.2013.07.013>
- González-Juárez, D., Solano, J.P., Herrero-Martín, R., Harvey, A.P., 2017. Residence time distribution in multiorifice baffled tubes: A numerical study. *Chem. Eng. Res. Des.* 118, 259–269. <https://doi.org/10.1016/j.cherd.2016.12.008>
- Green, S.I., Wang, Z., Waung, T., Vakil, A., 2008. Simulation of the flow through woven fabrics. *Comput. Fluids* 37, 1148–1156. <https://doi.org/10.1016/j.compfluid.2007.10.013>
- Groth, J., Johansson, A. V., 1988. Turbulence reduction by screens. *J. Fluid Mech.* 197, 139–155. <https://doi.org/10.1017/S0022112088003209>
- Habchi, C., Azizi, F., 2018. Heat transfer and turbulent mixing characterization in screen-type static mixers. *Int. J. Therm. Sci.* 134, 208–215. <https://doi.org/10.1016/j.ijthermalsci.2018.08.016>
- Habchi, C., Lemenand, T., Valle, D. Della, Peerhossaini, H., 2010. Turbulent mixing and residence time distribution in novel multifunctional heat exchangers-reactors. *Chem. Eng. Process. Process Intensif.* 49, 1066–1075. <https://doi.org/10.1016/j.cep.2010.08.007>
- Haddadi, M.M., Hosseini, S.H., Rashtchian, D., Ahmadi, G., 2019. CFD modeling of immiscible liquids turbulent dispersion in Kenics static mixers: Focusing on droplet behavior. *Chinese J. Chem. Eng.* 28, 348–361. <https://doi.org/10.1016/j.cjche.2019.07.020>
- Haddadi, M.M., Hosseini, S.H., Rashtchian, D., Olazar, M., 2020. Comparative analysis of different static mixers performance by CFD technique: An innovative mixer. *Chinese J. Chem. Eng.* 28, 672–684. <https://doi.org/10.1016/j.cjche.2019.09.004>
- Hartmann, H., Derksen, J.J., Akker, H.E.A. van den, 2006. Mixing Times in a Turbulent Stirred Tank by Means of LES. *AIChE J.* 52, 3696–3706. <https://doi.org/10.1002/aic>
- Heniche, M., Tanguy, P.A., Reeder, M.F., Fasano, J.B., 2005. Numerical investigation of blade shape in static mixing. *AIChE J.* 51, 44–58. <https://doi.org/10.1002/aic.10341>

- Hinze, J.O., 1975. Turbulence. McGraw-Hill – New York.
- Hobbs, D.M., Muzzio, F.J., 1998. Reynolds number effects on laminar mixing in the Kenics static mixer. *Chem. Eng. J.* 70, 93–104. [https://doi.org/10.1016/S1385-8947\(98\)00065-5](https://doi.org/10.1016/S1385-8947(98)00065-5)
- Hobbs, D.M., Swanson, P.D., Muzzio, F.J., 1998. Numerical characterization of low Reynolds number flow in the Kenics static mixer. *Chem. Eng. Sci.* 53, 1565–1584. [https://doi.org/10.1016/S0009-2509\(97\)00132-2](https://doi.org/10.1016/S0009-2509(97)00132-2)
- Irps, T., Kanjirakkad, V., 2016. On the interaction between turbulence grids and boundary layers. *EPJ Web Conf.* 114, 1–7. <https://doi.org/10.1051/epjconf/201611402048>
- Jegatheeswaran, S., Ein-Mozaffari, F., Wu, J., 2018. Process intensification in a chaotic SMX static mixer to achieve an energy-efficient mixing operation of non-newtonian fluids. *Chem. Eng. Process. Process Intensif.* 124, 1–10. <https://doi.org/10.1016/j.cep.2017.11.018>
- Kurian, T., Fransson, J.H.M., 2009. Grid-generated turbulence revisited. *Fluid Dyn. Res.* 41. <https://doi.org/10.1088/0169-5983/41/2/021403>
- Lane, G., 2015. Prediction the energy dissipation rate in a mechanically stirred tank. *Elev. Int. Conf. CFD Miner. Process Ind.* 7.
- Lau, Y.L., Baines, W.D., 1968. Flow of stratified fluid through curved screens. *J. Fluid Mech.* 33, 721–738. <https://doi.org/10.1017/S0022112068001643>
- Laws, E.M., Livesey, J.L., 1978. Flow Through Screens. *Annu Rev Fluid Mech* 10, 247–266. <https://doi.org/10.1146/annurev.fl.10.010178.001335>
- Leclaire, S., Vidal, D., Fradette, L., Bertrand, F., 2020. Validation of the pressure drop – flow rate relationship predicted by lattice Boltzmann simulations for immiscible liquid – liquid flows through SMX static mixers. *Chem. Eng. Res. Des.* 3, 350–368. <https://doi.org/10.1016/j.cherd.2019.10.035>
- Li, G., Mukhopadhyay, A., Cheng, C.Y., Dai, Y., 2010. Various approaches to compute fluid residence time in mixing systems. *Am. Soc. Mech. Eng. Fluids Eng. Div. FEDSM* 1, 295–304. <https://doi.org/10.1115/FEDSM-ICNMM2010-30771>
- Madhuranthakam, C.M.R., Pan, Q., Rempel, G.L., 2009. Residence time distribution and liquid holdup in Kenics® KMX static mixer with hydrogenated nitrile butadiene rubber solution and hydrogen gas system. *Chem. Eng. Sci.* 64, 3320–3328. <https://doi.org/10.1016/j.ces.2009.04.001>
- Mahammedi, A., Ameer, H., Ariss, A., 2017. Numerical Investigation of the Performance of Kenics Static Mixers for the Agitation of Shear Thinning Fluids. *J. Appl. Fluid Mech.* 10, 989–999. <https://doi.org/10.18869/acadpub.jafm.73.240.27314>
- Manas-Zloczower, I., 1994. Studies of Mixing Efficiency in Batch and Continuous Mixers.
- Mehta, R.D., 1985. Turbulent boundary layer perturbed by a screen. *AIAA J.* 23, 1335–1342. <https://doi.org/10.2514/3.9089>
- Meng, H., Han, M., Yu, Y., Wang, Z., Wu, J., 2020. Numerical evaluations on the

- characteristics of turbulent flow and heat transfer in the Lightnin static mixer. *Int. J. Heat Mass Transf.* 156. <https://doi.org/10.1016/j.ijheatmasstransfer.2020.119788>
- Meng, H., Song, M., Yu, Y., Wang, F., Wu, J., 2015. Chaotic mixing characteristics in static mixers with different axial twisted-tape inserts. *Can. J. Chem. Eng.* 93, 1849–1859. <https://doi.org/10.1002/cjce.22268>
- Meng, H., Song, M.Y., Yu, Y.F., Jiang, X.H., Wang, Z.Y., Wu, J.H., 2017. Enhancement of Laminar Flow and Mixing Performance in a Lightnin Static Mixer. *Int. J. Chem. React. Eng.* 15, 1–21. <https://doi.org/10.1515/ijcre-2016-0112>
- Meng, H., Wang, F., Yu, Y., Song, M., Wu, J., 2014. A numerical study of mixing performance of high-viscosity fluid in novel static mixers with multitwisted leaves. *Ind. Eng. Chem. Res.* 53, 4084–4095. <https://doi.org/10.1021/ie402970v>
- Middelstädt, F., Gerstmann, J., 2013. Numerical Investigations on Fluid Flow through Metal Screens. 5th Eur. Conf. Aeronaut. Sp. Sci.
- Mohand Kaci, H., Lemenand, T., Della Valle, D., Peerhossaini, H., 2009. Effects of embedded streamwise vorticity on turbulent mixing. *Chem. Eng. Process. Process Intensif.* 48, 1459–1476. <https://doi.org/10.1016/j.cep.2009.08.002>
- Montante, G., Coroneo, M., Paglianti, A., 2016. Blending of miscible liquids with different densities and viscosities in static mixers. *Chem. Eng. Sci.* 141, 250–260. <https://doi.org/10.1016/j.ces.2015.11.009>
- Okolo, P.N., Zhao, K., Kennedy, J., Bennett, G.J., 2019. Numerical assessment of flow control capabilities of three dimensional woven wire mesh screens. *Eur. J. Mech. B/Fluids* 76, 259–271. <https://doi.org/10.1016/j.euromechflu.2019.03.001>
- Owen, P.R., Zienkiewicz, H.K., 1957. The production of uniform shear flow in a wind tunnel. *J. Fluid Mech.* 2, 521–531. <https://doi.org/10.1017/S0022112057000336>
- Peschel, A., Hentschel, B., Freund, H., Sundmacher, K., 2012. Design of optimal multiphase reactors exemplified on the hydroformylation of long chain alkenes. *Chem. Eng. J.* 188, 126–141. <https://doi.org/10.1016/j.cej.2012.01.123>
- Pinker, R.A., Herbert, M.V., 1967. Pressure loss associated with compressible flow through square-mesh wire gauzes. *J. Mech. Eng. Sci.* 9, 11–23.
- Pope, S.B., 2001. *Turbulent Flows*.
- Rahmani, R.K., Keith, T.G., Ayasoufi, A., 2008. Numerical simulation of turbulent flow in an industrial helical static mixer. *Int. J. Numer. Methods Heat Fluid Flow* 18, 675–696. <https://doi.org/http://dx.doi.org/10.1108/09615530810885515>
- Rahmani, R.K., Keith, T.G., Ayasoufi, A., 2005. Three-dimensional numerical Simulation and performance study of an industrial helical static mixer. *J. Fluids Eng. Trans. ASME* 127, 467–483. <https://doi.org/10.1115/1.1899166>
- Ramesh, B., Nilesh, G., 2015. Modeling of Residence Time Distribution in FLUENT. *Ecol. Modell.* 35, 1–3.
- Roach, P.E., 1986. The generation of nearly isotropic turbulence by means of grids. *Int. J. Heat Fluid Flow* 82–92. [https://doi.org/10.1016/0142-727X\(87\)90001-4](https://doi.org/10.1016/0142-727X(87)90001-4)
- Santos, A.M., Souza, D.B., Costa, F.O., Farias, M.H., Massari, P.D.L., Araújo, S.,

- Zanirath, Y.B., 2016. Effects of screens set characteristics on the flow field in a wind tunnel. *J. Phys. Conf. Ser.* 733. <https://doi.org/10.1088/1742-6596/733/1/012001>
- Soman, S.S., Madhuranthakam, C.M.R., 2017. Effects of internal geometry modifications on the dispersive and distributive mixing in static mixers. *Chem. Eng. Process. Process Intensif.* 122, 31–43. <https://doi.org/10.1016/j.cep.2017.10.001>
- Stec, M., Synowiec, P.M., 2019. Study of fluid dynamic conditions in the selected static mixers part III—research of mixture homogeneity. *Can. J. Chem. Eng.* 97, 995–1007. <https://doi.org/10.1002/cjce.23290>
- Stec, M., Synowiec, P.M., 2017a. Study of fluid dynamic conditions in the selected static mixers part I- research of pressure drop. *Can. J. Chem. Eng.* 95, 2156–2167. <https://doi.org/10.1002/cjce.22929>
- Stec, M., Synowiec, P.M., 2017b. Study of fluid dynamic conditions in the selected static mixers part II-determination of the residence time distribution. *Can. J. Chem. Eng.* 95, 2410–2422. <https://doi.org/10.1002/cjce.22879>
- Stewart, E.J., Huq, P., 2006. Dissipation rate correction methods. *Exp. Fluids* 40, 405–421. <https://doi.org/10.1007/s00348-005-0078-5>
- Thakur, R.K., Vial, C., Nigam, K.D.P., Nauman, E.B., Djelveh, G., 2003. Static mixers in the process industries – a review. *Chem. Eng. Res. Des.* 81, 787–826. <https://doi.org/10.1205/026387603322302968>
- Torrano, I., Tutar, M., Martinez-Agirre, M., Rouquier, A., Mordant, N., Bourgoïn, M., 2015. Comparison of experimental and RANS-based numerical studies of the decay of grid-generated turbulence. *J. Fluids Eng. Trans. ASME* 137, 1–12. <https://doi.org/10.1115/1.4029726>

CHAPTER 5

DESIGN OF A NOVEL STATIC MIXER

Abstract

This study presents a design of a new static mixer. The proposed design builds on the dispersive capabilities of screen-type static mixers and suggests a method to enhance its distributive mixing performance. This was accomplished by means of inserts placed downstream of each screen element the role of which is to split the flow as well as generate additional vortices and flow perturbations necessary to promote mixing. A three-dimensional CFD model was used to investigate the hydrodynamic and mixing performance of this new mixer under turbulent flow conditions, where the pipe Reynolds number was varied between 5,000 and 30,000. The numerical model was validated experimentally by means of pressure drop data.

Compared to an empty pipe or one equipped with screens, the results showed that the new design could enhance both radial/distributive and dispersive mixing at low and high turbulence levels. This enhancement is however at the cost of additional pressure drop when compared to a screen, although its value is comparable to various commercial static mixers.

Keywords: Static mixer, Screens, CoV, mixing, extensional efficiency, pressure drop, design.

5.1 Introduction

Static mixing is fast replacing several traditional mixing units such as bubble columns, packed columns, and agitated tanks, among others. This is driven by their low operational cost, smaller reactor volumes, and enhanced safety (Al Taweel et al., 2013;

Ghanem et al., 2013; Madhuranthakam et al., 2009; Peschel et al., 2012; Thakur et al., 2003). Moreover, recent advances in computational fluid dynamics (CFD) is providing accurate predictions of their hydrodynamic and mixing performance, which makes it easier to assess their flow characteristics or study new geometries (Abou-Hweij and Azizi, 2020; Abou Hweij and Azizi, 2020; Azizi et al., 2021; Haddadi et al., 2020, 2019; Meng et al., 2020, 2015; Montante et al., 2016).

Plain woven meshes were recently used to process multiphase flows under turbulent flow conditions (Al Taweel et al., 2005). These screens (STSM) are characterized by the generation of high energy dissipation rates and elevated micro-mixing intensities in their immediate vicinity (Bourne and Lips, 1991). Because of this, they were found very efficient at promoting multiphase dispersions and mass transfer operations at low energy consumption rates (Al Taweel et al., 2013, 2007, 2005; Azizi and Al Taweel, 2015). Our previous studies detailed the hydrodynamic and mixing performance of bounded flows through screens under both laminar and turbulent flow regimes. In them, the effect of varying the screen geometry, number of screens, inter-screen spacing and operating conditions were investigated. It was found that STSM are incapable of efficiently promoting radial mixing under laminar and/or turbulent flow conditions but could provide good dispersive mixing.

Hence, this study proposes a new design that builds on this knowledge of flow through STSMs to propose modifications to enhance its distributive mixing performance. This mixer takes advantage of carefully designed inserts downstream of a woven mesh to promote radial mixing. Accordingly, the aim of this work is to numerically assess the hydrodynamic and mixing performance (both distributive and dispersive) of bounded turbulent flows through this new mixer using a Eulerian

approach. This is to be completed by analyzing the velocity contours, surface streamlines, CoV , and extensional efficiency at various operating conditions and design configurations.

5.2 Methodology

This section describes the methodology of this work. First, the new mixer geometry will be presented. This will be followed by a description of the computational domain as well as the boundary conditions and solution method.

5.2.1 Proposed mixer design

The proposed mixer design is shown schematically in Figure 5.1 and consists of a woven mesh followed by a pair of divergent inserts (or flaps) placed downstream of the screen. The geometry and various design parameters are also summarized in Table 5.1. These design parameters of the inserts can also be varied to meet various performance outcomes.

While the woven mesh can assume any geometry, in the current work, a screen characterized by a mesh opening ($M = 1.27$ mm), wire size ($b = 0.4064$ mm), fractional opening area ($\alpha = 0.462$), and mesh number ($Mn = 20$), was chosen. The mesh number, Mn , represents the number of openings per unit length (i.e., $Mn = 25.4$ mm/ M in mm). The downstream inserts (flaps) are placed normal to the flow at a distance, L_{sf} , of $D/2$. Although this length can vary to meet different performance efficiencies, it was chosen in this study as to coincide with a distance of $5M$ downstream of the screen. In addition, the main parameters that will have a direct impact on the performance of the mixer are

the length and thickness of the inserts (i.e., L_f and t_f), angle of rotation with respect to the axis of the pipe, θ_f , and the distance separating the centers of the two inserts, L_{ff} .

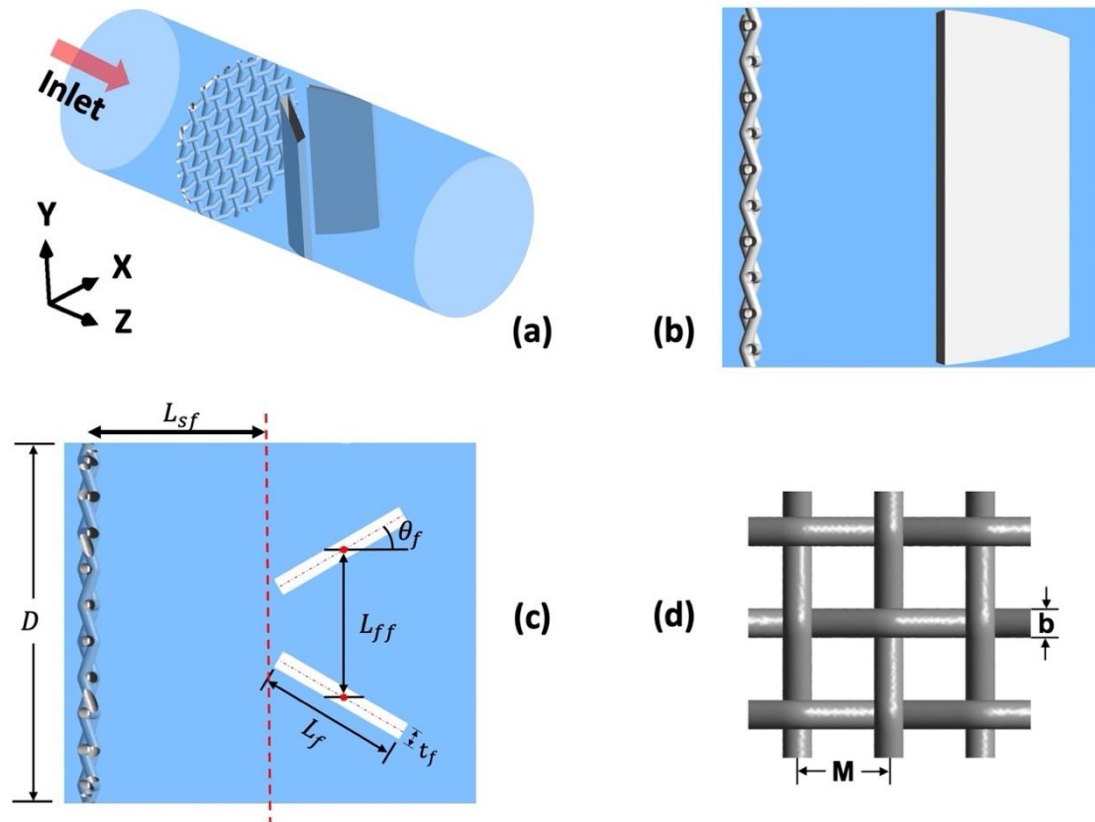


Figure 5.1. Schematic illustration of the new mixer design, (a) three-dimensional view of one mixer element, (b) side-view, (c) top view with various design parameters, and (d) section of a screen element with its geometrical characteristics.

Table 5.1. Various design parameters of the new mixer.

Design Parameter	Value
Pipe diameter, D	12.7 mm
Mesh opening, M	1.27 mm
Wire size, b	0.4064 mm
Fractional opening area, α	46.2
Flap's length, L_f	$2D/5$
Flap's thickness, t_f	0.635 mm
Flap's rotation, θ_f	30°
Inter-flap spacing, L_{ff}	$2D/5$
Inter-screen-flap spacing, L_{sf}	$D/2$

5.2.2 Computational domain

The geometry to be studied consists of a circular pipe with an inner diameter, $D = 12.7$ mm in which liquid water with constant physical properties flows ($\rho = 998.2$ kg·m⁻³; $\mu = 0.001003$ Pa·s). The computational domain is shown in Figure 5.2 and consists of 4 mixer elements placed equidistantly at $4D$ from each other in a fashion that consecutive flaps are rotated by 90° with respect to each other. It should be mentioned that an empty pipe length of $1D$ upstream of the first screen was used as an entry region and another of $5D$ was set downstream of the last screen.

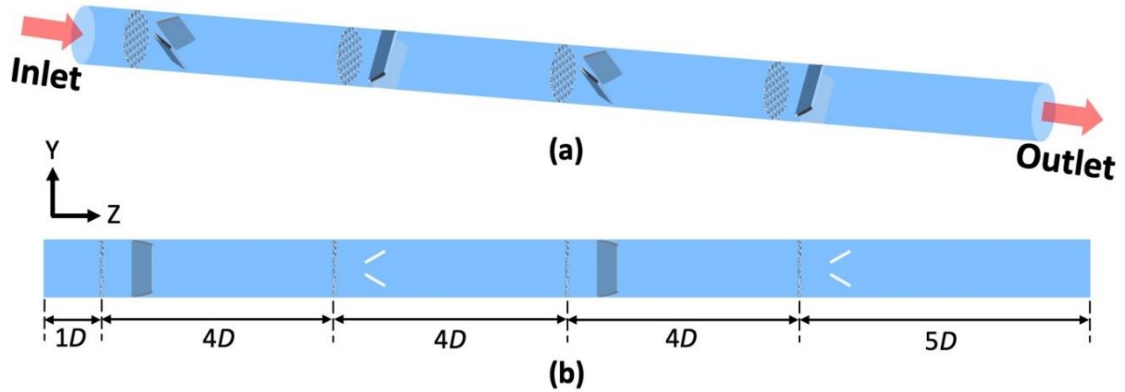


Figure 5.2. Schematic representation of the computational domain of a contactor equipped by 4 mixer elements rotated by 90° with respect to each other (a) three-dimensional view and (b) side view

Simulations were carried out by varying the pipe Reynolds number, Re_{pipe} , between 5,000 and 30,000 to create different turbulent conditions.

Table 5.2 presents these operating conditions that were selected as equidistant on a log scale, it also shows the corresponding average velocities, U_{avg} .

Table 5.2. Operating conditions based on the pipe Reynolds number (Re_{pipe}) and their corresponding average flow velocity, U_{avg} in ($m \cdot s^{-1}$)

Pipe Reynolds number, Re_{pipe}	Average velocity, U_{avg} ($m \cdot s^{-1}$)
5000	0.3956
9,100	0.72
16,500	1.3055
30,000	2.3736

The computational domain was discretized using the unstructured tetrahedral grid scheme using the ANSYS Mesher tool. Following the discretization approach presented in Chapter 4 §4.2.1, the computational domain was subdivided into 3

meshing regions, namely, the open pipe region, the near screen region which includes the inserts, and the screen region. Figure 5.3 illustrates the meshing configuration used in the current study for this new static mixer.

To account for the high gradients near solid walls i.e. near the pipe wall, near the screen surfaces, and near the walls of the inserts, several prism layers (inflation layers) were generated such that the dimensionless wall distance, y^+ , values stay as close to 1 as possible to accurately resolve the viscous sublayer (Habchi and Azizi, 2018).

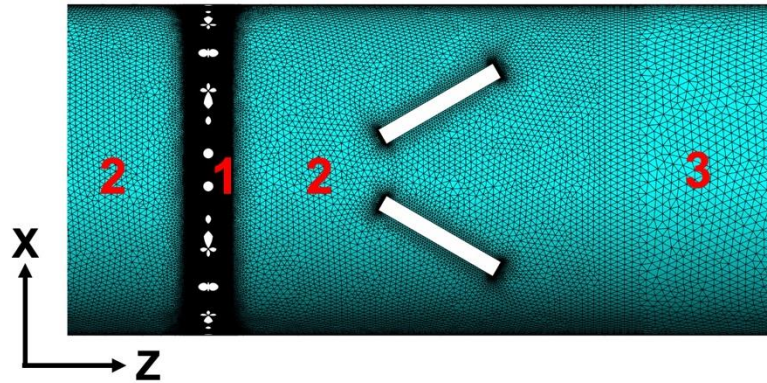


Figure 5.3. Grid discretization for the new mixer including zonal annotations. (1) Screen region, (2) Near screen region including inserts, and (3) Open pipe region.

5.2.3 *Boundary conditions and solution method*

To reduce the computational cost, the Reynolds-Averaged Navier Stokes (RANS) equations were solved for the turbulent flow. The continuity and momentum mean equations for steady incompressible and Newtonian fluid are presented in Equations (5.1) and (5.2), respectively. These equations were converted to algebraic equations using the finite volume method (FVM) which were then solved using the commercial CFD tool, ANSYS Fluent® v.18.2.

$$\nabla \cdot \langle \vec{U} \rangle = 0 \quad (5.1)$$

$$\rho \nabla \cdot \{ \langle \vec{U} \rangle \langle \vec{U} \rangle \} = -\nabla p + \mu \nabla^2 \langle \vec{U} \rangle - \rho \nabla \cdot \langle \vec{u}' \vec{u}' \rangle \quad (5.2)$$

$$\vec{U} = \langle \vec{U} \rangle + \vec{u}' \quad (5.3)$$

where $\langle \vec{U} \rangle$ and \vec{u}' are the mean and fluctuating velocity components of the instantaneous velocity \vec{U} , p is the mean static pressure resulting from Reynolds' averaging.

Using this model, the Reynolds stress tensor is assumed to be proportional to the mean velocity gradients, with the constant of proportionality being the turbulent viscosity, μ_t (Hinze, 1975). This turbulent viscosity could then be predicted using different eddy-viscosity models. In the current study, the Realizable $k-\varepsilon$ turbulence model was selected as it is suitable for complex shear flows involving rapid strain and vortices (ANSYS, 2014); the conditions that are omnipresent in the current study. While the validation of the turbulence model is outside the scope of this work, Okolo et al. (Okolo et al., 2019) recommended the use of the $k - \varepsilon$ family for the flow field investigation through woven screens. Moreover, the enhanced wall treatment model was selected in the current study to predict the flow behavior in the near-wall region (viscous sub-layer). More details about the turbulence and wall treatment models could be found in the ANSYS theory guide (ANSYS, 2017).

A fully developed flow was imposed at the inlet, while an outflow boundary condition (BC) was set at the outlet. All solid walls including the pipe wall, screen faces, and flap faces are set to the no-slip BC.

The solution methods used in the current study are summarized as follows:

- Solver: Pressure-based

- Pressure-Velocity coupling: Coupled Algorithm
- Gradient Terms: Least Square Cell Based
- Convection Terms: QUICK
- Pressure Interpolation: 2nd order

The velocity profile that was imposed at the inlet of the pipe was obtained by simulating a long empty pipe with a uniform inlet velocity profile and extracting the profile from the fully developed region. This approach resulted in an accurate solution when compared to the use of a power law profile.

5.2.4 *Mixing characterization*

Mixing can be characterized from distributive and dispersive perspectives. The former presents an overview of the spatial distribution of the fluid elements within a cross-section, while the latter reveals the breakup of fluid elements as the flow passes a mixer element.

Following the steady state assumption and a Eulerian approach, the species transport equation (Equation (5.4)), was solved to track the dispersion of tracers in water. This model will help predict the local mass fraction of each species, Y_l , resulting from Reynolds averaging, by solving the convection – diffusion equation for the l^{th} species (ANSYS, 2017).

$$\nabla \rho(\vec{U})Y_l = -\nabla \cdot \left[-\left(\rho D_{l,m} + \frac{\mu_t}{Sc_t} \right) \nabla Y_l \right] \quad (5.4)$$

where $D_{l,m}$ is the mass diffusion coefficient of species l in mixture m , μ_t is the turbulent viscosity, Sc_t is the Schmidt number given by $Sc_t = (\mu_t/\rho \cdot D_l)$, and D_l is the

turbulent diffusivity. The turbulent Schmidt number, Sc_t , was kept at the default value of 0.7. This value is commonly used by several authors (Coroneo et al., 2012; Hartmann et al., 2006; Montante et al., 2016). The tracer was given the same physical properties as the working fluid, and the diffusion coefficient was given a value of $D_{l,m} = 2.229 \times 10^{-9} \text{ m} \cdot \text{s}^{-1}$, which represents the self-diffusion coefficient of water at a temperature of 25°C (González-Juárez et al., 2017).

The spatial discretization of the convection term within the species transport equation was performed using the QUICK scheme (González-Juárez et al., 2017). In addition, scaled residuals for the continuity, momentum, and turbulence parameters were set to an order of 10^{-5} , while the convergence of the scaled species residuals was set to an order of 10^{-6} . Moreover, the standard deviation of the tracer mass fraction at the outlet was always monitored for convergence.

What follows will briefly present the theoretical background of the various methods used to quantify distributive and dispersive mixing.

5.2.4.1 Distributive mixing

5.2.4.1.1 Coefficient of Variation (CoV)

The coefficient of variation (CoV) is the most commonly used indicator to describe the intensity of segregation (Al-Hassan et al., 2021; Dbouk and Habchi, 2019). It is a statistical approach which evaluates the deviation of the mass fraction distribution at a given cross-section from its mean value. The CoV is presented in Equation (5.5).

$$CoV = \frac{\sigma_{CoV}}{\bar{Y}_t} \quad (5.5)$$

$$\sigma_{CoV} = \sqrt{\frac{1}{A} \sum_{i=1}^N (Y_{t,i} - \bar{Y}_t)^2 A_i} \quad (5.6)$$

$$\bar{Y}_t = \frac{1}{A} \sum_{i=1}^N Y_{t,i} A_i ; A = \sum_{i=1}^N A_i \quad (5.7)$$

where N , and i are the number of faces and the face index within a cross-section of area, A , respectively. $Y_{t,i}$ and A_i represent the tracer mass fraction and the area of a face i , respectively. \bar{Y}_t , and σ_{CoV} are the mean and standard deviation of the tracer mass fraction within the cross-section, respectively. It is to be noted that in the current work, \bar{Y}_t and σ_{CoV} were evaluated based on area-weighted average to account for variation of the cell area within a cross-section.

5.2.4.2 Dispersive mixing

A typical measure of the dispersive mixing is typically accomplished using the dispersive mixing coefficient given by Equation (5.8) (Manas-Zloczower, 1994). This parameter is also referred to as the extensional efficiency, which quantifies the balance between the extensional/elongational effect over rotational effect within the flow (De La Villéon et al., 1998). A value of $\beta = 1$ indicates pure elongation, $\beta = 0$ represents pure rotation, and $\beta = 0.5$ indicates simple shear flow. Therefore, good dispersive mixing is typically reflected by high values of β (Heniche et al., 2005; Meng et al., 2017, 2015).

$$\beta = \frac{|\langle S \rangle|}{|\langle S \rangle| + |\langle \Omega \rangle|} \quad (5.8)$$

where $|\langle S \rangle|$ is the magnitude of the mean strain rate tensor, $\langle S \rangle$, and $|\langle \Omega \rangle|$ is the magnitude of the mean vorticity tensor, $\langle \Omega \rangle$, and they are represented by equations (5.9) and (5.11), respectively.

$$\langle S \rangle = \frac{1}{2} \left(\nabla \langle \vec{U} \rangle + (\nabla \langle \vec{U} \rangle)^T \right) \quad (5.9)$$

$$|\langle S \rangle| = \sqrt{2 \langle S \rangle : \langle S \rangle} \quad (5.10)$$

$$\langle \Omega \rangle = \frac{1}{2} \left(\nabla \langle \vec{U} \rangle - (\nabla \langle \vec{U} \rangle)^T \right) \quad (5.11)$$

$$|\langle \Omega \rangle| = \sqrt{2 \langle \Omega \rangle : \langle \Omega \rangle} \quad (5.12)$$

5.3 Results and discussion

This section details the performance of the new mixer geometry under turbulent flow conditions. The grid independence test will first be presented, followed by the model validation and the hydrodynamic characterization of the mixer. This will be followed by a detailed description of its mixing performance.

5.3.1 Grid Independence

Grid independence tests were performed following the grid convergence index (GCI) proposed by Celik et al. (Celik et al., 2008). The GCI method presents the uncertainty in selecting a specified grid among three grid levels given that the refinement level between two consecutive grids is not lesser than 1.3 (Celik et al., 2008). In the current study, the grid independence test was performed at $Re_{pipe} = 30,000$. It should be mentioned that for the grid independence studies, only one mixer element was used when only woven meshes were employed. In contrast, two consecutive mixing elements were utilized when the new mixer geometry was being

studied. This scenario ensured the repeatability of the flow as it passes through consecutive elements.

Table 5.3 Table 4.3a presents the number of tetrahedral grid cells, $N_{e,t}$, at various grid levels for a contactor equipped with STSM and another one equipped with the new mixer. The pressure drop within the whole domain, the turbulent dissipation rate, ε , and the standard deviation of the tracer mass fraction, σ , were monitored at various zones (Zones 1 and 2 in Figure 5.3) and at several surfaces of interest for each grid level. The turbulent dissipation rate ε was monitored at $2M$, $8M$, $10M$, and $12M$ downstream of each screen, depending on the geometry. The standard deviation, σ was monitored at the pipe exit when one STSM was used but also midway and at exit when two elements of the new mixer were employed. The GCI values were evaluated for the various flow parameters and the maximum recorded GCI value among all tested parameters was only reported in Table 5.3a. This maximum GCI value was selected to show the worst-case scenario. Hence, for the new mixer, the maximum GCI value if the fine grid were to be selected is 5% and the maximum GCI value if the medium grid were to be selected is 13.4%. Therefore, the fine grid should be selected to ensure an acceptable numerical uncertainty (Al-Hassan et al., 2021; Okolo et al., 2019). This scenario was followed for the case where screens alone were used, where the fine grid was also found to render the best convergence.

To reduce the computational cost while maintaining an acceptable accuracy, the tetrahedral grids were then converted to polyhedral grids using Fluent[®] where the number of grid cells was significantly reduced (cf. fine grid in Table 4.3a, $N_{e,t}$, vs Table 4.3b, $N_{e,p}$). It should be mentioned that the relative difference between the results using

the fine tetrahedral or polyhedral grids did not exceed 9% (cf. Table 5.3Table 4.3b) for all the tested mixers at the various flow parameters.

Moreover, Table 5.3b presents the maximum y^+ value for the fine grid after conversion to polyhedral for the various mixer types where it did not exceed 3.1 indicating that the viscous sublayer was well resolved.

The numerical simulations were performed using the Octopus high performance computing (HPC) cluster available at the American University of Beirut using six parallel nodes each of 16 processors and 64GB RAM of Intel® Xeon® Processor E5-2665 @ 2.4 GHz.

Table 5.3a. Grid independence test for STSM and New mixer.

Mixer Type	Refinement Level	Number of grid cells, $N_{e,t}$	GCI %
STSM (1 pass)	Fine	17,386,766	4.3
	Medium	7,179,517	12
	Coarse	2,320,136	
New Mixer (2 passes)	Fine	39,163,454	5
	Medium	16,688,726	13.4
	Coarse	6,050,499	

Table 5.3b. Polyhedral fine grid characteristics including relative difference with respect to the tetrahedral fine grid.

Mixer Type	STSM (1 pass)	New Mixer (2 passes)
Number of fine grid cells, $N_{e,p}$	8,216,822	18,041,978
Relative difference (%)	6.8	8.6
y_{max}^+	2.43	3.01

5.3.2 Model Validation

To validate the CFD model, experimental runs to measure the pressure drop across the new mixer were performed. Tests using screens only were also conducted. These experiments were achieved in a vertical pipe, 25 mm in diameter, equipped with 4 mixer elements of either types. The spacing between two consecutive mixer elements was set to 4 pipe diameters. The pressure drop measurements were taken at points 270 mm upstream of the first screen element and 310 mm downstream of the last screen element. Two pressure transducers (Omega model PX303-050GV) were used for this purpose.

The pressure drop in a contactor equipped with a static mixer is the result of both the skin friction at the pipe wall and the pressure drop resulting from the flow through/around the mixer. Hence, the pressure drop across one mixer element was calculated using Equation (5.13)

$$\Delta p_{elt} = \frac{(p_{in} - p_{out}) - \Delta p_o}{N_{elts}} \quad (5.13)$$

where p_{in} and p_{out} are the static pressures at point measurements, and Δp_o is the empty pipe pressure drop, and N_{elts} is the number of mixer elements in the pipe.

Figure 5.4 presents the pressure drop per element of either mixer types. One cannot but notice the additional pressure drop induced using inserts downstream of the screens. The experimental results showed that for the same flow velocity, the pressure drop was increased by a factor of 3.1 for $U_{avg} \leq 1.2 \text{ m}\cdot\text{s}^{-1}$ and by a factor of 2.6 for $U_{avg} \geq 1.2 \text{ m}\cdot\text{s}^{-1}$.

The numerical and experimental pressure drop results for a STSM and the new mixer geometry are shown in Figure 5.5a and Figure 5.5b, respectively. Moreover, the pressure drop within the STSM was also evaluated using the recent correlation of Azizi (Azizi, 2019) which covers the wide range of laminar to turbulent flows. The results reveal that the numerical predictions overestimated the experimental pressure drop for most of the tested points; however, for the case of STSM, they are in close agreement with the published correlation with a maximum relative error of 5.18% and a mean relative error of 2.5%.

To better illustrate the deviation of the numerical predictions from experimental results, parity plots for both mixers were plotted in Figure 5.5c and Figure 5.5d, respectively. The results reveal that the numerical simulations predicted the experimental results within $\pm 20\%$.

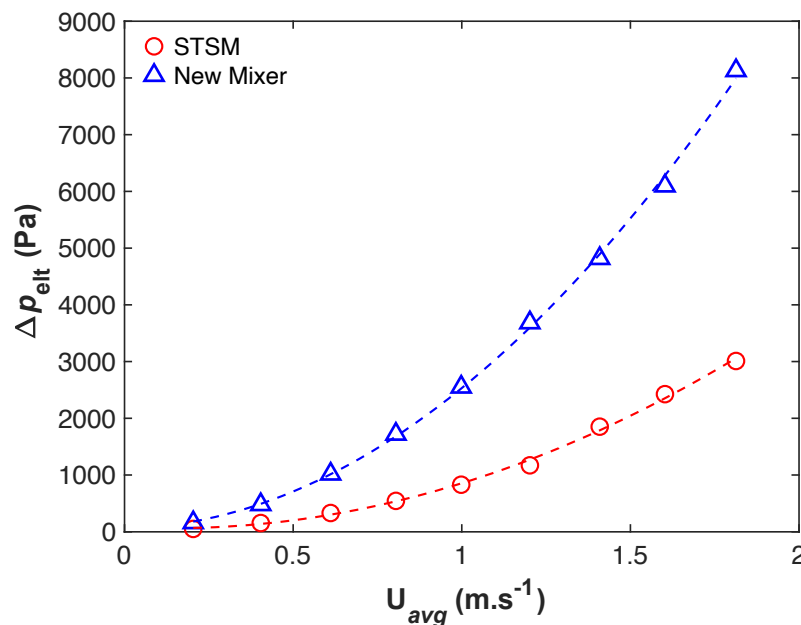
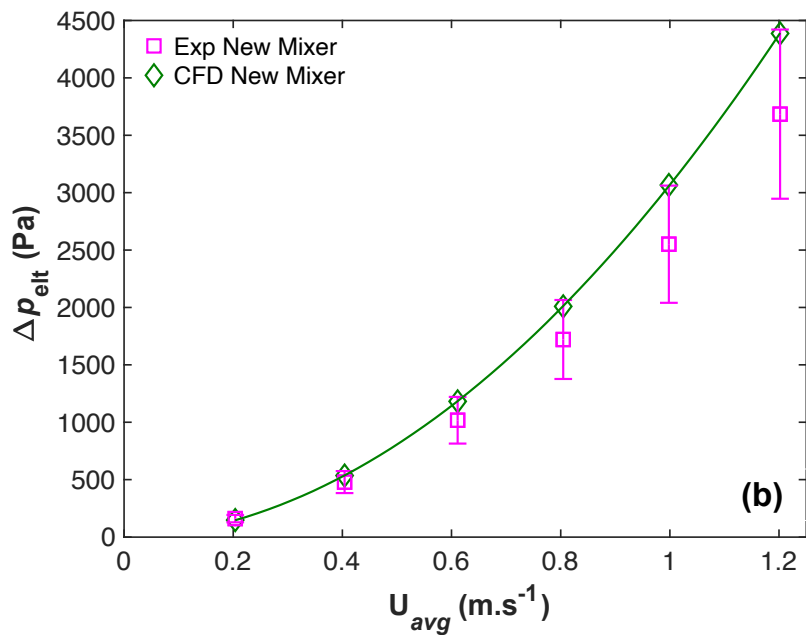
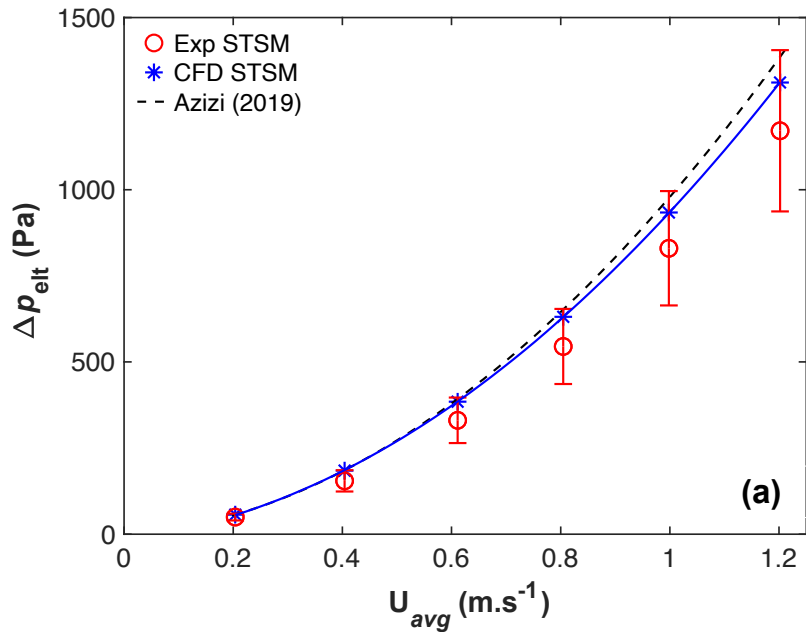


Figure 5.4. Experimental pressure drop predictions for empty pipe, STSM, and new mixer.



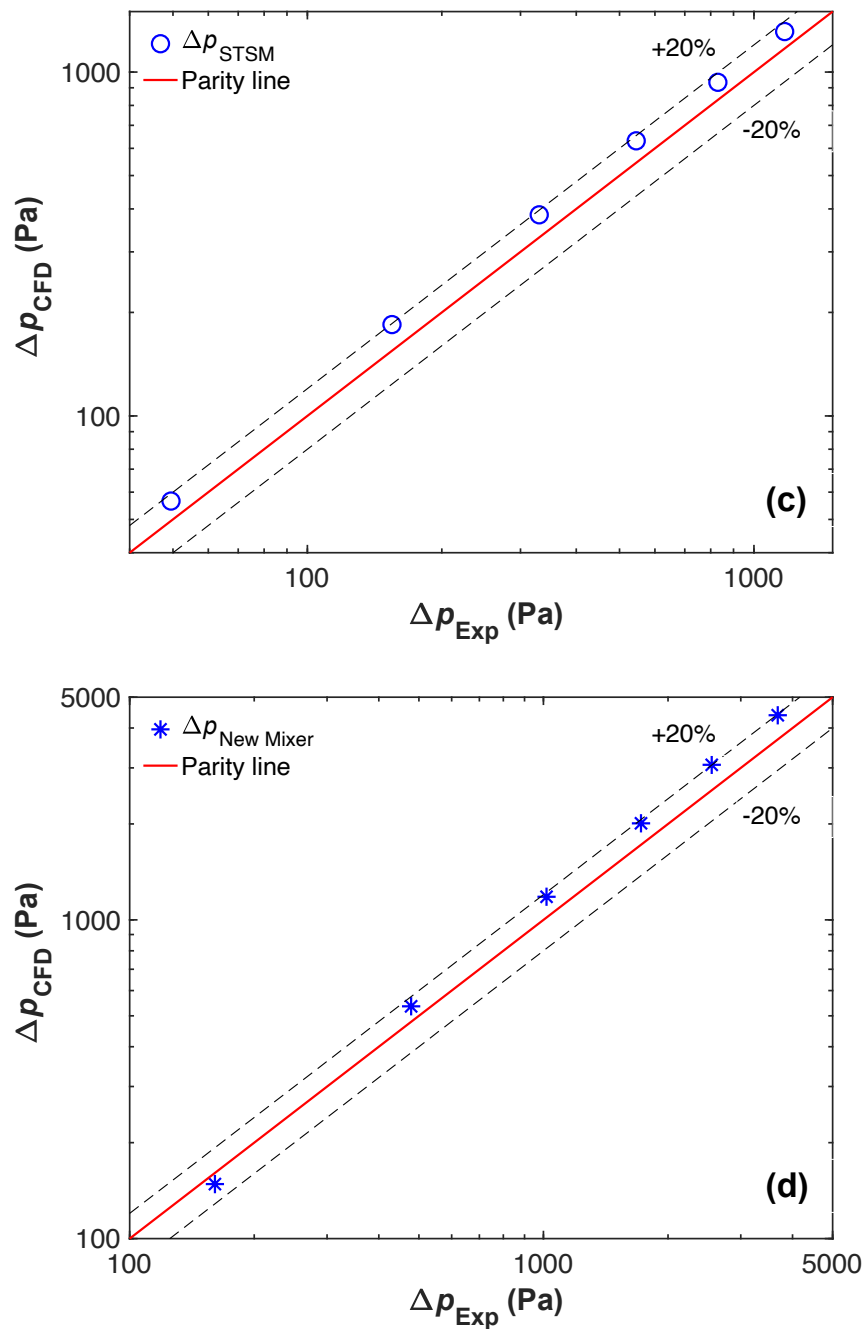


Figure 5.5. Numerical and experimental pressure drop predictions (a) STSM, (b) new mixer, (c) parity plot for STSM, and (d) parity plot for new mixer.

5.3.3 Hydrodynamic characterization

Knowledge of the velocity field helps identify regions of recirculation and flow irregularities. In the current work, the effect of adding flaps downstream of the screens was investigated in terms of velocity contours and streamlines.

5.3.3.1 Velocity field

Contour plots of the axial velocity, w , through the new mixer and screens alone are shown in Figure 5.6 at $Re_{pipe} = 16,500$ (i.e., $U_{avg} = 1.305 \text{ m}\cdot\text{s}^{-1}$). These contours are plotted along the central horizontal and vertical planes within the pipe. It should be mentioned that the axial velocity, w , is the z component of the mean velocity vector $\langle \vec{U} \rangle$. As the flow passes through a screen, it is accelerated and forms jets. The flow is further accelerated in the narrow regions located between the two inserts as well as between them and the pipe wall. In these zones of high velocity, w can reach local values that are 2.5-3 times the average flow velocity. This behavior causes some recirculation patterns which are clearly delineated in the zones of negative axial velocity (cf. Figure 5.6). This is a clear indication that the presence of these inserts should induce a noticeable improvement in radial mixing.

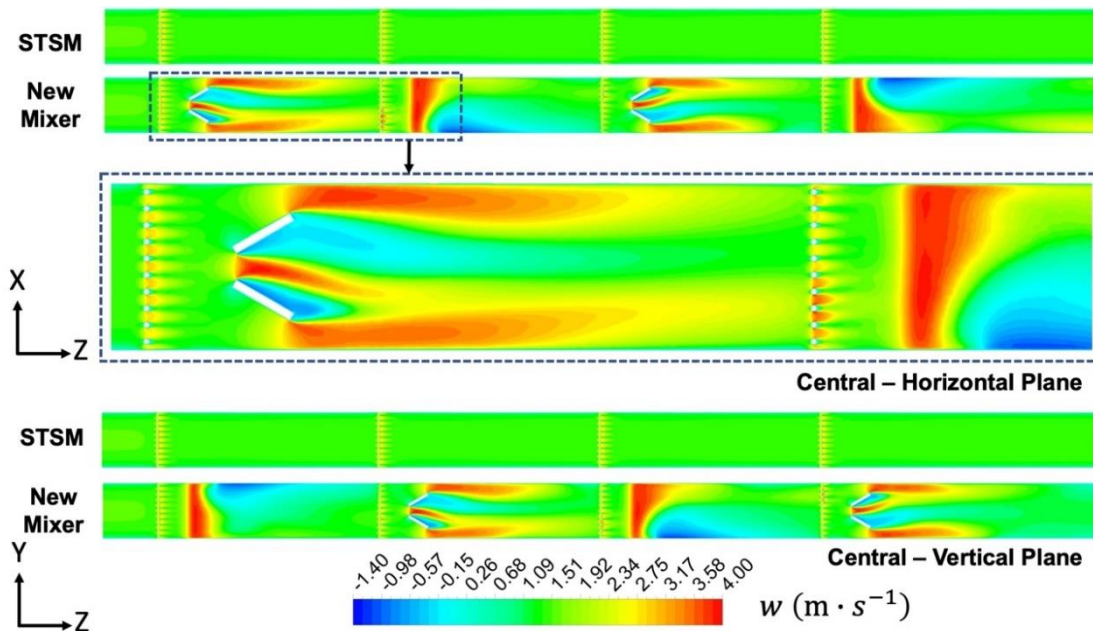


Figure 5.6. Axial velocity contours plotted at the central vertical and horizontal planes for a screen element as well as the new mixer geometry at $Re_{pipe} = 16,500$ ($U_{avg} = 1.305 \text{ m}\cdot\text{s}^{-1}$). A zoom-in plot for the first two mixer elements of the new mixer is also presented.

Figure 5.7 presents the contour plots of the axial velocity at various axial locations downstream of the 3rd and 4th screen at $Re_{pipe} = 16,500$ for the new mixer. These contour plots are overlaid by the resultant vector of the radial and tangential components i.e., u and v which are represented as surface streamlines shown as solid black lines. These surface streamlines will help better visualize local circulation patterns resulting from the addition of the inserts. These cross-sections were plotted such that their axial locations were normalized with respect to the pipe diameter, D , and measured from the center of the screen. Hence, $D^* = 0.5$ corresponds to a plane located $0.5D$ downstream of the respective screen. It should be mentioned that the flaps are located at an axial distance of $L_{sf} = D/2$ measured from the center of the screen. Since most of the flow perturbations were taking place downstream of the screen and flaps (cf. Figure 5.6), the axial locations were selected to be ranging between $D^* = 0.05$ to $D^* = 3.5$.

It is clear from the cross-sectional plots that the flow is exhibiting a repeatable behavior; however, with a rotation of 90 degrees given that the inserts are aligned 90 degrees with respect to each other. A closer look at the cross-sections located at $D^* = 0.5$ and 0.7 and downstream of the flaps ($D^* = 1$ and 2), one cannot but notice the presence of secondary flows that promote radial mixing.

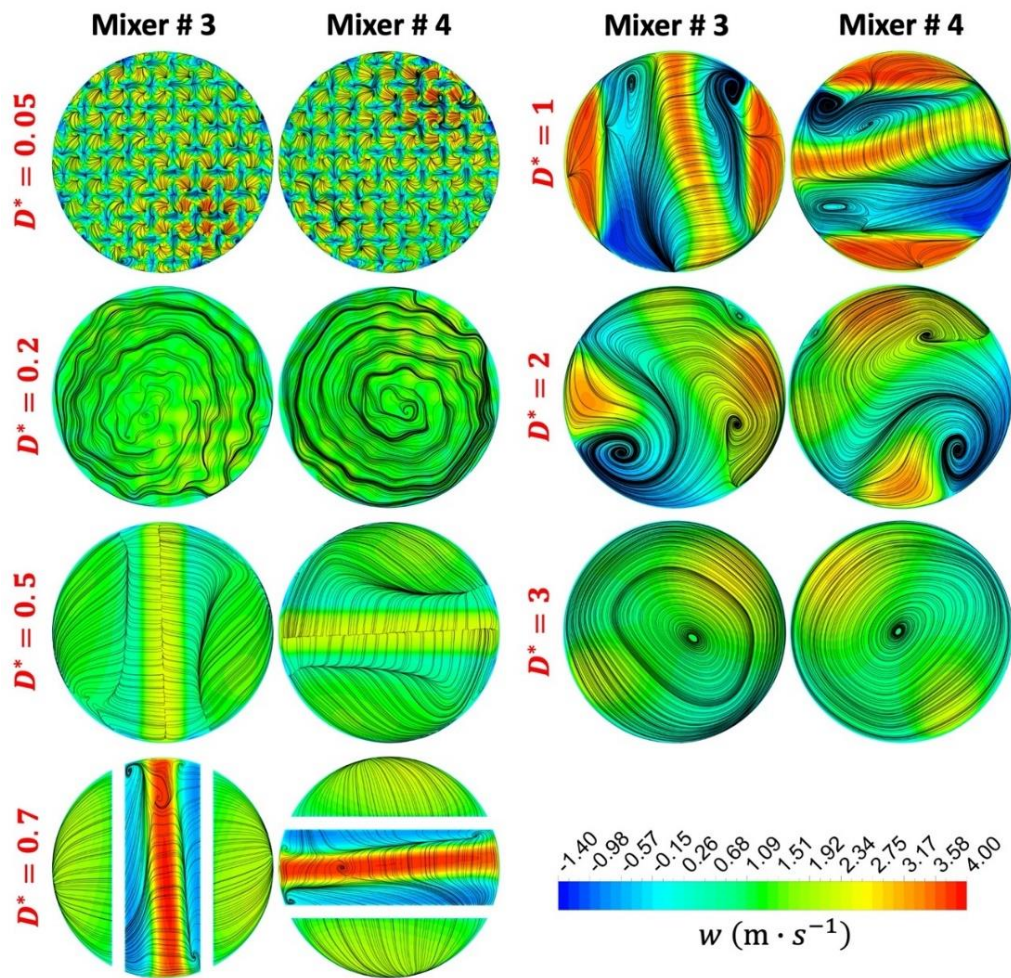


Figure 5.7. Contour plots of the axial velocity overlaid by the surface streamlines at various locations downstream of the 3rd and 4th mixer element at $\text{Re}_{\text{pipe}} = 16,500$ ($U_{\text{avg}} = 1.305 \text{ m} \cdot \text{s}^{-1}$).

5.3.4 *Mixing characterization*

This section characterizes micro-mixing from a distributive and dispersive mixing perspectives. The distributive mixing will first be presented using the CoV then the extensional efficiency will be used to characterize dispersive mixing.

5.3.4.1 Distributive mixing

To study the extent of distributive mixing, the inlet boundary was divided into two halves such that the mass fraction of the working fluid and the secondary fluid (tracer) was set to 0 and 1, respectively.

Figure 5.8 presents the cross-sectional contour plots of the tracer mass fraction at various locations downstream of the center of the first screen element. These locations are selected as a function of the pipe diameter, D , measured from the pipe inlet and correspond to a midway plane between two consecutive mixing elements. The contour plots presented in Figure 5.8 are for $Re_{pipe} = 5,000$ and $30,000$ and also show those obtained for an empty pipe.

Starting with a half pipe injection (cf. Figure 5.8a) three main features could be outlined. First, mixing is enhanced as the flow approaches the pipe outlet for all geometries. Second, the flow is almost completely homogeneous at $Re_{pipe} = 5,000$ regardless of the geometry; however, this observation does not hold at $Re_{pipe} = 30,000$. At these conditions, it can be clearly noted that the presence of screens did not enhance radial mixing in the empty pipe, however, the introduction of inserts downstream of them improved it dramatically. This is attributed to the additional secondary flow resulting from the use of these inserts which favors radial mixing. Third, one cannot but note the effect of the operating conditions on radial mixing whereby the mixing performance at $Re_{pipe} = 5,000$ outperformed that at $Re_{pipe} = 30,000$ for the various geometries. Due to the short pipe length the higher inertia limited the effect of turbulent diffusion which resulted in a better performance at the lowest Re_{pipe} .

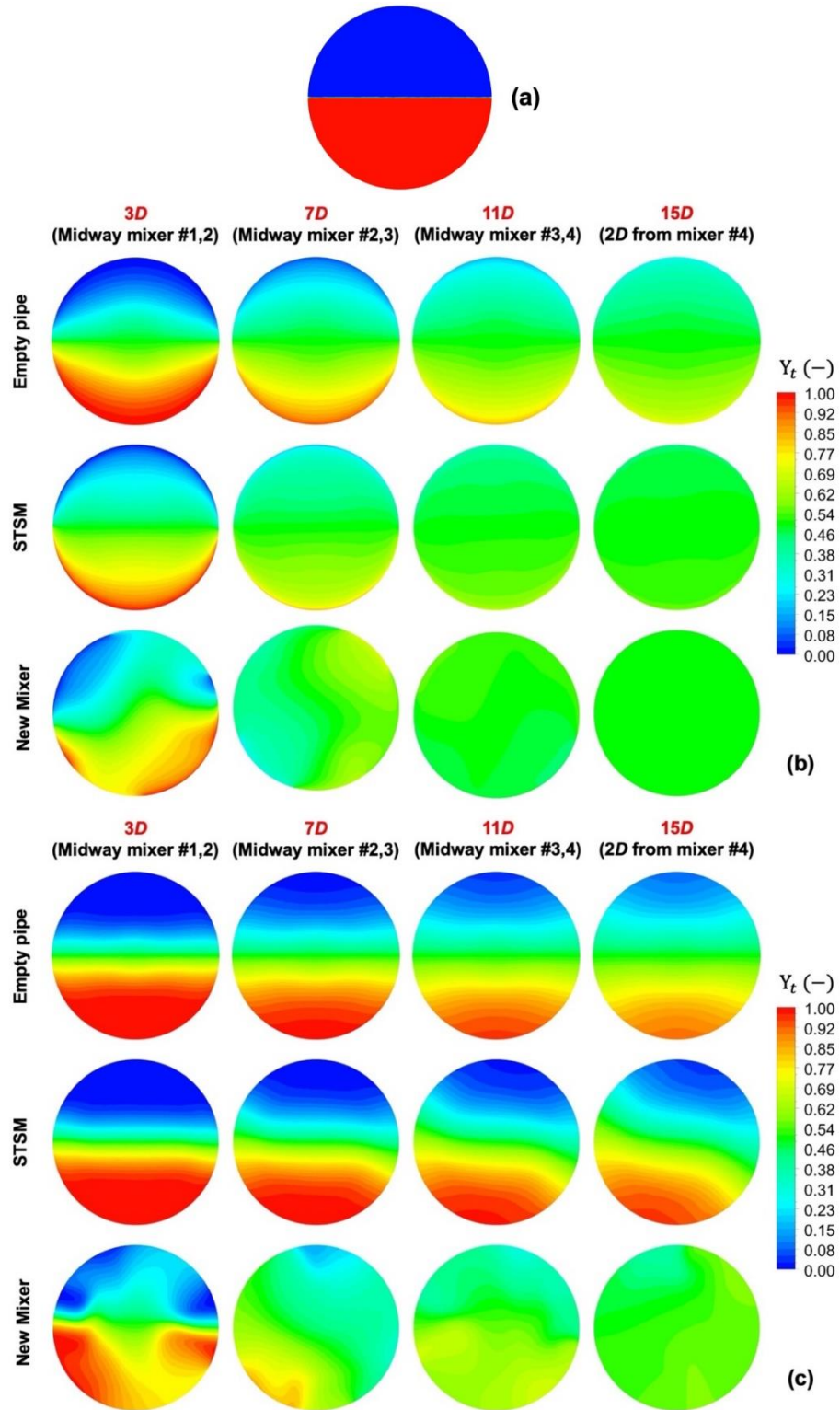


Figure 5.8. Contour plots of the tracer mass fraction at various cross-sections for different static mixers at (a) inlet (b) $Re_{pipe} = 5,000$ and (c) $Re_{pipe} = 30,000$.

Figure 5.9 presents the contours of the tracer mass fraction plotted at the vertical plane at $Re_{pipe} = 30,000$ for the various static mixers. It can be clearly discerned how the new mixer geometry improves the mixing performance by forcing the fluid elements to be scattered as they pass through the inserts.

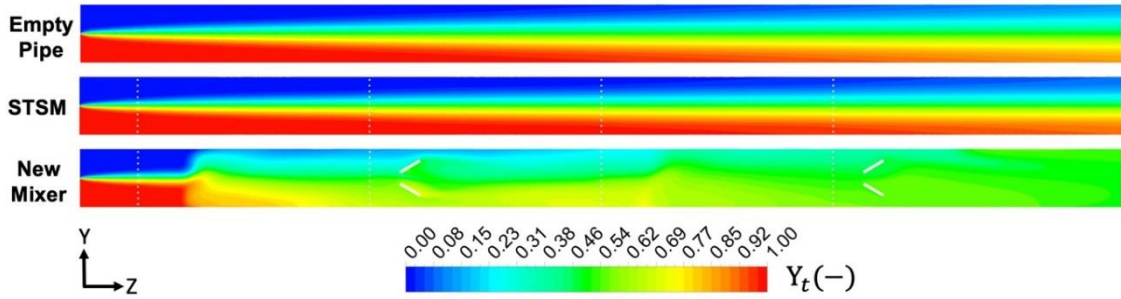


Figure 5.9. Contour plots of the tracer mass fraction at $Re_{pipe} = 30,000$ for different static mixers at central vertical plane YZ .

5.3.4.1.1 Coefficient of Variation

The qualitative description presented earlier could be quantified by means of measuring the intensity of segregation, CoV . Figure 5.10 presents the CoV at the same axial locations plotted earlier at various operating conditions. It should be mentioned that a CoV value of 0.05 or lower is considered an indicator of a well homogenized mixture (Myers et al., 1997; Stec and Synowiec, 2019). For ease of reference, this level is also shown on Figure 5.10 as a solid horizontal line and the center of screens are also shown as vertical dashed lines. Moreover, the reader is reminded that the center of the first mixer element is located $1D$ from the inlet.

Figure 5.10a clearly shows that at $Re_{pipe} = 5,000$ the use of any static mixer reduces the CoV to below 0.05, albeit at different speeds. While the use of a screen allowed a $CoV \cong 0.04$ at $\sim 15D$ or after 4 elements, the proposed mixer geometry reached the same level (i.e., $CoV \cong 0.04$) at almost $11D$ or after 3 elements. As Re_{pipe}

increases, the STSM couldn't reach the desired homogenization level for the current mixing chamber configuration; however, the new mixer was capable of promoting radial mixing where the CoV value was always close to 0.05. This is a clear indication that for the same mixing chamber length, the new mixer could provide a higher degree of homogenization, albeit at the cost of a higher pressure drop.

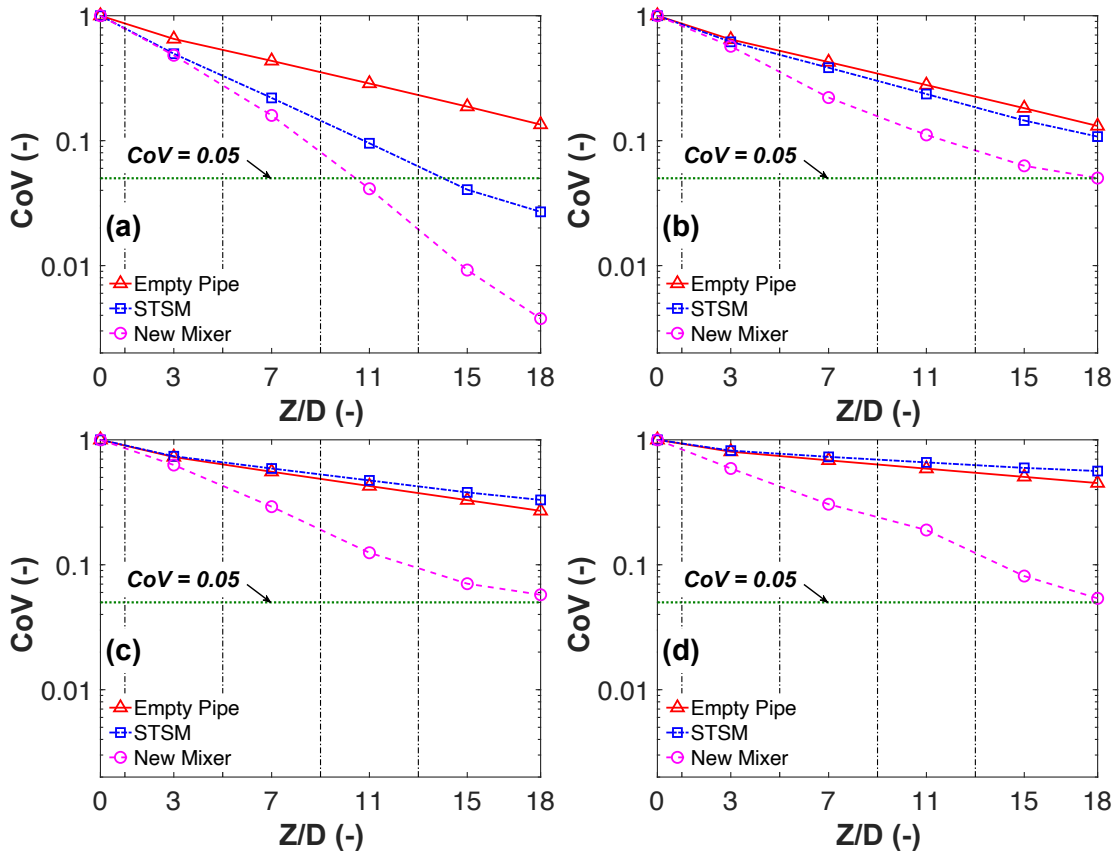


Figure 5.10. CoV for various geometries along the pipe length for (a) $Re_{pipe} = 5,000$ and (b) $Re_{pipe} = 9,100$, (c) $Re_{pipe} = 16,500$, and (d) $Re_{pipe} = 30,000$. The homogenized level is shown by a horizontal green solid line. The center of screen element is presented by vertical dashed line.

Figure 5.11 shows the variation of the CoV as a function of the pipe Reynolds number. It is clear that the value of the outlet CoV increases for the empty pipe and STSM with an increase in Re_{pipe} due to the high velocity of the flow and short pipe length. However, with the new mixer, the CoV values became almost constant at an

average value of $\cong 0.055$ for $Re_{pipe} \geq 9100$. The presence of inserts downstream of screens provided noticeable radial flow which enhanced mixing.

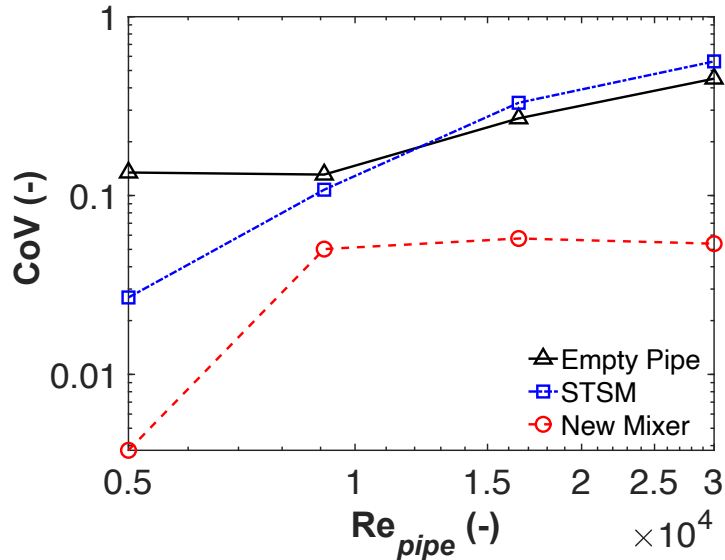


Figure 5.11. Plot of CoV at pipe exit ($18D$) for various mixer elements and operating conditions.

5.3.4.2 Dispersive mixing

Figure 5.12 shows the contour plots of the extensional efficiency for the STSM and the new mixer geometry at various axial locations around the 3rd and 4th mixer elements at $Re_{pipe} = 9,100$. The repeatability of the flow as it passes through these mixers is obvious while accounting for the rotation effect of the inserts behind the screens in the new geometry. One cannot but observe the high levels of extensional efficiency as the flow is passing through the inserts in the regions between $0.5 < D^* < 0.7$. These observations are better quantified in Figure 5.13 which shows the axial variation of the average extensional efficiency over the total length of the pipe at $Re_{pipe} = 9,100$. The axial length covered by the new mixer element is shaded such that the region between the screen and the leading edge of the inserts is considered within the mixer. From these plots and following the observations from Figure 5.12, a repeatable

flow behavior is observed starting from the second mixer element onward. Figure 5.13a shows the value of β along the pipe when screens only were used. One cannot but notice the high extensional/elongational values of 0.9 being reached as a result of the flow passing through the small openings of the screens. Away from the screens, the flow returns to a simple shear flow (i.e., $\beta \cong 0.5$) due to the empty pipe section. Moreover, by comparing the performance of the screen elements to the new mixer, it could be clearly observed that the addition of these inserts does not affect the extensional efficiency within the screen region but rather adds a longer additional region of high β values.

For a proper comparison of the performance of these two mixers, the cumulative volumetric percentage of the extensional efficiency within the flow domain was plotted in Figure 5.14. This was completed by evaluating the fraction of the volume of the domain that has a β value greater than or equal to a specified one. As shown in these plots, the new mixer geometry shows that a larger portion of the volume has higher β values compared to the screen elements alone. This further indicates that the new mixer provides better dispersive mixing over the investigated range of operating conditions. For example, at $Re_{pipe} = 9,100$, the new mixer has 14.3% of its volume at $\beta \geq 0.6$ compared to only 8.7% when screens alone are used. (cf. Figure 5.14b).

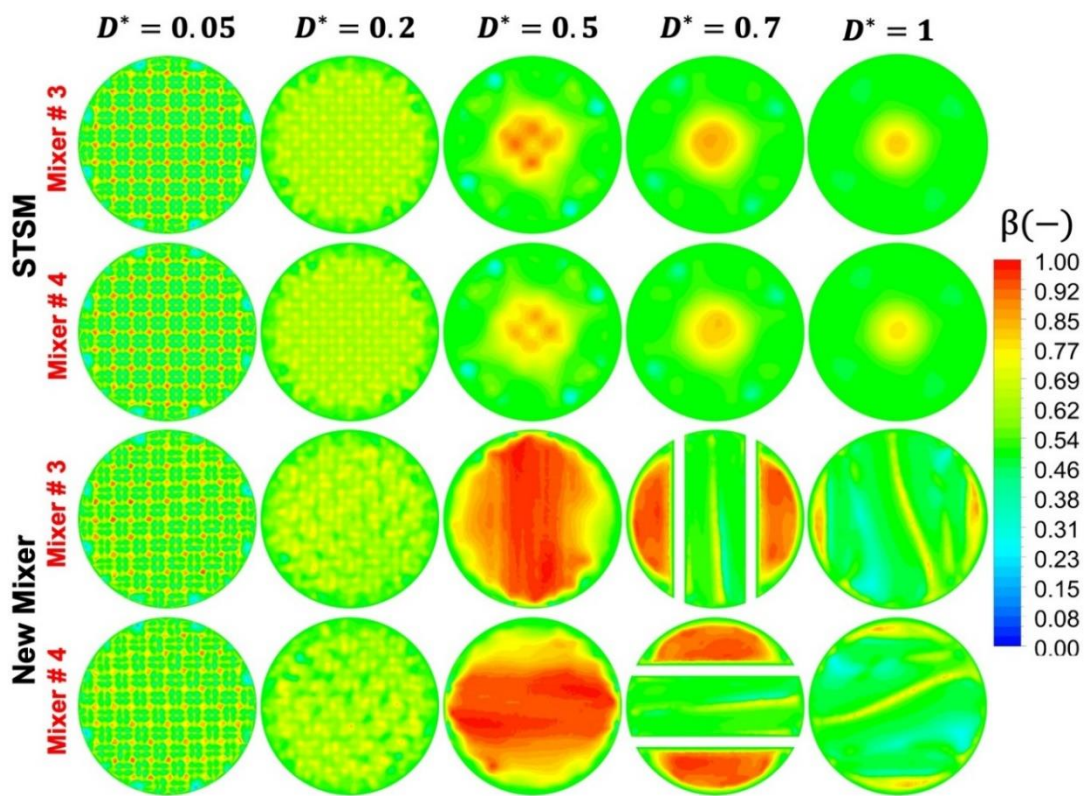


Figure 5.12. Contour plots of the extensional efficiency for a STSM and new mixer at various axial locations for $Re_{pipe} = 9,100$.

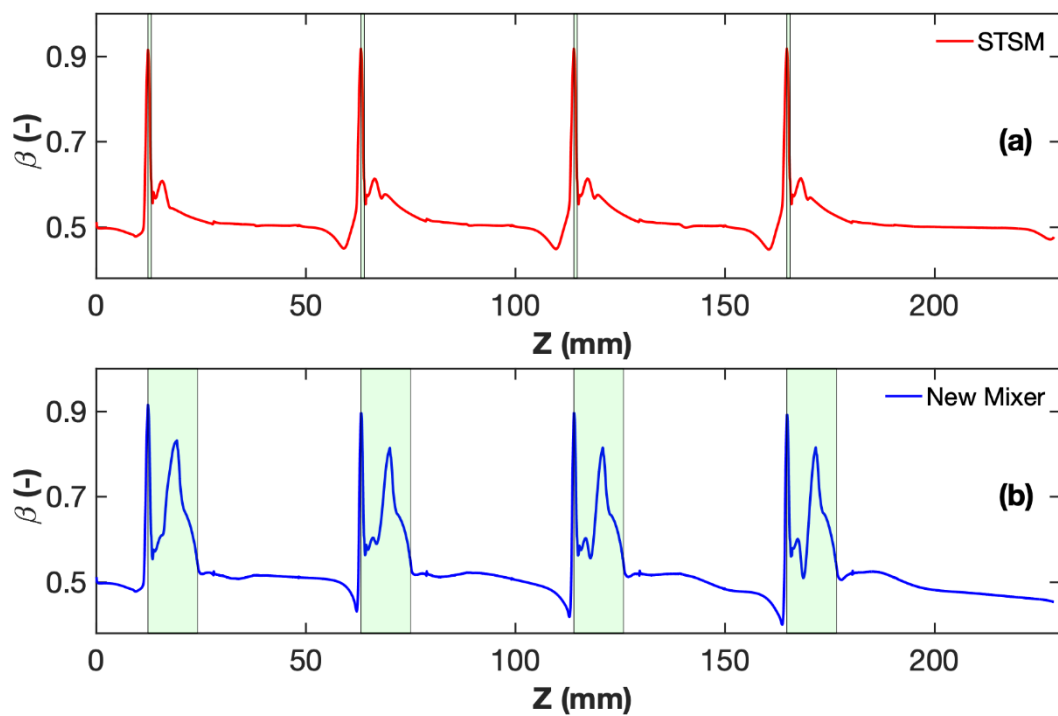


Figure 5.13. Plots for averaged extensional efficiency versus axial length for various static mixers at $Re_{pipe} = 9,100$ (a) STSM and (b) New Mixer.

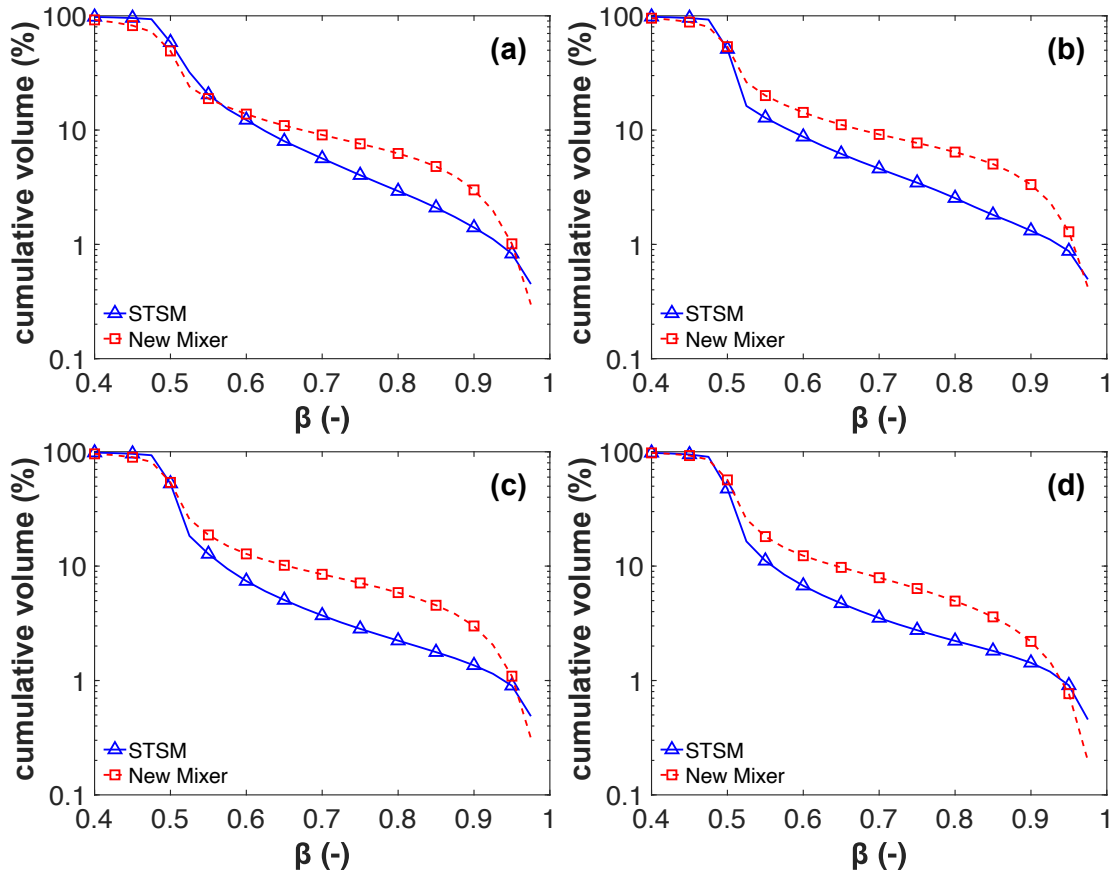


Figure 5.14. Cumulative volumetric percentage of extensional efficiency for various static mixers at (a) $Re_{pipe} = 5,000$, (b) $Re_{pipe} = 9,100$, (c) $Re_{pipe} = 16,500$, and (d) $Re_{pipe} = 30,000$.

5.4 Comparison with other commercial static mixers

While the enhancement of mixing performance of a novel static mixer could be at the expense of additional pressure, it is interesting to compare its pressure drop with other commercial static mixers. While most of the published data in the open literature is for laminar flow conditions, fewer data is available under turbulent flow conditions that covers fully turbulent flow regime. Heyouni et al. (Heyouni et al., 2002) published experimental data on Lightning static mixer over a turbulent regime ranging between Re_{pipe} of 10,000 and 95,000 which covers the range of the current study.

Dealing with geometries whose geometrical ratio could not be quantified by the ratio of the mixer length and the pipe diameter, the pressure drop within a mixer element was first obtained and the pressure loss coefficient, k_s , given by Equation (5.14) was then predicted. This coefficient could provide an acceptable way to compare the energy consumption of different static mixers.

$$k_s = \frac{\Delta p_{elt}}{\frac{1}{2} \rho U_{avg}^2} \quad (5.14)$$

Figure 5.15 presents the pressure loss coefficient for the STSM, new mixer, and Lightnin static mixers over for the range of $Re_{pipe} = 5,000$ and $45,000$. It is to be mentioned that a one mixer element of a Lightnin static mixer corresponds to one helix. The results clearly show that the pressure loss coefficient of the proposed mixer is comparable with that of Lightnin static mixer over the studied range.

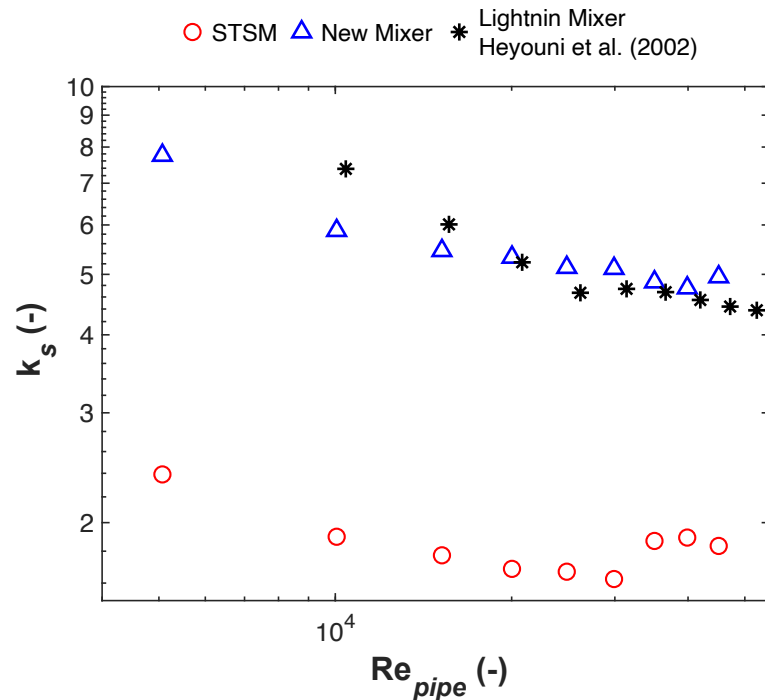


Figure 5.15. Pressure loss coefficient resulting from experimental pressure drop for various static mixers.

5.5 Conclusion

This study proposed a new static mixer geometry based on the use of a screen-type static mixer aided by downstream inserts in order to improve their radial mixing performance. A numerical investigation of its hydrodynamics and mixing performance was then conducted in the turbulent flow regime. The hydrodynamic performance was investigated by means of pressure drop, velocity contours and streamlines and clearly showed the potential of this novel mixer in generating secondary flows and inducing rotational flows. The CFD model was also validated by means of experimentally where the numerical pressure drop data fell within 20% error.

The mixing characterization was based on the CoV for quantifying distributive mixing and the extensional efficiency to quantify dispersive mixing. These studies showed superior improvements in CoV at different turbulence levels although this is at a higher pressure drop. Moreover, this study revealed that the new mixer could maintain high extensional efficiency values over a large portion of the mixing domain at various operating conditions compared to the screen elements.

Finally, these results showed that the new mixer geometry is promising, and that optimization of its geometry can further improve its performance.

5.6 Nomenclature

A_i	Area of a face i within a cross-section	mm^2
b	Wire diameter	mm
D	Pipe diameter	mm
D^*	Normalized axial distance based on pipe diameter	-
D_t	Turbulent diffusivity	$\text{m}^2 \cdot \text{s}^{-2}$

$D_{l,m}$	Mass diffusion coefficient of species l in mixture m	$\text{m}^2 \cdot \text{s}^{-2}$
L_f	Flap's length	mm
L_{ff}	Inter-flap spacing	mm
L_{sf}	Inter-screen-flap spacing	mm
l	Species	-
m	Mixture	-
M	Mesh size	mm
M^*	Normalized axial distance based on mesh size, M	-
Mn	Mesh number	-
N	Number of faces within a cross-section	faces
$N_{e,t}$	Number of tetrahedral grid cells	-
$N_{e,p}$	Number of polyhedral grid cells	-
N_{elts}	Number of mixer elements in a pipe	elements
p	Mean gauge static pressure resulting from Reynolds averaging	Pa
p_{in}	Static pressure at inlet	Pa
p_{out}	Static pressure at outlet	Pa
Sc_t	Schmidt number	-
$\langle S \rangle$	Mean strain rate tensor	s^{-1}
$ \langle S \rangle $	Magnitude of mean strain rate tensor	s^{-1}
t	Tracer species	-
t_f	Flap's thickness	mm
\vec{U}	Instantaneous velocity vector	$\text{m} \cdot \text{s}^{-1}$
$\langle \vec{U} \rangle$	Mean velocity vector resulting from Reynolds averaging	$\text{m} \cdot \text{s}^{-1}$
U_{avg}	Average velocity	$\text{m} \cdot \text{s}^{-1}$
u	Component of the mean velocity in the X direction	$\text{m} \cdot \text{s}^{-1}$

\vec{u}'	Fluctuating velocity vector	$\text{m} \cdot \text{s}^{-1}$
u^*	Normalized component of the mean velocity in the X direction	-
v	Component of the mean velocity in the Y direction	$\text{m} \cdot \text{s}^{-1}$
v^*	Normalized component of the mean velocity in the Y direction	-
w	Component of the mean velocity in the Z direction	$\text{m} \cdot \text{s}^{-1}$
w^*	Normalized component of the mean velocity in the Z direction	-
X	Distance away from the axis (Cartesian coordinates)	mm
Y	Distance away from the axis (Cartesian coordinates)	mm
y^+	Dimensionless wall distance	-
Y_l	Mean species mass fraction resulting from Reynolds averaging	-
$Y_{t,i}$	Mean tracer mass fraction resulting from Reynolds averaging within a face i of a cross-section	-
\bar{Y}_l	Mean species mass fraction of tracer over a cross-section	-
Z	Axial distance (Cartesian coordinates)	mm
Δp_o	Static pressure drop in an empty pipe	Pa
Δp_{screen}	Static pressure drop across a screen	Pa

Greek symbols

α	Percent opening area	%
β	Extensional efficiency	—
ε	Dissipation of turbulent kinetic energy	$\text{m}^2 \cdot \text{s}^{-3}$
θ_f	Flap's rotation	degrees
ρ	Density	$\text{kg} \cdot \text{m}^{-3}$
$\langle \Omega \rangle$	Mean vorticity tensor	s^{-1}
$ \langle \Omega \rangle $	Magnitude of mean vorticity tensor	s^{-1}
μ	Dynamic viscosity	$\text{Pa} \cdot \text{s}$
μ_t	Turbulent viscosity	$\text{Pa} \cdot \text{s}$

σ_{CoV} Standard deviation of mass fraction -

Dimensionless Group

Re_b Wire Reynolds number, $\rho Ub/\mu$

Re_{pipe} Pipe Reynolds number, $\rho UD/\mu$

CoV Coefficient of Variation

Abbreviations

CFD Computational Fluid Dynamics

FVM Finite volume method

GCI Grid Convergence Index

STSM Screen Type Static Mixer

5.7 Acknowledgments

The authors would like to acknowledge the financial support of both the Lebanese National Council for Scientific Research (CNRS-L) and the American University of Beirut through their University Research Board (URB) and their Research Computing Team.

5.8 References

- Abou-Hweij, W., Azizi, F., 2020. CFD simulation of wall-bounded laminar flow through screens. Part I: Hydrodynamic characterization. *Eur. J. Mech. B/Fluids* 84, 207–232. <https://doi.org/10.1016/j.euromechflu.2020.06.008>
- Abou Hweij, W., Azizi, F., 2020. CFD Simulation of Wall-Bounded Laminar Flow Through Screens: Part II -- Mixing Characterization. *Proc. ASME 2020 Fluids Eng. Div. Summer Meet. FEDSM2020 V003T05A01*, 1–10. <https://doi.org/10.1115/FEDSM2020-20120>
- Al-Hassan, T., Habchi, C., Lemenand, T., Azizi, F., 2021. CFD simulation of creeping flows in a novel split-and-recombine multifunctional reactor. *Chem. Eng. Process. - Process Intensif.* 162, 108353. <https://doi.org/10.1016/j.cep.2021.108353>
- Al Taweel, A.M., Azizi, F., Siriijeerachai, G., 2013. Static mixers: Effective means for

- intensifying mass transfer limited reactions. *Chem. Eng. Process. Process Intensif.* 72, 51–62. <https://doi.org/10.1016/j.cep.2013.08.009>
- Al Taweel, A.M., Li, C., Gomaa, H.G., Yuet, P., 2007. Intensifying mass transfer between immiscible liquids: Using screen-type static mixers. *Chem. Eng. Res. Des.* 85, 760–765. <https://doi.org/10.1205/cherd06180>
- Al Taweel, A.M., Yan, J., Azizi, F., Odedra, D., Gomaa, H.G., 2005. Using in-line static mixers to intensify gas-liquid mass transfer processes. *Chem. Eng. Sci.* 60, 6378–6390. <https://doi.org/10.1016/j.ces.2005.03.011>
- ANSYS, 2017. *Ansyes Fluent Theory Guide*, v.18.2. ANSYS Inc., USA.
- ANSYS, 2014. *ANSYS - Turbulence Modelling and the Law of the Wall: Tutorial*. ANSYS Inc., USA 1–48.
- Azizi, F., 2019. On the pressure drop of fluids through woven screen meshes. *Chem. Eng. Sci.* 207, 464–478. <https://doi.org/10.1016/j.ces.2019.06.046>
- Azizi, F., Abou-Hweij, W., Lebaz, N., Sheibat-Othman, N., 2021. A numerical evaluation of flows through an SMX-Plus mixer. *Chem. Eng. Res. Des.* <https://doi.org/10.1016/j.cherd.2021.12.030>
- Azizi, F., Al Taweel, A.M., 2015. Mass Transfer in an Energy-Efficient High-Intensity Gas-Liquid Contactor. *Ind. Eng. Chem. Res.* 54, 11635–11652. <https://doi.org/10.1021/acs.iecr.5b01078>
- Bourne, J.R., Lips, M., 1991. Micromixing in grid-generated turbulence: theoretical analysis and experimental study. *Chem. Eng. J.* 47, 155–162.
- Celik, I.B., Ghia, U., Roache, P.J., Freitas, C.J., Coleman, H., Raad, P.E., 2008. Procedure for estimation and reporting of uncertainty due to discretization in CFD applications. *J. Fluids Eng. Trans. ASME* 130, 0780011–0780014. <https://doi.org/10.1115/1.2960953>
- Coroneo, M., Montante, G., Paglianti, A., 2012. Computational fluid dynamics modeling of corrugated static mixers for turbulent applications. *Ind. Eng. Chem. Res.* 51, 15986–15996. <https://doi.org/10.1021/ie300398z>
- Dbouk, T., Habchi, C., 2019. On the mixing enhancement in concentrated non-colloidal neutrally buoyant suspensions of rigid particles using helical coiled and chaotic twisted pipes: A numerical investigation. *Chem. Eng. Process. - Process Intensif.* 141, 107540. <https://doi.org/10.1016/j.cep.2019.107540>
- De La Villéon, J., Bertrand, F., Tanguy, P.A., Labrie, R., Bousquet, J., Lebouvier, D., 1998. Numerical Investigation of Mixing Efficiency of Helical Ribbons. *AIChE J.* 44, 972–977. <https://doi.org/10.1002/aic.690440423>
- Ghanem, A., Lemenand, T., Della, D., Peerhossaini, H., 2013. Chemical Engineering Research and Design Static mixers : Mechanisms , applications , and characterization methods – A review. *Chem. Eng. Res. Des.* 92, 205–228.
- González-Juárez, D., Solano, J.P., Herrero-Martín, R., Harvey, A.P., 2017. Residence time distribution in multiorifice baffled tubes: A numerical study. *Chem. Eng. Res. Des.* 118, 259–269. <https://doi.org/10.1016/j.cherd.2016.12.008>
- Habchi, C., Azizi, F., 2018. Heat transfer and turbulent mixing characterization in

- screen-type static mixers. *Int. J. Therm. Sci.* 134, 208–215.
<https://doi.org/10.1016/j.ijthermalsci.2018.08.016>
- Haddadi, M.M., Hosseini, S.H., Rashtchian, D., Ahmadi, G., 2019. CFD modeling of immiscible liquids turbulent dispersion in Kenics static mixers: Focusing on droplet behavior. *Chinese J. Chem. Eng.* 28, 348–361.
<https://doi.org/10.1016/j.cjche.2019.07.020>
- Haddadi, M.M., Hosseini, S.H., Rashtchian, D., Olazar, M., 2020. Comparative analysis of different static mixers performance by CFD technique: An innovative mixer. *Chinese J. Chem. Eng.* 28, 672–684. <https://doi.org/10.1016/j.cjche.2019.09.004>
- Hartmann, H., Derksen, J.J., Akker, H.E.A. van den, 2006. Mixing Times in a Turbulent Stirred Tank by Means of LES. *AIChE J.* 52, 3696–3706.
<https://doi.org/10.1002/aic>
- Heniche, M., Tanguy, P.A., Reeder, M.F., Fasano, J.B., 2005. Numerical investigation of blade shape in static mixing. *AIChE J.* 51, 44–58.
<https://doi.org/10.1002/aic.10341>
- Heyouni, A., Roustan, M., Do-quang, Z., 2002. Hydrodynamics and mass transfer in gas – liquid flow through static mixers. *Chem. Eng. Sci.* 57, 3325–3333.
- Hinze, J.O., 1975. *Turbulence*. McGraw-Hill - New York.
- Madhuranthakam, C.M.R., Pan, Q., Rempel, G.L., 2009. Residence time distribution and liquid holdup in Kenics® KMX static mixer with hydrogenated nitrile butadiene rubber solution and hydrogen gas system. *Chem. Eng. Sci.* 64, 3320–3328. <https://doi.org/10.1016/j.ces.2009.04.001>
- Manas-Zloczower, I., 1994. *Studies of Mixing Efficiency in Batch and Continuous Mixers*.
- Meng, H., Han, M., Yu, Y., Wang, Z., Wu, J., 2020. Numerical evaluations on the characteristics of turbulent flow and heat transfer in the Lightnin static mixer. *Int. J. Heat Mass Transf.* 156. <https://doi.org/10.1016/j.ijheatmasstransfer.2020.119788>
- Meng, H., Song, M., Yu, Y., Wang, F., Wu, J., 2015. Chaotic mixing characteristics in static mixers with different axial twisted-tape inserts. *Can. J. Chem. Eng.* 93, 1849–1859. <https://doi.org/10.1002/cjce.22268>
- Meng, H., Song, M.Y., Yu, Y.F., Jiang, X.H., Wang, Z.Y., Wu, J.H., 2017. Enhancement of Laminar Flow and Mixing Performance in a Lightnin Static Mixer. *Int. J. Chem. React. Eng.* 15, 1–21. <https://doi.org/10.1515/ijcre-2016-0112>
- Montante, G., Coroneo, M., Paglianti, A., 2016. Blending of miscible liquids with different densities and viscosities in static mixers. *Chem. Eng. Sci.* 141, 250–260.
<https://doi.org/10.1016/j.ces.2015.11.009>
- Myers, K.J., Bakker, A., Ryan, D., 1997. Avoid Agitation by Selecting Static Mixers. *Chem. Eng. Prog.* 93, 28–38.
- Okolo, P.N., Zhao, K., Kennedy, J., Bennett, G.J., 2019. Numerical assessment of flow control capabilities of three dimensional woven wire mesh screens. *Eur. J. Mech. B/Fluids* 76, 259–271. <https://doi.org/10.1016/j.euromechflu.2019.03.001>
- Peschel, A., Hentschel, B., Freund, H., Sundmacher, K., 2012. Design of optimal

- multiphase reactors exemplified on the hydroformylation of long chain alkenes. Chem. Eng. J. 188, 126–141. <https://doi.org/10.1016/j.cej.2012.01.123>
- Stec, M., Synowiec, P.M., 2019. Study of fluid dynamic conditions in the selected static mixers part III—research of mixture homogeneity. Can. J. Chem. Eng. 97, 995–1007. <https://doi.org/10.1002/cjce.23290>
- Thakur, R.K., Vial, C., Nigam, K.D.P., Nauman, E.B., Djelveh, G., 2003. Static mixers in the process industries - a review. Chem. Eng. Res. Des. 81, 787–826. <https://doi.org/10.1205/026387603322302968>

CHAPTER 6

CONCLUSIONS AND RECOMMENDATIONS

The thesis is a compilation of various standalone manuscripts, and detailed conclusions regarding each section were given in the corresponding individual chapters. However, the most important conclusions are summarized here.

6.1 Hydrodynamics of laminar flows through STSM

The use of screen mixers was found to alter the laminar parabolic velocity profile and flatten it for a considerable distance downstream. Analysis of the velocity field also showed that the flow should be treated as three-dimensional where recirculation and vortices were observed near the walls at $Re < 1820$. Furthermore, the study revealed that a pressure recovery downstream of the screen was observed at high Re_b while this was inexistent at low Re_b .

6.2 Mixing performance of STSM under laminar flow conditions

Following a Lagrangian approach and for a $Re_b \leq 20$, a coarse screen could provide better distributive mixing when compared to fine meshes; however, at a relatively low mixing efficiency. This was illustrated through central injection of a single fluid and concentric injection of immiscible fluids. On the other side, STSM showed promising dispersive mixing potential where high extensional efficiency values were recorded near the screen vicinity.

6.3 Hydrodynamics of turbulent flows through STSM

The use of screens under turbulent flow regime ranging between 9,000 and 56,000 revealed that they could alter the velocity profile as being alternating/flattened for a noticeable distance downstream of the screen. Moreover, the inter-relation between vorticity and strain rate revealed that this type of static could provide good dispersive mixing over the mixing volume. This study also highlighted that the mean flow dissipation rate component cannot be neglected under the studied turbulent range. Finally, this study addressed the macromixing performance of STSM using RTDs and showed that near plug flow conditions were attainable using fine meshes.

6.4 Proposed enhanced mixer design

A new mixer design aiming at enhancing the mixing performance of STSM was proposed. It was based on the use of carefully oriented inserts downstream of the screen to promote chaotic/radial mixing. Using a popular method to quantify distributive mixing under turbulent flows, CoV , numerical simulations showed that major enhancements can be attained at low and high turbulence levels. In addition, dispersive mixing was further promoted.

6.5 Recommendations

The current investigations considered steady state RANS turbulence models. It is therefore recommended to investigate the performance of STSM using unsteady RANS turbulence models as well as Large eddy simulation (LES).

The investigations undertaken in the current work considered single phase flow through STSMs. It is therefore recommended that turbulently flowing multi-phase

flows (i.e., gas-liquid and liquid-liquid) be investigated by means of population balance modeling.

Furthermore, the current investigation proposed a new mixer design to enhance the performance of STSM. This relied on the use of inserts downstream of the screens. But the studies were performed using one screen geometry (i.e., $Mn = 20$). It is therefore recommended that the following parameters be investigated in future works to test their impact on the overall performance of the mixer:

- Study the effect of varying the new mixer geometry on its hydrodynamic and mixing performance. In particular, the following geometrical parameters of the inserts should be investigated: length, thickness, angle of rotation, orientation relative to each other, inter-insert spacing, screen-insert spacing, as well as the shape of the inserts (e.g., straight vs. curved).
- Investigate the impact of these aforementioned parameters on the pressure drop in this mixer.
- Predict the hydraulic friction factor for the new mixer which could provide better insight on how the new mixer compares with other static mixers.
- Investigate the effect of changing the screen geometry used in the new mixer design in terms of macro-, and micro-mixing performance under turbulent and laminar flow conditions.
- Conduct additional experimental measurements for the mixing performance to better validate the numerical results.
- Simulating multi-phase flows through this new type of mixer is also worth noting as a potential future work as it will help determine its mass transfer performance.

APPENDIX 1

COMPLEMENTARY INFORMATION REGARDING THE MACRO-MIXING CHARACTERIZATION WITHIN STSM USING RTD

1.1 RTD Theory

Residence time distribution or shortly RTD represents the distribution of times that different fluid elements have spent inside the reactor vessel boundaries. These residence times are affected by the velocity profiles and molecular diffusion (Nauman, 2008) and therefore RTD is considered a proper method to characterize macromixing within a static mixer.

Usually, two different methods are used to obtain RTDs, either through a sudden injection of a tracer (pulse injection) or through constant rate injection (step injection) at the inlet of the fluid stream (Adeosun and Lawal, 2009; Fogler, 2004) where then tracer concentration is measured at exit as a function of time. In the present study, to avoid numerical differentiation errors that is inherent in the step injection, the pulse injection method was used (Adeosun and Lawal, 2009).

Referring to Fogler (Fogler, 2004), the residence time distribution function $E(t)$, given by Equation (1.1) describes quantitatively how much time different fluid elements resided inside the reactor such that the term $E(t)dt$, measured at the outlet, represents the fraction of the fluid elements that resided inside the reactor between t and $t+dt$.

$$E(t) = \frac{C(t)}{\int_0^{\infty} C(t) dt} \quad (1.1)$$

where $C(t)$ is the molar concentration in the measured section.

To conserve mass within the flow domain, the $E(t)$ function should obey the constraint given by Equation (1.2). Hence, the fraction of all material elements that resided in the reactor between time $t = 0$ and time, t , represents the cumulative distribution function, $F(t)$, given by Equation (1.3).

$$\int_0^{\infty} E(t) dt = 1 \quad (1.2)$$

$$F(t) = \int_0^t E(t) dt \quad (1.3)$$

Moreover, using $E(t)$ function, one can obtain the first moment of distribution defined as the mean residence time, t_m , given by Equation (1.4). It represents the average time that the fluid elements have spent inside the reactor. This term reflects the presence of dead volumes or short-circuiting inside the mixer by comparing its value with the theoretical residence time, τ , that is calculated as the ratio of the reactor volume, V , to the volumetric flow rate, Q ($\tau = V/Q$) (Abou Hweij and Azizi, 2015).

$$t_m = \int_0^{\infty} tE(t) dt \quad (1.4)$$

The second moment of the distribution is defined as the variance, which is the square of the spread of the distribution, σ , given by Equation (1.5). Hence, the smaller the variance, the narrower is the RTD, the closer is the distribution to the mean residence time, and thus the closer the reactor to be treated as a plug flow reactor (Adeosun and Lawal, 2009).

$$\sigma^2 = \int_0^{\infty} (t - t_m)^2 E(t) dt \quad (1.5)$$

To provide proper analysis while dealing with different geometries, normalized functions will be used as defined by Equation (1.6).

$$E(\theta) = t_m E(t) \quad (1.6)$$

where θ is the normalized residence time calculated as the ratio of the residence time, t to the mean residence time, t_m , $\theta = (t/t_m)$.

1.2 Method used for obtaining the RTD in ANSYS Fluent

The common method used for obtaining the RTD could be divided into three stages (Adeosun and Lawal, 2009; Li et al., 2010; Ramesh and Nilesh, 2015; Stec and Synowiec, 2017a). Firstly, the steady state fluid flow problem was obtained where the continuity, momentum, k , and ε were solved using solution methods presented in Chapter 4 §4.2.2. Secondly, upon convergence, the species transport equation was solved under transient conditions, where the tracer was injected from the inlet such that the tracer mass fraction at the inlet surface was set to 1. Dealing with a pulse injection, the injection lasts for one-time step (Adeosun and Lawal, 2009; Fu, 2020; Ramesh and Nilesh, 2015). The time step is evaluated such that it allows the species front, at maximum, to spread out approximately less than one grid cell size (Li et al., 2010). Finally, the mass fraction of the tracer was set to 0 for the second and later time steps. The transient simulation was carried out until the entire amount of the tracer washed out from the system (Stec and Synowiec, 2017a). It should be mentioned that, for the species transport equation, the discretization of the transient term was done using the 2nd order implicit scheme (Adeosun and Lawal, 2009; González-Juárez et al., 2017) while the spatial discretization was done using the QUICK scheme (González-Juárez et

al., 2017). Moreover, by proper selection of the maximum number of iterations per step, the scaled species residuals dropped to an order $< 10^{-6}$ within each time step.

To select the independent grid for the RTD study, different grid levels were conducted at $Re_{pipe} = 30,000$ through monitoring the mean residence time, t_m , and the standard deviation, σ . Table 1.1 presents the GCI values if the medium grid or the fine grid were to be selected. The maximum GCI value within the tested parameters was 5.7% if the medium grid was selected and 3.6% if the fine grid was selected (cf. Table 1.1). Hence, the medium grid could be selected as it provides the best combination between the computational cost and results reliability, which also falls within the acceptable range of numerical uncertainty (Okolo et al., 2019). For the various geometries investigated here, the number of grid cells, N_e should be multiplied by the number of mixer elements to get the total number of grid cells within the computational domain.

Table 1.1. Grid independence test for different screen geometries.

Mesh number	Refinement Level	Number of grid cells, N_e	GCI % (RTD)
$Mn = 20$	Fine	19,193,100	2.1
	medium	7,108,637	5.7
	Coarse	2,632,137	
$Mn = 50$	Fine	27,094,857	1.2
	medium	11,641,548	4.9
	Coarse	4,176,324	

In an attempt to reduce the computational cost in the RTD studies, a polyhedral grid was used (ANSYS, 2017; Khan, 2012; Meng et al., 2020; Sosnowski et al., 2018,

2017). Therefore, the medium tetrahedral grid was converted into polyhedral grid and the final number of elements is reported in Table 1.2. Moreover, the relative difference between the tetrahedral grid and the polyhedral grid is also reported in Table 1.2, where a relative difference of less than 1% is reported. Hence, the polyhedral grid was used in further investigations of RTDs.

Table 1.2. Comparison between Tetrahedral and Polyhedral grids.

Mesh number	Refinement Level	Number of grid cells, N_e	Relative difference %
$Mn = 20$	Tetrahedral	7,108,637	0.92
	Polyhedral	2,648,082	
$Mn = 50$	Tetrahedral	11,641,548	0.74
	Polyhedral	6,804,699	

Furthermore, using the polyhedral grid, the computational cost for the transient simulation could be further reduced through increasing the time step. Hence, the time step was varied between three orders of magnitude and the GCI was evaluated if the medium or the fine time steps were to be selected as shown in Table 1.3. It could be clearly discerned that the medium time step could be selected while maintaining acceptable results at low computational cost. For future investigations, the time steps for $Mn = 20$ and $Mn = 50$ were set to 5.6×10^{-4} s and 2.4×10^{-4} s at $Re_{pipe} = 5,000$ and were set to 9.6×10^{-5} s and 4.4×10^{-5} s at $Re_{pipe} = 30,000$.

The numerical simulations were performed using the Octopus high performance computing (HPC) cluster available at the American University of Beirut using four parallel nodes each of 16 processors and 64GB RAM of Intel® Xeon® Processor E5-2665 @ 2.4 GHz.

Table 1.3. Temporal grid convergence using the polyhedral grid.

Mesh number	Temporal Refinement Level	<i>GCI</i> % (<i>RTD</i>)
<i>Mn</i> = 20	Δt	0.05
	$\Delta t \times 10$	1.2
	$\Delta t \times 100$	
<i>Mn</i> = 50	Δt	0.16
	$\Delta t \times 10$	1.2
	$\Delta t \times 100$	

APPENDIX 2

UDF AND MATLAB CODES

2.1 User defined function for the laminar parabolic profile

```
#include "udf.h"
DEFINE_PROFILE(velocity_z, thread, index)
{
    float p[3];
    float x;
    float y;
    face_t f;

    begin_f_loop(f, thread)
    {
        F_CENTROID(p,f,thread);
        x = p[0];
        y = p[1];

        F_PROFILE(f, thread, index) = 0.1*(1-(x*x + y*y)/(0.00635*0.00635));
    }
    end_f_loop(f, thread)
}
```

It is to be noted that the Custom field function (CFF) available in Fluent[®] was used to extract the values of the mean flow dissipation rate and extensional efficiency.

2.2 Grid convergence index (GCI)

The GCI is based on the method proposed by Celik et al. (Celik et al., 2008).

The equations used in the MATLAB code are listed.

Consider three grids N_1 , N_2 , and N_3 such that N_1 is the fine grid and denote by ϕ the flow variable over which grid independence test is done.

$$r_{21} = h_{coarse}/h_{fine} \quad (2.1)$$

Where r_{21} is the refinement factor, h_{coarse} is the average element size of the coarse grid and h_{fine} is the average element size of the fine grid.

$$\epsilon_{32} = \phi_3 - \phi_2 \quad (2.2)$$

$$\epsilon_{21} = \phi_2 - \phi_1$$

$$e_a^{21} = \left| \frac{\phi_2 - \phi_1}{\phi_1} \right| \quad (2.3)$$

Where e_a^{21} is the approximate relative error between the fine and medium grids.

$$G = \frac{1}{\ln(r_{21})} \left| \ln \left| \frac{\epsilon_{32}}{\epsilon_{21}} \right| + q(G) \right|$$

$$q(G) = \ln \left(\frac{r_{21}^f - s}{r_{32}^f - s} \right) \quad (2.4)$$

$$s = 1 \cdot \text{sign} \left(\frac{\epsilon_{32}}{\epsilon_{21}} \right)$$

Where G is the order of convergence.

$$GCI^{21} = \frac{1.25e_a^{21}}{r_{21}^G - 1} \quad (2.5)$$

Where GCI^{21} is the grid convergence index if the fine grid is selected.

```

%%%%%%%%%%%%%%%%%%%%%%%%%%%%%%%%%%%%%%%%%%%%%%%%%%%%%%%%%%%%%%%%%%%%%%%%
%%%%%%%%%%%%%%%%%%%%%%%%%%%%%%%%%%%%%%%%%%%%%%%%%%%%%%%%%%%%%%%%%%%%%%%%
% Calculation of GCI following Celik et al. approach (2008)
%%%%%%%%%%%%%%%%%%%%%%%%%%%%%%%%%%%%%%%%%%%%%%%%%%%%%%%%%%%%%%%%%%%%%%%%
%%%%%%%%%%%%%%%%%%%%%%%%%%%%%%%%%%%%%%%%%%%%%%%%%%%%%%%%%%%%%%%%%%%%%%%%
clc
clear
%% Extracting the field variables and applying Celik et al. approach
% The sheet file is named by the location at which data was extracted.
% Each column is titled by the field variable and the corresponding values
% at different grid values are reported such that first cell is for the fine
% followed by medium, then the coarse grid.
sheet = 'Mn20_local_2M';
Data = xlsread('local_results Mn20',sheet);
% Get average element size
h1 = (Data (1,1));
h2 = (Data (2,1));
h3 = (Data (3,1));
% Get refinement factor
r21=h2/h1;
r32=h3/h2;
% Loop over all the field variables
for j = 1:6
% Get field values
val1 =(Data (1,j+1));
val2 =(Data (2,j+1));
val3 =(Data (3,j+1));
% Get difference between two consecutive values
eps32=val3-val2;
eps21=val2-val1;

```

```

% Get order of convergence, G.
s = sign(eps32/eps21);
opts = optimset('Display','off');
G=fsolve(@(G) (G-abs(log(((r21^G)-s)/((r32^G)-s)))+...
(log(abs(eps32/eps21))))/log(r21)),1/log(r21),opts);
q_G=log(((r21^G)-s)/((r32^G)-s));
% Get extrapolated values
val21_ext=(((r21^G)*val1)-val2)/((r21^G)-1);
val32_ext=(((r32^G)*val2)-val3)/((r32^G)-1);
% Get approximate relative error
e21_a=abs((val1-val2)/val1);
e32_a=abs((val2-val3)/val2);
% Get extrapolated relative error
e21_ext=abs((val21_ext-val1)/val21_ext);
e32_ext=abs((val32_ext-val2)/val32_ext);
% Get GCI if fine grid (1) is to be selected
GCI21=100*1.25*e21_a/((r21^G)-1);
% Get GCI if medium grid (2) is to be selected
GCI32=100*1.25*e32_a/((r32^G)-1);
% Grouping the GCI values of each field variable in one array called
% GCI_list. This is also done for the relative error and the order of
% convergence.
GCI_21_list(j) = GCI21;
GCI_32_list(j) = GCI32;
e21_a_list(j) = 100*e21_a;
e32_a_list(j) = 100*e32_a;
order_list(j) = G;
end
%% Exporting Grid Independence data to an excel file
% Setting the field variable names
Field_variables = {'epsilon';'epsilon_mean';'kinetic';'kinetic_mean';'epsilon_total_2M';'kinetic_total'};
VarNames={'Field_variables','GCI_21_list','GCI_32_list','e21_a_list','e32_a_list','order_list'};
T =
table(Field_variables,GCI_21_list',GCI_32_list',e21_a_list',e32_a_list',order_list', 'VariableNames',VarNames);
filename = 'Grid_Independence_results.xlsx';
writetable(T,filename)

```

2.3 Point to nearest neighbor

The code generated by Kukukova et al. (Kukukova et al., 2011) was used and redesigned to fit the STSM.

```

%%%%%%%%%%%%%%%%%%%%%%%%%%%%%%%%%%%%%%%%%%%%%%%%%%%%%%%%%%%%%%%%%%%%%%%%
%%%%%%%%%%%%%%%%%%%%%%%%%%%%%%%%%%%%%%%%%%%%%%%%%%%%%%%%%%%%%%%%%%%%%%%%
% Calculation of Point-to-nearest-neighbour (PNN) distances
% (= for each sampling point in the grid, find the distance to the nearest
% particle).
%%%%%%%%%%%%%%%%%%%%%%%%%%%%%%%%%%%%%%%%%%%%%%%%%%%%%%%%%%%%%%%%%%%%%%%%
%%%%%%%%%%%%%%%%%%%%%%%%%%%%%%%%%%%%%%%%%%%%%%%%%%%%%%%%%%%%%%%%%%%%%%%%
clc
clear
% Normalization of data w.r.t pipe radius since we are taking quarter of
% the pipe hence the maximum distance between two particles will be the
% pipe radius i.e. = 1 in after normalization.
%% particle positions
% Each sheet represents the particles position at a specified
% cross-section. Hence, sheet 0 corresponds to the plane at the inlet and
% sheet 4 corresponds to the plane at the midway between screen 4 and 5.
sheets = 0:1:8;
% Loop over all the sheets i.e. each cross-sections.
for f = 1:length(sheets)

```

```

% Read the data within each sheet (cross-section).
sheet = num2str(sheets(f));
Data = xlsread('Mn20Reb20L50',sheet);
% Extract the position of each particle normalize it with
% respect to pipe radius since this study deals with a quarter pipe hence
% the maximum distance between two particles will be the pipe radius
% Normalization with respect to pipe radius
X = Data(:,1)/6.35e-3;
% Normalization with respect to pipe radius
Y = Data(:,2)/6.35e-3;
%% Grid point positions
% The "StaggeredGridGeneration" function is used to generate the grid
% points. This function generates two rectangular grids that are staggered
% with respect to each other such that the distance between two consecutive
% grids points in x direction is equal to that in the y-direction.
% These rectangular grids cover quarter pipe cross-section such that some
% of the grid points are within the quarter pipe domain and other are
% outside the quarter pipe domain.
% So, this function make use of another function "pointsincircle"
% which could be downloaded from Mathworks to find the grid points that
% are within the flow domain and those that are outside the flow domain.
% Cutoff radius. Here it is represented in normalized form.
radius_norm = 1;
% Horizontal divisions was taken such that the number of grid points within
% the quarter pipe should be very close to the number of particles as
% recommended by Kukukova et al. 2011 to make use of all particles in the
% domain.
hori_div = 134;
% Xref_in and Yref_in represents the coordinates of the grid points that
% are within the flow domain and Xref_out and Yref_out represents the
% coordinates of the grid points that are outside the flow domain.
[Xref_in,Yref_in,Xref_out,Yref_out] = ...
    StaggeredGridGeneration(hori_div,radius_norm);
% Total number of all grid points within the flow domain
Nsamp = length(Xref_in);
%% Running the code of Joelle Aubin and Alena Kukukova, 2010
% Get length of particles
L = length(X);
% Nearest_Distance represent the nearest distances corresponding for each
% grid point
Nearest_Distance = [];
% loop through all grid points of rectangular grid point 1
for n = 1:Nsamp
% Create column vectors Xp1 & Yp1 with L lines.
% All values in each column are the same and correspond to the
% coordinates of point, 'n', i.e. (x1_in(n),y1_in(n))
% The function ones(i,j) creates a i x j matrix with i lines
% and j columns
    Xp = ones(L,1)*Xref_in(n);
    Yp = ones(L,1)*Yref_in(n);
% Calculate the distance between all particles (u_norm, v_norm)
% and grid point 'n'(Xp1, Yp1).
    D = sqrt((X - Xp).^2 + (Y - Yp).^2);
% Sort the elements of D1 in increasing order. D1 is a column vector of
% length L i.e for the specified grid point n we have measured the
% nearest particle to it
    Dsort = sort(D);
% Take the second element of Dsort as the nearest point-event distance.
    dist = Dsort(2);
% Nearest_Distance is a colum vector of length equal to the number of sampling grid
% points.
    Nearest_Distance = [Nearest_Distance;dist] ;
end
result{1,f} = Nearest_Distance;

```

```

end
%% Reporting the nearest distances for each grid point within each cross-section
inlet = result{1,1};
Midway_scr_1_2 = result{1,2};
Midway_scr_2_3 = result{1,3};
Midway_scr_3_4 = result{1,4};
Midway_scr_4_5 = result{1,5};
Midway_scr_5_6 = result{1,6};
Midway_scr_6_7 = result{1,7};
Midway_scr_7_8 = result{1,8};
outlet = result{1,9};
VarNames={'inlet','Midway_scr_1_2','Midway_scr_2_3','Midway_scr_3_4','Midway_scr_4_5','Midway_sc
r_5_6','Midway_scr_6_7','Midway_scr_7_8','outlet'};
T =
table(inlet,Midway_scr_1_2,Midway_scr_2_3,Midway_scr_3_4,Midway_scr_4_5,Midway_scr_5_6,Midw
ay_scr_6_7,Midway_scr_7_8,outlet,'VariableNames',VarNames);

filename = 'results.xlsx';
writetable(T,filename)

```

The “StaggeredGridGeneration” function:

```

function [Xref_in,Yref_in,Xref_out,Yref_out] = StaggeredGridGeneration (hori_div,radius_norm)
% First rectangular grid
x0 = 0; x00 = 1; y0 = 0; y00 = 1; lx = x00-x0; ly = y00-y0;
M = hori_div; N = M/2;
dx = lx/M; dy = ly/N;
% origin for the second rectangular grid
dx_new = dx/2;
dy_new = dy/2;
% second rectangular grid
x10 = dx_new; x11 = 1-dx_new; y10 = dy_new; y11 = 1-dy_new;
lx1 = (x11-x10); ly1 = (y11-y10);
M1 = M-1; N1 = N-1;
dx1 = lx1/M1; dy1 = ly1/N1;
%% Matrix Mesh Generation using matlab Command
% Coordinates of the rectangular grid 1
[x1,y1] = meshgrid(x0:dx:x00,y0:dy:y00);
% Coordinates of the rectangular grid 2
[x2,y2] = meshgrid(x10:dx1:x11,y10:dy1:y11);
%% Finding the staggered grid points that are in and outside the flow field
% The function pointsincircle could be downloaded from Mathworks using the
% the link https://www.mathworks.com/matlabcentral/fileexchange/35791-rapidly-find-the-points-lying-inside-a-cut-off-radius
% Finding points of the grid that are in and outside the circle
hk = [0.000 0.000];
[points_1] = pointsincircle({x1 y1},radius_norm,hk);
% (x1_in,y1_in) and (x1_out,y1_out) are the coordinates of the grid
% points of rectangular grid 1 lying within and outside the
% flow domain (quarter pipe), respectively.
x1_in = points_1.in{1};
y1_in = points_1.in{2};
x1_out = points_1.out{1};
y1_out = points_1.out{2};
[points_2] = pointsincircle({x2 y2},radius_norm,hk);
% (x2_in,y2_in) and (x2_out,y2_out) are the coordinates of the grid
% points of rectangular grid 2 lying within and outside the
% flow domain (quarter pipe), respectively.
x2_in = points_2.in{1};
y2_in = points_2.in{2};
x2_out = points_2.out{1};
y2_out = points_2.out{2};
% Grouping all the grid points lying within the flow domain such that

```



```

% Xref_in represents x_ordinate and Yref_in respresents y_ordinate
Xref_in = [x1_in;x2_in];
Yref_in = [y1_in;y2_in];
% Grouping all the grid points lying outside the flow domain such that
% Xref_out represents x_ordinate and Yref_out respresents y_ordinate
Xref_out = [x1_out;x2_out];
Yref_out = [y1_out;y2_out];

```

The “pointsincircle” function:

Link for the code version 1.0.0.0:

<https://www.mathworks.com/matlabcentral/fileexchange/35791-rapidly-find-the-points-lying-inside-a-cut-off-radius>

```

function [points] = pointsincircle(xydata,radius,hk)
% POINTSINCIRCLE Identify points lying inside a circle
% COMPLETELY VECTORIZED
% Version 1.1 (Feb 29, 2012, 9:02 pm)
% Version 1.0 (Feb 23, 2012) of this function was not uploaded
% Find all points within a specified cut-off radius
% Copyright, Sunil Anandatheertha Feb 23, 2012
% INPUT:
% xydata: a cell in the form xydata = {XvaluesOfCoordinates YvaluesOfCoordinates}.
% radius: cut-off distance / cut-off radius
% hk - h and k are the starting point of the radius vector.
% OUTPUT:
% points: this is a structure containing upto 2 values.
%     points.in ---- cell of x- and y- coordinate data of all points inside the cut-off
%           radius
%     points.out ---- cell of x- and y- coordinate data of all points outside the cut-off
%           radius
dist = sqrt((hk(1) - xydata{1}(:)).^2 + (hk(2) - xydata{2}(:)).^2); % distance calc.
% Find points inside circle
in = find(dist<=radius);
points.in = {xydata{1}(in) xydata{2}(in)};
% Find points outside circle
% comment it out if its not needed
% its needed to run the testrun.m file though !!
out = find(dist>radius);
points.out = {xydata{1}(out) xydata{2}(out)};
% ADDITIONAL --- USE TESTRUN.M TO SEE HOW TO USE THIS CODE
end

```

2.4 Mixing efficiency

```

%%%%%%%%%%%%%%%%%%%%%%%%%%%%%%%%%%%%%%%%%%%%%%%%%%%%%%%%%%%%%%%%%%%%%%%%
%%%%%%%%%%%%%%%%%%%%%%%%%%%%%%%%%%%%%%%%%%%%%%%%%%%%%%%%%%%%%%%%%%%%%%%%
% This code evaluates the mixing efficiency within the STSM by applying
% the approach proposed by Medina et al. (2019).
%%%%%%%%%%%%%%%%%%%%%%%%%%%%%%%%%%%%%%%%%%%%%%%%%%%%%%%%%%%%%%%%%%%%%%%%
%%%%%%%%%%%%%%%%%%%%%%%%%%%%%%%%%%%%%%%%%%%%%%%%%%%%%%%%%%%%%%%%%%%%%%%%
%% Inputs
% Enter the horizontal and vertical division
m = 17;
n = 17;
% The excel files are divided into two files, one for the inner particle
% distributions and one for the outer particle distributions. Moreover,
% each excel file for either inner or outer particles include the

```

```

% particles locations at different cross-sections (sheet) extracted from
% fluent such that the sheet named '0' represents the inlet and '4'
% represents the midway between the 4th and 5th screen.
sheet_outer = '8';
sheet_inner = '8';
filename_outer = 'r_over_R_point5_outer_Reb20L50Mn20';
filename_inner = 'r_over_R_point5_inner_Reb20L50Mn20';
%% Generation of a grid m*n
% The grid was generated using the Matlab code TFI could be downloaded from Mathworks using the
% following link https://www.mathworks.com/matlabcentral/fileexchange/40681-transfinite-interpolation
% The TFI code is converted to a function to be used in the current code.
% Xref,Yref are the coordinates of the generated grid.
[Xref,Yref] = TFI(m,n);
%% Plotting the particles
% The inner particle distributions are colored red on the plots and the
% outer particle distributions are colored blue on the plots.
% blue particles ==> outer particles
Data = xlsread(filename_outer,sheet_outer);
Xp_blue = Data(:,1);
Yp_blue = Data(:,2);
xlim = 7e-3;
ylim = 7e-3;
hold on
plot(Xp_blue,Yp_blue,'bo','MarkerSize',3,'MarkerFaceColor','blue');
pbaspect([1 1 1]); % ratio of x-axis to the y-axis etc
axis([0 xlim 0 ylim])
% red particles ==> inner particles
Data = xlsread(filename_inner,sheet_inner);
Xp_red = Data(:,1);
Yp_red = Data(:,2);
xlim = 7e-3;
ylim = 7e-3;
hold on
plot(Xp_red,Yp_red,'ro','MarkerSize',3,'MarkerFaceColor','red');
pbaspect([1 1 1]); % ratio of x-axis to the y-axis etc
axis([0 xlim 0 ylim])
% plot of circle
hold on
rectangle('position',[-6.35e-3 -6.35e-3 12.7e-3 12.7e-3],'Curvature', [1 1],'EdgeColor','k','LineWidth',2);
axis([0 xlim 0 ylim])
%% Finding points of the grid that are outside circle
% xydata represents the coordinates of the generated grid which covers the
% quarter pipe as a rectangular grid.
xydata = {Xref,Yref};
% Dealing with a quarter pipe, the grids that are outside the flow domain
% should be excluded from the study.
% The function pointsincircle could be downloaded from Mathworks using the
% the link https://www.mathworks.com/matlabcentral/fileexchange/35791-rapidly-find-the-points-lying-inside-a-cut-off-radius
% Pipe origin
hk = [0.000 0.000];
% pipe radius that is the cutting edge.
radius = 6.35e-3;
% The points variable list all the grid points lying within and outside the
% flow domain. Hence, the grid points lying within the flow domain are
% reported as Xref_in and Yref_in.
[points] = pointsincircle(xydata,radius,hk);
% rounding is done up to 10 digits after the decimal point
Xref_in = round(points.in{1},10);
Yref_in = round(points.in{2},10);
%% Selecting the live cells and evaluating the number of particles in each live cell
% First, it is required to find the cells that fully fall within the flow
% domain, i.e. cells that fully or partially fall outside the flow domain
% are excluded from the study.

```

```

% Initialize the number_live_cells and number_dead_cells to be 0.
number_live_cells = 0;
number_dead_cells = 0;
% Run the loop over all the cells to extract the live cells.
for j = 2:n
    for i = 2:m
        % The below command lines check if each corner of the cell is
        % within the flow domain or outside by checking if the value of
        % that corner matches the coordinates of the grid points
        % (Xref_in,Yref_in) that fall within the flow domain. If the value of
        % cor_1,cor_2... resulted in an empty array then this cell is partially
        % or fully outside the flow domain. If there is a value for cor_1,
        % cor_2...then this value is the index of that grid point.
        % Note that cor_1 corresponds to the corner of the cell located
        % at the bottom right. Corners 2,3,4 follow the counter-clockwise starting
        % from cor_1.
        cor_1 = find(Xref_in==round((i-1)*6.35e-3/(m-1),10) & Yref_in==round((j-2)*6.35e-3/(n-1),10));
        cor_2 = find(Xref_in==round((i-1)*6.35e-3/(m-1),10) & Yref_in==round((j-1)*6.35e-3/(n-1),10));
        cor_3 = find(Xref_in==round((i-2)*6.35e-3/(m-1),10) & Yref_in==round((j-1)*6.35e-3/(n-1),10));
        cor_4 = find(Xref_in==round((i-2)*6.35e-3/(m-1),10) & Yref_in==round((j-2)*6.35e-3/(n-1),10));
        % A simple condition to check if all the corners of the cell fall
        % within the flow domain by checking if cor_1,cor_2... has an empty array.
        % Notice that an empty array has a length of 0.
        f1 = length(cor_1);
        f2 = length(cor_2);
        f3 = length(cor_3);
        f4 = length(cor_4);
        if f1 == 0
            cor_1 = 0;
        end
        if f2 == 0
            cor_2 = 0;
        end
        if f3 == 0
            cor_3 = 0;
        end
        if f4 == 0
            cor_4 = 0;
        end
        % If the prod is 0, then one or more of the corners of the cell fall
        % outside the flow domain. The cell will be excluded from the domain,
        % otherwise it will be a live cell.
        prod = cor_1*cor_2*cor_3*cor_4;
        if prod == 0
            % Increase the number of dead cells by 1.
            number_dead_cells = number_dead_cells + 1;
        else
            % Get coordinates of the live cell
            X_corner = [ Xref_in(cor_1) Xref_in(cor_2) Xref_in(cor_3) Xref_in(cor_4)];
            Y_corner = [ Yref_in(cor_1) Yref_in(cor_2) Yref_in(cor_3) Yref_in(cor_4)];
            % Get a logical array of the particles (red and blue particles)
            % if they fall within each live cell
            in_red = inpolygon(Xp_red,Yp_red,X_corner,Y_corner);
            in_blue = inpolygon(Xp_blue,Yp_blue,X_corner,Y_corner);
            % Increase the number of live cells by 1.
            number_live_cells = number_live_cells + 1;
            % N_red is an array of the number of red particles in each live cell.
            % N_blue is an array of the number of blue particles in each live cell.
            N_red(number_live_cells) = numel(Xp_red(in_red));
            N_blue(number_live_cells) = numel(Xp_blue(in_blue));
        end
    end
end
% An array representing total number of particles in each live cell

```

```

% Notice that the length of N_zetaM is the same as the number_live_cells
% array.
N_zetaM = N_blue + N_red;
%% Evaluation of the zeta_M parameter as defined by Medina et al. (2019)
for k = 1:length(N_zetaM)
% look for cells that has particles
    if N_zetaM(k)~=0
        x_b(k) = N_blue(k)./N_zetaM(k); % represents concentration of the species of outer particles in the
cell
        x_r(k) = N_red(k)./N_zetaM(k); % represents concentration of the species of inner particles in the
cell
% look for cells that doesn't contain particles
    else
        x_b(k) = 0;
        x_r(k) = 0;
% If a cell doesn't contain particles then report a message stating that
% the number of divisions should be changed.
        fprintf('One or more cells have no particles which is not logical, change m and n values')
    end
end
A_total = 0.00635^2; % area of a cell
ai = A_total/((m-1)*(n-1)); % all the cells are equal
A_total_new = ai*number_live_cells; % since we are dealing with live cells each having an ai value.
z_b = ai * sum(x_b)/A_total_new; % average concentration of the blue particles in a cross-section
z_r = ai * sum(x_r)/A_total_new; % average concentration of the red particles in a cross-section
z_cross_section = z_b + z_r; % Notice that z_b+z_r should add to 1
% finding delta_S_mix
for k = 1:length(N_zetaM)
    if x_b(k) == 0 || x_r(k) == 0
        h(k) = 0; % indication of no mixing
    else
        h(k) = x_b(k)*log(x_b(k)) + x_r(k)*log(x_r(k));
    end
end
delta_S_mix = -ai * sum(h)/A_total_new;
% finding delta_S_mix_max
delta_S_mix_max = -(z_b*log(z_b) + z_r*log(z_r));
% finding mixing efficiency parameter (zeta_M)
zeta_M = delta_S_mix/delta_S_mix_max;
%% Reporting the results
VarNames={'number_live_cells','number_dead_cells','z_cross_section','zeta_M'};
T = table(number_live_cells,number_dead_cells,z_cross_section,zeta_M,'VariableNames',VarNames)

```

The “TFI” function:

Link for the code:

<https://www.mathworks.com/matlabcentral/fileexchange/40681-transfinite-interpolation>

```

%% To demonstarte grid generation using Transfinite Interpolation (TFI)
%{
Author : Siva Srinivas Kolukula
        Senior Research Fellow
        Structural Mechanics Laboratory
        Indira Gandhi Center for Atomic Research
        India
E-mail : allwayzitzme@gmail.com
        http://sites.google.com/site/kolukulasivasrinivas/
%}
% Reference: Fundametnals of Grid Generation - Knupp, Steinberg
%% Setting the code to be as a fuction.

```

```

function [X, Y] = TFI(m,n)
% m,n are the number of discretizations along xi and eta axis
% if we have m = 10, then we will have 10 nodes and 9 elements.
% discretize along xi and eta axis
xi = linspace(0.,1,m) ;
eta = linspace(0.,1.,n) ;
% Initialize matrices in x and y axis
X = zeros(m,n) ;
Y = zeros(m,n) ;
for i = 1:m
    Xi = xi(i) ;
    for j = 1:n
        Eta = eta(j) ;
        % Transfinite Interpolation
        XY = (1-Eta)*Xb(Xi)+Eta*Xt(Xi)+(1-Xi)*Xl(Eta)+Xi*Xr(Eta).....
            -(Xi*Eta*Xt(1)+Xi*(1-Eta)*Xb(1)+Eta*(1-Xi)*Xt(0)+(1-Xi)*(1-Eta)*Xb(0)) ;
        X(i,j) = XY(1) ;
        Y(i,j) = XY(2) ;
    end
end
% plotting of the grid using the function plotgrid
plotgrid(X,Y) ;

```

<pre> function xyb = Xb(s) x = 0.00635*s ; y = 0 ; xyb = [x ; y] ; </pre>	<pre> function xyl = Xl(s) x = 0 ; y = 0.00635*s ; xyl = [x ; y] ; </pre>
<pre> function xyr = Xr(s) x = 0.00635 ; y = 0.00635*s ; xyr = [x ; y] ; </pre>	<pre> function xyt = Xt(s) x = 0.00635*s ; y = 0.00635 ; xyt = [x ; y] ; </pre>

```

function plotgrid(X,Y)
% plotgrid: To plot structured grid.
% plotgrid(X,Y)
% INPUT:
% X (matrix) - matrix with x-coordinates of gridpoints
% Y (matrix) - matrix with y-coordinates of gridpoints
if any(size(X)~=size(Y))
    error('Dimensions of X and Y must be equal');
end
[m,n]=size(X);
% Plot grid
figure
set(gcf,'color','w') ;
axis equal
axis on
box on
hold on
% Plot internal grid lines
for i=1:m
    plot(X(i,:),Y(i,:), 'k', 'linewidth', 1);
end
for j=1:n
    plot(X(:,j),Y(:,j), 'k', 'linewidth', 1);
end
hold off

```

2.5 Cumulative volume percentage for extensional efficiency

```
%%%%%%%%%%%%%%%%%%%%%%%%%%%%%%%%%%%%%%%%%%%%%%%%%%%%%%%%%%%%%%%%%%%%%%%%
%%%%%%%%%%%%%%%%%%%%%%%%%%%%%%%%%%%%%%%%%%%%%%%%%%%%%%%%%%%%%%%%%%%%%%%%
% Calculation of the cumulative volume percentage of extensional efficiency
%%%%%%%%%%%%%%%%%%%%%%%%%%%%%%%%%%%%%%%%%%%%%%%%%%%%%%%%%%%%%%%%%%%%%%%%
%%%%%%%%%%%%%%%%%%%%%%%%%%%%%%%%%%%%%%%%%%%%%%%%%%%%%%%%%%%%%%%%%%%%%%%%
% This code imports the data of the extensional efficiency and the cell
% volume and search for values where the extensional efficiency is greater
% than a specified value and then get the volume of the elements having
% that extensional efficiency and add them up and divide them by the total
% volume of the domain ==> This gives the % volume.
% After exporting the extensional efficiency and the cell volume from
% Fluent in ASCII format, the file is read as text file. This text file
% consists of 6 columns where the first column is the cell number
% and the following three columns are cell coordinates in X, Y, Z, followed
% by the Extensional efficiency and cell volume.
%% Reading text data
filename = 'Mn20_L15_Reb1000.txt';
A = importdata(filename);
Z_coordinate = A.data(:,4);
Ext_Eff = A.data(:,5);
Volume = A.data(:,6);

Ext_Eff_Bounded_indices = find(Z_coordinate <= 82.55e-3); % Get the indices
% of the data bounded between inlet and 1D downstream of the last mixer.
Ext_Eff_Bounded_values = Ext_Eff(Ext_Eff_Bounded_indices); % Get the
% extensional of the data having the aforementioned Z-coordinate.
Volume_Bounded_values = Volume(Ext_Eff_Bounded_indices); % Get the
% volume of the data having the aforementioned Z-coordinate.
domain_total_volume = sum(Volume_Bounded_values); % Get the volume of the
% domain bounded by the aforementioned Z-coordinate.

indices_ext_eff_point_4 = find(Ext_Eff_Bounded_values >= 0.4); % Get the
% indices from the bounded data having ext eff >=0.4
volume_point_4 = sum(Volume_Bounded_values(indices_ext_eff_point_4)); % Get
% the volume from the bounded data having ext eff >=0.4
ratio_point_4 = volume_point_4/domain_total_volume;

% Follow the same procedure for the other ranges.
indices_ext_eff_point_425 = find(Ext_Eff_Bounded_values >= 0.425);
volume_point_425 = sum(Volume_Bounded_values(indices_ext_eff_point_425));
ratio_point_425 = volume_point_425/domain_total_volume;
indices_ext_eff_point_45 = find(Ext_Eff_Bounded_values >= 0.45);
volume_point_45 = sum(Volume_Bounded_values(indices_ext_eff_point_45));
ratio_point_45 = volume_point_45/domain_total_volume;
indices_ext_eff_point_475 = find(Ext_Eff_Bounded_values >= 0.475);
volume_point_475 = sum(Volume_Bounded_values(indices_ext_eff_point_475));
ratio_point_475 = volume_point_475/domain_total_volume;
indices_ext_eff_point_5 = find(Ext_Eff_Bounded_values >= 0.5);
volume_point_5 = sum(Volume_Bounded_values(indices_ext_eff_point_5));
ratio_point_5 = volume_point_5/domain_total_volume;
indices_ext_eff_point_525 = find(Ext_Eff_Bounded_values >= 0.525);
volume_point_525 = sum(Volume_Bounded_values(indices_ext_eff_point_525));
ratio_point_525 = volume_point_525/domain_total_volume;
indices_ext_eff_point_55 = find(Ext_Eff_Bounded_values >= 0.55);
volume_point_55 = sum(Volume_Bounded_values(indices_ext_eff_point_55));
ratio_point_55 = volume_point_55/domain_total_volume;
indices_ext_eff_point_575 = find(Ext_Eff_Bounded_values >= 0.575);
volume_point_575 = sum(Volume_Bounded_values(indices_ext_eff_point_575));
ratio_point_575 = volume_point_575/domain_total_volume;
indices_ext_eff_point_6 = find(Ext_Eff_Bounded_values >= 0.6);
volume_point_6 = sum(Volume_Bounded_values(indices_ext_eff_point_6));
ratio_point_6 = volume_point_6/domain_total_volume;
```

```

indices_ext_eff_point_625 = find(Ext_Eff_Bounded_values >= 0.625);
volume_point_625 = sum(Volume_Bounded_values(indices_ext_eff_point_625));
ratio_point_625 = volume_point_625/domain_total_volume;
indices_ext_eff_point_65 = find(Ext_Eff_Bounded_values >= 0.65);
volume_point_65 = sum(Volume_Bounded_values(indices_ext_eff_point_65));
ratio_point_65 = volume_point_65/domain_total_volume;
indices_ext_eff_point_675 = find(Ext_Eff_Bounded_values >= 0.675);
volume_point_675 = sum(Volume_Bounded_values(indices_ext_eff_point_675));
ratio_point_675 = volume_point_675/domain_total_volume;
indices_ext_eff_point_7 = find(Ext_Eff_Bounded_values >= 0.7);
volume_point_7 = sum(Volume_Bounded_values(indices_ext_eff_point_7));
ratio_point_7 = volume_point_7/domain_total_volume;
indices_ext_eff_point_725 = find(Ext_Eff_Bounded_values >= 0.725);
volume_point_725 = sum(Volume_Bounded_values(indices_ext_eff_point_725));
ratio_point_725 = volume_point_725/domain_total_volume;
indices_ext_eff_point_75 = find(Ext_Eff_Bounded_values >= 0.75);
volume_point_75 = sum(Volume_Bounded_values(indices_ext_eff_point_75));
ratio_point_75 = volume_point_75/domain_total_volume;
indices_ext_eff_point_775 = find(Ext_Eff_Bounded_values >= 0.775);
volume_point_775 = sum(Volume_Bounded_values(indices_ext_eff_point_775));
ratio_point_775 = volume_point_775/domain_total_volume;
indices_ext_eff_point_8 = find(Ext_Eff_Bounded_values >= 0.8);
volume_point_8 = sum(Volume_Bounded_values(indices_ext_eff_point_8));
ratio_point_8 = volume_point_8/domain_total_volume;
indices_ext_eff_point_825 = find(Ext_Eff_Bounded_values >= 0.825);
volume_point_825 = sum(Volume_Bounded_values(indices_ext_eff_point_825));
ratio_point_825 = volume_point_825/domain_total_volume;
indices_ext_eff_point_85 = find(Ext_Eff_Bounded_values >= 0.85);
volume_point_85 = sum(Volume_Bounded_values(indices_ext_eff_point_85));
ratio_point_85 = volume_point_85/domain_total_volume;
indices_ext_eff_point_875 = find(Ext_Eff_Bounded_values >= 0.875);
volume_point_875 = sum(Volume_Bounded_values(indices_ext_eff_point_875));
ratio_point_875 = volume_point_875/domain_total_volume;
indices_ext_eff_point_9 = find(Ext_Eff_Bounded_values >= 0.9);
volume_point_9 = sum(Volume_Bounded_values(indices_ext_eff_point_9));
ratio_point_9 = volume_point_9/domain_total_volume;
indices_ext_eff_point_925 = find(Ext_Eff_Bounded_values >= 0.925);
volume_point_925 = sum(Volume_Bounded_values(indices_ext_eff_point_925));
ratio_point_925 = volume_point_925/domain_total_volume;
indices_ext_eff_point_95 = find(Ext_Eff_Bounded_values >= 0.95);
volume_point_95 = sum(Volume_Bounded_values(indices_ext_eff_point_95));
ratio_point_95 = volume_point_95/domain_total_volume;
indices_ext_eff_point_975 = find(Ext_Eff_Bounded_values >= 0.975);
volume_point_975 = sum(Volume_Bounded_values(indices_ext_eff_point_975));
ratio_point_975 = volume_point_975/domain_total_volume;
indices_ext_eff_1 = find(Ext_Eff_Bounded_values == 1);
volume_1 = sum(Volume_Bounded_values(indices_ext_eff_1));
ratio_1 = volume_1/domain_total_volume;
range = [0.4 0.425 0.45 0.475 0.5 0.525 0.55 0.575 0.6 0.625 0.65 0.675 ...
0.7 0.725 0.75 0.775 0.8 0.825 0.85 0.875 0.9 0.925 0.95 0.975 1];
cum_vol = 100*[ratio_point_4 ratio_point_425 ratio_point_45 ratio_point_475 ratio_point_5...
ratio_point_525 ratio_point_55 ratio_point_575 ratio_point_6 ratio_point_625...
ratio_point_65 ratio_point_675 ratio_point_7 ratio_point_725 ratio_point_75...
ratio_point_775 ratio_point_8 ratio_point_825 ratio_point_85 ratio_point_875...
ratio_point_9 ratio_point_925 ratio_point_95 ratio_point_975 ratio_1];
%% Reporting the results
VarNames={'range','cum_vol'};
T = table(range,'cum_vol','VariableNames',VarNames)

```

2.6 Residence time distribution (RTD)

```

%%%%%%%%%%%%%%%%%%%%%%%%%%%%%%%%%%%%%%%%%%%%%%%%%%%%%%%%%%%%%%%%%%%%%%%%
%%%%%%%%%%%%%%%%%%%%%%%%%%%%%%%%%%%%%%%%%%%%%%%%%%%%%%%%%%%%%%%%%%%%%%%%

```

```

% This codes evalutes E(theta) and F(theta)
%%%%%%%%%%%%%%%%%%%%%%%%%%%%%%%%%%%%%%%%%%%%%%%%%%%%%%%%%%%%%%%%%%%%%%%%
% This code evaluates E(theta), F(theta) at Re = 30,000 using the
% pulse injection method around the third screen for Mn = 20 and Mn = 50.
% The plots are compared to the empty pipe. It should be noted
% that the plug flow condition was added for F(theta).
% The excel file of particular test case for example Mn20_Re30000 consists
% a sheet named "outlet_3" where the first column is the time and the
% second column is the mass_fraction.
%% Mn 20, scr3, Re = 30000
% mass_fraction from Fluent
sheet_out_scr3_outlet_3_Mn20_Re30000 = 'Outlet_3';
Data_Cout_scr3_outlet_3_Mn20_Re30000 = xlsread('Mn20_Re30000',...
    sheet_out_scr3_outlet_3_Mn20_Re30000);
% Data was extracted up to theta = 2.
tout_scr3_outlet_3_Mn20_Re30000 = Data_Cout_scr3_outlet_3_Mn20_Re30000 (1:1376,1);
Cout_scr3_outlet_3_Mn20_Re30000 = Data_Cout_scr3_outlet_3_Mn20_Re30000 (1:1376,2);
% E(t)
Efluent_1_scr3_outlet_3_Mn20_Re30000 = Cout_scr3_outlet_3_Mn20_Re30000./...
    trapz(tout_scr3_outlet_3_Mn20_Re30000,Cout_scr3_outlet_3_Mn20_Re30000); % as Numerical
Integration
% Area under the curve of E(t)
area_under_curve_scr3_outlet_3_Mn20_Re30000 =
trapz(tout_scr3_outlet_3_Mn20_Re30000,Efluent_1_scr3_outlet_3_Mn20_Re30000);
% F(t)
Ffluent_scr3_outlet_3_Mn20_Re30000 =
cumtrapz(tout_scr3_outlet_3_Mn20_Re30000,Efluent_1_scr3_outlet_3_Mn20_Re30000);
% Tmean
t_mean_C_1_scr3_outlet_3_Mn20_Re30000 =
trapz(tout_scr3_outlet_3_Mn20_Re30000,tout_scr3_outlet_3_Mn20_Re30000.*Cout_scr3_outlet_3_Mn
20_Re30000)/trapz(tout_scr3_outlet_3_Mn20_Re30000,Cout_scr3_outlet_3_Mn20_Re30000); % as
Numerical Integration
% Evaluating theta
theta_scr3_outlet_3_Mn20_Re30000 =
tout_scr3_outlet_3_Mn20_Re30000./t_mean_C_1_scr3_outlet_3_Mn20_Re30000;
max_theta_scr3_outlet_3_Mn20_Re30000 = max(theta_scr3_outlet_3_Mn20_Re30000 );
%% Mn = 50, scr3, Re = 30000
% mass_fraction from Fluent
sheet_out_scr3_outlet_3_Mn50_Re30000 = 'Outlet_3';
Data_Cout_scr3_outlet_3_Mn50_Re30000 =
xlsread('Mn50_Re30000',sheet_out_scr3_outlet_3_Mn50_Re30000);
% Data was extracted up to theta = 2.
tout_scr3_outlet_3_Mn50_Re30000 = Data_Cout_scr3_outlet_3_Mn50_Re30000 (1:2995,1);
Cout_scr3_outlet_3_Mn50_Re30000 = Data_Cout_scr3_outlet_3_Mn50_Re30000 (1:2995,2);
% E(t)
Efluent_1_scr3_outlet_3_Mn50_Re30000 =
Cout_scr3_outlet_3_Mn50_Re30000./trapz(tout_scr3_outlet_3_Mn50_Re30000,Cout_scr3_outlet_3_M
n50_Re30000); % as Numerical Integration
% Area under the curve of E(t)
area_under_curve_scr3_outlet_3_Mn50_Re30000 =
trapz(tout_scr3_outlet_3_Mn50_Re30000,Efluent_1_scr3_outlet_3_Mn50_Re30000);
% F(t)
Ffluent_scr3_outlet_3_Mn50_Re30000 =
cumtrapz(tout_scr3_outlet_3_Mn50_Re30000,Efluent_1_scr3_outlet_3_Mn50_Re30000);
% Tmean
t_mean_C_1_scr3_outlet_3_Mn50_Re30000 =
trapz(tout_scr3_outlet_3_Mn50_Re30000,tout_scr3_outlet_3_Mn50_Re30000.*Cout_scr3_outlet_3_Mn
50_Re30000)/trapz(tout_scr3_outlet_3_Mn50_Re30000,Cout_scr3_outlet_3_Mn50_Re30000); % as
Numerical Integration
% Evaluating theta

```



```

theta_scr3_outlet_3_Mn50_Re30000 =
tout_scr3_outlet_3_Mn50_Re30000./t_mean_C_1_scr3_outlet_3_Mn50_Re30000;
max_theta_scr3_outlet_3_Mn50_Re30000 = max(theta_scr3_outlet_3_Mn50_Re30000 );
%% Empty, Re = 30000
% mass_fraction from Fluent
sheet_out_outlet_3_Empty_Re30000 = 'Outlet_3';
Data_Cout_outlet_3_Empty_Re30000 =
xlsread('Empty_Re30000',sheet_out_outlet_3_Empty_Re30000);
% Data was extracted up to theta = 2.
tout_outlet_3_Empty_Re30000 = Data_Cout_outlet_3_Empty_Re30000 (1:122,1);
Cout_outlet_3_Empty_Re30000 = Data_Cout_outlet_3_Empty_Re30000 (1:122,2);
% E(t)
Efluent_1_outlet_3_Empty_Re30000 =
Cout_outlet_3_Empty_Re30000./trapz(tout_outlet_3_Empty_Re30000,Cout_outlet_3_Empty_Re30000
); % as Numerical Integration
% Area under the curve of E(t)
area_under_curve_outlet_3_Empty_Re30000 =
trapz(tout_outlet_3_Empty_Re30000,Efluent_1_outlet_3_Empty_Re30000);
% F(t)
Ffluent_outlet_3_Empty_Re30000 =
cumtrapz(tout_outlet_3_Empty_Re30000,Efluent_1_outlet_3_Empty_Re30000);
% Tmean
t_mean_C_1_outlet_3_Empty_Re30000 =
trapz(tout_outlet_3_Empty_Re30000,tout_outlet_3_Empty_Re30000.*Cout_outlet_3_Empty_Re30000)/
trapz(tout_outlet_3_Empty_Re30000,Cout_outlet_3_Empty_Re30000); % as Numerical Integration
% Evaluating theta
theta_outlet_3_Empty_Re30000 =
tout_outlet_3_Empty_Re30000./t_mean_C_1_outlet_3_Empty_Re30000;
max_theta_outlet_3_Empty_Re30000 = max(theta_outlet_3_Empty_Re30000 );
%% Plottings
% E(theta)
figure
plot(theta_outlet_3_Empty_Re30000,t_mean_C_1_outlet_3_Empty_Re30000*Efluent_1_outlet_3_Emp
ty_Re30000,'k-', 'linewidth',2.5)
hold on
plot(theta_scr3_outlet_3_Mn20_Re30000,t_mean_C_1_scr3_outlet_3_Mn20_Re30000*Efluent_1_scr3
_outlet_3_Mn20_Re30000,'b-', 'linewidth',2)
plot(theta_scr3_outlet_3_Mn50_Re30000,t_mean_C_1_scr3_outlet_3_Mn50_Re30000*Efluent_1_scr3
_outlet_3_Mn50_Re30000,'r--', 'linewidth',2)
set(gcf,'fontsize',35,'linewidth',1.5,'FontName', 'Helvetica')
xlabel('\bf \theta (-)', 'fontsize',35,'FontName', 'Helvetica')
ylabel('\bf E(\theta) (-)', 'fontsize',35,'FontName', 'Helvetica')
ylim([0 10.2])
xlim([0 2])
legend ('Empty pipe', '{\itMn} = 20', '{\itMn} = 50', 'location', 'northeast', 'fontsize',35,'FontName', 'Helvetica')
legend box off
set(gcf,'position',[0,0,800,600])
% Saving
figurename = strcat('E(theta)_different_screens_Re30000','.fig');
saveas(gcf,figurename);
% This code give dimensions similar to the figure if copied.
set(gcf,'Units','inches');
screenposition = get(gcf,'Position');
set(gcf,...
    'paperPosition',[0 0 screenposition(3:4)],...
    'paperSize',screenposition(3:4));
print -dpdf -painters E(theta)_different_screens_Re30000
%F(theta)
x_plug = [0 0.25 0.5 0.75 1 1 1.25 1.5 1.75 2];
y_plug = [0 0 0 0 1 1 1 1 1 1];
figure
F_theta_scr3_outlet_3_Mn20_Re30000 =
cumtrapz(theta_scr3_outlet_3_Mn20_Re30000,t_mean_C_1_scr3_outlet_3_Mn20_Re30000*Efluent_1
_scr3_outlet_3_Mn20_Re30000);

```

```

F_theta_scr3_outlet_3_Mn50_Re30000 =
cumtrapz(theta_scr3_outlet_3_Mn50_Re30000,t_mean_C_1_scr3_outlet_3_Mn50_Re30000*Efluent_1
_scr3_outlet_3_Mn50_Re30000);
F_theta_outlet_3_Empty_Re30000 =
cumtrapz(theta_outlet_3_Empty_Re30000,t_mean_C_1_outlet_3_Empty_Re30000*Efluent_1_outlet_3
_Empty_Re30000);
plot(x_plug,y_plug,'color',[0 0.5 0],'linestyle',':', 'linewidth',3)
hold on
plot(theta_outlet_3_Empty_Re30000,F_theta_outlet_3_Empty_Re30000,'k-', 'linewidth',2.5)
plot(theta_scr3_outlet_3_Mn20_Re30000,F_theta_scr3_outlet_3_Mn20_Re30000,'b-', 'linewidth',2)
plot(theta_scr3_outlet_3_Mn50_Re30000,F_theta_scr3_outlet_3_Mn50_Re30000,'r--', 'linewidth',2)
set(gca,'fontsize',35,'linewidth',1.5,'FontName', 'Helvetica')
xlabel('\bf \theta (-)', 'fontsize',35,'FontName', 'Helvetica')
ylabel('\bf F(\theta) (-)', 'fontsize',35,'FontName', 'Helvetica')
xlim([0 2])
legend ('Plug flow', 'Empty pipe', '\itMn} = 20', '\itMn} =
50', 'location', 'southeast', 'fontsize',35,'FontName', 'Helvetica')
legend box off
set(gcf,'position',[0,0,800,600])
% Saving
figurename = strcat('F(theta)_different_screens_Re30000','.fig');
saveas(gcf,figurename);
% This code give dimensions similar to the figure if copied.
set(gcf,'Units','inches');
screenposition = get(gcf,'Position');
set(gcf,...
    'paperPosition',[0 0 screenposition(3:4)],...
    'paperSize',screenposition(3:4));
print -dpdf -painters F(theta)_different_screens_Re30000
L_outlet_3 = 152.4e-3;
% Average velocity as evaluated from inlet fluent
U_avg_scr3_outlet_3_Mn20_Re30000 = 2.373857;
U_avg_scr3_outlet_3_Mn50_Re30000 = 2.374295;
U_avg_outlet_3_Empty_Re30000 = 2.374384;
%% Theoretical Mean time
t_mean_theoretical_scr3_outlet_3_Mn20_Re30000 =
L_outlet_3/U_avg_scr3_outlet_3_Mn20_Re30000;
t_mean_theoretical_scr3_outlet_3_Mn50_Re30000 =
L_outlet_3/U_avg_scr3_outlet_3_Mn50_Re30000;
t_mean_theoretical_outlet_3_Empty_Re30000 = L_outlet_3/U_avg_outlet_3_Empty_Re30000;
%% Reporting mean time
t_mean_time = table
(t_mean_C_1_outlet_3_Empty_Re30000,t_mean_C_1_scr3_outlet_3_Mn50_Re30000,t_mean_C_1_s
cr3_outlet_3_Mn20_Re30000)
t_theractical = table
(t_mean_theoretical_outlet_3_Empty_Re30000,t_mean_theoretical_scr3_outlet_3_Mn50_Re30000,t_m
ean_theoretical_scr3_outlet_3_Mn20_Re30000)
t_max_theta = table
(max_theta_outlet_3_Empty_Re30000,max_theta_scr3_outlet_3_Mn50_Re30000,max_theta_scr3_outl
et_3_Mn20_Re30000)

```

REFERENCES

- A.Bennani, J.N.Gence, J.Mathieu, 1985. The Influence of a Grid-Generated Turbulence on the Development of Chemical Reactions. *AIChE J.* 31, 1157–1166.
- Abou-Hweij, W., Azizi, F., 2020. CFD simulation of wall-bounded laminar flow through screens. Part I: Hydrodynamic characterization. *Eur. J. Mech. B/Fluids* 84, 207–232. <https://doi.org/10.1016/j.euromechflu.2020.06.008>
- Abou Hweij, K., Azizi, F., 2015. Hydrodynamics and residence time distribution of liquid flow in tubular reactors equipped with screen-type static mixers. *Chem. Eng. J.* 279, 948–963. <https://doi.org/10.1016/j.cej.2015.05.100>
- Abou Hweij, W., Azizi, F., 2020. CFD Simulation of Wall-Bounded Laminar Flow Through Screens: Part II -- Mixing Characterization. *Proc. ASME 2020 Fluids Eng. Div. Summer Meet. FEDSM2020 V003T05A01*, 1–10. <https://doi.org/10.1115/FEDSM2020-20120>
- Adeosun, J.T., Lawal, A., 2009. Numerical and experimental studies of mixing characteristics in a T-junction microchannel using residence-time distribution. *Chem. Eng. Sci.* 64, 2422–2432. <https://doi.org/10.1016/j.ces.2009.02.013>
- Al-Hassan, T., Habchi, C., Lemenand, T., Azizi, F., 2021. CFD simulation of creeping flows in a novel split-and-recombine multifunctional reactor. *Chem. Eng. Process. - Process Intensif.* 162, 108353. <https://doi.org/10.1016/j.cep.2021.108353>
- Al Taweel, A.M., Azizi, F., Siriijeerachai, G., 2013. Static mixers: Effective means for intensifying mass transfer limited reactions. *Chem. Eng. Process. Process Intensif.* 72, 51–62. <https://doi.org/10.1016/j.cep.2013.08.009>
- Al Taweel, A.M., Chen, C., 1996. A novel static mixer for the effective dispersion of immiscible liquids. *Chem. Eng. Res. Des.*
- Al Taweel, A.M., Li, C., Gomaa, H.G., Yuet, P., 2007. Intensifying mass transfer between immiscible liquids: Using screen-type static mixers. *Chem. Eng. Res. Des.* 85, 760–765. <https://doi.org/10.1205/cherd06180>
- Al Taweel, A.M., Yan, J., Azizi, F., Oedra, D., Gomaa, H.G., 2005. Using in-line static mixers to intensify gas-liquid mass transfer processes. *Chem. Eng. Sci.* 60, 6378–6390. <https://doi.org/10.1016/j.ces.2005.03.011>
- Alberini, F., Simmons, M.J.H., Ingram, A., Stitt, E.H., 2013. Use of an Areal Distribution of Mixing Intensity to Describe Blending of Non-Newtonian Fluids in a Kenics KM Static Mixer Using PLIF. *AIChE J.* 60, 332–342. <https://doi.org/10.1002/aic>
- ANSYS, 2017. *ANSYS Fluent Theory Guide*, v.18.2. ANSYS Inc., USA.
- ANSYS, 2014. *ANSYS - Turbulence Modelling and the Law of the Wall: Tutorial*. ANSYS Inc., USA 1–48.
- Armour, J.C., Cannon, J.N., 1968. Fluid Flow Through Woven Screens. *AIChE J.* 14, 415–420.
- Avalosse, T., Crochet, M.J., 1997. Finite-element simulation of mixing: 2. Three-

- dimensional flow through a kenics mixer. *AIChE J.* 43, 588–597.
<https://doi.org/10.1002/aic.690430304>
- Azizi, F., 2019. On the pressure drop of fluids through woven screen meshes. *Chem. Eng. Sci.* 207, 464–478. <https://doi.org/10.1016/j.ces.2019.06.046>
- Azizi, F., Abou-Hweij, W., Lebaz, N., Sheibat-Othman, N., 2021. A numerical evaluation of flows through an SMX-Plus mixer. *Chem. Eng. Res. Des.* <https://doi.org/10.1016/j.cherd.2021.12.030>
- Azizi, F., Abou Hweij, K., 2017. Liquid-Phase Axial Dispersion of Turbulent Gas–Liquid Co-Current Flow Through Screen-Type Static Mixers. *AIChE J.* 63, 1390–1403. <https://doi.org/10.1002/aic>
- Azizi, F., Al Taweel, A.M., 2015. Mass Transfer in an Energy-Efficient High-Intensity Gas-Liquid Contactor. *Ind. Eng. Chem. Res.* 54, 11635–11652. <https://doi.org/10.1021/acs.iecr.5b01078>
- Azizi, F., Al Taweel, A.M., 2011a. Hydrodynamics of liquid flow through screens and screen-type static mixers. *Chem. Eng. Commun.* 198, 726–742. <https://doi.org/10.1080/00986445.2011.532748>
- Azizi, F., Al Taweel, A.M., 2011b. Turbulently flowing liquid-liquid dispersions. Part I: Drop breakage and coalescence. *Chem. Eng. J.* 166, 715–725. <https://doi.org/10.1016/j.cej.2010.11.050>
- Azizi, F., Al Taweel, A.M., 2007. Population balance simulation of gas-liquid contacting. *Chem. Eng. Sci.* 62, 7436–7445. <https://doi.org/10.1016/j.ces.2007.08.083>
- Bailey, B.J., Montero, J.J., Perez Parra, J., Robertson, A.P., Baeza, E., Kamaruddin, R., 2003. Airflow Resistance of Greenhouse Ventilators with and without Insect Screens. *Biosyst. Eng.* 86, 217–229. [https://doi.org/10.1016/S1537-5110\(03\)00115-6](https://doi.org/10.1016/S1537-5110(03)00115-6)
- Bałdyga, J., Pohorecki, R., 1995. Turbulent micromixing in chemical reactors - a review. *Chem. Eng. J. Biochem. Eng. J.* 58, 183–195. [https://doi.org/10.1016/0923-0467\(95\)02982-6](https://doi.org/10.1016/0923-0467(95)02982-6)
- Belhout, C., Bouzit, M., Menacer, B., Kamla, Y., Ameer, H., 2020. Numerical Study of Viscous Fluid Flows in a Kenics Static Mixer. *Mechanicka* 26, 206–211.
- Bourne, J.R., Lips, M., 1991. Micromixing in grid-generated turbulence: theoretical analysis and experimental study. *Chem. Eng. J.* 47, 155–162.
- Celik, I.B., Ghia, U., Roache, P.J., Freitas, C.J., Coleman, H., Raad, P.E., 2008. Procedure for estimation and reporting of uncertainty due to discretization in CFD applications. *J. Fluids Eng. Trans. ASME* 130, 0780011–0780014. <https://doi.org/10.1115/1.2960953>
- Chen, C., 1996. Dispersion and coalescence in static mixers.
- Coroneo, M., Montante, G., Paglianti, A., 2012. Computational fluid dynamics modeling of corrugated static mixers for turbulent applications. *Ind. Eng. Chem. Res.* 51, 15986–15996. <https://doi.org/10.1021/ie300398z>
- Costa, S.C., Barrutia, H., Esnaola, J.A., Tutar, M., 2013. Numerical study of the

- pressure drop phenomena in wound woven wire matrix of a Stirling regenerator. *Energy Convers. Manag.* 67, 57–65.
<https://doi.org/10.1016/j.enconman.2012.10.014>
- Dbouk, T., Habchi, C., 2019. On the mixing enhancement in concentrated non-colloidal neutrally buoyant suspensions of rigid particles using helical coiled and chaotic twisted pipes: A numerical investigation. *Chem. Eng. Process. - Process Intensif.* 141, 107540. <https://doi.org/10.1016/j.cep.2019.107540>
- De La Villéon, J., Bertrand, F., Tanguy, P.A., Labrie, R., Bousquet, J., Lebouvier, D., 1998. Numerical Investigation of Mixing Efficiency of Helical Ribbons. *AIChE J.* 44, 972–977. <https://doi.org/10.1002/aic.690440423>
- Ehrhardt, G., 1983. Flow Measurements for Wire Gauzes. *Int. Chem. Eng.*
- Fogler, H.S., 2004. Chemical reaction engineering, *The Engineering Handbook*, Second Edition. <https://doi.org/10.1201/9781420087567-13>
- Forde, O.O., 2012. Analysis of the Turbulent Energy Dissipation. Master Thesis 56.
- Fu, H., 2020. Heat transfer and residence time distribution of liquid flow in direct contact evaporation heat exchanger. *Chem. Eng. Process. - Process Intensif.* 149, 107829. <https://doi.org/10.1016/j.cep.2020.107829>
- G.B.Schubauer, W.G.Spangenberg, P.S.Klebanoff, 1948. Aerodynamic Characteristics of Damping Screens. Seventh Int. Congr. Appl. Mech. London, Sept. 5-11.
- Ghanem, A., Lemenand, T., Della, D., Peerhossaini, H., 2013. Chemical Engineering Research and Design Static mixers : Mechanisms , applications , and characterization methods – A review. *Chem. Eng. Res. Des.* 92, 205–228.
- González-Juárez, D., Solano, J.P., Herrero-Martín, R., Harvey, A.P., 2017. Residence time distribution in multiorifice baffled tubes: A numerical study. *Chem. Eng. Res. Des.* 118, 259–269. <https://doi.org/10.1016/j.cherd.2016.12.008>
- Green, S.I., Wang, Z., Waung, T., Vakil, A., 2008. Simulation of the flow through woven fabrics. *Comput. Fluids* 37, 1148–1156.
<https://doi.org/10.1016/j.compfluid.2007.10.013>
- Groth, J., Johansson, A. V., 1988. Turbulence reduction by screens. *J. Fluid Mech.* 197, 139–155. <https://doi.org/10.1017/S0022112088003209>
- Habchi, C., Azizi, F., 2018. Heat transfer and turbulent mixing characterization in screen-type static mixers. *Int. J. Therm. Sci.* 134, 208–215.
<https://doi.org/10.1016/j.ijthermalsci.2018.08.016>
- Habchi, C., Lemenand, T., Della Valle, D., Peerhossaini, H., 2009. Liquid/liquid dispersion in a chaotic advection flow. *Int. J. Multiph. Flow* 35, 485–497.
<https://doi.org/10.1016/j.ijmultiphaseflow.2009.02.019>
- Habchi, C., Lemenand, T., Valle, D. Della, Peerhossaini, H., 2010. Turbulent mixing and residence time distribution in novel multifunctional heat exchangers-reactors. *Chem. Eng. Process. Process Intensif.* 49, 1066–1075.
<https://doi.org/10.1016/j.cep.2010.08.007>
- Haddadi, M.M., Hosseini, S.H., Rashtchian, D., Ahmadi, G., 2019. CFD modeling of immiscible liquids turbulent dispersion in Kenics static mixers: Focusing on

- droplet behavior. *Chinese J. Chem. Eng.* 28, 348–361.
<https://doi.org/10.1016/j.cjche.2019.07.020>
- Haddadi, M.M., Hosseini, S.H., Rashtchian, D., Olazar, M., 2020. Comparative analysis of different static mixers performance by CFD technique: An innovative mixer. *Chinese J. Chem. Eng.* 28, 672–684. <https://doi.org/10.1016/j.cjche.2019.09.004>
- Hartmann, H., Derksen, J.J., Akker, H.E.A. van den, 2006. Mixing Times in a Turbulent Stirred Tank by Means of LES. *AIChE J.* 52, 3696–3706.
<https://doi.org/10.1002/aic>
- Heniche, M., Tanguy, P.A., Reeder, M.F., Fasano, J.B., 2005. Numerical investigation of blade shape in static mixing. *AIChE J.* 51, 44–58.
<https://doi.org/10.1002/aic.10341>
- Heyouni, A., Roustan, M., Do-quang, Z., 2002. Hydrodynamics and mass transfer in gas – liquid ow through static mixers. *Chem. Eng. Sci.* 57, 3325–3333.
- Hinze, J.O., 1975. *Turbulence*. McGraw-Hill - New York.
- Hirschberg, S., Koubek, R., F.Moser, Schöck, J., 2009. An improvement of the Sulzer SMXTM static mixer significantly reducing the pressure drop. *Chem. Eng. Res. Des.* 87, 524–532. <https://doi.org/10.1016/j.cherd.2008.12.021>
- Hobbs, D.M., Muzzio, F.J., 1998. Reynolds number effects on laminar mixing in the Kenics static mixer. *Chem. Eng. J.* 70, 93–104. [https://doi.org/10.1016/S1385-8947\(98\)00065-5](https://doi.org/10.1016/S1385-8947(98)00065-5)
- Hobbs, D.M., Muzzio, F.J., 1997a. Effects of injection location, flow ratio and geometry on kenics mixer performance. *AIChE J.* 43, 3121–3132.
<https://doi.org/10.1002/aic.690431202>
- Hobbs, D.M., Muzzio, F.J., 1997b. The Kenics static mixer: A three-dimensional chaotic flow. *Chem. Eng. J.* 67, 153–166. [https://doi.org/10.1016/S1385-8947\(97\)00013-2](https://doi.org/10.1016/S1385-8947(97)00013-2)
- Hobbs, D.M., Swanson, P.D., Muzzio, F.J., 1998. Numerical characterization of low Reynolds number flow in the Kenics static mixer. *Chem. Eng. Sci.* 53, 1565–1584.
[https://doi.org/10.1016/S0009-2509\(97\)00132-2](https://doi.org/10.1016/S0009-2509(97)00132-2)
- Irps, T., Kanjirakkad, V., 2016. On the interaction between turbulence grids and boundary layers. *EPJ Web Conf.* 114, 1–7.
<https://doi.org/10.1051/epjconf/201611402048>
- J. Baldyga, J.R.Bourne, 1989. Simplification of Micromixing Calculations. I. Derivation and Application of New Model. *Chem. Eng. J.* 42, 83–92.
- J.R.Sodre, J.A.R.Parise, 1997. Friction Factor Determination for Flow Tlrough Finite Wire-IVlesh Woven-Screen Matrices. *J. Fluids Eng.* 119, 847–851.
- Jegatheeswaran, S., Ein-Mozaffari, F., Wu, J., 2018. Process intensification in a chaotic SMX static mixer to achieve an energy-efficient mixing operation of non-newtonian fluids. *Chem. Eng. Process. Process Intensif.* 124, 1–10.
<https://doi.org/10.1016/j.cep.2017.11.018>
- Jerzy Baldyga, Bourne, J.R., 1999. *Turbulent Mixing and Chemical reactions*. Wiley. Chichester.

- Kandhai, D., Vidal, D.J.E., Hoekstra, A.G., Hoefsloot, H., Iedema, P., Slood, P.M.A., 1999. Lattice-Boltzmann and finite element simulations of fluid flow in a SMRX static mixer reactor. *Int. J. Numer. Methods Fluids* 31, 1019–1033. [https://doi.org/10.1002/\(SICI\)1097-0363\(19991130\)31:6<1019::AID-FLD915>3.0.CO;2-I](https://doi.org/10.1002/(SICI)1097-0363(19991130)31:6<1019::AID-FLD915>3.0.CO;2-I)
- Khan, L.A., 2012. CFD model to evaluate performance of a Kenics static mixer. *World Environ. Water Resour. Congr. 2012 Crossing Boundaries, Proc. 2012 Congr.* 658–668. <https://doi.org/10.1061/9780784412312.069>
- Kołodziej, A., Jaroszyński, M., Janus, B., Kleszcz, T., Łojewska, J., Łojewski, T., 2009. An experimental study of the pressure drop in fluid flows through wire gauzes. *Chem. Eng. Commun.* 196, 932–949. <https://doi.org/10.1080/00986440902743851>
- Kukukova, A., Aubin, J., Kresta, S.M., 2011. Measuring the scale of segregation in mixing data. *Can. J. Chem. Eng.* 89, 1122–1138. <https://doi.org/10.1002/cjce.20532>
- Kukukova, A., Noe'l, B., Kresta, uzanne M., 2008. Impact of Sampling Method and Scale on the Measurement of Mixing and the Coefficient of Variance. *AIChE J.* 54, 3068–3083. <https://doi.org/DOI 10.1002/aic.11639>
- Kumar, V., Shirke, V., Nigam, K.D.P., 2008. Performance of Kenics static mixer over a wide range of Reynolds number. *Chem. Eng. J.* 139, 284–295. <https://doi.org/10.1016/j.cej.2007.07.101>
- Kurian, T., Fransson, J.H.M., 2009. Grid-generated turbulence revisited. *Fluid Dyn. Res.* 41. <https://doi.org/10.1088/0169-5983/41/2/021403>
- Lane, G., 2015. Prediction the energy dissipation rate in a mechanically stirred tank. *Elev. Int. Conf. CFD Miner. Process Ind.* 7.
- Lau, Y.L., Baines, W.D., 1968. Flow of stratified fluid through curved screens. *J. Fluid Mech.* 33, 721–738. <https://doi.org/10.1017/S0022112068001643>
- Laws, E.M., Livesey, J.L., 1978. Flow Through Screens. *Annu Rev Fluid Mech* 10, 247–266. <https://doi.org/10.1146/annurev.fl.10.010178.001335>
- Leclaire, S., Vidal, D., Fradette, L., Bertrand, F., 2020. Validation of the pressure drop – flow rate relationship predicted by lattice Boltzmann simulations for immiscible liquid – liquid flows through SMX static mixers. *Chem. Eng. Res. Des.* 153, 350–368. <https://doi.org/10.1016/j.cherd.2019.10.035>
- Li, G., Mukhopadhyay, A., Cheng, C.Y., Dai, Y., 2010. Various approaches to compute fluid residence time in mixing systems. *Am. Soc. Mech. Eng. Fluids Eng. Div. FEDSM 1*, 295–304. <https://doi.org/10.1115/FEDSM-ICNMM2010-30771>
- Madhuranthakam, C.M.R., Pan, Q., Rempel, G.L., 2009. Residence time distribution and liquid holdup in Kenics® KMX static mixer with hydrogenated nitrile butadiene rubber solution and hydrogen gas system. *Chem. Eng. Sci.* 64, 3320–3328. <https://doi.org/10.1016/j.ces.2009.04.001>
- Mahammedi, A., Ameer, H., Ariss, A., 2017. Numerical Investigation of the Performance of Kenics Static Mixers for the Agitation of Shear Thinning Fluids. *J. Appl. Fluid Mech.* 10, 989–999. <https://doi.org/10.18869/acadpub.jafm.73.240.27314>

- Manas-Zloczower, I., 1994. Studies of Mixing Efficiency in Batch and Continuous Mixers.
- McCabe, W.L., Smith, J.C., Harriot, P., 2004. Unit Operations of Chemical Engineering 7th edition, McGraw-Hill, New York.
- Medina, H., Thomas, M., Eldredge, T., Adebajo, A., 2019. The M Number: A Novel Parameter to Evaluate the Performance of Static Mixers. *J. Fluids Eng. Trans. ASME* 141. <https://doi.org/10.1115/1.4044070>
- Mehta, R.D., 1985. Turbulent boundary layer perturbed by a screen. *AIAA J.* 23, 1335–1342. <https://doi.org/10.2514/3.9089>
- Meijer, H.E.H., Singh, M.K., Anderson, P.D., 2012. On the performance of static mixers: A quantitative comparison. *Prog. Polym. Sci.* 37, 1333–1349. <https://doi.org/10.1016/j.progpolymsci.2011.12.004>
- Meng, H., Han, M., Yu, Y., Wang, Z., Wu, J., 2020. Numerical evaluations on the characteristics of turbulent flow and heat transfer in the Lightning static mixer. *Int. J. Heat Mass Transf.* 156. <https://doi.org/10.1016/j.ijheatmasstransfer.2020.119788>
- Meng, H., Song, M., Yu, Y., Wang, F., Wu, J., 2015. Chaotic mixing characteristics in static mixers with different axial twisted-tape inserts. *Can. J. Chem. Eng.* 93, 1849–1859. <https://doi.org/10.1002/cjce.22268>
- Meng, H., Song, M.Y., Yu, Y.F., Jiang, X.H., Wang, Z.Y., Wu, J.H., 2017. Enhancement of Laminar Flow and Mixing Performance in a Lightning Static Mixer. *Int. J. Chem. React. Eng.* 15, 1–21. <https://doi.org/10.1515/ijcre-2016-0112>
- Meng, H., Wang, F., Yu, Y., Song, M., Wu, J., 2014. A numerical study of mixing performance of high-viscosity fluid in novel static mixers with multitwisted leaves. *Ind. Eng. Chem. Res.* 53, 4084–4095. <https://doi.org/10.1021/ie402970v>
- Middelstädt, F., Gerstmann, J., 2013. Numerical Investigations on Fluid Flow through Metal Screens. 5th Eur. Conf. Aeronaut. Sp. Sci.
- Mohand Kaci, H., Lemend, T., Della Valle, D., Peerhossaini, H., 2009. Effects of embedded streamwise vorticity on turbulent mixing. *Chem. Eng. Process. Process Intensif.* 48, 1459–1476. <https://doi.org/10.1016/j.cep.2009.08.002>
- Montante, G., Coroneo, M., Paglianti, A., 2016. Blending of miscible liquids with different densities and viscosities in static mixers. *Chem. Eng. Sci.* 141, 250–260. <https://doi.org/10.1016/j.ces.2015.11.009>
- Myers, K.J., Bakker, A., Ryan, D., 1997. Avoid Agitation by Selecting Static Mixers. *Chem. Eng. Prog.* 93, 28–38.
- Nauman, E.B., 2008. Residence Time Theory 3752–3766.
- Okolo, P.N., Zhao, K., Kennedy, J., Bennett, G.J., 2019. Numerical assessment of flow control capabilities of three dimensional woven wire mesh screens. *Eur. J. Mech. B/Fluids* 76, 259–271. <https://doi.org/10.1016/j.euromechflu.2019.03.001>
- Owen, P.R., Zienkiewicz, H.K., 1957. The production of uniform shear flow in a wind tunnel. *J. Fluid Mech.* 2, 521–531. <https://doi.org/10.1017/S0022112057000336>
- P.G.Morgan, 1959. High Speed Flow Through Wire Gauzes. *J. R. Aeronaut. Soc.* 63,

- 474–475. https://doi.org/10.1300/J184v06n04_07
- Peschel, A., Hentschel, B., Freund, H., Sundmacher, K., 2012. Design of optimal multiphase reactors exemplified on the hydroformylation of long chain alkenes. *Chem. Eng. J.* 188, 126–141. <https://doi.org/10.1016/j.cej.2012.01.123>
- Pianko-Oprych, P., Jaworski, Z., 2010. Prediction of liquid-liquid flow in an SMX static mixer using large eddy simulations. *Chem. Pap.* 64, 203–212. <https://doi.org/10.2478/s11696-009-0112-9>
- Pinker, R.A., Herbert, M.V., 1967. Pressure loss associated with compressible flow through square-mesh wire gauzes. *J. Mech. Eng. Sci.* 9, 11–23.
- Pope, S.B., 2001. *Turbulent Flows*.
- Rahmani, R.K., Keith, T.G., Ayasoufi, A., 2008. Numerical simulation of turbulent flow in an industrial helical static mixer. *Int. J. Numer. Methods Heat Fluid Flow* 18, 675–696. <https://doi.org/http://dx.doi.org/10.1108/09615530810885515>
- Rahmani, R.K., Keith, T.G., Ayasoufi, A., 2005. Three-dimensional numerical Simulation and performance study of an industrial helical static mixer. *J. Fluids Eng. Trans. ASME* 127, 467–483. <https://doi.org/10.1115/1.1899166>
- Ramesh, B., Nilesh, G., 2015. Modeling of Residence Time Distribution in FLUENT. *Ecol. Modell.* 35, 1–3.
- Rauline, D., Le Blévec, J.M., Bousquet, J., Tanguy, P.A., 2000. A Comparative Assessment of the Performance of the Kenics and SMX Static Mixers. *Chem. Eng. Res. Des.* 78, 389–396. <https://doi.org/http://dx.doi.org/10.1205/026387600527284>
- Rauline, D., TANGUY, P.A., Blevec, J.-M. Le, Bousquet, J., 1998. Numerical investigation of the performance of several static mixers.
- Raymond Mulley, 2004. *Flow of Industrial Fluids-Theory and Equations*, CRC Press.
- Regner, M., Östergren, K., Trägårdh, C., 2006. Effects of geometry and flow rate on secondary flow and the mixing process in static mixers-a numerical study. *Chem. Eng. Sci.* 61, 6133–6141. <https://doi.org/10.1016/j.ces.2006.05.044>
- Roach, P.E., 1986. The generation of nearly isotropic turbulence by means of grids. *Int. J. Heat Fluid Flow* 8, 82–92. [https://doi.org/10.1016/0142-727X\(87\)90001-4](https://doi.org/10.1016/0142-727X(87)90001-4)
- Santos, A.M., Souza, D.B., Costa, F.O., Farias, M.H., Massari, P.D.L., Araújo, S., Zanirath, Y.B., 2016. Effects of screens set characteristics on the flow field in a wind tunnel. *J. Phys. Conf. Ser.* 733. <https://doi.org/10.1088/1742-6596/733/1/012001>
- Soman, S.S., Madhuranthakam, C.M.R., 2017. Effects of internal geometry modifications on the dispersive and distributive mixing in static mixers. *Chem. Eng. Process. Process Intensif.* 122, 31–43. <https://doi.org/10.1016/j.cep.2017.10.001>
- Sosnowski, M., Krzywanski, J., Gnatowska, R., 2017. Polyhedral meshing as an innovative approach to computational domain discretization of a cyclone in a fluidized bed CLC unit. *E3S Web Conf.* 14. <https://doi.org/10.1051/e3sconf/20171401027>

- Sosnowski, M., Krzywanski, J., Grabowska, K., Gnatowska, R., 2018. Polyhedral meshing in numerical analysis of conjugate heat transfer. *EPJ Web Conf.* 180, 4–9. <https://doi.org/10.1051/epjconf/201817002096>
- Stec, M., Synowiec, P.M., 2019. Study of fluid dynamic conditions in the selected static mixers part III—research of mixture homogeneity. *Can. J. Chem. Eng.* 97, 995–1007. <https://doi.org/10.1002/cjce.23290>
- Stec, M., Synowiec, P.M., 2017a. Study of fluid dynamic conditions in the selected static mixers part II-determination of the residence time distribution. *Can. J. Chem. Eng.* 95, 2410–2422. <https://doi.org/10.1002/cjce.22879>
- Stec, M., Synowiec, P.M., 2017b. Study of fluid dynamic conditions in the selected static mixers part I- research of pressure drop. *Can. J. Chem. Eng.* 95, 2156–2167. <https://doi.org/10.1002/cjce.22929>
- Stewart, E.J., Huq, P., 2006. Dissipation rate correction methods. *Exp. Fluids* 40, 405–421. <https://doi.org/10.1007/s00348-005-0078-5>
- Thakur, R.K., Vial, C., Nigam, K.D.P., Nauman, E.B., Djelveh, G., 2003. Static mixers in the process industries - a review. *Chem. Eng. Res. Des.* 81, 787–826. <https://doi.org/10.1205/026387603322302968>
- Torrano, I., Tutar, M., Martinez-Agirre, M., Rouquier, A., Mordant, N., Bourgoïn, M., 2015. Comparison of experimental and RANS-based numerical studies of the decay of grid-generated turbulence. *J. Fluids Eng. Trans. ASME* 137, 1–12. <https://doi.org/10.1115/1.4029726>
- Wakeland, R.S., Keolian, R.M., 2003. Measurements of Resistance of Individual Square-Mesh Screens to Oscillating Flow at Low and Intermediate Reynolds Numbers. *J. Fluids Eng. Trans. ASME* 125, 851–862. <https://doi.org/10.1115/1.1601254>
- Wu, W.T., Liu, J.F., Li, W.J., Hsieh, W.H., 2005. Measurement and correlation of hydraulic resistance of flow through woven metal screens. *Int. J. Heat Mass Transf.* 48, 3008–3017. <https://doi.org/10.1016/j.ijheatmasstransfer.2005.01.038>
- York, B.T., MacDonald, B.D., 2021. Influence of misalignment and spacing on the pressure drop through wire mesh Stirling engine regenerators. *Energy Convers. Manag.* 245, 114588. <https://doi.org/10.1016/j.enconman.2021.114588>